CR-171725
C.1

Axiomatix

(NASA-CR-171725) ENGINEERING EVALUATIONS AND STUDIES. VOLUME 2: EXHIBIT B, PART 1 Final Report (Axiomatix, Los Angeles, Calif.) 322 p HC A14/MF A01 CSCL 22B

N84-15175

Unclas
G3/16 43326

ENGINEERING EVALUATIONS AND STUDIES

FINAL REPORT FOR CONTRACT NAS 9-16067

VOLUME II, EXHIBIT B Part 1

Part 1

Technical Monitor: William Teasdale

Prepared for

NASA Lyndon B. Johnson Space Center
Houston, Texas 77058

Prepared by

Unjeng Cheng
James G. Dodds
Gaylord K. Huth
Jack K. Holmes
Richard S. Iwasaki
Robert G. Maronde
Peter W. Nilsen
Andreas Polydoros
Don Roberts
Sergei Udalov
Charles L. Weber

Axiomatix
9841 Airport Blvd., Suite 912
Los Angeles, California 90045

Axiomatix Report No. R8310-6
October 31, 1983

TABLE OF CONTENTS

TABLE OF CONTENTS (CONTINUED)

6.0 KU-BAND COMMUNICATION SYSTEM ANALYSIS

The studies and investigations of the Ku-band communication system were focussed in the following areas:

(1) Shuttle/TDRSS sidelobe avoidance

(2) Shuttle/TDRSS acquisition and tracking performance

(3) Ku-band TDRSS ground station, two-channel, Costas-loop tracking performance for unbalanced quadriphase-shift-keying (UQPSK) with arbitrary data formats

(4) Ku-band bent-pipe mode 2 BER performance

(5) Degradation due to dither of the antenna during angle tracking

(6) Potential Ku-band sidelobe reduction.

Analyses of Shuttle/TDRSS sidelobe avoidance as well as Shuttle/TDRSS acquisition and tracking performance are presented in sections 6.1 and 6.2, respectively. Analysis of the two-channel Costas-loop tracking with UQPSK signals with arbitrary data formats is presented in Axiomatix Report No. R8010-8, dated October 30, 1980, which is included in this section. The analysis in this report was kept general, so the results can apply to a variety of Shuttle payload data formats. Specifically, the mean-square, phase-jitter performance is determined for the TDRSS ground station, two-channel Costas loop with active arm filters, synchronous or asynchronous symbol clocks, and arbitrary data formats.

The analysis of the Ku-band return-link mode 2 BER degradation is presented in Axiomatix Report No. R8102-4, "Ku-Band Bent-Pipe Mode 2 BER Performance Degradation," dated February 18, 1981. There are three inputs to the FM modulator in mode 2. First, on channel 3, there is the bent-pipe wideband signal which is amplitude (peak) regulated to provide 22 MHz peak-to-peak (p/p) carrier deviation. In addition, channel 1 has operations data from the network signal processor, and channel 2 receives data from the payload recorder, operations recorder, payload low-data-rate link or the payload interrogator narrowband bent-pipe signal. Channels 1 and 2 together provide for a p/p FM frequency deviation of 12 MHz. The specific case of concern in this report is the one wherein the signal of channel 1 is a 192-kbps biphase-L (Manchester) baseband data stream without thermal-noise corruption, channnel 2 has an NRZ baseband data stream plus thermal noise, and channel 3 is composed of two subcarriers, one at 1.024 MHz and one at 1.7 MHz, plus thermal noise.

Table 6.1. Sidelobe-Discrimination Budget [1]

	Weakest Mainlobe	Strongest Sidelobe	Cumulative Difference
Pointing Loss, dB	-3.0	-22.0	19.0 dB
Flux Density, dBW/m^2	-126.9	-113.5	
Antenna Gain, dB	37.1	37.1	
Effective Area (omni), dBm^2 (at 13.775 GHz)	-44.2	-44.2	
Effective Area, dBm^2	-7.1	-7.1	
Polarization Loss, dB	-0.2	0.0	
Received Power, dBW	-137.2	-142.6	5.4 dB
System Temperature, dB°K (at antenna terminals)	30.6	28.9	
Boltzmann's Constant	-228.6	-228.6	
C/N_0 dB-Hz (at EA-1 input)	60.8	57.1	3.7 dB
Threshold Setting, dB	-0.3	0.3	
Noise Immunity Margin, dB	-0.6	1.2	
Effective C/N_0, dB-Hz (at Detector)	59.9	58.6	1.3 dB

Another aspect of the Ku-band investigations performed was determining the degradation in the Ku-band communication system performance due to the introduction of dither during antenna angle tracking. The dither is introduced to overcome the effects of stiction and the resultant limit cycling of the antenna during angle tracking. The analysis for this performance degradation is presented in Axiomatix Technical Memorandum No. M8105-1, "Degradation Due To Dither," dated May 11, 1981. It is shown that the dither has no significant degradation on either angle-tracking or communication performance. However, a minor improvement in steady-state angle-tracking accuracy is required to maintain the 0.3-dB allowable pointing error with dither present.

Finally, Axiomatix Technical Memorandum No. M8302-1, "Potential Ku-Band Sidelobe Reduction Recommendation," dated February 16, 1983, presents an approach to modify the Ku-band antenna-feed-support structure in order to reduce the sidelobes. The relatively high sidelobes found in radar and communication systems have caused problems with acquisition throughout the development stage. The high (~ 20 dB) sidelobes in the communication system continue to be of concern during TDRSS acquisition. From the antenna measurements, the dominant cause of the high sidelobes appears to be due to antenna-aperture blockage by the feed-support structure. By using a wedge-shaped ridge along this structure, polarizing characteristics can be achieved. The linear polarization, consisting of both RHCP and LHCP components, will then contribute some offsetting aperture illumination versus none with the existing configuration. Axiomatix feels that this modification can achieve sidelobes of at least -22 dB.

6.1 Shuttle/TDRSS Sidelobe Avoidance

6.1.1 Introduction

Some concern has been expressed about the possibility of sidelobe acquisition of a TDRS signal, particularly in light of revised flux-density specifications at the Orbiter. Note that Table 6.1 [1] gives the minimum flux density as -126.9 dBW/M^2 and the maximum flux density is -113.5 dBW/M^2. The resultant margin is given as 1.3 dB. Several assumptions were made [1] to arrive at this margin, and the specified dynamic range of received flux density will be slightly increased in the revised specification. In the following sections, we develop a new pair of sidelobe-discrimination budgets. One is based on the new revised flux-density specification which includes a margin at the low level, and the other is based on actual expected values of flux density. In both cases, a more realistic assumption is made concerning polarization loss.

6.1.2 Derivation of Sidelobe Discrimination Budgets

The following derivation of the sidelobe-discrimination budgets follows the format of Table 6.1 [1] so that the results may be compared. This includes the threshold settings and noise-immunity margins. In Table 6.2 [2], we present a conservative estimate of the sidelobe-discrimination margin based on a minimum received flux density of -126.0 dBW/M^2 and a maximum of -110.5 dBW/M^2. The minimum flux includes a margin of 2.5 dB added by Rockwell to the estimated -123.5 dBW/M^2, based on the Orbiter ICD [2] which includes polarization loss. Table 6.3 [2, Table 4-IX] is reproduced herein and the flux-density values are calculated based on a minimum loss of -162.0 dB M^{-2} and a worst-case loss of -613.5 dB M^{-2}. In addition, polarization loss on a sidelobe should be greater than on a mainlobe: typically, polarization loss increases monotonically off boresight. For our conservative estimate, Table 6.2 [2], we assume that the sidelobe and mainlobe polarization losses are equal. The net margin is -0.6 dB which, as we have stated, includes a 2.5-dB margin added by Rockwell to the flux-density specification.

Table 6.4 [2] presents a more liberal estimate of the sidelobe discrimination budget without a margin added to the expected flux density. In this budget, we assume a polarization loss at the first sidelobe down 1 dB from the mainlobe, which we feel is realistic. The result is a positive margin of 2.9 dB.

6.1.3 Conclusions

Based on realistic estimates of received flux density and polarization loss, sidelobe acquisition should not be a problem. Moreover, the maximum flux density of -110.5 dBW/M^2 is predicated on the TDRS pointing directly at the Orbiter. The TDRS Ku-band antenna full beamwidth is 0.28° and is open-loop pointed at the Orbiter during acquisition. We feel that the most likely event which would cause the maximum flux during acquisition is an attempted reacquisition immediately following loss of track while the TDRS is still accurately pointed toward the Orbiter. This should not be a problem but, in order to more accurately quantify the performance, the axial ratio at the most significant sidelobes should be measured.

Table 6.2. Sidelobe-Discrimination Budget [2]

	Weakest Mainlobe	Strongest Sidelobe	Cumulative Difference
Pointing Loss, dB	-3.0	-22.0	19.0 dB
Flux Density, dBW/m^2	-126.0	-110.5	
Antenna Gain, dB	37.1	37.1	
Effective Area (omni), dBm^2 (at 13.775 GHz)	-44.2	-44.2	
Effective Area, dBm^2	-7.1	-7.1	
Polarization Loss, dB	0.0	0.0	
Received Power, dBW	-136.1	-139.6	35 dB
System Temperature, dB°K (at Antenna Terminals)	30.6	28.9	
Boltzmann's Constant	-228.6	-228.6	
C/N_0 dB-Hz (at EA-1 Input)	61.9	60.1	1.8 dB
Threshold Setting, dB	-0.3	0.3	
Noise Immunity Margin, dB	-0.6	1.2	
Effective C/N_0, dB-Hz (at Detector)	61.0	61.6	-0.6 dB

Table 6.3 TDRSS-To-SSO Ku-Band Forward-Link Mode 1 Interface Characteristics [2]

Information		Time-Division-Multiplexing		Spectrum Spreading d	TDRSS Transmission				SSO Min. G/T	SSO Required P_{rec} / N_0
Channel	Rate	Operational TDM c	216 kbps TDM		Carrier Modulation	Carrier Frequency	EIRP	Polarization		
Voice 1	32 kbps	Rate: 72 kbps Sync Pattern: 76571440_8	Bit Rate: 216 kbps ± 0.001% Format: Biphase-L Sync Pattern: 26772706354_8	PN Sequence: Gold Code Chip Rate. (31/141024) x Cxr Freq Format: NRZ-L Period: 1023 chips	PSK $\beta = \pi/2$ rad ±3°	13.775 GHz e	Acquisition: f 40.0 - 49.5 dBW Tracking: g Normal power: 46.5 - 49.5 dBW High power: 48.5 - 51.5 dBW	RCP Axial ratio ≤1 dB g	6.0 dB/K h	64.0 dB-Hz i 65.4 dB-Hz j
Voice 2	32 kbps									
Command	6.4 kbps[a]									
Sync	1.6 kbps[b]									
Forward Data	128 kbps	N/A								
Sync	16 kbps	N/A								

Legend:
a - Encoded and permuted command data
b - 1.2 kbps synchronization pattern plus 0.4 kbps arbitrary fill bits
c - Same as S-band high data rate uplink and forward link operational TDM; encrypted for transmission
d - Unspread capability exists
e - Doppler compensated in TDRSS for 17.5 kHz at SSO
f - Effective EIRP toward SSO during acquisition with open-loop TDRSS antenna pointing and allowing for SSO of 6 dB; not to exceed upper limit
g - With Ku-band return link acquired
h - Based on SSO antenna temperature of 10 K(no Earth or Sun intercept)
i - SSO link acquisition threshold
j - For BER of 10^{-5}, subject to specifications in 4.4.2.1

Table 6.4. Sidelobe-Discrimination Budget [2]

	Weakest Mainlobe	Strongest Sidelobe	Cumulative Difference
Pointing Loss, dB	-3.0	-22.0	19.0 dB
Flux Density, dBW/m^2	-123.5	-110.5	
Antenna Gain, dB	37.1	37.1	
Effective Area (omni), dBm^2 (at 13.775 GHz)	-44.2	-44.2	
Effective Area, dBm^2	-7.1	-7.1	
Polarization Loss, dB	0.0	-1.0	
Received Power, dBW	-133.6	-140.6	7.0 dB
System Temperature, dB°K (at Antenna Terminals)	30.6	28.9	
Boltzmann's Constant	-228.6	-228.6	
C/N_0 dB-Hz (at EA-1 Input)	64.4	59.1	5.3 dB
Threshold Setting, dB	-0.3	0.3	
Noise Immunity Margin, dB	-0.6	1.2	
Effective C/N_0, dB-Hz (at Detector)	63.5	60.6	2.9 dB

6.2 Shuttle/TDRSS Acquisition and Tracking Performance

6.2.1 Introduction

The current scenario for Shuttle/TDRSS acquisition consists of having the TDRS open-loop point toward the Shuttle and radiate a minimum of 40.0 dBW in the direction of the Shuttle. TDRS pointing-loss considerations are discussed in [3]. The Shuttle Ku-band high-gain antenna then executes a spiral scan to acquire the forward link. Once the Shuttle Ku-band system detects the forward link and re-radiates on the return link, the TDRS can initiate closed-loop tracking. When the TDRS is accurately closed-loop tracking, the minimum received flux at the Shuttle is increased due to the more accurate TDRS pointing and the Shuttle, in turn, can maintain more accurate pointing toward the TDRS.

Hughes Aircraft Company (HAC) had recently expressed concern that the Ku-band system cannot accommodate the wide variation in expected signal strength (dynamic range) and still maintain accurate pointing. This concern stems from observations that the variation in received flux density at the Orbiter, combined with unit-to-unit variations, thermal effects and detector weak-signal suppression, add up to provide the communication-track servo with an error signal having an estimated 39-dB dynamic range. The incident flux density variation was taken from the Rockwell specification, Rev. B.

6.2.2 Dynamic-Rate Limitations

Hardware limitations affecting Ku-band performance are discussed in Section 3 of this report. Briefly, a combination of manufacturing variability, AGC performance and temperature effects combine with the input-signal flux variability to produce a 39-dB dynamic range at the angle-track servo input. The servo was not designed to accommodate this wide dynamic range and, in fact, the capability of the servo is unknown at the present time.

HAC system engineering has partitioned the problem between the servo and the detector: Investigate whether or not the servo can handle a 15-dB dynamic range and explore detector design changes and specification-relief options which can reduce the dynamic range from 39 dB down to 15 dB or less. Hughes has compiled a list of 10 candidate options to improve the detector performance, one option is simply 11 dB of incident flux-density specification relief with a slightly narrower track IF bandpass filter. The flux-density relief is needed at the low end, e.g., the minimum signal level for accurate tracking would

have to be boosted up to 11 dB. While this seems like a prodigious amount, an examination of the Rockwell specification indicates that it is possible. This is discussed in the next section.

6.2.3 Flux-Density Specification Considerations

HAC dynamic-range calculations using received flux density are based on the Rockwell Rev. B specification. Apparently, Table 6.5, which appears on page 29 of the specification as Table 3-I, was used to determine minimum flux. This table is reproduced herein and gives "minimum EIRP required for autotrack" as 35 dBW at the TDRS. Using a worst-case space loss of -163.5 dB/M^2 and a polarization loss of 0.5 dB, we arrive at a minimum flux density of -129 dBW/M^2. This is the worst-case flux density used by HAC as a requirement for accurate tracking.

Table 6.5. TDRS RF Interface Requirements [1]

Parameter	Return Link	Forward Link
Center frequency	15.0034 GHz (nominal)	13.775 GHz ± 10 kHz
Bandwidth (3 dB)	225 MHz (transponder throughput)	50 MHz (transponder throughput)
Antenna gain (55% eff.)	52.6 dB	52 dB
Antenna polarization	RHC	RHC
EIRP	N/A	48.8 dBW end-of-life for data transfer 40.0 dBW minimum for detection in the direction of the Orbiter
Maximum-allowable EIRP	60 dBW at Orbiter	55 dBW at TDRS
Minimum EIRP required for autotrack	30 dBW at Orbiter	35 dBW at TDRS

A flux density of -129.0 dBW/M^2 is overly pessimistic since the Shuttle ICD [4] guarantees a mininum of 40.0 dBW toward the Orbiter, including polarization loss. This is equivalent to a flux density of -123.5 dBW. Moreover, this flux represents open-loop TDRS pointing. When the TDRS is illuminated by the Orbiter return-link signal, the flux density will increase to a minimum of 46.5 dBW for an equivalent flux density of -117.0 dBW/M^2. The maximum TDRS EIRP toward the Orbiter is 51.5 dBW. With a minimum space loss of -162 dBW/M^2, the maximum flux density is -110.5 dBW/M^2. The EIRP values come from the Shuttle ICD. From Table 6.3, note that, when the TDRS is closed-loop pointing, the flux density at the Orbiter is 12 dB higher than the worst-case flux used by HAC in the dynamic-range calculation. The maximum flux density of -110.5 dBW/M^2 is 3.7 dB less than the -106.8 dBW/M^2 employed by HAC in their dynamic-range calculation.

6.2.4 Summary and Conclusions

The revised flux-density dynamic range provided by using the EIRP values from the ICD, which are more current than those in the Rev. B Rockwell specification, plus about 3-dB relief from a narrower bandpass filter at the detector input, will allow the Ku-band system to provide adequate communication tracking. This conclusion assumes that one servo will indeed accommodate a 15-dB dynamic range. Axiomatix has made this recommendation to Rockwell and NASA. As a consequence, Rockwell will be revising the flux-density specification. The maximum flux density will be specified at -110.5 dBW/M^2, and the two minimum flux-density numbers, including a 2.5-dB pad, will be specified at -119.5 dBW/M^2 and -126.0 dBW/M^2. The former applies when the TDRS is accurately closed-loop pointing, and accurate SSO pointing will be required at this flux density. The latter will be specified for acquisition only and assumes open-loop TDRS pointing.

TWO-CHANNEL COSTAS LOOP-TRACKING PERFORMANCE FOR UQPSK SIGNALS WITH ARBITRARY DATA FORMATS

Interim Report

Contract No. NAS 9-16067

Exhibit "B"

Prepared for

NASA Lyndon B. Johnson Space Center
Houston, Texas 77058

(Contract Monitor: W. E. Teasdale)

Prepared by

M. K. Simon

Axiomatix
9841 Airport Blvd., Suite 912
Los Angeles, California 90045

Axiomatix Report No. R8010-8
October 30, 1980

TWO-CHANNEL COSTAS LOOP-TRACKING PERFORMANCE FOR UQPSK SIGNALS WITH ARBITRARY DATA FORMATS

By

Marvin K. Simon

1.0 INTRODUCTION

In a recent pair of papers [1,2], the authors investigated the carrier-tracking performance of a two-channel Costas-type loop for unbalanced quadriphase (UQPSK) signals. Such a loop evolves naturally as a closed-loop system motivated by the maximum a posteriori (MAP) phase estimation approach. Although not explicitly stated, the performance results presented in these papers pertain only to the case where both data channels have NRZ formats. In many applications [3-5], the data formats on the two channels are different; for example, the high data rate channel might be Manchester coded, while the low data rate channel might be NRZ, or vice versa. Alternately, both channels could be Manchester coded.

In this report, we generalize the results given in [1] so they will apply to any of the mixed-format cases mentioned above. Specifically, we examine the mean-square phase jitter performance of two-channel Costas loops with active arm filters, synchronous or asynchronous symbol clocks, and arbitrary data formats on the two channels. Also considered will be the performance of such loops with hard limiters in the in-phase channels. Here again, we shall follow the approach taken in [7], with the exception that the data formats on the two channels can be arbitrary.

2.0 PERFORMANCE ANALYSIS OF TWO-CHANNEL COSTAS-TYPE LOOP WITH ACTIVE ARM FILTERS WITHOUT HARD LIMITERS

2.1 System Model and Loop Equation of Operation

To avoid duplication of effort, we shall draw heavily upon the notation, definitions and results given in [1]. Consider the two-channel Costas loop with integrate-and-dump arm filters illustrated in Figure 1. The input x(t) is an unbalanced QPSK (UQPSK) signal-plus-noise, i.e.,

$$x(t) = \sqrt{2P_1}\, d_1(t) \cos(\omega_0 t + \theta) + \sqrt{2P_2}\, d_2(t) \sin(\omega_0 t + \theta) + n(t) \quad (1)$$

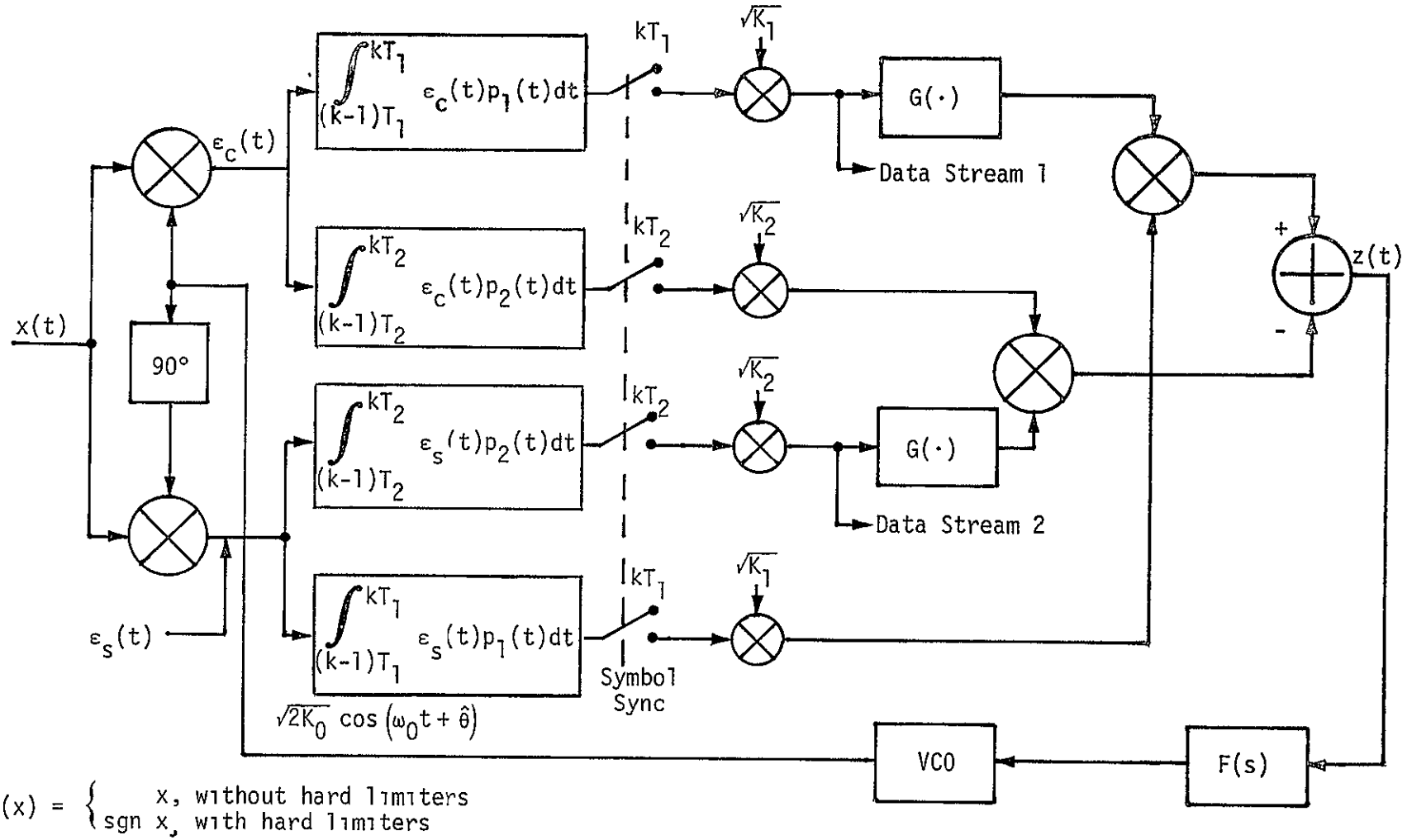

$$G(x) = \begin{cases} x, & \text{without hard limiters} \\ \operatorname{sgn} x, & \text{with hard limiters} \end{cases}$$

Channel i is NRZ $(i=1,2)$

$$p_1(t) = \begin{cases} 1, & 0 \leq t \leq T_1 \\ 0, & \text{otherwise} \end{cases}$$

Channel i is Manchester $(i=1,2)$

$$p_1(t) = \begin{cases} 1, & 0 \leq t \leq T_1/2 \\ -1; & T_1/2 < t \leq T_1 \\ 0, & \text{otherwise} \end{cases}$$

Figure 1 Two-Channel Costas-Type Loop with Active Arm Filters

where ω_0 is the radian carrier frequency, P_1 and P_2 represent the power in the two quadrature components, $d_1(t)$ and $d_2(t)$ are two independent binary waveforms (arbitrary format) with respective data symbol rates $R_1 = 1/T_1$ and $R_2 = 1/T_2$, and θ is the carrier phase to be tracked by the loop. The additive channel noise $n(t)$ has the usual narrowband process representation, i.e.,

$$n(t) = \sqrt{2}\left\{N_c(t)\cos(\omega_0 t+\theta) - N_s(t)\sin(\omega_0 t+\theta)\right\} \tag{2}$$

where $N_c(t)$ and $N_s(t)$ are approximately statistically independent, stationary, white Gaussian noise processes with single-sided noise spectral density N_0 W/Hz and single-sided bandwidth $B_H < \omega_0/2\pi$.

The input signal is demodulated twice by the quadrature reference signals

$$r_s(t) = \sqrt{2K_0}\sin(\omega_0 t+\theta)\ ,\quad r_c(t) = \sqrt{2K_0}\cos(\omega_0 t+\theta) \tag{3}$$

to yield the phase detector $\left(\text{gain } \sqrt{K_m}\right)$ outputs

$$\begin{aligned}
\varepsilon_c(t) &\triangleq \sqrt{K_m}\, x(t)\, r_c(t) \\
&= \sqrt{K_0K_m}\left\{\left[\sqrt{P_1}\, d_1(t)+N_c(t)\right]\cos\varphi(t) + \left[\sqrt{P_2}\, d_2(t)-N_s(t)\right]\sin\varphi(t)\right\} \\
\varepsilon_s(t) &\triangleq \sqrt{K_m}\, x(t)\, r_s(t) \\
&= \sqrt{K_0K_m}\left\{\left[\sqrt{P_1}\, d_1(t)+N_c(t)\right]\sin\varphi(t) - \left[\sqrt{P_2}\, d_2(t)-N_s(t)\right]\cos\varphi(t)\right\}
\end{aligned} \tag{4}$$

where $\phi = \theta - \hat{\theta}$ is the loop phase error which shall be assumed constant (in time) over the duration T_2 of a symbol corresponding to the lowest data rate $d_2(t)$*.

The signals $\varepsilon_c(t)$ and $\varepsilon_s(t)$ are each passed through integrate and dumps which are matched to the pulse shapes $p_1(t)$ and $p_2(t)$ respectively of the two quadrature modulations $d_1(t)$ and $d_2(t)$ The outputs of like

*As in [1], we arbitrarily assume that $d_1(t)$ is the higher rate channel.

integrate and dumps are multiplied, and the difference of these multiplications is used to form the loop error signal. This error signal is then passed through the loop filter F(s) whose output drives the VCO, generating the pair of demodulation reference signals given in (3). Without belaboring the details, we may follow the identical approach taken in [1] and immediately write the linearized loop ($\sin 2\varphi = 2\varphi$) equation of operation in Heaviside operator notation as*

$$2\varphi = H_{2\varphi}(p)\left[\frac{N(t)}{S'(0)}\right] , \tag{5}$$

where

$$H_{2\varphi}(s) = \frac{S'(0)\,F(s)}{s + S'(0)F(s)} , \tag{6}$$

$S'(0)$ is the slope of the normalized loop S-curve at the origin ($\varphi = 0$) given by

$$S'(0) = K_1T_1^2\left[P_1 - P_2\,\overline{d_{21}^2(t)}\right] + K_2T_2^2\left[P_2 - P_1\,\overline{d_{12}^2(t)}\right] \tag{7}$$

and $N(t) = N_1(t) - N_2(t)$ is the equivalent zero mean additive noise with

$$N_i(t) = \sum_{\ell=1}^{3} N_{i\ell}(t) ; \qquad i = 1,2$$

$$N_{i1}(t) = K_i\left[N_{ci}^2(t) - N_{si}^2(t)\right]\sin 2\varphi + 2K_i\,N_{si}(t)\,N_{ci}(t)\cos 2\varphi$$

$$N_{i2}(t) = 2K_iT_i\left\{\left[\sqrt{P_1}\,d_{1i}(t)\,N_{c1}(t) + \sqrt{P_2}\,d_{2i}(t)\,N_{s1}(t)\right]\sin 2\varphi + \left[\sqrt{P_1}\,d_{1i}(t)\,N_{si}(t) - \sqrt{P_2}\,d_{2i}(t)\,N_{ci}(t)\right]\cos 2\varphi\right\}$$

$$N_{i3}(t) = K_iT_i^2\left\{P_{3-i}\left[d_{3-i,i}^2(t) - \overline{d_{3-i,i}^2(t)}\right]\sin 2\varphi + 2\sqrt{P_1P_2}\,d_{1i}(t)d_{2i}(t)\cos 2\varphi\right\} \tag{8}$$

*The linearization of the equation of operation as characterized by [1,' (28)-(31)] is incorrectly scaled.

In (7) and (8), the overbar denotes statistical expectation and

$$d_{\ell i}(t) \triangleq \frac{1}{T_i} \int_{(k-1)T_i}^{kT_1} d_\ell(s)\, p_i(s)\, ds \; ; \quad (k-1)T_i < t \leq kT_i, \; i=1,2$$

$$N_{ci}(t) \triangleq \int_{(k-1)T_1}^{kT_i} N_c(s)\, p_1(s)\, ds \; ; \quad (k-1)T_i < t \leq kT_i, \; i=1,2$$

$$N_{si}(t) \triangleq \int_{(k-1)T_i}^{kT_i} N_s(s)\, p_1(s)\, ds \; ; \quad (k-1)T_1 < t \leq kT_i, \; 1=1,2 \qquad (9)$$

Note that (9) differs from the corresponding expressions in [1] in that the channel pulse shapes $p_1(t)$ and $p_2(t)$ are included as weighting factors in the integrands.

Assuming that the bandwidth of $H_{2\varphi}(s)$ (loop bandwidth) is much narrower than the bandwidth of N(t), the variance of 2φ can be approximated by

$$\sigma_{2\varphi}^2 = \frac{N_0' B_L}{[S'(0)]^2} \qquad (10)$$

where B_L is the single-sided loop bandwidth and N_0' is the single-sided spectral density of the equivalent noise N(t).

The next two sections are devoted to an evaluation of S'(0) and N_0' for the various data combination formats on the two channels

2.2 Evaluation of the Loop Signal Component S'(0)

From (7), we observe that evaluation of S'(0) reduces to the evaluation of the two mean-square crosstalk quantities $\overline{d_{21}^2(t)}$ and $\overline{d_{12}^2(t)}$ for the four combinations of NRZ- and Manchester-coded data on the two channels. Such evaluations have already been performed in [6] under the guise of a different notation. In particular, [6, Table 1] evaluates what is herein referred to as $\overline{d_{21}^2(t)}$ for the case of synchronous symbol clocks, and [6, Table 2] gives the corresponding results for asynchronous symbol clocks. In the former case, the ratio of data rates R_1/R_2 is constrained

to be an integer. Translating these results into the notation of this report, we obtain the following tables.

Table 1.* Evaluation of $\overline{d_{21}^2(t)}$; Synchronous Symbols Clocks, $R_1/R_2 = n$ (n an integer)

$d_2(t)$ \ $d_1(t)$	Manchester	NRZ
Manchester	0 ; n even $\frac{1}{n}$; n odd	1 ; n even $\frac{n-1}{n}$; n odd
NRZ	0	1

Table 2. Evaluation of $\overline{d_{21}^2(t)}$; Asynchronous Symbol Clocks; $R_1/R_2 = n$ (n need not be an integer)

$d_2(t)$ \ $d_1(t)$	Manchester	NRZ
Manchester	$\frac{1}{6}\left[n^2 - \frac{5}{n} + 12 - 6n\right]$; $R_2 \leq R_1 \leq 2R_2$ $\frac{1}{2n}$, $R_1 \geq 2R_2$	$n - \frac{1}{6}n^2 - 1 + \frac{1}{3n}$, $R_2 \leq R_1 \leq R_2$ $1 - \frac{1}{n}$; $R_1 \geq 2R_2$
NRZ	$\frac{1}{6n}$	$1 - \frac{1}{3n}$

Also, from the definitions of $d_{12}(t)$ and $d_{21}(t)$ in (9), it is straightforward to show that

*Note that [6, Table 1] contains an error for the Manchester-Manchester case.

$$\overline{d_{12}^2(t)} = \frac{1}{n}\overline{d_{21}^2(t)} \tag{11}$$

for all entries in both Tables 1 and 2. Thus, further introducing the notation [1]

$$P_1 \triangleq P_1 + P_2 \; ; \; \lambda \triangleq \frac{P_2}{P_1} \; ; \; \zeta_1 \triangleq \frac{PT_1}{N_0} \tag{12}$$

the loop signal component of (7) simplifies to*

$$\boxed{S'(0) = K_1 T_1^2 P(1+\lambda)^{-1}\left\{1 - \lambda\,\overline{d_{21}^2} + \left(\frac{K_2}{K_1}\right) n\left(n\lambda - \overline{d_{21}^2}\right)\right\}} \tag{13}$$

where $\overline{d_{21}^2}$ is obtained from the appropriate entry of Table 1 or 2.

2.3 Evaluation of the Equivalent Noise Spectral Density N_0'

The single-sided noise spectral density N_0' of the equivalent noise N(t) whose components are defined in (8) is obtained from

$$N_0' = 2\int_{-\infty}^{\infty} R_N(\tau)\, d\tau \tag{14}$$

where

$$R_N(\tau) = \langle \overline{N(t)\, N(t+\tau)} \rangle = \langle R_N(t,t+\tau) \rangle \tag{15}$$

and $\langle\ \rangle$ denotes the time average. Using (8) and taking the statistical average required in (15) gives [1]

---

*Herein we eliminate the notational dependence of $\overline{d_{21}^2(t)}$ on t.

$$R_N(t_1,t_2) = 4\sum_{\ell=1}^{2} K_\ell^2\left[\sigma_\ell^4+\sigma_\ell^2 T_\ell^2\left(P_\ell+P_{\underline{\ell}}\overline{d_{\ell\underline{\ell}}^2}\right) + T_\ell^4 P_1P_2\ \overline{d_{\ell\underline{\ell}}^2}\right] I_\ell(t_1,t_2)$$

$$- 4K_1K_2\sum_{\ell=1}^{2}\Bigg\{R^2_{N_{c1}N_{c2}}\left(t_\ell+t_{\underline{\ell}}\right) + T_1T_2$$

$$\times\left[P_1R_{d_{11}d_{12}}\left(t_\ell,t_{\underline{\ell}}\right)+P_2R_{d_{21}d_{22}}\left(t_\ell,t_{\underline{\ell}}\right)\right]R_{N_{c1}N_{c2}}\left(t_\ell,t_{\underline{\ell}}\right)$$

$$+ T_1^2T_2^2\ P_1P_2\ R_{d_{11}d_{12}}\left(t_\ell,t_{\underline{\ell}}\right)\ R_{d_{21}d_{22}}\left(t_\ell,t_{\underline{\ell}}\right)\Bigg\} \quad (16)$$

where we have introduced the simplifying notation

$$\underline{\ell} = \begin{cases} 1 \ ; \ \ell = 2 \\ 2 \ , \ \ell = 1 \end{cases} \quad (17)$$

Also in (16),

$$\sigma_\ell^2 \triangleq \frac{N_0T_\ell}{2} \ ; \qquad \ell = 1,2 \quad (18)$$

and

$$I_\ell(t_1,t_2) = \begin{cases} 1 \ ; \text{ if } t_1 \text{ and } t_2 \text{ are both in the interval} \\ \quad \left(kT_\ell,\ (k+1)\ T_\ell\right) \\ 0 \ ; \text{ otherwise} \end{cases} \qquad \ell = 1,2 \quad (19)$$

Clearly then, we must evaluate, for each of the mixed data format combinations, the various nonstationary correlation functions required in (16) before performing the time-averaging operation which finally results in $R_N(\tau)$.

We begin by presenting some general results which relate these correlation functions to one another, namely, it can be shown that analogous to (11),

$$R_{d_{11}d_{12}}(t_1,t_2) = \frac{1}{n} R_{d_{21}d_{22}}(t_1,t_2) \tag{20}$$

where again n is the ratio of data rates. Furthermore,

$$R_{N_{c1}N_{c2}}(t_1,t_2) = \sigma_1^2 R_{d_{21}d_{22}}(t_1,t_2) \tag{21}$$

The above two relations are valid independent of the data formats on the two channels and whether or not these data streams are time synchronized. Using (20) and (21), we can determine the products of correlation functions needed to evaluate (16). Thus, we obtain

$$\begin{aligned}
R^2_{N_{c1}N_{c2}}(t_1,t_2) &= \sigma_1^4 R^2_{d_{21}d_{22}}(t_1,t_2) \\
R_{d_{11}d_{12}}(t_1,t_2)\, R_{N_{c1}N_{c2}}(t_1,t_2) &= \frac{\sigma_1^2}{n} R^2_{d_{21}d_{22}}(t_1,t_2) \\
R_{d_{21}d_{22}}(t_1,t_2)\, R_{N_{c1}N_{c2}}(t_1,t_2) &= \sigma_1^2 R^2_{d_{21}d_{22}}(t_1,t_2) \\
R_{d_{11}d_{12}}(t_1,t_2)\, R_{d_{21}d_{22}}(t_1,t_2) &= \frac{1}{n} R^2_{d_{21}d_{22}}(t_1,t_2)
\end{aligned} \tag{22}$$

from which we observe that it is sufficient to evaluate only $R^2_{d_{21}d_{22}}(t_1,t_2)$ for the various data format combinations on the two channels. These specific relationships will now be given in summary form.

Channel 1 is NRZ, Channel 2 is Manchester; Synchronized Symbol Clocks, n an integer

$$R^2_{d_{21}d_{22}}(t_1,t_2) = \begin{cases} 1 \; ; \; 0 \leq t_1 \leq T_1 \; , \; 0 \leq t_2 \leq nT_1 \\ 1 \; ; \; T_1 \leq t_1 \leq nT_1 \; , \; nT_1 \leq t_2 \leq 2nT_1 \\ 0 \; ; \; \text{otherwise} \end{cases} \tag{23}$$

Channel 1 is Manchester, Channel 2 is NRZ; Synchronized Symbol Clocks; n an integer

$$R^2_{d_{21}d_{22}}(t_1,t_2) = 0 \qquad \text{all } t_1,t_2 \tag{24}$$

Channel 1 is NRZ, Channel 2 is Manchester; Synchronized Symbol Clocks; n an integer

n even

$$R^2_{d_{21}d_{22}}(t_1,t_2) = \begin{cases} 1 \; ; \; 0 \leq t_1 \leq T_1 \; , \; 0 \leq t_2 \leq nT_1 \\ 1 \; ; \; T_1 \leq t_1 \leq \left(\frac{n}{2}+1\right)T_1 \; , \; nT_1 \leq t_2 \leq 2nT_1 \\ 1 \; ; \; \left(\frac{n}{2}+1\right)T_1 \leq t_1 \leq nT_1 \; , \; nT_1 \leq t_2 \leq 2nT_1 \\ 0 \; ; \; \text{otherwise} \end{cases} \tag{25}$$

n odd

$$R^2_{d_{21}d_{22}}(t_1,t_2) = \begin{cases} 1 \; ; \; 0 \leq t_1 \leq T_1 \; , \; 0 \leq t_2 \leq nT_1 \\ 1 \; ; \; T_1 \leq t_1 \leq \left(\frac{n+1}{2}\right)T_1 \; , \; nT_1 \leq t_2 \leq 2nT_1 \\ 0 \; ; \; \left(\frac{n+1}{2}\right)T_1 \leq t_1 \leq \left(\frac{n+3}{2}\right)T_1 \; , \; nT_1 \leq t_2 \leq 2nT_1 \\ 1 \; ; \; \left(\frac{n+3}{2}\right)T_1 \leq t_1 \leq nT_1 \; , \; nT_1 \leq t_2 \leq 2nT_1 \\ 0 \; , \; \text{otherwise} \end{cases} \tag{26}$$

Channel 1 is Manchester, Channel 2 is Manchester, Synchronized Symbol Clocks; n an integer

n even

$$R^2_{d_{21}d_{22}}(t_1,t_2) = 0 \qquad \text{all } t_1,t_2 \tag{27}$$

n odd

$$R^2_{d_{21}d_{22}}(t_1,t_2) = \begin{cases} 0 \; ; \; 0 \leq t_1 \leq T_1 \; , \; 0 \leq t_2 \leq nT_1 \\ 0 \; ; \; T_1 \leq t_1 \leq \left(\frac{n+1}{2}\right)T_1 \; , \; nT_1 \leq t_2 \leq 2nT_1 \\ 1 \; ; \; \left(\frac{n+1}{2}\right)T_1 \leq t_1 \leq \left(\frac{n+3}{2}\right)T_1 \; , \; nT_1 \leq t_2 \leq 2nT_1 \\ 0 \; ; \; \left(\frac{n+3}{2}\right)T_1 \leq t_1 \leq nT_1 \; , \; nT_1 \leq t_2 \leq 2nT_1 \\ 0 \; ; \; \text{otherwise} \end{cases} \tag{28}$$

Letting $t_1 = t$, $t_2 = t+\tau$ and averaging over t yields the following results for the stationary correlation function

$$\Delta(\tau) \triangleq \frac{1}{nT_1}\int_0^{nT_1} R^2_{d_{21}d_{22}}(t,t+\tau)\, dt \tag{29}$$

Channel 1 is NRZ, Channel 2 is NRZ; Synchronized Symbol Clocks, n an integer

$$\Delta(\tau) = \begin{cases} \frac{1}{nT_1}\,(T_1+\tau) \; , & -T_1 \leq \tau \leq (n-1)T_1 \\ \frac{1}{nT_1}\left[(2n-1)T_1-\tau\right]; & (n-1)T_1 \leq \tau \leq (2n-1)T_1 \\ 0 \; ; \; \text{otherwise} \end{cases} \tag{30}$$

Channel 1 is Manchester, Channel 2 is NRZ; Synchronized Symbol Clocks, n an integer

$$\Delta(\tau) = 0 \quad ; \quad \text{all } \tau \tag{31}$$

Channel 1 is NRZ, Channel 2 is Manchester; Synchronized Symbol Clocks, n an integer

n even

$$\Delta(\tau) = \begin{cases} \frac{1}{nT_1}\,(T_1+\tau) \; ; & -T_1 \leq \tau \leq (n-1)T_1 \\ \frac{1}{nT_1}\left[(2n-1)T_1-\tau\right]; & (n-1)T_1 \leq \tau \leq (2n-1)T_1 \\ 0 \; , \; \text{otherwise} \end{cases} \tag{32}$$

n odd

$$\Delta(\tau) = \begin{cases} \frac{1}{nT_1}(T_1 + \tau) ; & -T_1 \leq \tau \leq \left(\frac{n-3}{2}\right)T_1 \\ \frac{n-1}{2n} ; & \left(\frac{n-3}{2}\right)T_1 \leq \tau \leq \left(\frac{n-1}{2}\right)T_1 \\ \frac{\tau}{nT_1} ; & \left(\frac{n-1}{2}\right)T_1 \leq \tau \leq (n-1)T_1 \\ \frac{1}{nT_1}\left[(2n-2)T_1 - \tau\right] ; & (n-1)T_1 \leq \tau \leq \left(\frac{3n-3}{2}\right)T_1 \\ \frac{n-1}{2n} ; & \left(\frac{3n-3}{2}\right)T_1 \leq \tau \leq \left(\frac{3n-1}{2}\right)T_1 \\ \frac{1}{nT_1}\left[(2n-1)T_1 - \tau\right] ; & \left(\frac{3n-1}{2}\right)T_1 \leq \tau \leq (2n-1)T_1 \\ 0 ; & \text{otherwise} \end{cases} \quad (33)$$

Channel 1 is Manchester, Channel 2 is Manchester; Synchronized Symbol Clocks; n an integer

n even

$$\Delta(\tau) = 0 ; \quad \text{all } \tau \quad (34)$$

n odd

$$\Delta(\tau) = \begin{cases} 0 ; & -T_1 \leq \tau \leq \left(\frac{n-3}{2}\right)T_1 \\ \frac{1}{nT_1}\left[\left(\frac{3-n}{2}\right)T_1 + \tau\right] ; & \left(\frac{n-3}{2}\right)T_1 \leq \tau \leq \left(\frac{n-1}{2}\right)T_1 \\ \frac{1}{n} , & \left(\frac{n-1}{2}\right)T_1 \leq \tau \leq \left(\frac{3n-3}{2}\right)T_1 \\ \frac{1}{nT_1}\left[\left(\frac{3n-1}{2}\right)T_1 - \tau\right], & \left(\frac{3n-3}{2}\right)T_1 \leq \tau \leq \left(\frac{3n-1}{2}\right)T_1 \\ 0 ; & \text{otherwise} \end{cases} \quad (35)$$

Making the same substitutions in (16) and averaging over t yields

$$R_N(\tau) \triangleq \frac{1}{nT_1}\int_0^{nT_1} R_N(t,t+\tau)dt$$

$$= 4\sum_{\ell=1}^{2} K_\ell^2\left[\sigma_\ell^4 + \sigma_\ell^2 T_\ell^2\left(P_\ell + P_{\underline{\ell}}\,\overline{d_{\underline{\ell}\ell}^2}\right) + T_\ell^4 P_1 P_2\,\overline{d_{\underline{\ell}\ell}^2}\right]\left(1 - \frac{|\tau|}{T_\ell}\right)$$

$$- 4K_1K_2\left[\sigma_1^4 + \sigma_1^2 T_1T_2\left(\frac{P_1}{n} + P_2\right) + T_1^2T_2^2\,P_1P_2\left(\frac{1}{n}\right)\right]\left(\Delta(\tau)+\Delta(-\tau)\right) \quad (36)$$

where we have also made use of the relations in (22). Finally, performing the doubly infinite integration on τ gives the desired results for N_0' of (14), namely

$$N_0' = 8\sum_{\ell=1}^{2} K_\ell^2 T_\ell\left[\sigma_\ell^4 + \sigma_\ell^2 T_\ell^2\left(P_\ell + P_{\underline{\ell}}\,\overline{d_{\underline{\ell}\ell}^2}\right) + T_\ell^4 P_1 P_2\,\overline{d_{\underline{\ell}\ell}^2}\right]$$

$$- 16K_1K_2\left[\sigma_1^4 + \sigma_1^2 T_1T_2\left(\frac{P_1}{n} + P_2\right) + T_1^2T_2^2\,P_1P_2\,\frac{1}{n}\right] I\left(\Delta(\tau)\right) \quad (37)$$

where

$$I\left(\Delta(\tau)\right) \triangleq \int_{-\infty}^{\infty} \Delta(\tau)d\tau \quad (38)$$

All that remains to put (37) into its final form is to evaluate $I(\Delta(\tau))$ for the various mixed data format combinations.

Substituting (30) - (35) into (38) and carrying out the integrations enables us to put the results in a surprisingly simple and compact form, namely,

$$I\left(\Delta(\tau)\right) = nT_1\,\overline{d_{21}^2} \quad (39)$$

where $\overline{d_{21}^2}$ is obtained from Table 1.

Finally, then, substituting (39) into (37) and making use of (11), we obtain, after some simplification,

$$\begin{aligned} N_0' = 2N_0T_1^3\Bigg\{ & K_1^2\left[N_0 + 2T_1\left(P_1 + P_2\,\overline{d_{21}^2}\right)\right] \\ & + K_2^2n^2\left[nN_0 + 2nT_1\left(P_1\,\overline{d_{21}^2} + nP_2\right)\right] \\ & - 2K_1K_2n\,\overline{d_{21}^2}\left[N_0 + 2T_1\left(P_1 + nP_2\right)\right]\Bigg\} \\ & + 4T_1^5\,P_1P_2\left[\left(K_1^2 + K_2^2\,n^4\right)\overline{d_{21}^2} - 2K_1K_2\,n^2\,\overline{d_{21}^2}\right] \end{aligned} \tag{40}$$

Although the result in (40) has been derived for the case of synchronized symbol clocks, with some effort, it can also be shown that it also applies for the unsynchronized symbol clock case with the caveat that $\overline{d_{21}^2}$ is now found from Table 2.

2.4 Squaring Loss Evaluation

The "squaring loss" of the two-channel Costas loop of Figure 1 is defined by

$$\mathscr{S}_L \triangleq \frac{4N_0B_L}{\sigma_{2\varphi}^2P} \tag{41}$$

where $\sigma_{2\varphi}$ is found from (10). As is traditional in suppressed-carrier types of tracking loops, this loss represents the degradation relative to the mean-square phase jitter performance of a linear loop caused by SxS, SxN and NxN distortions. Using (10) in (41) allows $\mathscr{S}_L$ to be rewritten in the form

$$\mathscr{S}_L = \frac{4\left[S'(0)\right]^2}{P\left(N_0'/N_0\right)} \tag{42}$$

Substituting (13) and (40) into (42) and simplifying using the definitions in (12) gives the desired result, namely,

$$\mathscr{S}_L = \frac{\left[K_1\left(1-\lambda\overline{d_{21}^2}\right)+K_2 n\left(n\lambda-\overline{d_{21}^2}\right)\right]^2 (1+\lambda)^{-1}}{\left(1+\frac{1+\lambda}{2\zeta_1}\right)\left(K_1^2+K_2^2 n^3-2K_1K_2 n\overline{d_{21}^2}\right)+\lambda\overline{d_{21}^2}\left(1+\frac{2\zeta_1}{1+\lambda}\right)\left(K_1-n^2K_2\right)^2-K_2^2 n^3(1-n\lambda)\left(1-\overline{d_{21}^2}\right)} \tag{43}$$

or using the optimum* ratio of the gain constants

$$\frac{K_2}{K_1} = \frac{P_2T_1}{P_1T_2} = \frac{\lambda}{n} \quad , \tag{44}$$

we have

$$\mathscr{S}_L = \frac{\left[1-2\lambda\overline{d_{21}^2}+n\lambda^2\right]^2 (1+\lambda)^{-1}}{\left(1+\frac{1+\lambda}{2\zeta_1}\right)\left(1-2\lambda\overline{d_{21}^2}+n\lambda^2\right)+\lambda\overline{d_{21}^2}\left(1+\frac{2\zeta_1}{1+\lambda}\right)(1-n\lambda)^2-n\lambda^2(1-n\lambda)\left(1-\overline{d_{21}^2}\right)} \tag{45}$$

Comparing the above result with [1, (38)], we observe that the only modification necessary to make the previous result applicable to the more general data format situation is to calculate the single parameter $\overline{d_{21}^2}$ from either Table 1 or Table 2 and use it where appropriate in (45). Also observe that by letting $K_2 = 0$ in (43), we get the result for a single-channel Costas loop, namely,

$$\mathscr{S}_L = \frac{\left(1-\lambda\overline{d_{21}^2}\right)^2(1+\lambda)^{-1}}{1+\frac{1+\lambda}{2\zeta_1}+\lambda\left(1+\frac{2\zeta_1}{1+\lambda}\right)\overline{d_{21}^2}} \tag{46}$$

which agrees with [6, (32)] if the appropriate changes in notation are made.

*The word "optimum" is used here in the same sense as that used in [1], namely, the ratio of gains motivated by the MAP estimation approach. Note that this gain ratio does not necessarily minimize squaring loss or mean-square phase jitter, as demonstrated in the next section.

2.5 Optimization of Channel Gain Ratio to Minimize Mean-Square Phase Jitter

In the previous sections, we developed a theory for calculating the mean-square phase-tracking jitter based on a linear loop model as a function of such system parameters as signal-to-noise ratio in each channel, the ratio of powers in the two channels, and the ratio of data rates in the two channels. Although the general results were derived as a function of the ratio of the gains in the two channels, specific results were presented only for the "optimum" choice for this ratio based upon MAP estimation theory.

Unfortunately, as we shall see shortly, selection of this gain ratio as motivated by MAP estimation theory does not necessarily optimize the tracking performance. In fact, selection of this gain ratio to directly optimize the tracking performance in the sense of minimum mean-squared phase-tracking jitter can yield considerable improvement in this performance relative to the MAP estimation choice of gain ratio.

To illustrate this point, we shall begin by rewriting (41) in the form

$$\mathscr{S}_L \triangleq \frac{4N_0 B_L}{\sigma_{2\varphi}^2 P} = \frac{\left[A_0 + A_1\left(\frac{K_2}{K_1}\right)\right]^2}{(1+\lambda)\left[B_0 + B_1\left(\frac{K_2}{K_1}\right) + B_2\left(\frac{K_2}{K_1}\right)^2\right]} \tag{47}$$

where

$$\begin{aligned}
A_0 &= 1 - \lambda\overline{d_{21}^2} \\
A_1 &= n\left(n\lambda - \overline{d_{21}^2}\right) \\
B_0 &= 1 + \frac{1+\lambda}{2\zeta_1} + \lambda\overline{d_{21}^2}\left(1 + \frac{2\zeta_1}{1+\lambda}\right) \\
B_1 &= -2n\,\overline{d_{21}^2}\left[1 + \frac{1+\lambda}{2\zeta_1} + \lambda n\left(1 + \frac{2\zeta_1}{1+\lambda}\right)\right] \\
B_2 &= n^3\left\{1 + \frac{1+\lambda}{2\zeta_1} + n\lambda\left[1 + \overline{d_{21}^2}\left(\frac{2\zeta_1}{1+\lambda}\right)\right] - \left(1 - \overline{d_{21}^2}\right)\right\}
\end{aligned} \tag{48}$$

Clearly, from (47), minimizing the phase-tracking jitter $\sigma_{2\varphi}^2$ is directly equivalent to maximizing S_L (minimizing the squaring loss). From the form of (47), it is a simple matter to differentiate this equation with respect to K_2/K_1 and thus find that value of channel gain ratio which maximizes $\mathscr{S}_L$. After some routine algebra, the solution to the equation

$$\frac{\partial \mathscr{S}_L}{\partial\left(K_2/K_1\right)} = 0 \tag{49}$$

is

$$\left(\frac{K_2}{K_1}\right)_{opt} = \frac{2A_1B_0 - A_0B_1}{2A_0B_2 - A_1B_1} \tag{50}$$

$$= \left(\frac{\lambda}{n}\right) \frac{\left(1+\frac{1+\lambda}{2\zeta_1}\right)\left[n-\left(\overline{d_{21}^2}\right)^2\right] + \left(1+\frac{2\zeta_1}{1+\lambda}\right)\left(\overline{d_{21}^2}\right)\left[n-\overline{d_{21}^2}+n\lambda\left(1-\overline{d_{21}^2}\right)\right]}{\left(1+\frac{1+\lambda}{2\zeta_1}+n\lambda\right)\left[n-\left(\overline{d_{21}^2}\right)^2\right]+\left(\frac{2\zeta_1}{1+\lambda}\right)\left(n\lambda\overline{d_{21}^2}\right)\left[n-\overline{d_{21}^2}+n\lambda\left(1-\overline{d_{21}^2}\right)\right]-\left(1-\overline{d_{21}^2}\right)\left(n-n\lambda\overline{d_{21}}\right.} \tag{51}$$

Note that the first factor in (51) is the "optimum" value of K_2/K_1 as motivated by the MAP estimation theory, namely, that given by (44), which is independent of signal-to-noise ratio. Only when the channels have equal energy, i.e., $\lambda=1/n$, are the results of (44) and (51) equal, i.e., $K_2/K_1 = \lambda^2$.

Substituting (51) into (47) results in an expression for the minimum squaring loss, namely,

$$\mathscr{S}_L = \frac{2A_1\left[A_0 + A_1\left(\frac{K_2}{K_1}\right)_{opt}\right]}{(1+\lambda)\left[B_1 + 2B_2\left(\frac{K_2}{K_1}\right)_{opt}\right]} = \frac{\left(A_0^2B_2 + A_1^2B_0 - A_0A_1B_1\right)}{(1+\lambda)\left(B_0B_2 - \frac{B_1^2}{4}\right)} \tag{52}$$

where A_0, A_1, B_0, B_1 and B_2 are found from (48).

As an example, when both channels have NRZ data and synchronous symbol clocks, from Table 1, we then have that $\overline{d_{21}^2} = 1$ and (52) simplifies to

$$\mathscr{L}_L = \frac{\left(1+\frac{1+\lambda}{2\zeta_1}\right)\left(1-2\lambda+n\lambda^2\right)+\lambda\left(n-1\right)\left(1+\frac{2\zeta_1}{1+\lambda}\right)}{\left(1+\lambda\right)\left(1+\frac{1+\lambda}{2\zeta_1}\right)\left[\left(1+\frac{1+\lambda}{2\zeta_1}\right)+n\lambda\left(1+\frac{2\zeta_1}{1+\lambda}\right)\right]} \tag{53}$$

On the other hand, letting $\overline{d_{21}^2} = 1$ in (45) gives the result obtained in [1], namely,

$$\mathscr{L}_L = \frac{\left(1-2\lambda+n\lambda^2\right)^2}{\left(1+\lambda\right)\left[\left(1+\frac{1+\lambda}{2\zeta_1}\right)\left(1-2\lambda+n\lambda^2\right)+\lambda\left(1+\frac{2\zeta_1}{1+\lambda}\right)\left(1-n\lambda\right)^2\right]} \tag{54}$$

Figure 2 illustrates $\mathscr{L}_L$ as computed from (53) and (54) versus the power ratio λ with $n = 10$ and $\zeta_1 = -3$ dB and 10 dB. It is clear from this figure that considerable reduction of squaring loss is possible by choosing the channel gain ratio so as to minimize this quantity.

Another illustration of the squaring loss improvement obtained by optimizing the channel gain ratio is given in Figure 3 Here we consider a mixed data format where the high data rate channel (channel 1) is Manchester coded, while the low data rate channel (channel 2) is again NRZ. Furthermore, we now assume asynchronous symbol clocks, which implies that the value of $\overline{d_{21}^2}$ to be used in (48) and, hence (52), is obtained from Table 2, namely, $\overline{d_{12}^2} = 1/6n = 1/60$ (for $n = 10$). Comparing Figure 3 with Figure 2, we observe that the small value of cross-modulation loss $\left(\overline{d_{12}^2}\right)$ for the mixed format case (Figure 3), as compared with a unity value for the case where both channels have NRZ data (Figure 2), results in a considerable reduction in squaring loss for both the optimum and MAP estimate selections of the channel gain ratio.

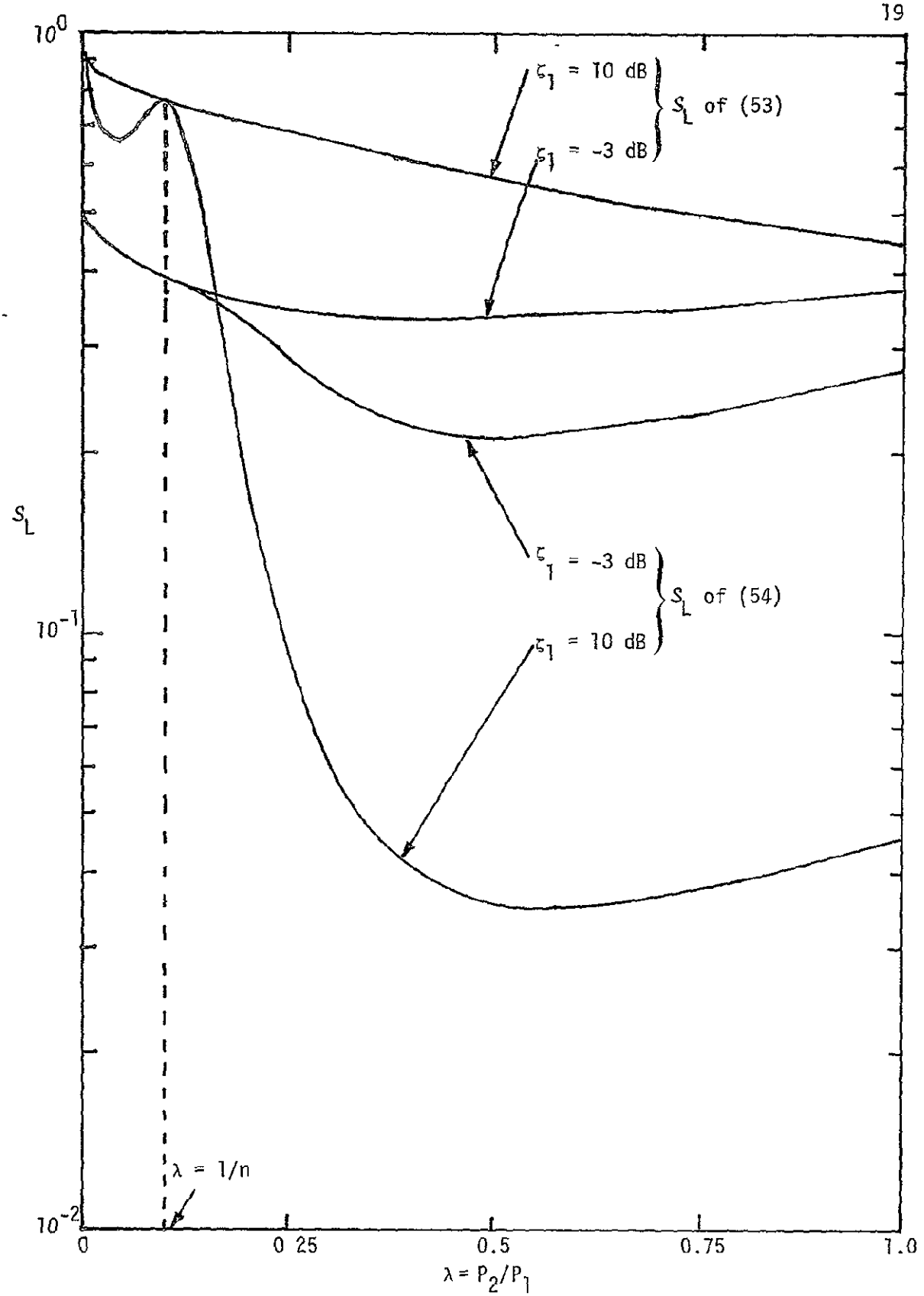

Figure 2. Squaring Loss versus Power Ratio for Unbalanced QPSK, Two-Channel Costas Loop; $n = T_2/T_1 = 10$

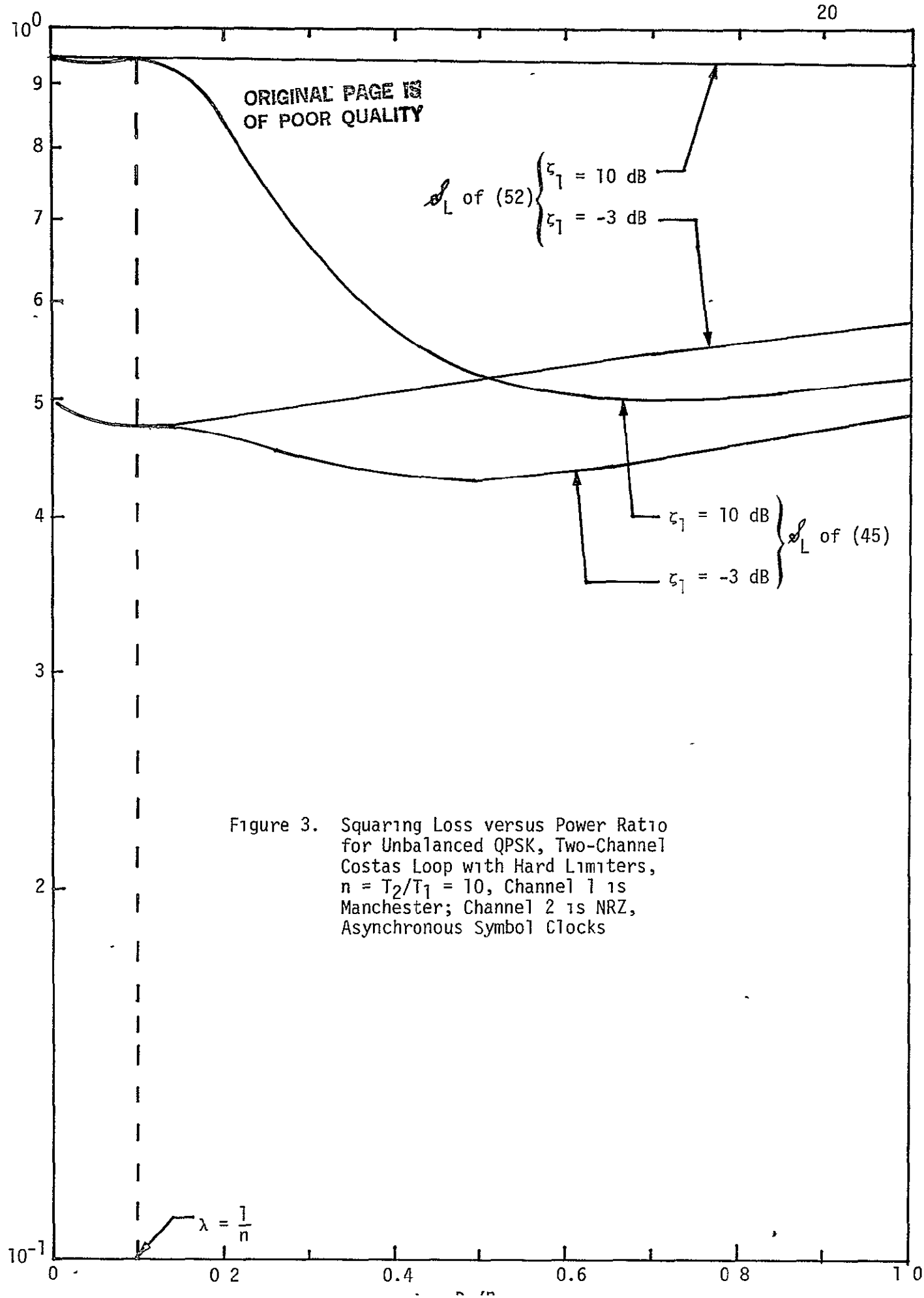

Figure 3. Squaring Loss versus Power Ratio for Unbalanced QPSK, Two-Channel Costas Loop with Hard Limiters, $n = T_2/T_1 = 10$, Channel 1 is Manchester; Channel 2 is NRZ, Asynchronous Symbol Clocks

3.0 PERFORMANCE ANALYSIS OF TWO-CHANNEL COSTAS-TYPE LOOP WITH ACTIVE ARM FILTERS AND HARD LIMITERS

3.1 System Model and Loop Equation of Operation

Here again, we draw heavily upon the notations, definitions and results given in [1]. The loop is still represented by the block diagram of Figure 1 except that now $G(x) = \operatorname{sgn} x$. Thus, the dynamic phase error $z(t)$ now becomes

$$\begin{aligned} z(t) &= \sqrt{K_1}\, z_{s1}(t) \operatorname{sgn}\left[\sqrt{K_1}\, z_{c1}(t)\right] - \sqrt{K_2}\, z_{c2}(t) \operatorname{sgn}\left[\sqrt{K_2}\, z_{s2}(t)\right] \\ &= \sqrt{K_1}\, z_{s1}(t) \operatorname{sgn}\left[z_{c1}(t)\right] - \sqrt{K_2}\, z_{c2}(t) \operatorname{sgn}\left[z_{s2}(t)\right] \end{aligned} \tag{55}$$

where

$$\begin{aligned} z_{s1}(t) &= \int_{(k-1)T_i}^{kT_1} \varepsilon_s(t)\, p_1(t)dt \; ; \quad kT_1 < t \leq (k+1)T_i \\ & \qquad\qquad\qquad\qquad\qquad\quad i=1,2 \\ z_{c1}(t) &= \int_{(k-1)T_i}^{kT_1} \varepsilon_c(t)\, p_i(t)dt \; ; \quad kT_1 < t \leq (k+1)T_1 \\ & \qquad\qquad\qquad\qquad\qquad\quad i=1,2 \end{aligned} \tag{56}$$

are the integrate-and-dump outputs. Splitting $z(t)$ into its random and nonrandom parts, i.e.,

$$z(t) = E\{z(t)|\varphi\} + N(t,\varphi) = S(\varphi) + N(t,\varphi) \tag{57}$$

where $S(\varphi)$ is the loop S-curve and $N(t,\varphi)$ is the equivalent zero-mean additive noise process, then the loop equation can be written in Heaviside operator notation as

$$p\varphi = -K_v\, F(p)\, z(t) = -K_v\, F(p)\left[S(\varphi) + N(t,\varphi)\right] \tag{58}$$

where K_v is the VCO gain in rad/s/v. Finally, linearizing the loop by letting

$$S(\varphi) = S'(0)\varphi \quad ; \qquad N(t,\varphi) = N(t,0) \tag{59}$$

we get an equivalent form analogous to (5), namely,

$$\varphi = H_{\varphi}(p)\left[\frac{N(t,0)}{S'(0)}\right] \tag{60}$$

where

$$H_{\varphi}(s) = \frac{S'(0)\,K_v\,F(s)}{s + S'(0)\,K_v\,F(s)} \tag{61}$$

Assuming, as before, that the bandwidth of $H_{\varphi}(s)$ is much narrower than the bandwidth of $N(t,0)$, the variance of φ is approximated by

$$\sigma_{\varphi}^2 = \frac{N_0'\,B_L}{[S'(0)]^2} \tag{62}$$

where N_0' is the single-sided spectral density of $N(t,0)$ and B_L, the single-sided loop bandwidth, is simply

$$B_L = \frac{1}{2\pi}\int_0^{\infty} \left|H_{\varphi}(j\omega)\right|^2 d\omega \tag{63}$$

3.2 Evaluation of the Loop Signal Component S'(0)

Comparing (55) with (57), we immediately observe that the loop S-curve is defined by

$$S(\varphi) = \sqrt{K_1}\,S_1(\varphi) - \sqrt{K_2}\,S_2(\varphi) \tag{64}$$

where

$$\begin{aligned} S_1(\varphi) &\triangleq E\left\{z_{s1}(t)\ \mathrm{sgn}\left[z_{c1}(t)\right]\middle|\varphi\right\} \\ S_2(\varphi) &\triangleq E\left\{z_{c2}(t)\ \mathrm{sgn}\left[z_{s2}(t)\right]\middle|\varphi\right\} \end{aligned} \tag{65}$$

Substituting (4) into (56) and carrying out the integration gives (assuming $K_0 K_m = 1$)

$$z_{si}(t) = \left[T_i \sqrt{P_1}\, d_{1i}(t) + N_{ci}(t)\right] \sin\varphi - \left[T_i \sqrt{P_2}\, d_{2i}(t) + N_{si}(t)\right] \cos\varphi$$

$$z_{ci}(t) = \left[T_i \sqrt{P_1}\, d_{1i}(t) + N_{ci}(t)\right] \cos\varphi + \left[T_i \sqrt{P_2}\, d_{2i}(t) + N_{si}(t)\right] \sin\varphi; \quad i=1,2 \qquad (66)$$

Performing the statistical expectations first with respect to the noise components in $z_{si}(t)$ and $z_{ci}(t)$, keeping $d_{1i}(t)$ and $d_{2i}(t)$ fixed, gives the conditional S-curve components

$$\begin{aligned} S_1\left(\varphi \middle| d_{11}, d_{21}\right) &= E_{N_{c1}, N_{s1}} \left\{ z_{s1} \operatorname{sgn}\left(z_{c1}\right) \middle| \varphi, d_{11}, d_{21} \right\} \\ &= \frac{1}{2}\left[T_1 \sqrt{P_1}\, d_{11} \sin\varphi - T_1 \sqrt{P_2}\, d_{21} \cos\varphi\right] \\ &\quad \times \operatorname{erfc}\left\{\left[- T_1 \sqrt{P_1}\, d_{11} \cos\varphi - T_1 \sqrt{P_2}\, d_{21} \sin\varphi\right] / \sqrt{2}\, \sigma_1\right\} \\ &\quad - \frac{1}{2}\left[T_1 \sqrt{P_1}\, d_{11} \sin\varphi - T_1 \sqrt{P_2}\, d_{21} \cos\varphi\right] \\ &\quad \times \operatorname{erfc}\left\{\left[T_1 \sqrt{P_1}\, d_{11} \cos\varphi + T_1 \sqrt{P_2}\, d_{21} \sin\varphi\right] / \sqrt{2}\, \sigma_1\right\} \end{aligned} \qquad (67)$$

where erfc x is the complementary error function defined by

$$\operatorname{erfc} x = \frac{2}{\sqrt{\pi}} \int_x^\infty \exp\left(-y^2\right) dy \qquad (68)$$

Since

$$\operatorname{erfc}(-x) - \operatorname{erfc}(x) = 1 + \operatorname{erf} x - (1 - \operatorname{erf} x) = 2 \operatorname{erf} x \qquad (69)$$

then

$$S_1\left(\varphi\middle|d_{11},d_{21}\right) = T_1\left[\sqrt{P_1}\,d_{11}\sin\varphi - \sqrt{P_2}\,d_{21}\cos\varphi\right]\operatorname{erf}\left[\frac{T_1\left[\sqrt{P_1}\,d_{11}\cos\varphi+\sqrt{P_2}\,d_{21}\sin\varphi\right]}{\sqrt{2}\,\sigma_1}\right] \tag{70}$$

where σ_1 is given by (18). Similarly,

$$S_2\left(\varphi\middle|d_{12},d_{22}\right) \triangleq E_{N_{c2},N_{s2}}\left\{z_{c2}\,\operatorname{sgn}\left(z_{s2}\right)\middle|\varphi,d_{12},d_{22}\right\}$$

$$= T_2\left[\sqrt{P_1}\,d_{12}\cos\varphi + \sqrt{P_2}\,d_{22}\sin\varphi\right]\operatorname{erf}\left[\frac{T_2\left[\sqrt{P_1}\,d_{12}\sin\varphi - \sqrt{P_2}\,d_{22}\cos\varphi\right]}{\sqrt{2}\,\sigma_2}\right] \tag{71}$$

Since evaluation of σ_φ^2 from (62) requires only the slope of the loop S-curve at the origin, we next proceed to differentiate (70) and (71) with respect to φ and evaluate these conditional results at $\varphi = 0$. Thus,

$$S_1'\left(0\middle|d_{11},d_{21}\right) \triangleq \left.\frac{\partial S_1\left(\varphi\middle|d_{11},d_{21}\right)}{\partial\varphi}\right|_{\varphi=0}$$

$$= T_1\sqrt{P_1}\,d_{11}\operatorname{erf}\left(\frac{T_1\sqrt{P_1}\,d_{11}}{\sqrt{2}\,\sigma_1}\right) - \frac{2}{\sqrt{\pi}}\,d_{21}^2\left(\frac{T_1^2P_2}{\sqrt{2}\,\sigma_1}\right)\exp\left[-\left(\frac{T_1\sqrt{P_1}\,d_{11}}{\sqrt{2}\,\sigma_1}\right)^2\right]$$

$$= T_1\sqrt{P_1}\,d_{11}\operatorname{erf}\left(\sqrt{\frac{\zeta_1}{1+\lambda}}\,d_{11}\right) - \frac{2}{\sqrt{\pi}}\,d_{21}^2\left(T_1\sqrt{P_2}\right)\left(\sqrt{\frac{\lambda\zeta_1}{1+\lambda}}\right)\exp\left[-\frac{\zeta_1}{1+\lambda}\,d_{11}^2\right] \tag{72}$$

Similarly,

$$S_2'\left(0\middle|d_{12},d_{22}\right) = -T_2\sqrt{P_2}\,d_{22}\operatorname{erf}\left(\sqrt{\frac{n\lambda\zeta_1}{1+\lambda}}\,d_{22}\right) + \frac{2}{\sqrt{\pi}}\,d_{12}^2\left(T_2\sqrt{P_1}\right)\left(\sqrt{\frac{n\zeta_1}{1+\lambda}}\right)\exp\left[-\frac{n\lambda\zeta_1}{1+\lambda}\,d_{22}^2\right] \tag{73}$$

Since, from their definition in (9), d_{11} and d_{22} take on only ± 1 values with equal probability, then (72) and (73) simplify to

$$S_1'\left(0\middle|d_{21}\right) = T_1\sqrt{\frac{P}{1+\lambda}}\left\{\operatorname{erf}\left(\sqrt{\frac{\zeta_1}{1+\lambda}}\right) - \frac{2}{\sqrt{\pi}}\lambda\, d_{21}^2\sqrt{\frac{\zeta_1}{1+\lambda}}\exp\left(-\frac{\zeta_1}{1+\lambda}\right)\right\}$$

$$S_2'\left(0\middle|d_{12}\right) = -nT_1\sqrt{\frac{\lambda P}{1+\lambda}}\left\{\operatorname{erf}\left(\sqrt{\frac{n\lambda\zeta_1}{1+\lambda}}\right) - \frac{2}{\sqrt{\pi}}d_{12}^2\sqrt{\frac{n\zeta_1}{\lambda(1+\lambda)}}\exp\left(-\frac{n\lambda\zeta_1}{1+\lambda}\right)\right\} \qquad (74)$$

Finally, then, averaging over d_{21} and d_{12} and recalling (11) gives the desired result, namely,

$$\begin{aligned} S'(0) &= \sqrt{K_1}\,E_{d_{21}}\left\{S_1'\left(0\middle|d_{21}\right)\right\} - \sqrt{K_2}\,E_{d_{12}}\left\{S_2'\left(0\middle|d_{12}\right)\right\} \\ &= \sqrt{K_1}\,T_1\sqrt{\frac{P}{1+\lambda}}\left\{\operatorname{erf}\left(\sqrt{\frac{\zeta_1}{1+\lambda}}\right) - \frac{2}{\sqrt{\pi}}\lambda\left(\overline{d_{21}^2}\right)\sqrt{\frac{\zeta_1}{1+\lambda}}\exp\left(-\frac{\zeta_1}{1+\lambda}\right)\right. \\ &\quad + \sqrt{\frac{K_2}{K_1}}\,n\sqrt{\lambda}\left[\operatorname{erf}\left(\sqrt{\frac{n\lambda\zeta_1}{1+\lambda}}\right) - \frac{2}{\sqrt{\pi}}\left(\frac{1}{n\sqrt{\lambda}}\right)\left(\overline{d_{21}^2}\right)\right. \\ &\quad \left.\left. \times\sqrt{\frac{n\zeta_1}{1+\lambda}}\exp\left(-\frac{n\lambda\zeta_1}{1+\lambda}\right)\right]\right\} \end{aligned} \qquad (75)$$

For the ratio of channel gains as specified by (44), (75) further simplifies to

$$\begin{aligned} S'(0) = \sqrt{K_1}\,T_1\sqrt{\frac{P}{1+\lambda}}\left\{\operatorname{erf}\left(\sqrt{\frac{\zeta_1}{1+\lambda}}\right) + \lambda\sqrt{n}\operatorname{erf}\left(\sqrt{\frac{n\lambda\zeta_1}{1+\lambda}}\right)\right. \\ - \frac{2}{\sqrt{\pi}}\lambda\left(\overline{d_{21}^2}\right)\sqrt{\frac{\zeta_1}{1+\lambda}}\exp\left(-\frac{\zeta_1}{1+\lambda}\right) \\ \left. - \frac{2}{\sqrt{\pi}}\sqrt{\lambda}\left(\overline{d_{21}^2}\right)\sqrt{\frac{\zeta_1}{1+\lambda}}\exp\left(-\frac{n\lambda\zeta_1}{1+\lambda}\right)\right\} \end{aligned} \qquad (76)$$

3.3 Evaluation of the Equivalent Noise Spectral Density N_0'

To evaluate N_0', we must first find the correlation function of $N(t,0)$, namely,

$$R_N(\tau) = \langle \overline{N(t,0)\ N(t+\tau,0)} \rangle \tag{77}$$

then integrate it between $-\infty$ and ∞, as in (14). Since the value of the loop S-curve $S(\varphi)$ at $\varphi = 0$ is zero, from (57), we then equivalently have

$$R_N(\tau) = \langle \overline{z(t|\varphi=0)\ z(t+\tau|\varphi=0)} \rangle \tag{78}$$

Letting $\varphi = 0$ in (66) and substituting in (55) gives

$$\begin{aligned} z(t|\varphi=0) = &-\sqrt{K_1}\left[T_1\sqrt{P_2}\,d_{21}(t) + N_{s1}(t)\right]\ \mathrm{sgn}\left[T_1\sqrt{P_1}\,d_{11}(t) + N_{c1}(t)\right] \\ &+\sqrt{K_2}\left[T_2\sqrt{P_1}\,d_{12}(t) + N_{c2}(t)\right]\ \mathrm{sgn}\left[T_2\sqrt{P_2}\,d_{22}(t) + N_{s2}(t)\right] \end{aligned} \tag{79}$$

Substituting (79) into (78) and carrying out the statistical averages over the various noise components and data process results in, after much simplification,

$$\begin{aligned} \overline{z\left(t_1|\varphi=0\right)z\left(t_2|\varphi=0\right)} = {} & K_1\left[T_1^2P_2\,\overline{d_{21}^2} + \sigma_1^2\right]A_1\left(t_1,t_2\right) + K_2\left[T_2^2P_1\,\overline{d_{12}^2} + \sigma_2^2\right]A_2\left(t_1,t_2\right) \\ & -\sqrt{K_1K_2}\left[T_1\sqrt{P_2}\,R_{d_{21}d_{22}}\left(t_1,t_2\right)\mathrm{erf}\left(\frac{T_2\sqrt{P_2}}{\sqrt{2}\,\sigma_2}\right) + \frac{2\sigma_1}{\sqrt{2\pi n}}\exp\left(-\frac{T_2^2P_2}{2\sigma_2^2}\right)B\left(t_1,t_2\right)\right] \\ & \times\left[T_2\sqrt{P_1}\,R_{d_{11}d_{12}}\left(t_1,t_2\right)\mathrm{erf}\left(\frac{T_1\sqrt{P_1}}{\sqrt{2}\,\sigma_1}\right) + \frac{2\sigma_2}{\sqrt{2\pi n}}\exp\left(-\frac{T_1^2P_1}{2\sigma_1^2}\right)B\left(t_1,t_2\right)\right] \\ & -\sqrt{K_1K_2}\left[T_1\sqrt{P_2}\,R_{d_{21}d_{22}}\left(t_1,t_2\right)\mathrm{erf}\left(\frac{T_2\sqrt{P_2}}{\sqrt{2}\,\sigma_2}\right) + \frac{2\sigma_1}{\sqrt{2\pi n}}\exp\left(-\frac{T_2^2P_2}{2\sigma_2^2}\right)B\left(t_2,t_1\right)\right] \\ & \times\left[T_2\sqrt{P_1}\,R_{d_{11}d_{12}}\left(t_1,t_2\right)\mathrm{erf}\left(\frac{T_1\sqrt{P_1}}{\sqrt{2}\,\sigma_1}\right) + \frac{2\sigma_2}{\sqrt{2\pi n}}\exp\left(-\frac{T_1^2P_1}{2\sigma_1^2}\right)B\left(t_2,t_1\right)\right] \end{aligned} \tag{80}$$

where

$$A_i(t_1,t_2) = \begin{cases} 1 \ ; \ t_1 \text{ and } t_2 \text{ are both in the interval} \\ \quad (kT_i,(k+1)T_i) \text{ for some } k \\ 0 \ ; \ \text{otherwise} \end{cases}$$

$$i=1,2$$

$$B(t_1,t_2) = R_{d_{21}d_{22}}(t_1,t_2) \tag{81}$$

Using (11) and (20), we are able to simplify (80) whereupon, averaging over t_1 with $t_2 = t_1 + \tau$, we get

$$\begin{aligned} R_N(\tau) = {} & K_1\left[T_1^2P_2\,\overline{d_{21}^2} + \sigma_1^2\right]\left(1 - \frac{|\tau|}{T_1}\right) + K_2\left[T_2^2P_1\left(\frac{1}{n}\right)\overline{d_{21}^2} + \sigma_2^2\right]\left(1 - \frac{|\tau|}{T_2}\right) \\ & - \sqrt{K_1K_2}\left[T_1\sqrt{P_2}\,\operatorname{erf}\left(\frac{T_2\sqrt{P_2}}{\sqrt{2}\,\sigma_2}\right) + \frac{2\sigma_1}{\sqrt{2\pi n}}\exp\left(-\frac{T_2^2P_2}{2\sigma_2^2}\right)\right] \\ & \times\left[T_2\sqrt{P_1}\,\operatorname{erf}\left(\frac{T_1\sqrt{P_1}}{\sqrt{2}\,\sigma_1}\right) + \frac{2\sigma_2}{\sqrt{2\pi n}}\exp\left(-\frac{T_1^2P_1}{2\sigma_1^2}\right)\right]\left[\Delta(\tau) + \Delta(-\tau)\right] \end{aligned} \tag{82}$$

where $\Delta(\tau)$ is defined in (29) and evaluated in (30)-(35). Finally, integrating on τ as required in (14) gives the desired result, namely,

$$\begin{aligned} N_0' = {} & 2N_0T_1^2K_1\left\{\frac{\lambda\zeta_1}{1+\lambda}\left(\overline{d_{21}^2}\right) + \frac{1}{2} + \left(\frac{K_2}{K_1}\right)n^2\left[\frac{\zeta_1}{1+\lambda}\left(\overline{d_{21}^2}\right) + \frac{1}{2}\right]\right. \\ & - 2\sqrt{\frac{K_2}{K_1}}\,n\,\overline{d_{21}^2}\left[\sqrt{\frac{\lambda\zeta_1}{1+\lambda}}\,\operatorname{erf}\left(\sqrt{\frac{n\lambda\zeta_1}{1+\lambda}}\right) + \frac{1}{\sqrt{n\pi}}\exp\left(-\frac{n\lambda\zeta_1}{1+\lambda}\right)\right] \\ & \left.\times\left[\sqrt{\frac{\zeta_1}{1+\lambda}}\,\operatorname{erf}\left(\sqrt{\frac{\zeta_1}{1+\lambda}}\right) + \frac{1}{\sqrt{\pi}}\exp\left(-\frac{\zeta_1}{1+\lambda}\right)\right]\right\} \end{aligned} \tag{83}$$

or for K_2/K_1 as in (44),

$$N_0' = 2N_0T_1^2K_1\left\{\frac{\lambda\zeta_1}{1+\lambda}\left(\overline{d_{21}^2}\right) + \frac{1}{2} + n\lambda\left[\frac{\zeta_1}{1+\lambda}\left(\overline{d_{21}^2}\right) + \frac{1}{2}\right]\right.$$
$$- 2\sqrt{n\lambda}\left(\overline{d_{21}^2}\right)\left[\sqrt{\frac{\lambda\zeta_1}{1+\lambda}}\,\mathrm{erf}\left(\sqrt{\frac{n\lambda\zeta_1}{1+\lambda}}\right) + \frac{1}{\sqrt{n\pi}}\exp\left(-\frac{n\lambda\zeta_1}{1+\lambda}\right)\right]$$
$$\left.\times\left[\sqrt{\frac{\zeta_1}{1+\lambda}}\,\mathrm{erf}\left(\sqrt{\frac{\zeta_1}{1+\lambda}}\right) + \frac{1}{\sqrt{\pi}}\exp\left(-\frac{1}{1+\lambda}\right)\right]\right\} \tag{84}$$

3.4 Squaring Loss Evaluation

Analogous to (41), the squaring loss of the two-channel Costas loop with hard limiters in its in-phase arms is given by

$$\mathscr{S}_L = \frac{N_0B_L}{\sigma_\varphi^2 P} \tag{85}$$

where σ_φ^2 is found from (62). Making this substitution gives

$$\mathscr{S}_L = \frac{[S'(0)]^2}{P\left(N_0'/N_0\right)} \tag{86}$$

Finally, substituting (75) and (83) into (86) gives the desired result, namely,

$$\mathscr{S}_L = \frac{\left[A\left(\zeta_1,\lambda,n,\overline{d_{21}^2}\right)\right]^2}{(1+\lambda)B\left(\zeta_1,\lambda,n,\overline{d_{21}^2}\right)} \tag{87}$$

where

$$A\left(\zeta_1,\lambda,n,\overline{d_{21}^2}\right) \triangleq \frac{S'(0)}{\sqrt{K_1}\,T_1\sqrt{\frac{P}{1+\lambda}}} = \operatorname{erf}\left(\sqrt{\frac{\zeta_1}{1+\lambda}}\right) - \frac{2}{\sqrt{\pi}}\lambda\left(\overline{d_{21}^2}\right)\sqrt{\frac{\zeta_1}{1+\lambda}}\exp\left(-\frac{\zeta_1}{1+\lambda}\right)$$

$$+\sqrt{\frac{K_2}{K_1}}\,n\sqrt{\lambda}\left[\operatorname{erf}\left(\sqrt{\frac{n\lambda\zeta_1}{1+\lambda}}\right) - \frac{2}{\sqrt{\pi}}\left(\frac{1}{n\sqrt{\lambda}}\right)\left(\overline{d_{21}^2}\right)\sqrt{\frac{n\zeta_1}{1+\lambda}}\exp\left(-\frac{n\lambda\zeta_1}{1+\lambda}\right)\right]$$

$$B\left(\zeta,\lambda,n,\overline{d_{21}^2}\right) \triangleq \frac{N_0'}{K_1T_1^2N_0} = \frac{2\lambda\zeta_1}{1+\lambda}\left(\overline{d_{21}^2}\right) + 1 + \left(\frac{K_2}{K_1}\right)n^2\left[\frac{2\zeta_1}{1+\lambda}\left(\overline{d_{21}^2}\right) + 1\right]$$

$$- 4\sqrt{\frac{K_2}{K_1}}\,n\left(\overline{d_{21}^2}\right)\left[\sqrt{\frac{\lambda\zeta_1}{1+\lambda}}\operatorname{erf}\left(\sqrt{\frac{n\lambda\zeta_1}{1+\lambda}}\right) + \frac{1}{\sqrt{n\pi}}\exp\left(-\frac{n\lambda\zeta_1}{1+\lambda}\right)\right]$$

$$\times\left[\sqrt{\frac{\zeta_1}{1+\lambda}}\operatorname{erf}\left(\sqrt{\frac{\zeta_1}{1+\lambda}}\right) + \frac{1}{\sqrt{\pi}}\exp\left(-\frac{\zeta_1}{1+\lambda}\right)\right] \tag{88}$$

For $K_2/K_1 = \lambda/n$ as in (44), (88) simplifies in the same manner that (75) becomes (76) and (83) becomes (84).

3.5 Optimization of Channel Gain Ratio to Minimize Mean-Square Phase Jitter

As for the double-channel Costas loop without hard limiters, here we can choose the channel gain ratio to minimize mean-square phase jitter. From (87) and (88), we observe that the squaring loss can be written in the form

$$\mathscr{S}_L = \frac{\left[C_0 + C_1\sqrt{\frac{K_2}{K_1}}\right]^2}{(1+\lambda)\left[D_0 + D_1\sqrt{\frac{K_2}{K_1}} + D_2\left(\sqrt{\frac{K_2}{K_1}}\right)^2\right]} \tag{89}$$

where

$$C_0 = \operatorname{erf}\left(\sqrt{\frac{\zeta_1}{1+\lambda}}\right) - \frac{2}{\sqrt{\pi}}\lambda\left(\overline{d_{21}^2}\right)\sqrt{\frac{\zeta_1}{1+\lambda}}\exp\left(-\frac{\zeta_1}{1+\lambda}\right)$$

$$C_1 = n\sqrt{\lambda}\left[\operatorname{erf}\left(\sqrt{\frac{n\lambda\zeta_1}{1+\lambda}}\right) - \frac{2}{\sqrt{\pi}}\left(\frac{1}{n\sqrt{\pi}}\right)\left(\overline{d_{21}^2}\right)\sqrt{\frac{n\zeta_1}{1+\lambda}}\exp\left(-\frac{n\lambda\zeta_1}{1+\lambda}\right)\right]$$

$$D_0 = \frac{2\lambda\zeta_1}{1+\lambda}\left(\overline{d_{21}^2}\right) + 1$$

$$D_1 = -4n\left(\overline{d_{21}^2}\right)\left[\sqrt{\frac{\lambda\zeta_1}{1+\lambda}}\operatorname{erf}\left(\sqrt{\frac{n\lambda\zeta_1}{1+\lambda}}\right) + \frac{1}{\sqrt{n\pi}}\exp\left(-\frac{n\lambda\zeta_1}{1+\lambda}\right)\right]$$

$$\times\left[\sqrt{\frac{\zeta_1}{1+\lambda}}\operatorname{erf}\left(\sqrt{\frac{\zeta_1}{1+\lambda}}\right) + \frac{1}{\sqrt{\pi}}\exp\left(-\frac{\zeta_1}{1+\lambda}\right)\right]$$

$$D_2 = n^2\left[\frac{2\zeta_1}{1+\lambda}\left(\overline{d_{21}^2}\right) + 1\right] \tag{90}$$

From (40) and (50), it is obvious that the gain ratio that minimizes the phase-tracking jitter is

$$\left(\sqrt{\frac{K_2}{K_1}}\right)_{opt} = \frac{2C_1D_0 - C_0D_1}{2C_0D_2 - C_1D_1} \tag{91}$$

with the corresponding minimum squaring loss

$$\mathscr{S}_L = \frac{\left(C_0^2D_2 + C_1^2D_0 - C_0C_1D_1\right)}{(1+\lambda)\left(D_0D_2 - \frac{D_1^2}{4}\right)} \tag{92}$$

For the case of NRZ data on both channels with synchronized symbol clocks, Figure 4 illustrates $\mathscr{S}_L$ as computed from (92) versus the power ratio λ with $n = 10$ and $\zeta_1 = -3$ dB and 10 dB. For comparison purposes, $\mathscr{S}_L$ as computed from (88) with $K_2/K_1 = \lambda/n$ is superimposed on these same curves.

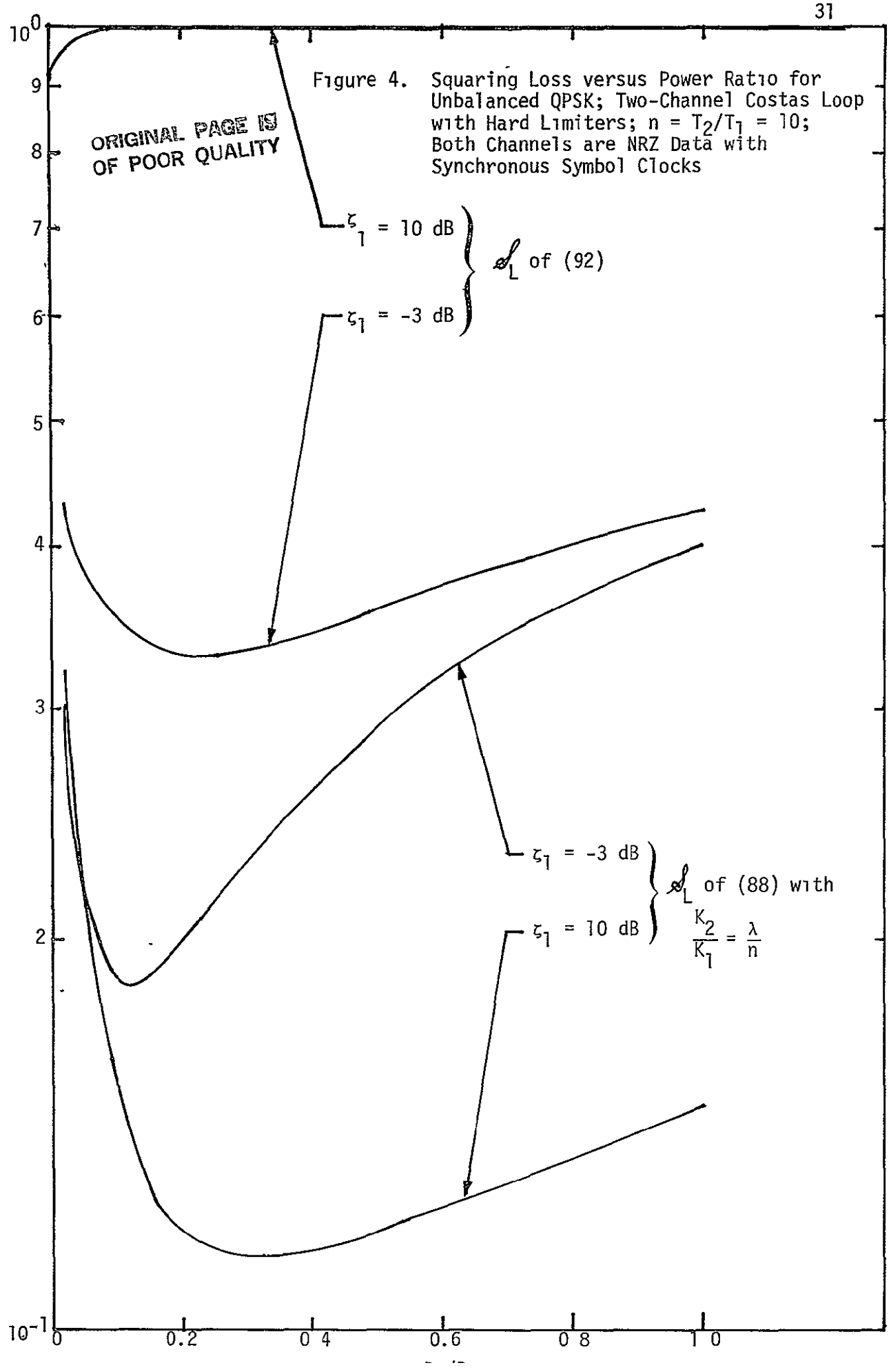

Figure 4. Squaring Loss versus Power Ratio for Unbalanced QPSK; Two-Channel Costas Loop with Hard Limiters; $n = T_2/T_1 = 10$; Both Channels are NRZ Data with Synchronous Symbol Clocks

Clearly, optimization of the channel gain ratio in accordance with (91) offers a significant reduction in squaring loss relative to the values obtained by choosing this ratio in accordance with the MAP estimation relationship of (44).

To further illustrate the effect of power unbalance on squaring loss performance, we consider the case of equal bit energy in the two channels, namely,

$$P_1T_1 = P_2T_2 \triangleq E_b \tag{93}$$

or, equivalently, from (12) and the definition of n,

$$n\lambda = 1 \tag{94}$$

Substituting first (94) into (87), then letting $K_2/K_1 = \lambda/n = \lambda^2$ gives

$$\mathscr{S}_L = \frac{\left[\operatorname{erf}\sqrt{\zeta} - \frac{2}{\sqrt{\pi}}\sqrt{\zeta\lambda}\left(\overline{d_{21}^2}\right)\exp(-\zeta)\right]^2}{\zeta(1+\lambda)\left(\overline{d_{21}^2}\right) + 1 - 2\sqrt{\lambda}\left(\overline{d_{21}^2}\right)\left[\sqrt{\zeta}\operatorname{erf}\sqrt{\zeta} + \frac{1}{\sqrt{\pi}}\exp(-\zeta)\right]^2}\left[\frac{\left(1+\sqrt{\lambda}\right)^2}{2(1+\lambda)}\right] \tag{95}$$

where

$$\zeta \triangleq \frac{\zeta_1}{1+\lambda} = \frac{P_1T_1}{N_0} = \frac{P_2T_2}{N_0} = \frac{E_b}{N_0} \tag{96}$$

Equation (95) represents the generalization of [1, (70)] for the case of arbitrary data formats on the two channels and either synchronous or asynchronous symbol clocks. Figure 5 is a plot of $\mathscr{S}_L$ as determined from (95) versus λ with E_b/N_0 as a parameter and NRZ data on both channels.

The corresponding curves for the optimum channel gain ratio are obtained by substituting (94) into (93) and also are illustrated in Figure 5. Unlike the two-channel Costas loop without hard limiters, the two results here are not, in general, equal when the channel energies are made equal. In fact, for large unbalance in power and large values of E_b/N_0,

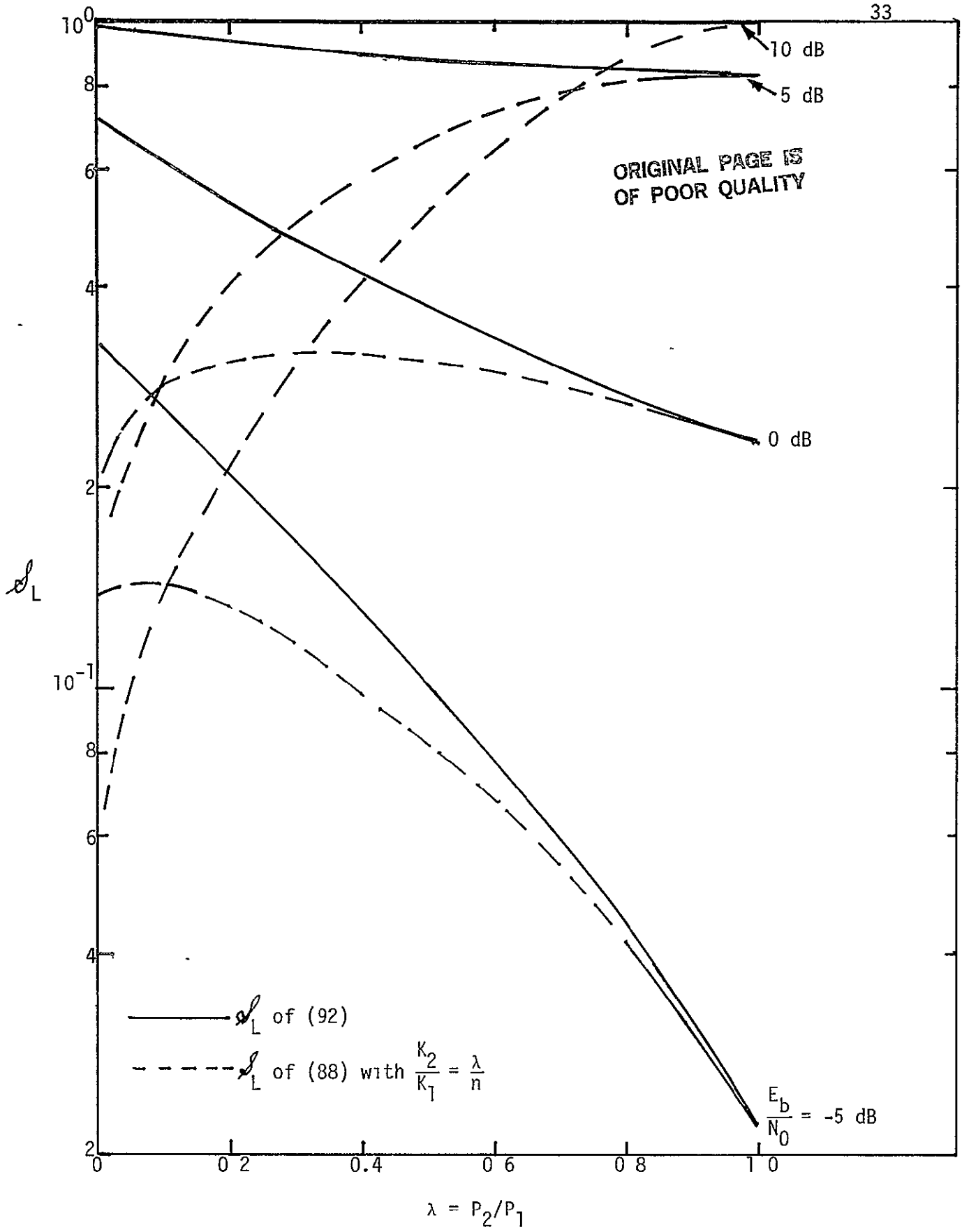

Figure 5. Squaring Loss versus Power Ratio for Unbalanced QPSK; Two-Channel Costas Loop with Hard Limiters, $n = 1/\lambda$ (Both Channels have Equal Bit Energy), Both Channels are NRZ Data with Synchronous Symbol Clocks

much benefit is derived by optimizing the channel gain ratio. Only when both the power and data rate ratios are equal to one (i.e., balanced QPSK) do the two results agree exactly as one would expect.

Figure 6 is another example of the effect of channel power unbalance on squaring loss performance when the bit energies in both channels are equal. Here we assume that channel 1 has a Manchester data format while channel 2 is still NRZ data. The symbol clocks, however, are now assumed to be asynchronous. Thus, the appropriate cross-modulation loss factor is determined from Table 2 as $\overline{d_{21}^2} = (6n)^{-1} = \lambda/6$. For large power unbalance (small λ), the cross-modulation loss is small and, thus, we observe an improvement in squaring loss performance relative to the previous case where $\overline{d_{21}^2} = 1$ for all λ.

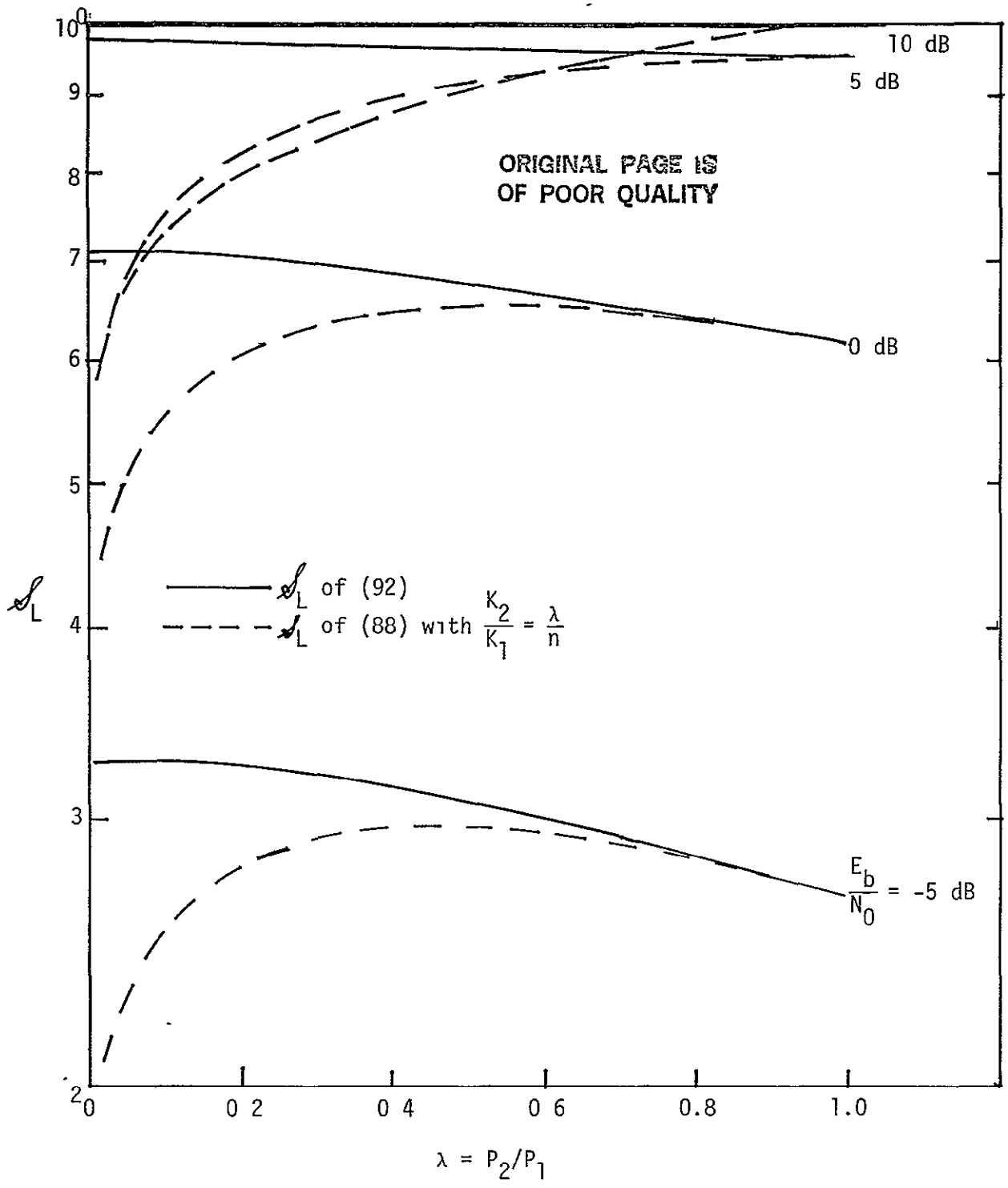

Figure 6. Squaring Loss versus Power Ratio for Unbalanced QPSK; Two-Channel Costas Loop with Hard Limiters, n = 1/λ (Both Channels have Equal Bit Energy), Channel 1 is Manchester, Channel 2 is NRZ, Asynchronous Symbol Clocks

REFERENCES

1. W. R. Braun and W. C. Lindsey, "Carrier Synchronization Techniques for Unbalanced QPSK Signals--Part I," IEEE Transactions on Communications, Vol. COM-26, No. 9, September 1978, pp. 1325-1333.

2. W. R. Braun and W. C. Lindsey, "Carrier Synchronization Techniques for Unbalanced QPSK Signals--Part II," IEEE Transactions on Communications, Vol. COM-26, No. 9, September 1978, pp. 1334-1341.

3. C. L. Weber, "Candidate Receivers for Unbalanced QPSK," ITC'76 Proceedings, Vol. XII, pp. 455-464.

4. H. C. Osborne, "Effect of Noisy Phase Reference on Coherent Detection of UQPSK Signals," NTC'78 Conference Record, Birmingham, Alabama, December 1978, pp. 2.2.1-2.2.6.

5. D. Divsalar and J. H. Yuen, "Performance of Unbalanced QPSK in the Presence of Noisy Reference and Crosstalk," NTC'79 Conference Record, Washington, D.C., November 1979, pp. 44.4.1-44.4.7.

6. M. K. Simon, "Tracking Performance of Unbalanced QPSK Demodulators: Part II--Biphase Costas Loop with Active Arm Filters," IEEE Trans. on Comm., Vol. COM-26, No. 8, August 1978, pp. 1157-1166.

KU-BAND BENT-PIPE MODE 2 BER PERFORMANCE DEGRADATION

Contract No. NAS 9-16067, Exhibit B

(Technical Monitor: W. E. Teasdale)

Interim Report

Prepared for

NASA Lyndon B. Johnson Space Center
Houston, Texas 77058

Prepared by

J.K. Holmes

Axiomatix
9841 Airport Blvd., Suite 912
Los Angeles, California 90045

Axiomatix Report No. R8102-4
February 18, 1981

1.0 INTRODUCTION AND DISCUSSION OF PROBLEM

The purpose of this report is to determine the bit error rate (BER) degradation for the Ku-band return link mode 2. Figure 1 illustrates the overall Ku-band return link. The typical return link data sources are indicated in Table 1. In mode 2, there are three inputs to the FM modulator. First, there is the bent-pipe wideband signal which is amplitude (peak) regulated so as to provide 22 MHz peak-to-peak carrier deviation, which is channel 3. In addition, there is channel 1, which has operations data from the network signal processor, and channel 2, which receives data from the payload recorder, operations recorder, payload low data rate link or low data rate payload interrogator. Channels 1 and 2 together provide for a peak-to-peak FM frequency deviation of 12 MHz

Table 1. Ku-Band Return Link Data Sources

Source	Type	Rate or Bandwidth
CHANNEL 1 (MODE 1/MODE 2)		
Operations data--Network Signal Processor (1,2)	Digital	192 kbps (biphase)
CHANNEL 2 (MODE 1/MODE 2)		
Payload Recorder	Digital	25.5 - 1024 kbps (biphase)
Operations Recorder	Digital	25.5 - 1024 kbps (biphase)
Payload Low Data Rate	Digital	16 - 2000 kbps (NRZ) 16 - 1024 kbps (biphase)
Payload Interrogator (1,2) Low Data Rate	Digital/ Analog	16 - 2000 kbps (NRZ) 16 - 1024 kbps (biphase) 1.024 MHz (PSK or FM)
CHANNEL 3 (MODE 1)		
Payload MUX	Digital	2 - 50 Mbps (NRZ)
CHANNEL 3 (MODE 2)		
Payload Interrogator (1,2) High Data Rate	Digital/ Analog	16 - 4000 kbps 0 - 4 5 MHz
Payload	Analog	0 - 4.5 MHz
Payload High Data Rate	Digital	16 - 4000 kbps
Television	Analog	0 - 4.5 MHz

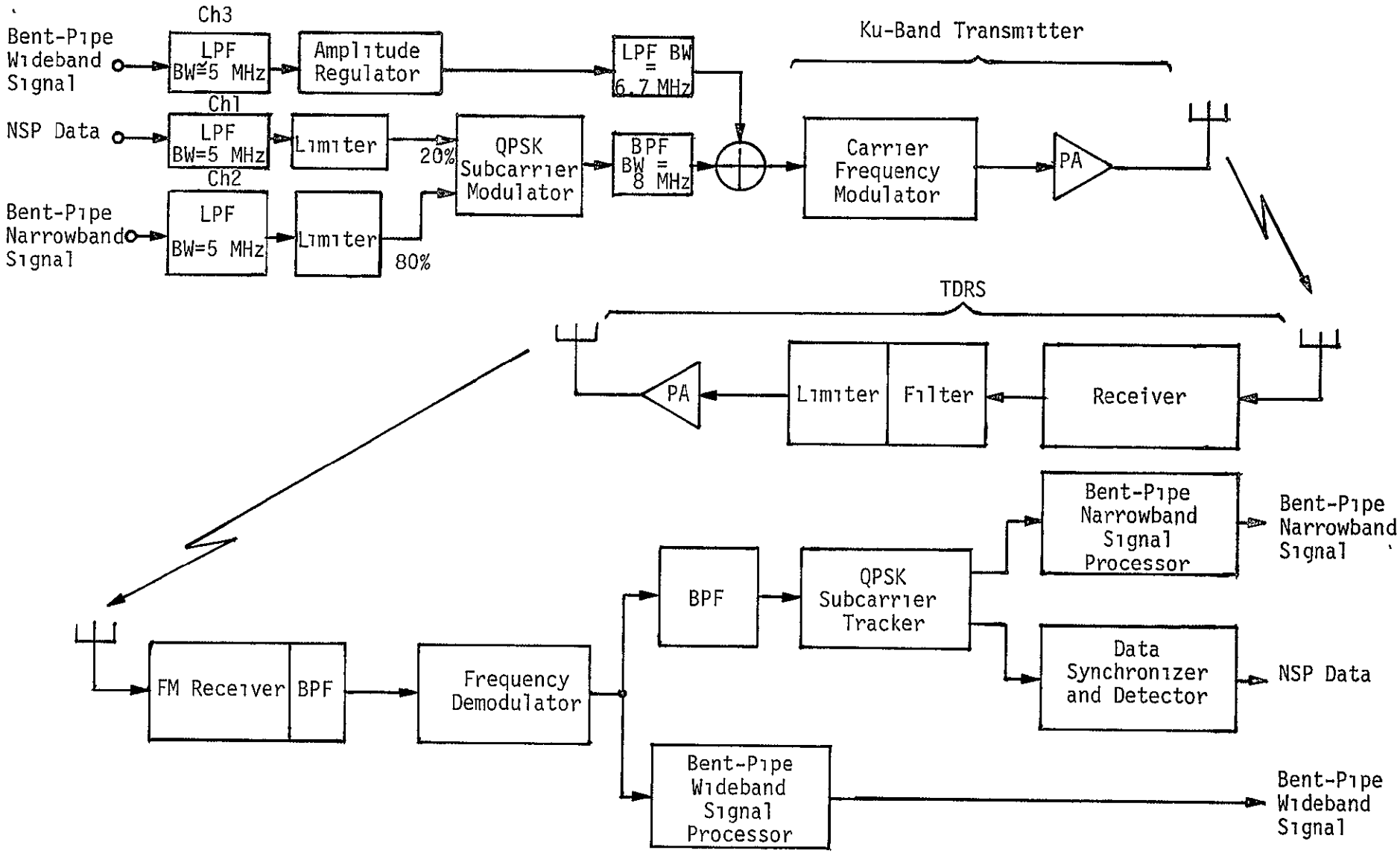

Figure 1. Ku-Band Bent-Pipe FM Return Link

Both channels 1 and 2 are hard limited by TTL receivers (essentially limiters) and QPSK modulated onto an 8.5 MHz subcarrier. This quadriphase subcarrier is added to channel 3 at baseband and frequency modulated onto the carrier. Figure 2 gives a more detailed block diagram of the modulation process. In Figure 2, both modes 1 and 2 are illustrated; however, in this report, we are concerned with mode 2 only, the FM mode.

The specific case of concern in this report is the case wherein the signal of channel 1 is a 192 kbps biphase-L (Manchester) baseband data stream without thermal noise corruption, channel 2 has a 2 Mbps NRZ baseband data stream plus thermal noise, and channel 3 is composed of two subcarriers, one at 1.024 MHz and one at 1.7 MHz, plus thermal noise.

The power spectral density (PSD) for the case in which channel 1 is 192 kbps Manchester, channel 2 is 2 Mbps NRZ and the 1.7 and 1.024 MHz tones are unmodulated and are sketched in Figure 3 along with the respective lowpass and bandpass filters (into the summer) of Figure 2.

2.0 CHANNELS 1 AND 2 QUADRIPHASE SIGNAL

In this section, we discuss the Hughes Aircraft Company (HAC) implementation of the quadriphase modulator. A digital subcarrier oscillator (SCO) running at 8.5 MHz supplies a clock and its complement. Both clocks are passed through a fixed-time delay (τ) corresponding to a fixed-phase delay $2\theta_0$ in the square-wave fundamental. When not filtered, the result is a constant-envelope four-phase signal, as shown on the I-Q diagram of Figure 4 that has a ratio of I Q of 4:1 The actual signal wave is filtered so that only the first harmonics are applied to the FM modulator.

In order to understand the power relationships of the I and Q channels, we establish the form of the filtered quadriphase signal following the work of Cager [3] in the case of no noise. The digital subcarrier phase modulator is described by

$$s(t) = \left[\right] \text{in}(\omega_{sc}t+\phi(t)) \qquad (1)$$

where

$$\phi(t) = \theta d_1(t)d_2(t) - \frac{\pi}{2}(d_2(t)-1) \qquad (2)$$

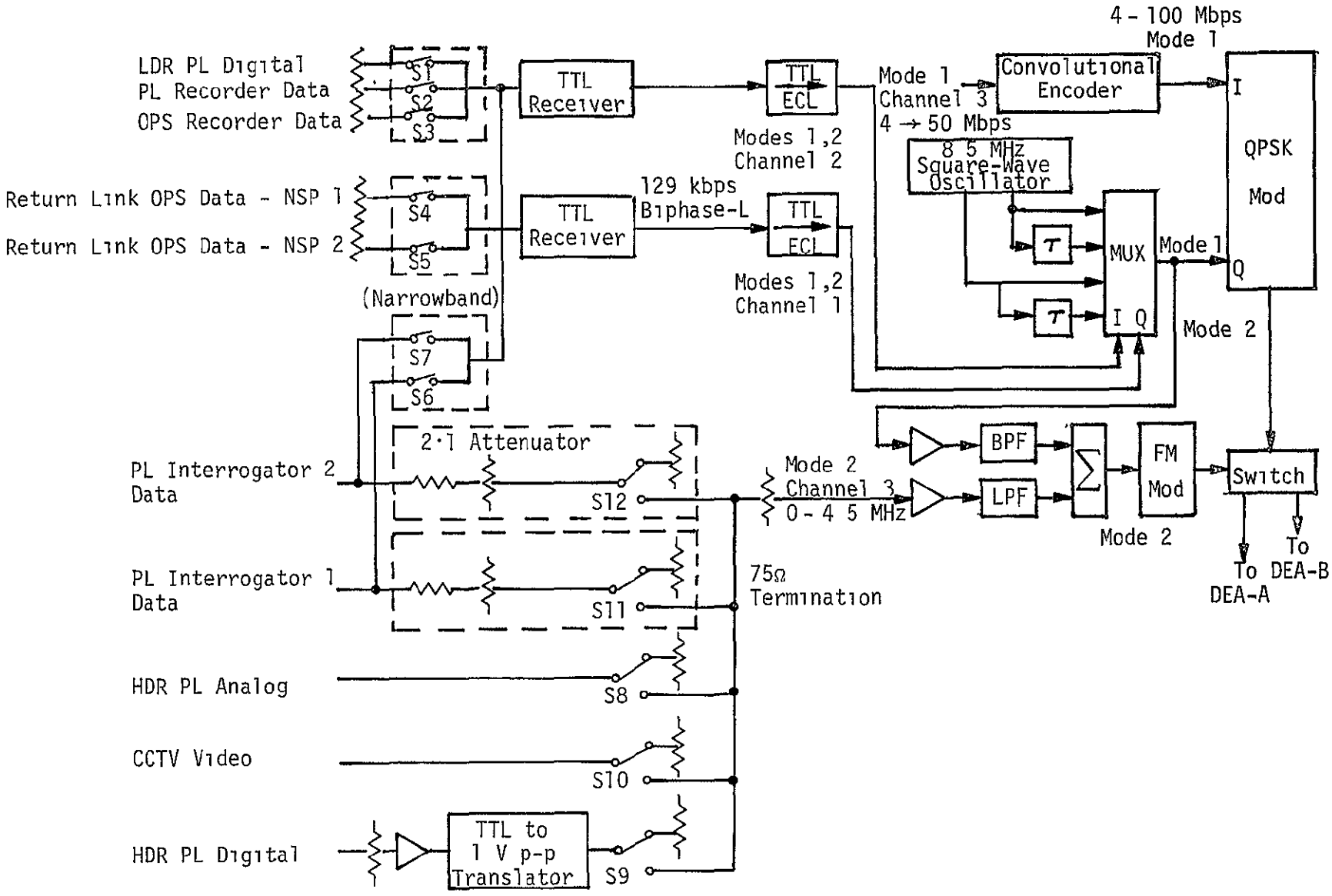

Figure 2 Ku-Band Return Link Transmitter-Modulator

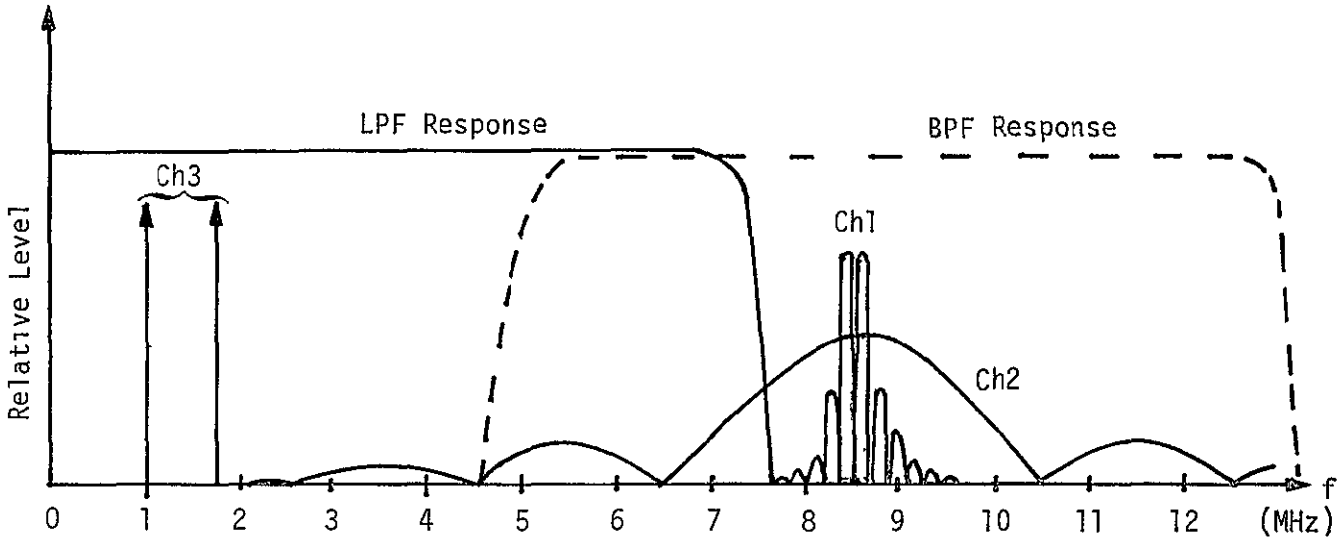

Figure 3. Sketch of the FM Input Spectra Along With the Associated Separating Filters

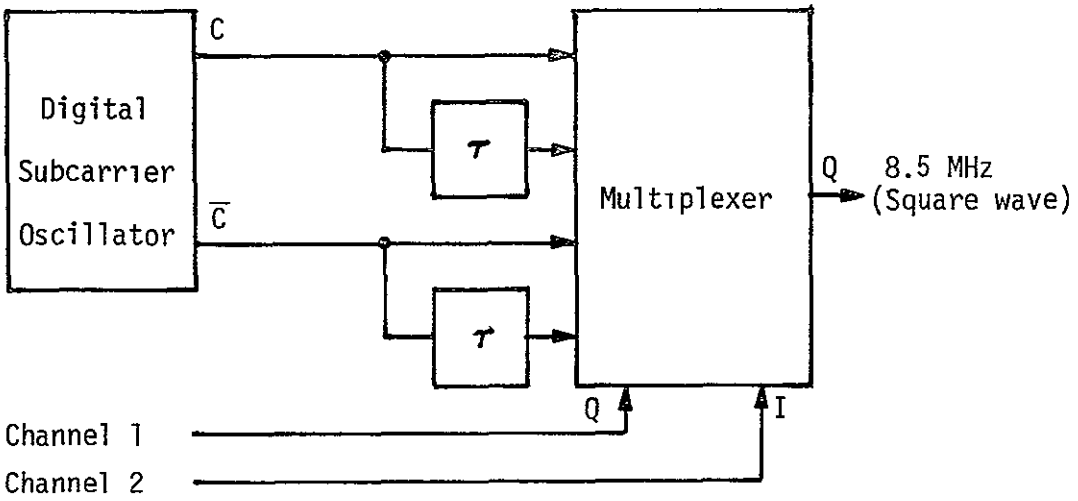

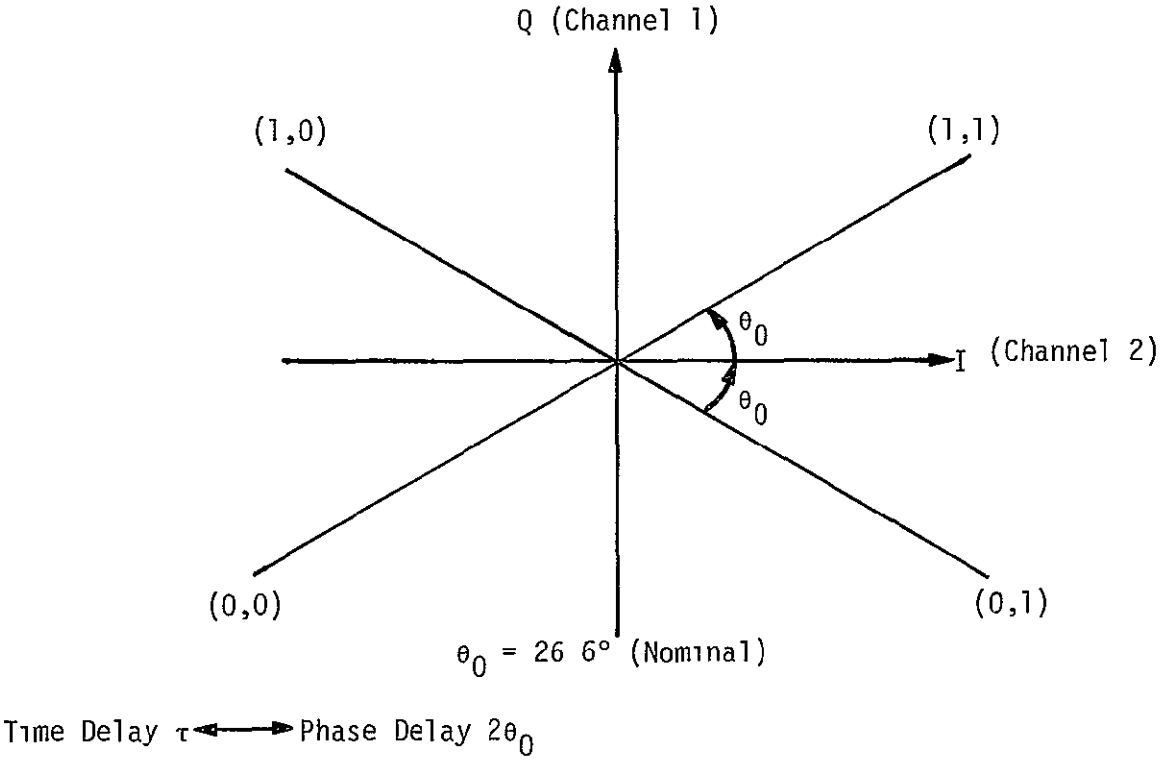

Figure 4 QPSK Subcarrier Oscillator Modulator
for Mode 2 Ku-Band Return Link

with $d_1(t)$ the channel 1 baseband modulation and $d_2(t)$ the channel 2 baseband modulation so that the four phases of $\phi(t)$ are described by Table 2 below.

Table 2. Square-Wave Oscillator Phase Relationship

$\phi(t)$	$d_1(t)$	$d_2(t)$
θ	1	1
$-\theta+\pi$	1	-1
$\theta+\pi$	-1	-1
$-\theta$	-1	1

The value of θ_0 is the value of θ such that the I and Q relationship yields a power ratio of 4:1 in the first harmonic. Expanding (1) in a sine-Fourier series yields

$$s(t) = \sum_{n=1}^{\infty} \frac{4}{n\pi} \sin\left[n\left(\omega_{sc}t + \phi(t)\right)\right] \tag{3}$$

where $\sum$ denotes summation on the odd terms. Expanding (3) yields

$$s(t) = \sum_{n=1}^{\infty} \frac{4}{n\pi} \cos[n\phi(t)] \sin n\omega_{sc}t + \sum_{n=1}^{\infty} \frac{4}{n\pi} \sin[n\phi(t)] \cos n\omega_{sc}t \tag{4}$$

Using (2) for $\phi(t)$ yields

$$\cos[n\phi(t)] = \cos\left[n\, d_1 d_2\, \theta\right] \cos\left[n(d_2-1)\pi/2\right] \tag{5}$$

$$\sin[n\phi(t)] = \sin\left[n\, d_1 d_2\, \theta\right] \cos\left[n(d_2-1)\pi/2\right] \tag{6}$$

since $\sin\left[n(d_2-1)\pi/2\right]$ equals zero. Simplifying (5) and (6) yields

$$\cos[n\phi(t)] = d_2 \cos n\theta \qquad n \text{ odd} \tag{7}$$

$$\sin[n\phi(t)] = d_1 \sin n\theta \qquad n \text{ odd} \tag{8}$$

Therefore, the quadriphase signal is of the form

$$s(t) = d_2(t) \sum_{n=1}^{\infty} \frac{4}{n\pi} \cos(n\theta) \sin(n\omega_{sc}t) + d_1(t) \sum_{n=1}^{\infty} \frac{4}{n\pi} \sin(n\theta) \cos(n\omega_{sc}t) \tag{9}$$

Let

$$U(t) = \sum_{n=1}^{\infty} \frac{4}{n\pi} \cos n\theta \sin(n\omega_{sc}t) \tag{10}$$

$$V(t) = \sum_{n=1}^{\infty} \frac{4}{n\pi} \sin n\theta \cos(n\omega_{sc}t) \tag{11}$$

then

$$s(t) = d_2(t)\, U(t) + d_1(t)\, V(t) \tag{12}$$

To identify the waveforms expressed by (9), note that

$$U(t) = \sum_{n=1}^{\infty} \frac{4}{n\pi} \cos(n\theta) \sin(n\omega_{sc}t) = \frac{\lfloor \sin(\omega_{sc}t - \theta) + \lfloor \sin(\omega_{sc}t + \theta)}{2} \tag{13}$$

where $\lfloor \sin(\omega_{sc}t + \theta)$ is a hard-limited sine wave of the argument $(\omega_{sc}t+\theta)$.

Since

$$\lfloor \sin(\omega_{sc}t-\theta) + \lfloor \sin(\omega_{sc}t+\theta) = \sum_{n=1}^{\infty} \frac{4}{n\pi} \cos(-n\theta) \sin(n\omega_{sc}t) + \sin(-n\theta) \cos(n\omega_{sc}t)$$

$$+ \sum_{n=1}^{\infty} \frac{4}{n\pi} \cos(n\theta) \sin(n\omega_{sc}t) + \sin(n\theta) \cos(n\omega_{sc}t) \tag{14}$$

It can also be shown in the same manner that

$$V(t) = \sum_{n=1}^{\infty} \frac{4}{n\pi} \sin n\theta \cos(n\omega_{sc}t) = \frac{\left[\right] in(\omega_{sc}t+\theta) - \left[\right] in(\omega_{sc}t-\theta)}{2} \quad (15)$$

Now the right-hand sides of (13) and (15) can easily be plotted as shown in Figure 5. Thus, we see that the digital quadriphase signal can be broken down into two orthogonal basis functions that span the space of periodic functions Note that the sum of U(t) and V(t) yields a square-wave signal that is early (from t= 0) by $2\theta/\omega_{sc}$ seconds, whereas U(t) - V(t) generates a square wave with a delay of θ/ω_{sc} seconds, etc.

Note that the total power in the waveform of (9) is given by

$$P_s = \frac{1}{2} \sum_{n=1}^{\infty} \frac{16}{n^2\pi^2} (\cos^2(n\theta) + \sin^2(n\theta)) = \frac{8}{\pi^2} \sum_{n=1}^{\infty} \frac{1}{n^2} = 1 \quad (16)$$

Furthermore, the power in channel 1 is given by

$$P_v = P_1 = \sum_{n=1}^{\infty} \frac{1}{2} \frac{16}{n^2\pi^2} \sin^2 n\theta = \frac{2\theta}{\pi} \qquad \frac{\pi}{2} \geqslant \theta \geqslant 0 \quad (17)$$

and the power in channel 2 is given by

$$P_u = P_2 = \sum_{n=1}^{\infty} \frac{1}{2} \frac{16}{n^2\pi^2} \cos^2 n\theta = 1 - \frac{2\theta}{\pi} \qquad \frac{\pi}{2} \geqslant \theta \geqslant 0 \quad (18)$$

Notice that, when θ = 0.464 radians (26 58°), the power split is

$$P_1 = 0.295 \quad (19)$$

$$P_2 = 0.705 \quad (20)$$

and P_2/P_1 is 2.38:1 However, since the BPF at the output of the MUX (quadriphase modulator) passes only the fundamental, the expression for the respective channel powers become

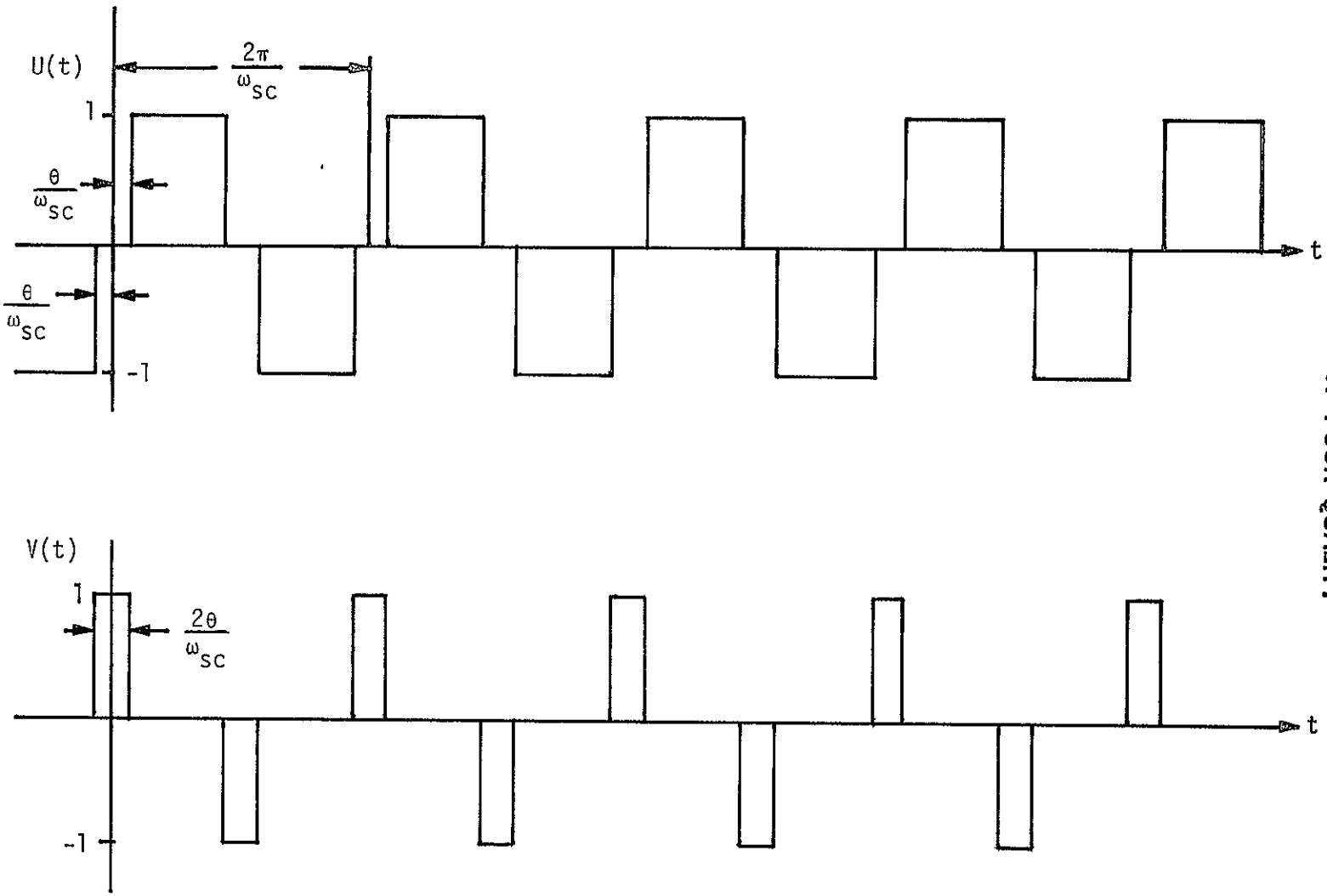

Figure 5 Two Basis Functions for QPSK Channels 1 and 2 Signal

$$P_1 = \frac{8}{\pi^2} \sin^2\theta \tag{21}$$

$$P_2 = \frac{8}{\pi^2} \cos^2\theta \tag{22}$$

and, for $\theta = 0.464$, we have that P_2/P_1 is 4:1, as was desired.

We note from (9) using only the first harmonics that the signal can be expressed as

$$s_f(t) = \frac{4}{\pi} d_1(t) \sin\theta \cos(\omega_{sc}t) + \frac{4}{\pi} d_2(t) \cos\theta \sin(\omega_{sc}t) \tag{23}$$

where $d_1(t)$ is the output of the channel 1 limiter and $d_2(t)$ is the output of channel 2. Thus, we see that we can model the bandpass process in terms of its baseband processes.

3.0 IMPERFECT CARRIER REFERENCE LOSSES

Since we have a quadriphase signal with both a low rate NRZ waveform and a high rate Manchester waveform, we must consider two cases of cross-channel interference: (1) a high rate NRZ interferes with a low rate Manchester data stream, and (2) a low rate Manchester data stream interferes with a high data rate data stream. The two data streams are illustrated in Figure 6. Besides the cross-channel interference, the imperfect carrier reference loss also exists and is, in general, not negligible. We essentially follow the approach of Osborne [8] in the following.

First consider the case in which the low rate Manchester signal interferes with the high rate NRZ signal. We model the received RF quadriphase signal by

$$r(t) = \underbrace{\sqrt{2P_2}\, d_2(t) \sin(\omega_{sc}t+\theta_0)}_{\text{NRZ}} + \underbrace{\sqrt{2P_1}\, d_1(t) \cos(\omega_{sc}t+\theta_0)}_{\text{Manchester}} + n(t) \tag{24}$$

where P_i is the channel power in the ith channel, $d_i(t)$ is the ith data stream (i=1,2), and ω_{sc} and θ_0 are the angular frequency and phase of the 8.5 MHz subcarrier frequency, and finally, $n(t)$ is white Gaussian noise. The pulse shapes $P_i(t)$ are either NRZ or Manchester symbols. The demodulation circuit is shown in Figure 7.

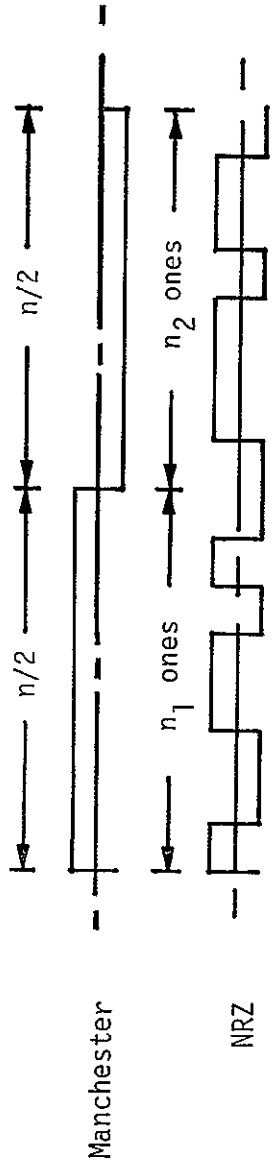

Figure 6 Data Sequence Model for NRZ and Manchester Cross-Channel Interference

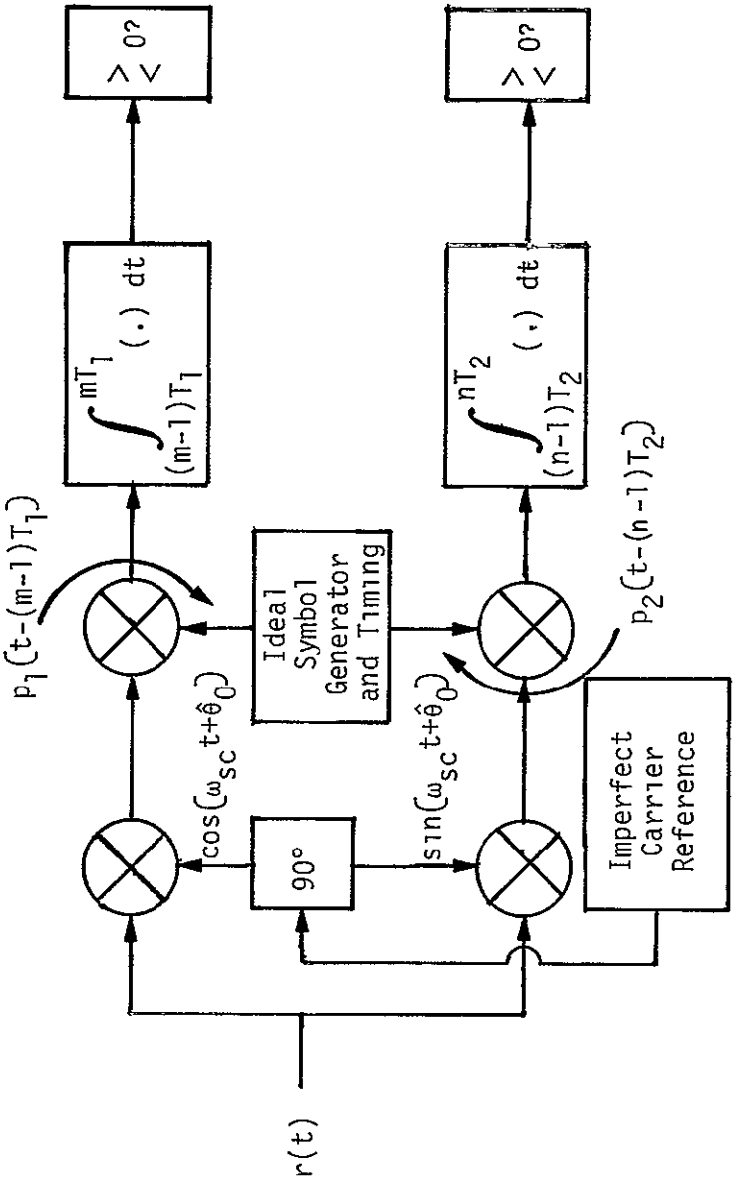

Figure 7 Quadriphase Demodulator Model

In channel 2, after demodulation by $\sqrt{2}\sin(\omega_{sc}t+\hat{\theta}_0)$, we have

$$r(t)\sqrt{2}\sin\left(\omega_{sc}t+\hat{\theta}_0\right) = \sqrt{P_2}\,d_2(t)\cos\phi - \sqrt{P_1}\,d_1(t)\sin\phi + n'(t) \quad (25)$$

where $\phi = \theta_0 - \hat{\theta}_0$ and is the phase error, and $n'(t)$ is an essentially white Gaussian noise process. Assuming that the bit transition probability is 50%, the conditional bit error probability is given by (assuming $\phi(t)$ is essentially constant over $\max(T_1,T_2)$) ,

$$PE(\phi) = \frac{1}{2}\left[Q\left(\sqrt{\frac{2P_2T_2}{N_0}}\cos\phi - \sqrt{\frac{2P_1T_2}{N_0}}\sin\phi\right) + Q\left(\sqrt{\frac{2P_2T_2}{N_0}}\cos\phi + \sqrt{\frac{2P_1T_2}{N_0}}\sin\phi\right)\right] \quad (26)$$

where

$$Q(x) = \frac{1}{\sqrt{2\pi}}\int_x^\infty e^{-t^2/2}\,dt \quad (27)$$

In order to evaluate (25), it is necessary to specify the phase error probability density. To do this, we assume, for lack of a better model, that $p(\phi)$ (for a CW loop) is Tikhonov, i.e.,

$$p(\phi') = \frac{\exp(\alpha\cos\phi')}{2\pi\, I_0(\alpha)}, \qquad -\pi < \phi' < \pi \quad (28)$$

To convert to a loop having an S-curve that has a period of π radians (such as a Costas loop or a quadriphase with power unbalance of 4 1), we let $\phi' = 2\phi$ so that

$$p(\phi) = \frac{\exp(\alpha\cos 2\phi)}{\pi\, I_0(\alpha)}, \qquad -\frac{\pi}{2} \leq \phi \leq \frac{\pi}{2} \quad (29)$$

To determine the meaning of α in this modified Tikhonov density, let α be large so that we can use the asymptotic expression for (28), producing

$$p(\phi) \cong \frac{\exp\left(\frac{-\phi^2}{2(1/4\alpha)}\right)}{\left(\frac{\sqrt{2\pi}}{\sqrt{4\alpha}}\right)} \qquad -\frac{\pi}{2} \leq \phi \leq \frac{\pi}{2} \quad . \tag{30}$$

implying that the linearized phase error variance is given by

$$\sigma_L^2 = \frac{1}{4\alpha} \tag{31}$$

In the same manner, loops having S-curves periodic over $\pm\pi/4$ radians, such as balanced quadriphase tracking loops, have a density given by

$$p(\phi) = \frac{2\exp(\alpha \cos 4\phi)}{\pi I_0(\alpha)} \qquad -\frac{\pi}{4} \leq \phi \leq \frac{\pi}{4} \tag{32}$$

and the linearized phase error variance satisfies

$$\sigma_L^2 = \frac{1}{16\alpha} \tag{33}$$

The power ratio and data rate ratio for channels 1 and 2 satisfies

$$\frac{P_2}{P_1} = 4 \quad ; \quad \frac{R_2}{R_1} = 10 \tag{34}$$

Using (29) to average over (26) produces the results shown in Figure 8. The parameter α_E is the inverse of the linearized phase error variance so that

$$\alpha_E = \frac{1}{\sigma_L^2} = 4\alpha \tag{35}$$

We now consider the case where the high rate Manchester signal interferes with the low rate NRZ signal.

From the received signal of (24), after demodulation by $\sqrt{2}\cos(\omega_{sc}t + \hat{\theta}_0)$, we have

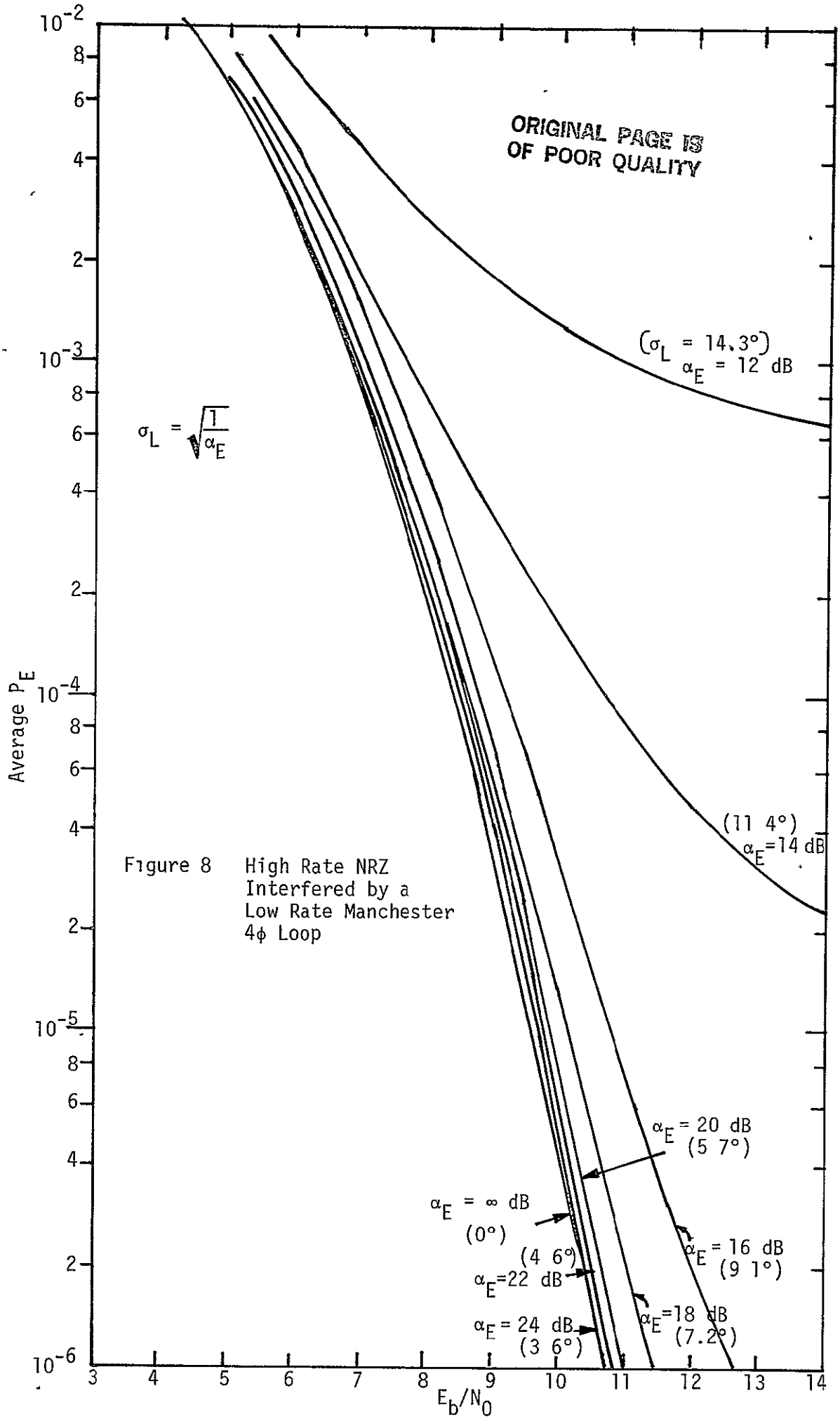

Figure 8 High Rate NRZ Interfered by a Low Rate Manchester 4ϕ Loop

$$r(t)\ \sqrt{2}\ \cos\left(\omega_{sc}t+\hat{\theta}\right) = \sqrt{P_2}\ d_2(t)\ \sin\phi + \sqrt{P_1}\ d_1(t)\ \cos\phi + n''(t) \qquad (36)$$

(HR) (LR)

where n"(t) is an essentially white Gaussian noise process and is independent of n"(t). Again we notice that, if $\phi = 0$ identically, there is no cross-channel interference.

When the transition probability is 50% after matched filtering, the detected signal is given by

$$s_d\left[\frac{2(n_2 - n_1)}{n},\ \phi\right] = \sqrt{P_1}T_1\cos\phi + \left[\frac{\left(\frac{n}{2} - n_1\right) - n_1}{n} - \frac{\left(\frac{n}{2} - n_2\right) - n_2}{n}\right]\sqrt{P_2}T_1\sin\phi \qquad (37)$$

where n_1 denotes the number of ones in the first half of the Manchester bit and n_2 denotes the number of ones in the second half of the Manchester bit and n is the total number of ones in a Manchester bit (see Figure 6). It follows that the conditional average bit error rate is given by (n even)

$$P(E|\phi) = \frac{1}{2^{n/2}}\frac{1}{2^{n/2}}\sum_{n_1=0}^{n/2}\binom{n/2}{n_1}\sum_{n_2=0}^{n/2}\binom{n/2}{n_2}Q\left(\sqrt{\frac{2P_1T_1}{N_0}}\cos\phi - \frac{2(n_2-n_1)}{n}\sqrt{\frac{2P_2T_1}{N_0}}\sin\phi\right) \qquad (38)$$

However, by direct numeration, it can be shown that a single summation form of (38) is given by

$$P(E|\phi) = \frac{1}{2^n}\sum_{i=0}^{n}\binom{n}{i}Q\left(\sqrt{\frac{2P_1T_1}{N_0}}\cos\phi - \left(\frac{n-2i}{n}\right)\sqrt{\frac{2P_2T_1}{N_0}}\sin\phi\right) \qquad (39)$$

Since this is simpler, we shall use this.

In our present case, $n = 10$ and $P_2 = 4P_1$ Evaluating (39) by averaging over ϕ, i e ,

$$PE = \int_{-\pi/2}^{\pi/2} P(E|\phi)\ p(\phi)\ d\phi \qquad (40)$$

yields the results of Figure 9. Note that these curves assume that $\phi(t)$ is essentially constant over $\max(T_1, T_2)$.

By comparing Figure 8 and 9, we see that the case of the low rate Manchester signal being interfered by the high rate and high power NRZ wave has more degradation than the case of the low rate Manchester interfering with the high rate NRZ signal.

We note that both cross-channel effects and an imperfect carrier reference have been degradation sources for Figures 8 and 9.

4.0 CHANNEL 3 NOISE INTERFERENCE EFFECTS ON CHANNELS 1 AND 2

We assume in this section that noise dominates channel 3's input and that the amplifer is linear (neglect clipping) since the degradation is expected to be quite small anyway. The filter preceding the amplitude regulator is a three-pole Butterworth filter so that the noise spectral density shape is given by

$$\frac{N_0}{2}|H(f)|^2 = \frac{N_0}{2}\frac{1}{1+(f/f_0)^6} \tag{41}$$

where $f_0 = 5$ MHz It is known that the lowpass filter (LPF) of Figure 3 has a rejection of 21.6 dB at 8.5 MHz. Furthermore, the 5 MHz LPF is down $10\log[1+(8\ 5/5)^6] = 14$ dB at 8.5 MHz so that the total noise is down by about 35.6 dB. Since channel 3 is only roughly $(22/12)^2 = 5.3$ dB larger, we conclude that the noise is down about 30 dB in the band of channels 1 and 2.

Consider this in greater detail We have, since channels 1 and 2 together deviate the carrier 12 MHz, that

$$P_{CH1} + P_{CH2} = K^2(12)^2 \tag{42}$$

where K is the constant relating signal voltage to frequency deviation. Now

$$\frac{P_{CH1}}{P_{CH2}} = \frac{1}{4} \tag{43}$$

so that

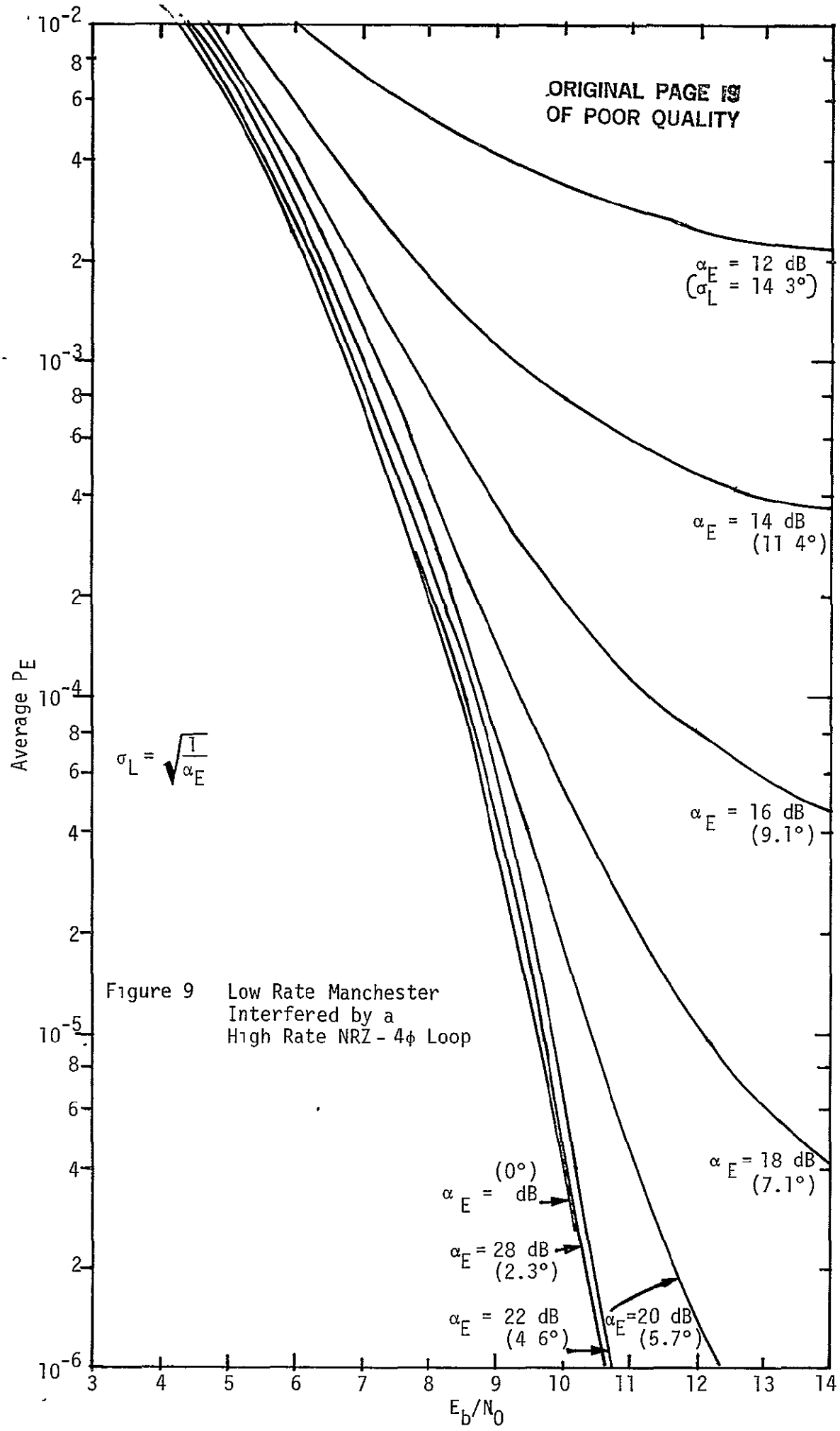

Figure 9 Low Rate Manchester Interfered by a High Rate NRZ - 4ϕ Loop

$$5\ P_{CH1} = K^2(12)^2 \tag{44}$$

or

$$\sqrt{P_{CH1}} = 5.37\ K = \sqrt{P_{S_1}+P_{N_1}} \tag{45}$$

and

$$\sqrt{P_{CH2}} = 10.7\ K = \sqrt{P_{S_2}+P_{N_2}} \tag{46}$$

Now the new noise degradation in channels 1 and 2 due to channel 3 is given by

$$DEGR_1 = \frac{P_{N_1} + P_{N_3} L}{P_{N_1}} \tag{47}$$

and

$$DEGR_2 = \frac{P_{N_2} + P_{N_3} L}{P_{N_2}} \tag{48}$$

where L is the reduction in channel 3 noise at 8.5 MHz. From (45) and (46), we have that

$$P_{N_1} = \frac{(5.37)^2 K^2}{\left[1 + \frac{P_{S1}}{P_{N1}}\right]} \tag{49}$$

and

$$P_{N_2} = \frac{(10.7)^2 K^2}{\left[1 + \frac{P_{S2}}{P_{N2}}\right]} \tag{50}$$

From (49) and (50), and (47) and (48), we obtain

$$DEGR_{CH1} = 10\log\left\{1 + 16.8L\left[1 + \frac{P_{S_1}}{P_{N_1}}\right]\right\} \tag{51}$$

$$DEGR_{CH2} = 10\log\left\{1 + 4.23L\left[1 + \frac{P_{S_2}}{P_{N_2}}\right]\right\} \tag{52}$$

Recall that L = -35.6 dB so that, at minimum noise conditions, i.e.,

$$\frac{E_{B_2}}{N_0} = \frac{E_{B_1}}{N_0} = 20 \text{ dB} \tag{53}$$

we have

$$SNR_1 = \frac{E_{B_1}}{N_0} - 10\log(B_1T_1) \tag{54}$$

$$SNR_2 = \frac{E_{B_2}}{N_0} - 10\log(B_2T_2) \tag{55}$$

Using (53) in (54) and (55) yields

$$SNR_1 = 5.9 \text{ dB} \tag{56}$$

and

$$SNR_2 = 16 \text{ dB} \tag{57}$$

Using (56) and (57) in (51) and (52), respectively, yields

$$DEGR_{CH1} = 0.1 \text{ dB}$$

$$DEGR_{CH2} = 0.2 \text{ dB} \tag{58}$$

We conclude that the degradation in channels 1 and 2 from the noise in channel 3 under worst-case conditions is essentially negligible.

5.0 UPLINK AND DOWNLINK NOISE COMBINING

In this section, we briefly discuss the effect of uplink noise on the received signal. The signal flow in the bent-pipe mode goes from the user to the Shuttle, from the Shuttle to the TDRSS, and from the TDRSS to earth.

The signal power to the total noise power is given by

$$\frac{S}{N_{0_1}+N_{0_2}} = \frac{1}{\frac{N_{0_1}}{S}+\frac{N_{0_2}}{S}} \tag{59}$$

where S denotes the signal power at the ground, N_{0_1} is the Shuttle noise spectral density received on earth, and N_{0_2} is the receiver noise at the earth receiver. Equation (59) can be written in the form

$$\frac{S}{N_{0_1}+N_{0_2}} = \frac{1}{\frac{N_{0_1}}{S}+\left(1+\frac{N_1}{S}\right)\left(\frac{N_{0_2}}{S+N_1}\right)} \tag{60}$$

where N_1/S is the noise power to signal power ratio at the Shuttle (K-band) transmitter. Notice that the right-hand side of (60) is expressed in terms of S/N_{0_1} on the user to Shuttle link, the SNR at the Shuttle transmitter (S/N_1), and ratio of received downlink power to the earth receiver noise spectral density $((S+N_1)/N_{0_2})$. From (60) or (59), we see that, when S/N_{0_2} is large, (60) approaches S/N_{0_1}, as would be expected (according to [10, pages 4-7 and 4-8]).

6.0 HARMONICS OF CHANNEL 3 TONES

We now use Appendix III to evaluate the level of the harmonics of both tones from channel 3 in order to see if they will degrade channels 2 and 3 BER performance. We accomplish this task by comparing the amplitude coefficient h_{010} with h_{070}. See Appendix III for details, particularly equation (III-9). The term h_{070} corresponds to the seventh harmonic of 1.024 MHz and, as such, corresponds to an interfering tone at about 7.2 MHz which lies in the band of channel 2 when operating at 2 Mbps.

From Appendix IV, equation (46), we have for K= 0, $m_1 = 1$ and $m_2 = 0$ (see Appendix III, equation (9)) that

$$h_{010} = \sqrt{2}\,\frac{a}{d}\,b\left[\frac{\sigma_n^2 + P_2}{2}\right]^{1/2} \sqrt{\rho_i}\; e^{-b^2/2} \sum_{\ell=0}^{\infty} \frac{\rho_i^{\ell/2}}{\ell!(m+\ell)!} \cdot \frac{{}_1F_1\left[\frac{3-2\ell-1}{2}, \frac{3}{2}, \frac{b^2}{2}\right]}{\Gamma\left(\frac{2-2\ell-1}{2}\right)} \qquad (61)$$

where

a. output clipping level of clipping amplifier

d. input clipping level of clipping amplifier

b: $b = \dfrac{d}{\sqrt{\sigma_n^2 + \dfrac{A_2^2}{2}}}$

σ_n^2 $\sigma_n^2 = N_0 B G$

G: power gain of AGC in Appendix III, Figure 1

$\dfrac{A_2^2}{2}$ $P_2 = \dfrac{A_2^2}{2}$, power in the 1.7 MHz tone

ρ_1: $\rho_1 = \dfrac{P_1}{\left(\sigma_n^2 + P_2\right)}$ input SNR of tone 1 regarding tone 2 as noise

${}_1F_1\,(a,b,z)$. confluent hypergeometric function

$$\rho_1 = \frac{P_1}{\left(\sigma_n^2 + \frac{2}{3} P_2\right)}$$

$$\rho_2 = \frac{P_2}{\left(\sigma_n^2 + \frac{2}{3} P_1\right)}$$

To account for the AGC effects on the clipper amplifier (see Appendix III), we note that the RMS power into the AGC is given by

$$P_1 + P_2 + \sigma_n^2 = P_{RMS} \qquad (62)$$

If we let

$$\alpha_1^2 = \frac{P_1}{P_{RMS}} \tag{63}$$

and

$$\alpha_2^2 = \frac{P_2}{P_{RMS}} \tag{64}$$

then it is easy to show that

$$\alpha_1^2 = \frac{SNR_1}{1 + SNR_1 + SNR_2} \tag{65}$$

and

$$\alpha_2^2 = \frac{SNR_2}{1 + SNR_1 + SNR_2} \tag{66}$$

where $SNR_1 = P_1/\sigma_n^2$ and $SNR_2 = P_2/\sigma_n^2$. If we assume a representative tone power to noise power ratio of each tone to be -17 dB in the 5 MHz bandwidth, then,

$$\rho_1 = \rho_2 = 0.019 \tag{67}$$

Set

$$P_1 + P_2 + \sigma_n^2 = 2^2 = 4 \text{ watts} \tag{68}$$

and set the clipping level at the output of the clipper to be 4 volts (two-sigma clipping level) so that $a = d = 4$. We have by calculation

$$\begin{aligned} \alpha_1^2 &= \alpha_2^2 = 0.183 \\ \sigma_n^2 &= [1 - 2(0.0183)]2^2 = 3\ 854 \text{ watts} \\ P_1 &= P_2 = 0.073 \text{ watts} . \end{aligned} \tag{69}$$

Evaluating (61) produces

$$h_{010} = 0.195 \tag{70}$$

and the corresponding tone autocorrelation function is given by

$$R_1(\tau) = 2(0.195)^2 \cos \omega_1 \tau \tag{71}$$

where

$$\frac{\omega_1}{2\pi} = 1.024 \text{ MHz} \tag{72}$$

Now we will determine h_{070} We have from Appendix IV, equation (46) that

$$h_{070} = \sqrt{2}\,\frac{a}{d}\,b \left[\frac{\sigma_n^2 + A_2^2/2}{2}\right]^{1/2} \rho_1^{7/2}\, e^{-b^2/2} \sum_{\ell=0}^{\infty} \frac{\rho_1^{\ell/2}}{\ell!\,(m_1+\ell)!} \times \frac{{}_1F_1\left[\frac{3-2\ell-7}{2}\,;\,\frac{3}{2}\,;\,\frac{b^2}{2}\right]}{\Gamma\left(\frac{2-2\ell-7}{2}\right)} \tag{73}$$

Evaluating (73) after some algebra, we obtain

$$h_{070} = 3\ 13 \times 10^{-7} \tag{74}$$

so that

$$R_1(\tau) = 2\left(3\ 13 \times 10^{-7}\right)^2 \cos \omega_1 \tau \tag{75}$$

By comparing (71) and (75), we see that the seventh harmonic is down 116 dB from the original tone. We conclude that harmonics are totally negligible.

7.0 BANDPASS FILTER LOSSES: CHANNELS 1 AND 2

In this section, we estimate the losses associated with filtering the quadriphase channels 1 and 2 signals and matched-filtering them. In Figure 10, a sketch indicates the block diagram including the bandpass filter under consideration. The multipole channels 1 and 2 BPF has (upper left portion of Figure 10) a 3 dB bandwidth (specified) of about 8 MHz. For channel 1 at 192 kbps Manchester data (approximately 384 kbps NRZ data), we have that

$$BT \cong 21 \tag{76}$$

and

$$(BT)^{-1} \cong 0.05 \tag{77}$$

By estimating the predetection filter losses compared in [9, Figure 7] with the transmission filter degradation from the transmission filter degradation of [9, Figure 6], we conclude that, for channel 1, the BER degradation is approximately

$$DEGR_1 \cong 0.06 \text{ dB}$$

However, the 0.5 dB ripple (filter specification) causes about 0 25 dB degradation based on [9, Figure 9]. The total degradation to channel 1 is then given by

$$DEGR_1 = 0.31 \text{ dB} \tag{78}$$

We now consider channel 2 filter losses. Channel 2 has a 2 Mbps NRZ waveform so that

$$BT \cong 4$$

and

$$(BT)^{-1} \cong 0.25 \tag{79}$$

so that the BER degradation, using [9, Figure 6] (seven-pole curve) and [9, Figure 7] to relate predetection and transmission filter losses, is about 0.4 dB. Additionally, the 0.5 dB ripple in the filter bandwidth could produce about 0.25 dB degradation. Consequently, the total channel 2 bandpass filter loss is about

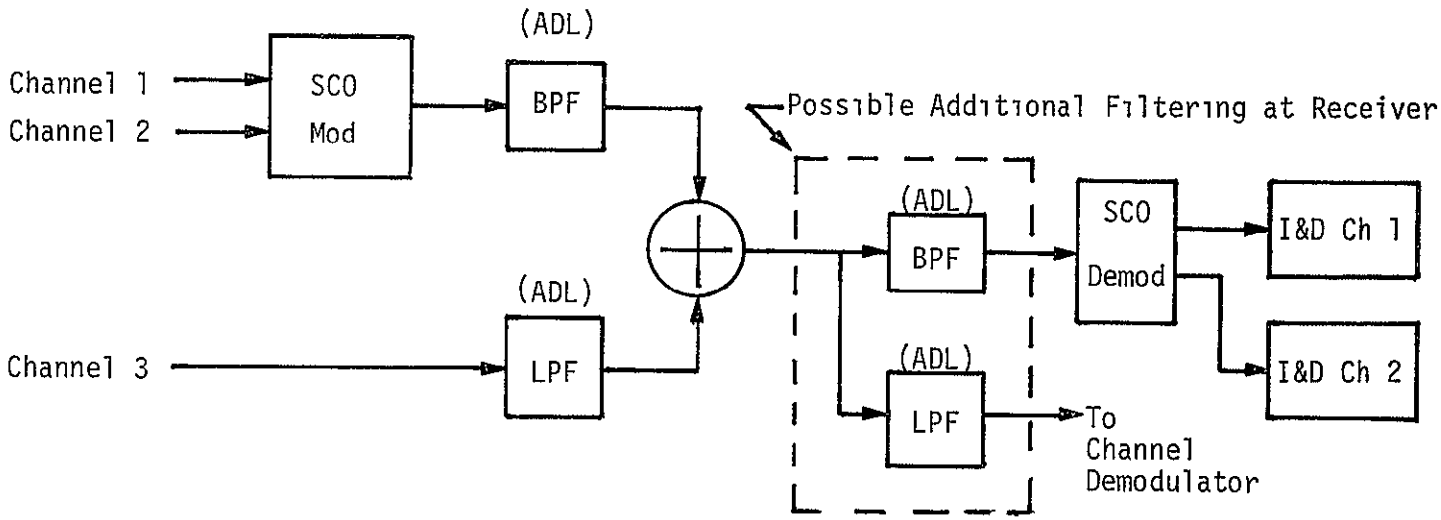

Figure 10 Baseband Transmission Reception Model with FM Modulation and FM Demodulation Removed

$$DEGR_2 = 0.65 \text{ dB} \tag{80}$$

Now we estimate the BER degradation when the additional BPF and LPF shown in Figure 10 are used to reduce channel 3 tone interference of channels 1 and 2. These filters are identical in filtering characteristics to that of transmitter bandpass and lowpass filters of Figure 2. From [9, Figure 6], it is estimated that the cascade of BPF's increases the BER degradation less than 0.05 dB for channel 1 and less than 0.2 dB for channel 2. We conclude that the overall BPF BER degradations are given by

$$DEGR_1' = 0.36 \text{ dB} \tag{81}$$

$$DEGR_2' = 0.85 \text{ dB} . \tag{82}$$

8.0 RF-FM MODULATION/DEMODULATION LOSSES

The main thrust of this analysis has been at baseband; however, the FM modulation/demodulation process is not perfect, so BER degradation at $PE = 1 \times 10^{-5}$ has been assumed to be

$$DEGR = 0.5 \text{ dB} \tag{83}$$

This degradation estimate includes nonlinearities as well as the effect of thermal noise in the FM demodulation process.

9.0 DEGRADATION OF CHANNEL 2 DUE TO CHANNEL 3 TONES

From Figure 10, we see that the two tones of channel 3 will be "seen" by the integrate-and-dump matched-filter detector for channels 1 and 2.

Therefore, if the additional filters are not included as shown in Figure 10, the cross-channel interference of channel 3 onto channel 2 will not be negligible. In Figure 11, the two tones of Figure 3 are illustrated along with the channel 2 matched-filter response. Since channel 2 has a much higher data rate, its response is affected more by the channel 3 signals modeled in the report as two unmodulated tones. The channel 2 matched-filter response is given by (in both time and frequency)

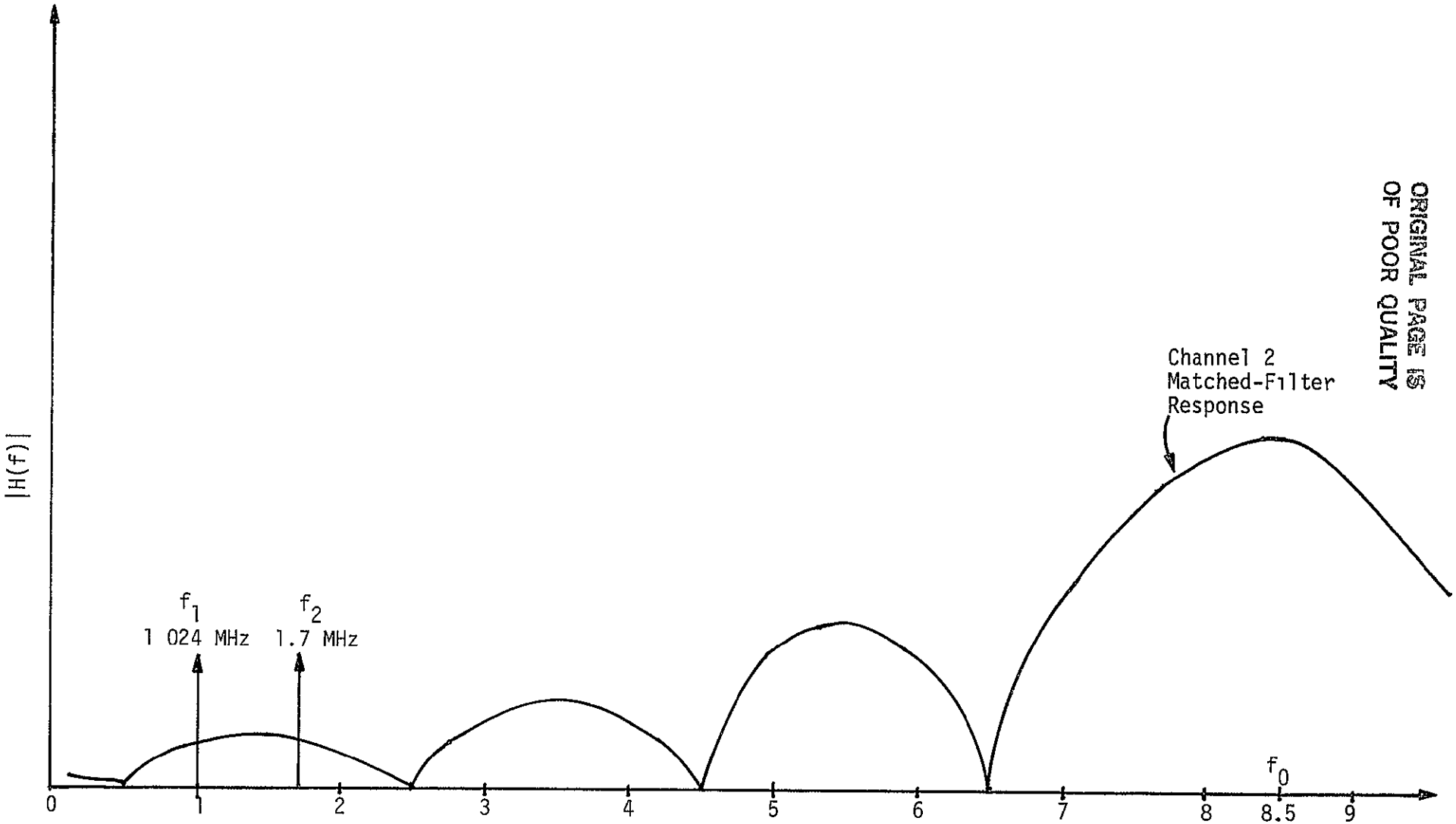

Figure 11. Response of Channel and the Two Channel 3 Interfering Tones

$$\frac{1}{T}\int_0^T (\ )dt$$

with corresponding frequency response

$$H(f) = \frac{\sin(\pi fT)}{\pi fT} e^{-j\omega T/2} \tag{84}$$

Define the channel 2 signal-plus-received noise as

$$y(t) = \sqrt{2}\, A\, d(t) \sin \omega_0 t + \sqrt{2}\, n_s(t) \sin \omega_0 t + \sqrt{2}\, n_c(t) \cos \omega_0 t$$
$$+ \sqrt{2}\, A_{I_1} \sin \omega_1 t + \sqrt{2}\, A_{I_2} \sin \omega_2 t \tag{85}$$

where $n_c(t)$ and $n_s(t)$ are independent, bandlimited, baseband, Gaussian noise processes. When this signal is coherently demodulated by $\sqrt{2}\sin\omega_0 t$, there remains

$$e_D(t) = A\, d(t) + n_s(t) + A_{I_1} \cos\left[(\omega_0-\omega_1)t\right] + A_{I_1} \cos\left[(\omega_0+\omega_1)t\right]$$
$$+ A_{I_2} \cos\left[(\omega_0-\omega_2)t\right] + A_{I_2} \cos\left[(\omega_0+\omega_2)t\right] \tag{86}$$

where

$$f_0 = 8.5 \text{ MHz}$$
$$f_1 = 1.024 \text{ MHz}$$
$$f_2 = 1.7 \text{ MHz} \tag{87}$$

We see that the interfering signals and noise have powers given by

$$P_T = \text{Var}(n_s) + P_{I_1} + P'_{I_1} + P_{I_2} + P'_{I_2} \tag{88}$$

where

$$\mathrm{Var}(n_s) = \frac{1}{T^2}\int_0^T\int_0^T \overline{n(t)n(u)}\,dt\,du \tag{89}$$

or

$$\mathrm{Var}(n_s) = \frac{N_0}{2T} \tag{90}$$

with $N_0/2$ the two-sided noise spectral density and P_{I_1} and P'_{I_1} corresponding to the A_{I_1} interference terms in (86) and P_{I_2} and P'_{I_2} being the A_{I_2} interference terms in (86).

We now evaluate the channel 2 interference terms. We have

$$\begin{aligned}
P_{I_1} &= \frac{\sin^2(7.48\pi\times10^6/2\times10^6)}{(7.48\pi/2)^2}\,P_{1.024} = 0.0039\,P_{1.024}\\
P'_{I_1} &= \frac{\sin^2(9.52\pi/2)}{(9.52\pi/2)^2}\,P_{1.024} = 0.0021\,P_{1.024}\\
P_{I_2} &= \frac{\sin^2(6.8\pi/2)}{(6.8\pi/2)^2}\,P_{1.7} = 0.0079\,P_{1.7}\\
P'_{I_2} &= \frac{\sin^2(10.2\pi/2)}{(10.2\pi/2)^2}\,P_{1.7} = 0.00037\,P_{1.7}
\end{aligned} \tag{91}$$

In order to compute the total degradation, we must evaluate the tone power levels Assume that channel 3 is at maximum SNR (no noise) so that the sum of both tones modulate the carrier to 22 MHz peak-to-peak. Therefore, for channel 3,

$$2(A_1+A_2) = K\,22\times10^6 \tag{92}$$

where A_1 and A_2 are the tone peak amplitudes of channel 2. Since

$$P_{T_3} = \frac{A_1^2}{2} + \frac{A_1^2}{2} = A_1^2 \tag{93}$$

It follows that

$$\sqrt{P_{T_3}} = A_1 = \frac{11K \times 10^6}{2} \triangleq \frac{11}{2} K' \quad (K' = Kx10^6) \tag{94}$$

So

$$P_{T_3} = 30.25(K')^2 \tag{95}$$

and the individual tone powers are

$$P_{T_{31}} = P_{T_{32}} = 15.13\ (K')^2 \tag{96}$$

Now in channels 1 and 2, we have, since the filtered quadriphase is in quadrature, that

$$2\sqrt{A_I^2 + A_Q^2} = 12K \times 10^6 \tag{97}$$

where A_I is the peak channel 1 subcarrier amplitude and A_2 is the peak channel 2 subcarrier amplitude. Also,

$$P_{T_{I,Q}} = \frac{5}{8} A_Q^2 \quad , \quad A_Q = 2A_I \tag{98}$$

Solving (97) and (98), we obtain

$$\begin{aligned} A_Q &= 5\ 37\ K' \\ A_I &= 2.68\ K' \\ P_{T_{I,Q}} &= 18.1\ (K')^2 \end{aligned} \qquad (K' = K \times 10^6) \tag{99}$$

Now, if the SNR in channel 2 is 10 dB, then the noise power in the Q channel is given by

$$\frac{1}{11}(14.4)(K')^2 \tag{100}$$

Therefore,

$$(N_0B)_{CH2} = 1.3(K')^2 \tag{101}$$

where B is the equivalent 4 MHz lowpass process from the 8 MHz bandpass process. It follows that

$$(N_0)_{CH2} = \frac{1.3(K')^2}{B} \tag{102}$$

Therefore, (89) can be written using (90), (91) and (102) as $\left(T=1/2x10^6\right)$

$$\begin{aligned}(P_{T_N})_{CH2} = \frac{1}{2TB}\,1.3(K')^2 &+ 0.0039\,(15.13)(K')^2 + 0.0021\,(15\,13)(K')^2 \\ &+ 0.0079\,(15.3)(K')^2 + 0.00037\,(15.3)(K')^2\end{aligned} \tag{103}$$

This can be factored as $\left(B = 4 \times 10^6\right)$

$$P_{T_N} = 0.325(K')^2\,[1 + 0.66] \tag{104}$$

We conclude that the degradation is given by

$$DEGR_{CH2} = 2.2\ dB \tag{105}$$

Now we consider the same calculation utilizing the benefit of the BPF and LPF in Figure 10 at the receiver to chop out the I&D filter response near the channel 3 tones Figure 12 illustrates this point. Equation (103) can now be written as

$$\begin{aligned}P_{T_N} = \frac{1}{2TB}\,(1.3)(K')^2 &+ 0.0039\,(15.13)(K')^2\left(\frac{0\ 02}{0.8}\right)^2 \\ &+ 0.0021\,(15\ 3)(K')^2\left(\frac{0.02}{0.8}\right)^2 + 0.0079\,(15.13)(K')^2\left(\frac{0.02}{0.8}\right)^2 \\ &+ 0.00037\,(15\ 13)(K')^2\left(\frac{0.02}{0.8}\right)^2\end{aligned} \tag{106}$$

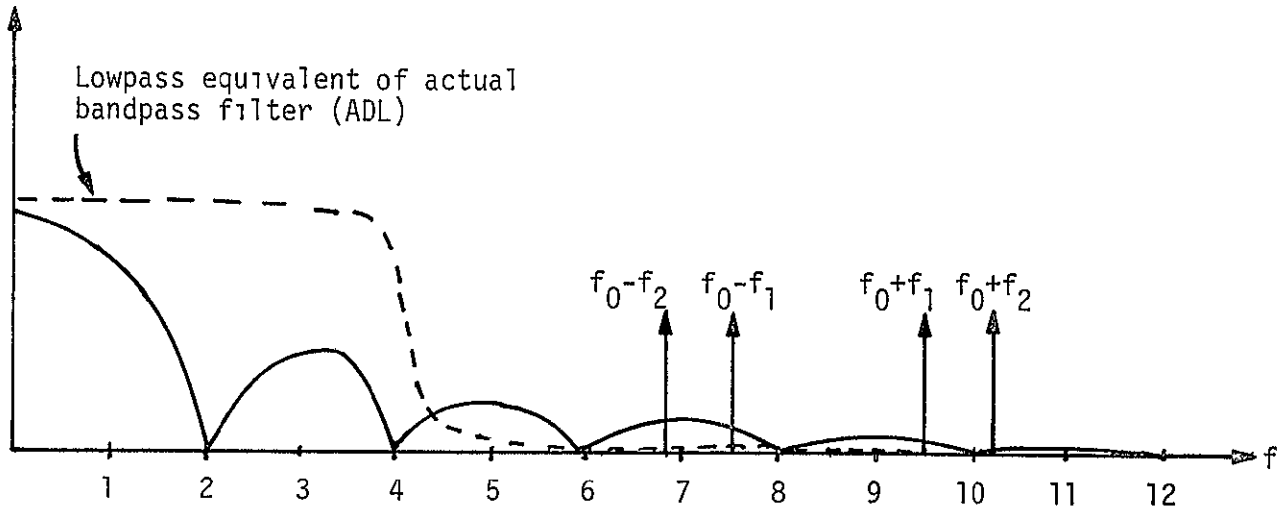

Figure 12 Spectra After Demodulation

where the factor

$$\left(\frac{0.02}{0.8}\right)^2$$

is the reduction in filter voltage response (squared) due to the presence of the ADL BPL.

Evaluating and factoring as in (104), we obtain

$$P_{T_N} = 2.6(K')^2\ [1 + 0.0004] \tag{107}$$

We conclude that the degradation due to the channel 3 tones is less than 0.01 dB for channel 2 when the transmitter BPF is also used on the receiver.

10.0 CHANNEL 3 DEGRADATION DUE TO CHANNEL 2 NOISE

This source of degradation is based on the fact that channel 2 noise can get into channel 3, thereby increasing the noise level. The transmitter BPL, however, limits the noise interference as well as the 5 MHz lowpass filters into the channel 2 limiter. It should be noted that the additional BPL and LPF at the receiver does not affect this phenomena.

From the ADL filter response data, the filter reduces the channel 3 noise by

$$L = 10\log\left(\frac{0.02}{0\ 81}\right)^2 = -32.1\ \text{dB} \tag{108}$$

When channels 2 and 3 are near the same SNR's, we see that this additional noise will be essentially 32 dB down, plus or minus a few decibels due to the different FM drive levels. It follows that this noise has negligible effects on channel 3 performance

Now consider the degradation to channel 1. Equation (88) still applies, but now Var(n) denotes the variance of channel 1 noise. The response of the Manchester matched filter is given by

$$H(f) = \frac{\sin^2(\pi fT/2)}{(\pi fT/2)}\, e^{-J\omega T/2} \tag{109}$$

Equation (91) becomes, for this case,

$$P_{I_1} = \frac{\sin^4(\pi 7.48\times10^6/0.4\times10^6)}{(7.48\pi/0.4)^2} P_{1.024} = 0.00012\ P_{1.024}$$

$$P'_{I_1} = \frac{\sin^4(9.52\pi/0.4)}{(9.52\pi/0.4)^2} P_{1.024} \cong 0.000021\ P_{1.024}$$

$$P_{I_2} = \frac{\sin^4(6.8\pi/0.4)}{(6.8\pi/0.4)^2} P_{1.7} \cong 0$$

$$P'_{I_2} = \frac{\sin^4(10.2\pi/0.4)}{(10.2\pi/0.4)^2} P_{1.7} = 0.00016\ P_{1.7} \qquad (110)$$

From (99) and assuming that channel 1 is at 10 dB, the noise power is then given by

$$\frac{1}{11}(3\ 59)(K')^2 \qquad (111)$$

Therefore,

$$(N_0B)_{CH1} = 0.33(K')^2 \qquad (112)$$

It follows that

$$(N_0)_{CH1} = \frac{0.33}{B}(K')^2 \qquad (113)$$

Hence, using (88), (90), (110) and (112), we have

$$\left(P_{T_N}\right)_{CH1} = \frac{1}{2TB}(0.33)(K')^2 + 0.00012(15\ 13)(K')^2 + 0.000021(15.13)(K')^2 + 0\ 00016(15.13)(K')^2 \qquad (114)$$

This can be factored as

$$P_{T_N}{}_{CH1} = 0.0825(K')^2 [1 + 0.055] \quad (115)$$

We conclude from (115) that the degradation is given by

$$DEGR_{CH1} = 0.23 \text{ dB} . \quad (116)$$

11.0 BER E_B/N_0 DEGRADATION SUMMARY

In this section, we summarized the E_B/N_0 BER degradation for channels 1, 2 and 3. The link budget for channel 1 is given in Table 3 and the link budget for channel 2 is given in Table 4.

Table 3. Channel 1 BER Degradation

Component	No Receiver Filters (dB)	Receiver Filters (dB)
1. Imperfect carrier reference including crosstalk (assumes σ_L = 4.5° @ BER = 1×10^{-5})	0.2	0.2
2 Channel 3 noise interference	0.1	0.1
3. Harmonics of channel 3 tones	0.0	0.0
4. Lowpass filter losses	0.31	0.36
5. RF-FM modulation/demodulation losses	0.5	0.5
6. Matched-filter response of channel 1 to channel 3 tones	0.23	0.0
7. Channel 3 degradation due to channel 2 noise	0.1	0.1
Totals	1.44	1.26

Table 4. Channel 2 BER Degradation

Component	No Receiver Filters (dB)	Receiver Filters (dB)
1. Imperfect carrier reference including crosstalk (assumes σ_L = 4.5° @ BER = 1×10^{-5})	0.7	0.7
2. Channel 3 noise interference	0.2	0.2
3. Harmonics of channel 3 tones	0.0	0.0
4. Bandpass filter losses	0.65	0.85
5. RF/FM modulation/demodulation losses	0.5	0.5
6. Matched-filter response of channel 2 to channel 3 tones	2.2	0.01
7. Channel 3 degradation due to channel 2 noise	0.1	0.1
Totals	4.35	2.36

These tables do not include bit synchronizer degradations or relay losses or take into account that the modulation BPF centered at 8.5 MHz is not narrowband, so that additional losses may be present. In addition, they do not include the C/N_0 loss out of the limiters in channels 1 and 2 (see Appendix II). Also, numerous assumptions on SNR were made to obtain the estimates, with most of them based on worst-case conditions. Therefore, the two BER degradation tables represent, for the most part, a worst-case estimate for each entry.

Channel 3 BER degradation was found to be negligible due to additional thermal noise from channels 1 and 2

12.0 CONCLUSIONS

Estimates of BER degradation have been obtained, in most cases, by assuming worst-case conditions. One exception is the four-phase loop which demodulates the quadriphase signal of channels 1 and 2. There an RMS phase error of 4.5° was assumed as a reasonable guess.

It is seen that the additional filters of Figure 10 reduced BER degradation in decibels almost in half for channel 2 and about 10% for channel 1.

REFERENCES

1. R. H. Cager, D. T. LaFlame and L. C. Parode, "Orbiter Ku-Band Integrated Radar and Communications Subsystems," IEEE Transactions on Communications, Vol. COM-26, No. 11, November 1978.

2. J. C. Springett and S. Udalov, "Communication with Shuttle Payloads," IEEE Transactions on Communications, Vol. COM-26, No. 11, November 1978.

3. R. H. Cager, "Phase-State/Power Division Relationships in the Return Link Baseband Modulator," Hughes IOC No. HS237-782, June 14, 1977.

4. J. C. Springett, "Shuttle Payload S-Band Communications Study," Axiomatix Report No. R7903-1, March 9, 1979.

5. "Ku-Band Integrated Radar and Communication Equipment for the Space Shuttle Orbiter Vehicle," Hughes Aircraft Co. Preliminary Design Review, March 14-24, 1978.

6. M. Abramowitz and I. Stegun, Handbook of Mathematical Functions, National Bureau of Standards, Applied Mathematics Series 55, June 1964.

7. R. J. Helgeson, "PI-PSP BER Degradation Due to PI Baseband Output Limiting Amplifier," TRW IOC SCE-50-79-491/RJH, September 5, 1979.

8. H. C. Osborne, "Effect of Noisy Reference on Coherent Detection of Unbalanced QPSK Signals," NTC '78 Proceedings, Birmingham, Alabama.

9. J. J. Jones, "Filter Distortion and Intersymbol Interference Effects on PSK Signals," IEEE Transactions on Communication Technology, Vol. COM-19, No. 2, April 1971

10. "Space Shuttle Communications and Tracking RF Link Circuit Margin Summary," Lyndon B. Johnson Space Center, EH2-M/79-309, April 1979.

APPENDIX I

BASEBAND DIGITAL SIGNAL-PLUS-NOISE THROUGH A HARD LIMITER

In this appendix, we determine the output spectral density of a baseband digital signal plus bandlimited Gaussian noise. This calculation allows one to determine the output C/N_0 value as a function of the input C/N_0 value. The derivation of the autocorrelation function follows that of Painter [1] with minor corrections in the final results. The model is shown in Figure 1 below.

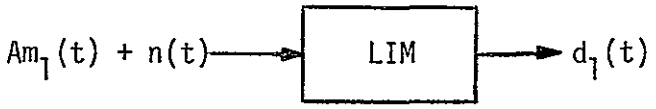

Figure I-1. Baseband Limiter Model

where $m_1(t)$ is an NRZ or Manchester binary-valued digital waveform, $n(t)$ is bandlimited, white Gaussian noise, and $d_1(t)$ is the output binary-valued waveform. Let

$$x(t) = Ad(t) + n(t) \tag{I-1}$$

$$y(t) = \text{sgn}[x(t)] \tag{I-2}$$

The first- and second-order density functions are given by

$$p_x(x_t,t) = \frac{1}{\sqrt{2\pi}} \exp\left[-\frac{1}{2\sigma^2}(x_t-\mu_t)\right] \tag{I-3}$$

$$p_x(x_t,x_\tau) = \frac{1}{2\pi\sigma^2\sqrt{1-\rho^2}} \exp\left[-\frac{1}{2(1-\rho^2)}\left\{\frac{(x_\tau-\mu_\tau)^2}{\sigma^2} - \frac{2\rho(x_\tau-\mu_\tau)(x_t-\mu_t)}{\sigma^2} + \frac{(x_t-\mu_t)^2}{\sigma^2}\right\}\right] \tag{I-4}$$

where

$$x_t = x(t)$$

$$x_\tau = x(t+\tau)$$

$$\mu_t = E[x(t)] = Ad(t) \triangleq s(t)$$

$$\mu_\tau = E[x(t+\tau)] = Ad(t+\tau) \triangleq s(t+\tau)$$

$$\sigma^2 = E\left[(x_t-\mu_t)^2\right] = E\left[(x_\tau-\mu_\tau)^2\right]$$

$$\rho = \frac{1}{\sigma^2} E\left[(x_\tau-\mu_\tau)(x_t-\mu_t)\right]$$

or

$$\rho = \frac{1}{\sigma^2} E\left[n(t+\tau)n(t)\right] = \frac{R_n(\tau)}{\sigma^2} \qquad \text{(I-5)}$$

First let us compute the mean value of our process. We will temporarily drop the time subscript.

$$\mu = \int_{-\infty}^{\infty} \operatorname{sgn}(x)\, p_x(x)\, dx \qquad \text{(I-6)}$$

which can be expressed as

$$\mu = \int_0^{\infty} \frac{1}{\sqrt{2\pi}\,\sigma} \exp\left[-\frac{1}{2\sigma^2}(x-s)^2\right]dx - \int_{-\infty}^{0} \frac{1}{\sigma\sqrt{2\pi}} \exp\left[-\frac{1}{2\sigma^2}(x-s)^2\right]dx \qquad \text{(I-7)}$$

where $s = s(t) = Ad(t)$. Letting $\frac{x-s}{\sqrt{2}\sigma} = v$ produces

$$\mu = \frac{2}{\sqrt{\pi}} \int_0^{2/\sqrt{2}\sigma} e^{-v^2}\, dv = \operatorname{erf}\left[\frac{s(t)}{\sqrt{2}\sigma}\right] \qquad \text{(I-8)}$$

Now let us determine the output autocorrelation function defined by

$$R_y(t+\tau,t) = E[y(t+\tau)y(t)] = \int_{-\infty}^{\infty}\int_{-\infty}^{\infty} \operatorname{sgn}[x_t]\, \operatorname{sgn}[x_\tau]\, p_x(x_t,x_\tau)dx_t dx_\tau \qquad \text{(I-9)}$$

Equation (9) can be written

$$R_y(t+\tau,\tau) = \int_0^\infty\int_0^\infty p_x(x_t,x_\tau)\,dx_t dx_\tau + \int_{-\infty}^0\int_{-\infty}^0 p_x(x_t,x_\tau)\,dx_t dx_\tau$$
$$- \int_0^\infty\int_{-\infty}^0 p_x(x_t,x_\tau)\,dx_t dx_\tau - \int_{-\infty}^0\int_0^\infty p_x(x_t,x_\tau)dx_t dx_\tau \quad \text{(I-10)}$$

Letting $x_t - \mu_t = u\sigma$, $x_\tau - \mu_\tau = v\sigma$ produces

$$R_y(t+\tau,\tau) = \int_{-\frac{\mu_t}{\sigma}}^\infty\int_{-\frac{\mu_\tau}{\sigma}}^\infty g(u,v,\rho)\,dudv + \int_{-\infty}^{-\frac{\mu_t}{\sigma}}\int_{-\infty}^{\frac{\mu_\tau}{\sigma}} g(u,v,\rho)\,dudv$$
$$- \int_{-\frac{\mu_t}{\sigma}}^\infty\int_{-\infty}^{-\frac{\mu_\tau}{\sigma}} g(u,v,\rho)\,dudv - \int_{-\infty}^{-\frac{\mu_t}{\sigma}}\int_{-\frac{\mu_\tau}{\sigma}}^\infty g(u,v,\rho)dudv \quad \text{(I-11)}$$

where $g(u,v,\rho)$ is the density function of the random variables u and v induced from the variables x_t and x_τ.

Let

$$h = \frac{\mu_t}{\sigma} \qquad k = \frac{\mu_\tau}{\sigma}$$

then

$$R_{yy}(\tau,t) = L(-h,-k,\rho) + L(h,k,\rho) - L(-h,k,-\rho) - L(h,-k,-\rho) \quad \text{(I-12)}$$

so using [2]

$$L(h,k,\rho) = Q(h)Q(k) + \sum_{n=0}^{\infty} \frac{z^{(n)}(h)z^{(n)}(k)}{(n+1)!}\,\rho^{n+1} \quad \text{(I-13)}$$

and

$$Q(h) = \frac{1}{\sqrt{2\rho}} \int_h^\infty e^{-t^2/2}\, dt \tag{I-14}$$

we arrive at

$$R_{yy}(t,\tau) = Q(-h)Q(-k) + \sum_{n=0}^{\infty} \frac{z^n(-h)z^{(n)}(-k)\rho^{n+1}}{(n+1)!}$$

$$+ Q(h)Q(k) + \sum_{n=0}^{\infty} \frac{z^n(h)z^n(k)\rho^{n+1}}{(n+1)!}$$

$$- Q(-h)Q(k) - \sum_{0}^{\infty} \frac{z^{(n)}(-h)z^{(n)}(k)(-\rho)^{n+1}}{(n+1)!}$$

$$- Q(h)Q(-k) - \sum_{n=0}^{\infty} \frac{z^{(n)}(h)z^{(n)}(-k)(-\rho)^{n+1}}{(n+1)!} \tag{I-15}$$

where

$$z^{(n)}(x) = \frac{d^n}{dx^n}\left\{\frac{1}{\sqrt{2\pi}} e^{-x^2/2}\right\} \tag{I-16}$$

Now

$$R_y(\tau,t) = [Q(h) - Q(-h)][Q(k) - Q(-k)]$$

$$+ \sum_{n=0}^{\infty} \frac{\rho^{n+1}}{(n+1)!}\left\{z^{(n)}(-h)z^n(-k) + z^{(n)}(h)z^{(n)}(k)\right.$$

$$\left. - (-1)^{n+1}\left[z^{(n)}(-h)z^{(n)}(k) + z^{(n)}(h)z^{(n)}(-k)\right]\right\} \tag{I-17}$$

Now note that

$$Q(-x) - Q(x) = \operatorname{erf}\left(\frac{x}{\sqrt{2}}\right) \tag{I-18}$$

Also note that

$$\begin{aligned} z^{(n)}(x) &= z^{n}(-x) \quad , \quad n \text{ even} \\ z^{(n)}(x) &= -z^{n}(-x) \quad , \quad n \text{ odd} \end{aligned} \tag{I-19}$$

So

$$R_y(t,\tau) = \operatorname{erf}\left(\frac{h}{\sqrt{2}}\right) \operatorname{erf}\left(\frac{k}{\sqrt{2}}\right) + \sum_{n=0}^{\infty}{}^{e} 4 \frac{z^{(n)}(h) z^{(n)}(k) \rho^{n+1}}{(n+1)!}$$

$$+ 4 \sum_{n=1}^{\infty} \frac{z^{(n)}(h) z^{(n)}(k) \rho^{n+1}}{(n+1)!} \tag{I-20}$$

where $\sum$ denotes sums over n odd and $\sum^{e}$ denotes sums over n even. Changing indices yields

$$R_y(t,\tau) = \operatorname{erf}\left(\frac{\mu_t}{\sqrt{2}\sigma}\right) \operatorname{erf}\left(\frac{\mu_\tau}{\sqrt{2}\sigma}\right) + 4 \sum_{m=0}^{\infty} z^{(2m+1)}\left(\frac{\mu_t}{\sigma}\right) z^{(2m+1)}\left(\frac{\mu_\tau}{\sigma}\right) \frac{\rho^{2m+2}}{(2m+2)!}$$

$$+ 4 \sum_{m=0}^{\infty} \frac{\rho^{2m+1}}{(2m+1)!} z^{(2m)}\left(\frac{\mu_t}{\sigma}\right) z^{(2m)}\left(\frac{\mu_\tau}{\sigma}\right) \tag{I-21}$$

We have, since $s(t) = Ad(t)$,

$$R_y(t,\tau) = d(t)d(t+\tau)\ \mathrm{erf}^2\left[\sqrt{\frac{S}{2N}}\right] + 4\,d(t+\tau)\,d(t)\sum_{m=0}^{\infty}\left[z^{(2m+1)}\left(\sqrt{\frac{S}{N}}\right)\right]^2\left[\frac{\bar{R}_n(\tau)}{\sigma^2}\right]^{2m+2}\Big/(2m+2)! + 4\sum_{m=0}^{\infty}\left[z^{(2m)}\left(\sqrt{\frac{S}{N}}\right)\right]^2\left[\frac{\bar{R}_n(\tau)}{\sigma^2}\right]^{2m+1}\Big/(2m+1)! \qquad \text{(I-22)}$$

where we have let

$$\frac{A^2}{\sigma^2} = \frac{S}{N} \qquad \text{(I-23)}$$

Now consider d(t),

$$d(t) = \sum_{i=-\infty}^{\infty} d_i\ p(t-iT)$$

where $p(t) = 1, t\varepsilon(0,T)$ and $d_i = \pm 1$ with equal likelihood. Hence, the time and ensemble average of $d(t)d(t+\tau)$ yields

$$R_d(\tau) = \left\langle \overline{d(t)d(t+\tau)} \right\rangle = \left\langle \sum_{i=-\infty}^{\infty} p(t-iT)\ p(t+\tau-iT) \right\rangle$$

or

$$R_d(\tau) = \left[1 - \frac{|\tau|}{T}\right], \qquad \text{NRZ waveforms ,}$$

so that we have

C-2

$$R_y(\tau) = R_d(\tau)\,\mathrm{erf}^2\left[\sqrt{\frac{S}{2N}}\right] + 4\,R_d(\tau)\sum_{m=0}^{\infty}\left[z^{(2m+1)}\left(\sqrt{\frac{S}{N}}\right)\right]^2\left[\frac{R_n(\tau)}{2}\right]^{2m+2}\Big/(2m+2)!$$

$$+ 4\sum_{m=0}^{\infty}\left[z^{(2m)}\left(\sqrt{\frac{S}{N}}\right)\right]^2\left[\frac{R_n(\tau)}{2}\right]^{(2m+1)}\Big/(2m+1)! \qquad \text{(I-24)}$$

The first term is the SxS term, second is the SxN terms, and the last term is the NxN term. Notice at high SNR

$$R_y(\tau) \cong R_d(\tau) \qquad \text{(I-25)}$$

At low SNR

$$\lim_{\frac{S}{N}\to 0}\mathrm{erf}\left(\sqrt{\frac{S}{N}}\right) = 0$$

$$\lim_{\frac{S}{N}\to 0}\left[z^{(2m)}\left(\sqrt{\frac{S}{N}}\right)\right]^2 = \frac{1}{2\pi}\left(\frac{1}{2}\right)^{2m}\left[\frac{(2m)!}{m!}\right]^2$$

$$\lim_{\frac{S}{N}\to 0}\left[z^{2m+1}\left(\sqrt{\frac{S}{N}}\right)\right]^2 \longrightarrow 0 \qquad \text{(I-26)}$$

Therefore, (I-24) converges at S/N = 0 to

$$\lim_{\frac{S}{N}\to 0} R_y(\tau) = 4\sum_{m=0}^{\infty}\left(\frac{1}{2\pi}\right)\left(\frac{1}{2}\right)^{2m}\left[\frac{2m!}{m!}\right]^2\frac{1}{(2m+1)!}\left[\frac{R_{nn}(\tau)}{2}\right]^{2m+1} \qquad \text{(I-27)}$$

or

$$R_y(\tau) = \frac{2}{\pi}\arcsin\left[\frac{R_n(\tau)}{\sigma^2}\right] \qquad \text{(I-28)}$$

which is a well-known result. It is easy to show that $R_d(\tau)$ is given by

$$\left.\begin{aligned} R_d(\tau) &= \left[1 - \frac{|\tau|}{T}\right] && |\tau| \leq T \\ &= 0 && |\tau| > T \end{aligned}\right\} \text{NRZ} \qquad \text{(I-29)}$$

$$\left.\begin{aligned} R_d(\tau) &= \left[1 - \frac{3|\tau|}{T}\right] && |\tau| \leq \frac{T}{2} \\ &= \left[\frac{|\tau|}{T} - 1\right] && \frac{T}{2} \leq |\tau| \leq T \end{aligned}\right\} \text{Manchester} \qquad \text{(I-30)}$$

Therefore, at the input to the FM summer due to channels 1 and 2, we have

$$s(t) = A\frac{4}{\pi} d_2(t)\cos\theta \sin(\omega_{sc}t) + A\frac{4}{\pi} d_1(t)\sin\theta\cos(\omega_{sc}t) \qquad \text{(I-31)}$$

where $d_2(t)$ has the spectral density given by

$$\mathcal{S}_{d_2}(f) = \mathcal{S}_d(f)\left[\operatorname{erf}\left(\sqrt{\frac{S_2}{N_2}}\right)\right]^2 + 4\mathcal{F}\left\{R_d(\tau)\sum_{m=0}^{\infty}\left[z^{(2m+1)}\left(\sqrt{\frac{S_2}{N_2}}\right)\right]^2\left[\frac{R_n(\tau)}{\sigma_2^2}\right]^{2m+2}\Big/(2m+2)!\right\}$$

$$+ 4\mathcal{F}\left\{\sum_{m=0}^{\infty}\left[z^{(2m)}\left(\sqrt{\frac{S_2}{N_2}}\right)\right]^2\left[\frac{R_n(\tau)}{\sigma_2^2}\right]^{2m+1}\Big/(2m+1)!\right\} \qquad \text{(I-32)}$$

with $\mathcal{F}(\cdot)$ the Fourier transform and where $d_1(t)$ has the spectral density given by

$$\mathcal{S}_{d_1}(f) = \mathcal{S}_d(f)\operatorname{erf}\left(\sqrt{\frac{S_1}{N_1}}\right)^2 + 4\mathcal{F}\left\{R_d(\tau)\sum_{m=0}^{\infty}\left[z^{(2m+1)}\left(\sqrt{\frac{S_1}{N_1}}\right)\right]^2\left[\frac{R_n(\tau)}{\sigma_1^2}\right]^{2m+2}\Big/(2m+2)!\right\}$$

$$+ 4\mathcal{F}\left\{\sum_{m=0}^{\infty}\left[z^{(2m)}\left(\sqrt{\frac{S_1}{N_1}}\right)\right]^2\left[\frac{R_n(\tau)}{\sigma_1^2}\right]^{2m+1}\Big/(2m+1)!\right\} \qquad \text{(I-33)}$$

and where $\mathscr{S}_d(t)$ denotes the data spectrum of that respective channel.

Evaluation of the SxN and NxN spectral densities is made in Appendix II.

REFERENCES

1. J. H. Painter, "Ideal Limiting of Digital Signals in Gaussian Noise," IEEE Transactions on Information Theory, Vol. IT-16, #1, Jan 1970.

2. M. Abramowitz and I. A. Stegar, Handbook of Mathematical Functions, Dover Publications, Inc , New York, 1965.

APPENDIX II

SPECTRAL DENSITY OF SxN AND NxN TERMS OUT OF THE LIMITER

The purpose of this appendix is to obtain the analytical form of the NxN and SxN terms at the output of the limiter when the input is a baseband signal plus bandlimited Gaussian noise. We follow Helgeson's [2] work in this section and slightly extend his results to cover fifth-order NxN terms. We model the lowpass filter into the limiter as an ideal LPF of the form illustrated in Figure II-1 below.

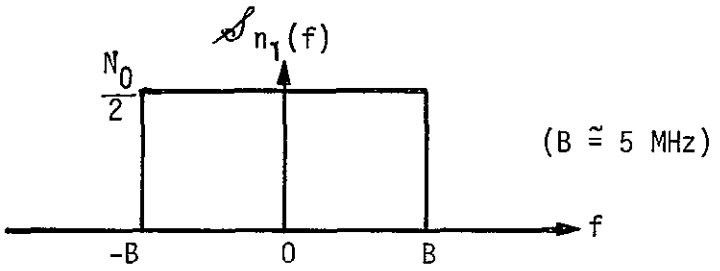

Figure II-1. Baseband Noise Spectral Density Model

We therefore model the limiter input noise spectral density by

$$\mathscr{S}_{n_1}(f) = \frac{N_0}{2}\,[u(f+B) - u(f-B)] \tag{II-1}$$

where n_1 denotes the original process and n_k is the $\underline{k}$th-order convolution. Now, using Figure II-2, we have

$$n_2(f) = \int_{-\infty}^{\infty} \mathscr{S}_{n_1}(f_1)\, \mathscr{S}n(f-f_1)\, df_1 \tag{II-2}$$

$$= \left(\frac{N_0}{2}\right)^2 \int_{-\infty}^{\infty} \Big[u(f_1+B) - u(f_1-B)\Big]\Big[u(f-f_1+B) - u(f_1-f_1-B)\Big]df \tag{II-3}$$

Evaluating

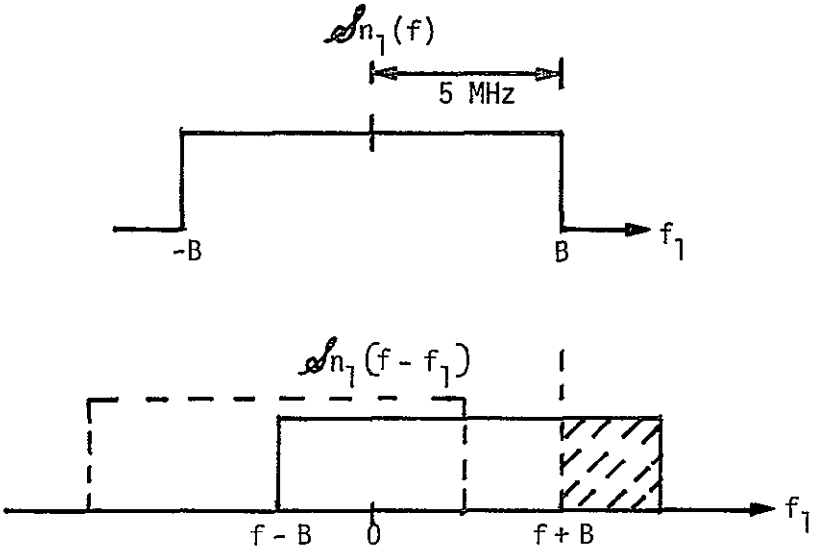

Figure II-2 Spectra for Determining $\mathscr{S}_{n_2}(f)$

$$\frac{\mathscr{S}_{n_2}(f)}{\left(\frac{N_0}{2}\right)^2} = 2B-f \qquad f > 0$$
$$= 2B+f \qquad f < 0 \qquad \text{(II-4)}$$

so that

$$\mathscr{S}_{n_2}(f) = \left(\frac{N_0}{2}\right)^2 [2B - |f|] \qquad |f| \leq 2B$$
$$= 0 \qquad |f| > 2B \qquad \text{(II-5)}$$

Now determine $\mathscr{S}_{n_3}(f)$ Using Figure II-3, we have

$$\mathscr{S}_{n_3}(f) = \int_{-\infty}^{\infty} \mathscr{S}_{n_2}(f_1)\mathscr{S}_{n_1}(f - f_1)\, df_1 \qquad \text{(II-6)}$$

So that

$$\frac{\mathscr{S}_{n_3}(f)}{\left(\frac{N_0}{2}\right)^3} = \int_{-\infty}^{\infty} (2B - |f_1|) \left(u(f - f_1 + B) + u(f - f_1 - B)\right) df_1 \qquad \text{(II-7)}$$

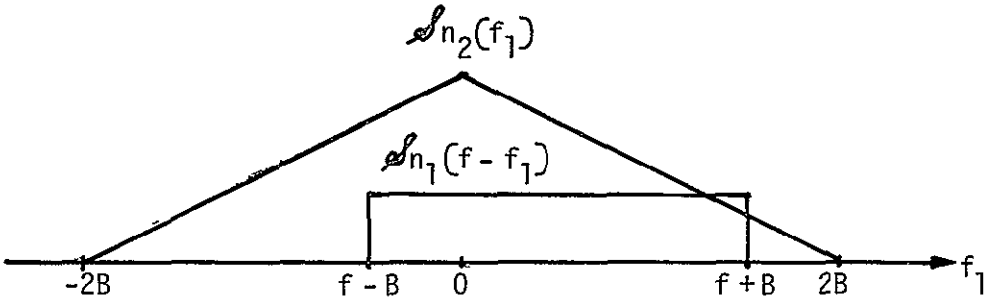

Figure II-3. Spectra for Determining $\mathscr{S}_{n_3}(f_1)$

In the region $0 < f < B$, we then have

$$\frac{\mathscr{S}_{n_3}(f)}{\left(\frac{N_0}{2}\right)^3} = \int_{f-B}^{0} (2B - |f_1|)df_1 + \int_{0}^{f+B} (2B - |f_1|)df_1 \qquad \text{(II-8)}$$

Since $\mathscr{S}_{n_3}(f)$ is an even function, we obtain

$$\mathscr{S}_{n_3}(f) = \left(\frac{N_0}{2}\right)^3 (3B^2 - |f|^2) \qquad 0 \leq |f| < B \qquad \text{(II-9)}$$

Now in the region $B < f < 3B$, we have

$$\frac{\mathscr{S}_{n_3}(f)}{\left(\frac{N_0}{2}\right)^3} = \int_{f-B}^{2B} \left[2B - |f|\right] df$$

Since $\mathscr{S}_{n_3}(f)$ is an even function of f, we have

$$\frac{\mathscr{S}_{n_3}(f)}{\left(\frac{N_0}{2}\right)^3} = \frac{9}{2}B^2 - 3B|f| + \frac{f^2}{2} \qquad B < |f| < 3B \quad \text{(II-10)}$$

To summarize, we obtain

$$\mathcal{S}_{n_3}(f) = \left(\frac{N_0}{2}\right)^3 = (3B^2 - f^2) \qquad 0 < |f| \leq B$$

$$\mathcal{S}_{n_3}(f) = \left(\frac{N_0}{2}\right)^3 \left(\frac{9}{2}B^2 - 3B|f| + \frac{f^2}{2}\right) \qquad B \leq f \leq 3B \qquad \text{(II-11)}$$

Note that the two equations are equal at $f = B$. Now consider $\mathcal{S}_{n_4}(f)$. Figure II-4 illustrates the spectra involved in the convolution.

$$\mathcal{S}_{n_4}(f) = \int_{-\infty}^{\infty} \mathcal{S}_{n_3}(f_1)\mathcal{S}_{n_1}(f - f_1)\, df_1 \qquad \text{(II-12)}$$

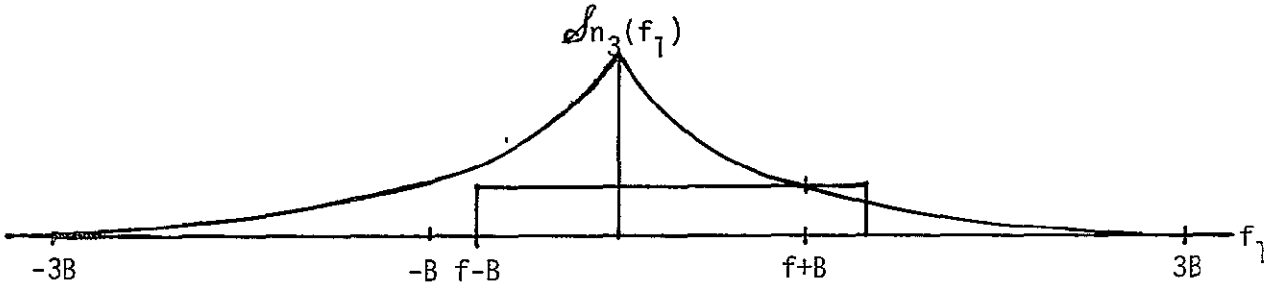

Figure II-4. Spectra Used for the Fourth-Order Convolution of the Noise Spectra

Consider the case $0 < f < 2B$. We have

$$\frac{\mathcal{S}_{n_4}(f)}{\left(\frac{N_0}{2}\right)^4} = \int_{f-B}^{B} \left(3B^2 - f^2\right) df + \int_{B}^{f+B} \left(\frac{9}{2}B^2 - 3Bf + \frac{f^2}{2}\right) df \qquad \text{(II-13)}$$

or, using symmetry,

$$\frac{\mathscr{S}_{n_4}(f)}{\left(\frac{N_0}{2}\right)^4} = \frac{16}{3}B^3 - 2Bf^2 + \frac{1}{2}|f|^3 \qquad 0 \leq |f| \leq 2B \quad \text{(II-14)}$$

In the region $2B < f < 4B$, we have that

$$\frac{\mathscr{S}_{n_4}(f)}{\left(\frac{N_0}{2}\right)^4} = \int_{f-B}^{3B} \left(\frac{9}{2}B^2 - 3B|f| + \frac{f^2}{2}\right) df \qquad 2B \leq f \leq 4B \quad \text{(II-15)}$$

After evaluating, we obtain

$$\frac{\mathscr{S}_{n_4}(f)}{\left(\frac{N_0}{2}\right)^4} = \frac{16}{3}B^3 - 2Bf^2 + \frac{1}{2}|f|^3 \qquad 0 \leq |f| \leq 2B \quad \text{(II-16)}$$

$$\frac{\mathscr{S}_{n_4}(f)}{\left(\frac{N_0}{2}\right)^4} = \frac{32}{3}B^3 - 8B^2|f| + 2B|f|^2 - \frac{|f|^3}{6} \qquad 2B \leq |f| \leq 4B \quad \text{(II-17)}$$

Now compute $\mathscr{S}_{n_5}(f)$. Figure II-5 illustrates the spectra involved. Now

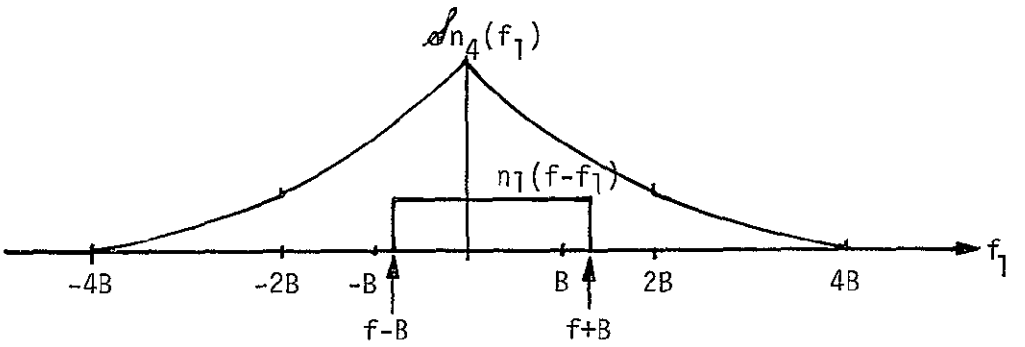

Figure II-5 Spectra Used for the Fifth-Order Convolution ($0 \leq f \leq B$)

$$\mathcal{S}_{n_5}(f) = \int_{-\infty}^{\infty} \mathcal{S}_{n_4}(f_1)\mathcal{S}_n(f - f_0)\, df_1 \tag{II-18}$$

Evaluating for $0 \leq f \leq B$, we have

$$\frac{\mathcal{S}_{n_5}(f)}{\left(\frac{N_0}{2}\right)^5} = \int_{f-B}^{f+B} \left(\frac{16}{3} B^3 - 2Bf^2 + \frac{1}{2}|f|^3\right) df \tag{II-19}$$

so that, after some algebra for $0 \leq f \leq B$, we have

$$\frac{\mathcal{S}_{n_5}(f)}{\left(\frac{N_0}{2}\right)^5} = \frac{115}{12} B^4 - \frac{5}{2} B^2 f^2 + \frac{f^4}{4} \tag{II-20}$$

Now consider the region $B \leq f \leq 3B$ illustrated in Figure II-6

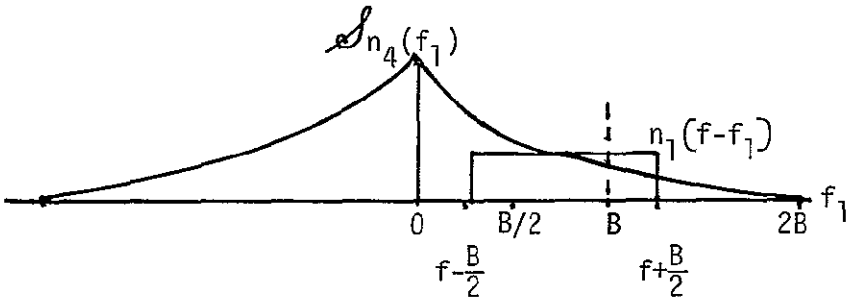

Figure II-6 Spectra Used for the Fifth-Order Convolution ($B < f \leq 3B$)

$$\frac{\mathcal{S}_{n_5}(f)}{\left(\frac{N_0}{2}\right)^5} = \int_{f-B}^{2B} \left(\frac{16}{3} B^3 - 2Bf^2 + \frac{1}{2} f^3\right) df + \int_{2B}^{f+B} \left(\frac{32}{3} B^3 - 8B^2 f + 2Bf^2 - \frac{f^3}{6}\right) df \tag{II-21}$$

Evaluating (II-21), we obtain by symmetry

$$\frac{\mathscr{S}_{n_5}(f)}{\left(\frac{N_0}{2}\right)^5} = \frac{55}{6}B^4 + \frac{5}{3}B^3|f| - 5B^2f^2 + \frac{5}{3}B|f|^3 - \frac{1}{6}f^4 \qquad B \leq |f| \leq 3B \qquad \text{(II-22)}$$

Now consider the case when $3B \leq f \leq 5B$ is illustrated in Figure II-7.

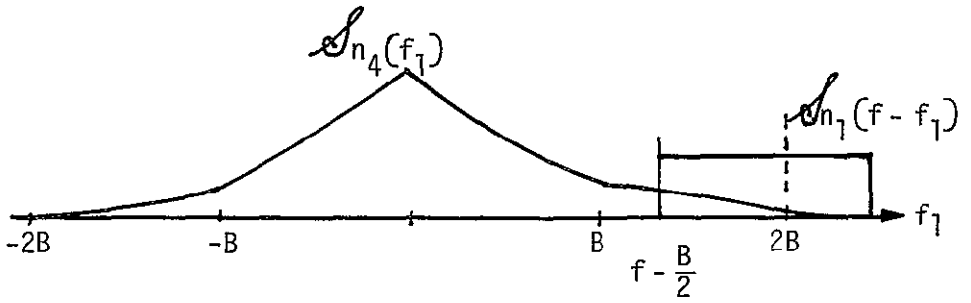

Figure II-7 Spectra Used for the Fifth-Order Convolution ($3B < f \leq 5B$)

We have

$$\frac{\mathscr{S}_n(f)}{\left(\frac{N_0}{2}\right)^5} = \int_{-\infty}^{\infty} \mathscr{S}_{n_4}(f_1)\,\mathscr{S}_n(f - f_1)\,df_1 \qquad \text{(II-23)}$$

$$= \int_{f-B}^{4B} \left(\frac{32}{3}B^3 - 8B^2|f| + 2B|f|^2 - \frac{|f|^3}{6}\right) df \qquad \text{(II-24)}$$

After some tedious algebra, we obtain by symmetry

$$\frac{\mathscr{S}_{n_5}(t)}{\left(\frac{N_0}{2}\right)^5} = \frac{1875}{72}B^4 - \frac{125}{6}B^3f + \frac{25}{4}B^2f^2 - \frac{5}{6}Bf^3 + \frac{1}{24}f^4 \qquad 3B \leq |f| \leq 5B \qquad \text{(II-25)}$$

In conclusion, for the fifth-order convolution, we have

$$\frac{\mathcal{S}_{n_5}(f)}{\left(\frac{N_0}{2}\right)} = \frac{55}{6}B^4 + \frac{5}{3}B^3 f - 5B^2 f^2 + \frac{5}{3}Bf^3 - \frac{1}{6}f^4 \qquad 0 \leq |f| \leq 3B$$

$$\frac{\mathcal{S}_{n_5}(f)}{\left(\frac{N_0}{2}\right)^5} = \frac{115}{12}B^4 - \frac{5}{2}B^2 f^2 + \frac{f^4}{4} \qquad 0 \leq |f| \leq B$$

$$\frac{\mathcal{S}_{n_5}(f)}{\left(\frac{N_0}{2}\right)^5} = \frac{1875}{72}B^4 - \frac{125}{6}B^3 f + \frac{25}{4}B^2 f^2 - \frac{5}{6}Bf^3 + \frac{1}{24}f^4 \qquad 3B \leq |f| \leq 5B \quad \text{(II-26)}$$

From equation (I-22), we have that the spectral density out of the limiter is given by

$$\begin{aligned}\mathcal{S}_y(f) = {} & \operatorname{erf}^2\left(\sqrt{\frac{S}{2N}}\right)\mathcal{S}_d(f) + \frac{2}{\sigma^4}\left[z^{(1)}\left(\sqrt{\frac{S}{N}}\right)\right]^2 \mathcal{F}\left\{R_d(\tau)\, R_n{}^2(\tau)\right\} \\ & + \frac{1}{6\sigma^8}\left[z^{(3)}\left(\sqrt{\frac{S}{N}}\right)\right]^2 \mathcal{F}\left\{R_d(\tau)\, R_n{}^4(\tau)\right\} + 4\left[z^{(0)}\left(\sqrt{\frac{S}{N}}\right)\right]^2 \frac{1}{\sigma^2}\mathcal{S}_n(f) \\ & + \frac{2}{3}\left[z^{(2)}\left(\sqrt{\frac{S}{N}}\right)\right]^2 \frac{1}{\sigma^6}\mathcal{S}_{n_3}(f) + \frac{4}{51}\left[z^{(4)}\left(\sqrt{\frac{S}{N}}\right)\right]^2 \frac{1}{\sigma^{10}}\mathcal{S}_{n_5}(f) \qquad \text{(II-27)}\end{aligned}$$

where $\mathcal{S}_n(f)$, $\mathcal{S}_{n_3}(f)$ and $\mathcal{S}_{n_5}(f)$ are given in equations (II-1), (II-11) and (II-26), respectively.

The second and third terms are SxN terms and are yet to be evaluated Consider the spectral density at f = 0.

$$\mathcal{S}_{SxN}(0) = \frac{2}{\sigma^4}\left[z^{(1)}\left(\sqrt{\frac{S}{N}}\right)\right]^2 \mathcal{F}\left\{R_d(\tau)\, R_n{}^2(\tau)\right\} + \frac{1}{6\sigma^8}\left[z^{(3)}\left(\sqrt{\frac{S}{N}}\right)\right]^2 \mathcal{F}\left\{R_d(\tau)\, R_n{}^4(\tau)\right\} \qquad \text{(II-28)}$$

or

$$\mathcal{S}_{SxN}(0) \leq \frac{2}{\sigma^4}\left[z^{(1)}\left(\sqrt{\frac{S}{N}}\right)\right]^2 \mathcal{F}\{R_n^2(\tau)\} \qquad \text{(II-29)}$$

$$+ \frac{1}{6\sigma^8}\left[z^{3}\left(\sqrt{\frac{S}{N}}\right)\right]^2 \mathcal{F}\{R_n^4(\tau)\}$$

$$= \left[z^{(1)}\left(\sqrt{\frac{S}{N}}\right)\right]^2 N_0^2/B + 0.056\left[z^{(3)}\left(\sqrt{\frac{S}{N}}\right)\right]^2 N_0^4/B \qquad \text{(II-30)}$$

The output signal power first term of equation (II-27) to NxN and SxN spectral density is evaluated in Table II-1 using equations (II-27), (II-1), (II-11), (II-26) and (II-30).

Table II-1. Input and Output SNR Comparisons

$\left(\frac{S}{N}\right)_{IN}$ (dB)	$\left(\frac{C}{N_0}\right)_{IN}$ (dB-Hz)	$\left(\frac{S}{N_0'B}\right)_{OUT}$ (dB)	$\left(\frac{C}{N_0'}\right)_{OUT}$ dB-Hz
10	77	27.3	94.3
5	72	10.4	77.4
0	67	- 1.3	65 7
- 5	62	- 6.2	60.8
-10	57	-12.15	54.85
-15	52	-17.4	49.6

Notice that the output C/N_0' ratio is greater than the input C/N_0 ratio at 5 dB SNR_{IN} and higher. Due to this apparent improvement (which parallels the bandpass limiter I/O ratio improvement [1]), we conclude that knowing C/N_0 is not sufficient to estimate BER degradation. Consequently, we leave this component out in the BER degradation tables.

REFERENCES

1. W. C. Lindsey, Synchronization Systems in Communications and Control, Appendix I of Chapter 4, Prentice-Hall, Inc., 1972.

2. R. J. Helgeson, "PI-PSP BER Degradation Due to RF Baseband Output Limiting Amplifier," TRW IOC #SCTE-50-79-491/RJH, September 5, 1979.

APPENDIX III

TWO TONES PLUS THERMAL NOISE INTO A CLIPPER

The clipper model is shown in Figure III-1. In this section, we follow the work of Davenport and Root [1], Helgeson [2], Shaft [3] and Shaft [4]. We extend the analysis to the two-tone case using an approximation due to M. Gyi [5] and an extension of that approximation due to the author of this report [6].

The input to the clipper is modeled as the sum of two tones and bandlimited thermal noise:

$$x(t) = \sqrt{2P_1}\cos\Big(\underbrace{\omega_{sc_1}}_{1.024\ \text{MHz}}t+\theta_1\Big) + \sqrt{2P_2}\cos\Big(\underbrace{\omega_{sc_2}}_{1.7\ \text{MHz}}t+\theta_2\Big) + n(t) \quad \text{(III-1)}$$

where P_1 and P_2 are the respective powers of the two tones. We use the indirect approach [1] and form the autocorrelation function

$$R_y(t_1,t_2) = E\Big\{g\Big[x(t_1)\Big]\ g\Big[x(t_2)\Big]\Big\} \quad \text{(III-2)}$$

From [1, section 13-3], we can write that

$$R_y(t_1,t_2) = \frac{1}{(2\pi J)^2}\int_C f(\omega_1)\,d\omega_1 \int_C f(\omega_2)\,d\omega_2\, M_x(\omega_1\omega_2) \quad \text{(III-3)}$$

where $M_x(\omega_1,\omega_2)$ is the joint characteristic function of x_{t_1} and x_{t_2}. Now for independent noise and signal processes, we have

$$M_x(\omega_1,\omega_2) = M_{s_1}(\omega_1,\omega_2)\, M_n(\omega_1,\omega_2)\, M_{s_2}(\omega_1,\omega_2)\, M_{s_3}(\omega_1,\omega_2)\ldots \quad \text{(III-4)}$$

From Shaft [3], we can write

(a) Block Diagram

(b) Nonlinearity Transfer Function Model

Figure III-1 Clipper Model Used in the Analysis

$$M_x(\omega_1,\omega_2) = \sum_{m_1=0}^{\infty}\sum_{m_2=0}^{\infty}\cdots\sum_{m_n=0}^{\infty}\varepsilon_{m_1}\varepsilon_{m_2}\cdots\varepsilon_{m_n}\ , \quad \left(\frac{A_i^2}{2} = P_i\right)$$

$$I_{m_1}(A_1\omega_1)\ I_{m_2}(A_2\omega_2)\cdots I_{m_n}(A_n\omega_n)$$

$$\cos\left(m_1\omega_{sc_1}\tau\right)\cdot\cos\left(m_2\omega_{sc_2}\tau\right)\cdots\cos\left(m_n\omega_{sc_n}\tau\right) \qquad \text{(III-5)}$$

where

$$\varepsilon_{m_1} = 1 \qquad m_i = 0$$
$$= 2 \qquad m_i \neq 0$$

Now $I_{m_i}(x)$ is the modified Bessel function of the first kind and of order m_1. Hence, we obtain

$$R_y(t_1,t_2) = \left(\frac{1}{2\pi J}\right)^2\int_C f(\omega_1)\int_C f(\omega_2)\sum_{m_1=0}^{\infty}\cdot\sum_{m_n=0}^{\infty}\varepsilon_{m_1}\cdots\varepsilon_{m_2}\ I_{m_1}(A_1\omega_1)\ I_{m_n}(A_n\omega_1)$$

$$\cdots I_{m_1}(A_1\omega_2)\cdots I_{m_n}(A_n\omega_2)\cdot\exp\left[\frac{\sigma_n^2}{2}\left(\omega_1^2+\omega_2^2\right)\right]$$

$$\times\sum_{k=0}^{\infty}\frac{R_n^{\,k}(\tau)\omega_1^{\,k}\omega_2^{\,k}}{k!}\cdot\cos\left(m_1\omega_{sc_1}\tau\right)\cdot\cdot\cos\left(m_n\omega_{sc_n}\tau\right) \qquad \text{(III-6)}$$

This can be written as

$$R_y(t_1,t_2) = \sum_{k=0}^{\infty}\sum_{m_1=0}^{\infty}\sum_{m_n=0}^{\infty}\frac{\left(R_n(\tau)\right)^k}{k!}\varepsilon_{m_1}\varepsilon_{m_2}\cdots\varepsilon_{m_n}\ h^2{}_{km_1m_2}\cdots m_n$$

$$\cos\left(m_1\omega_{sc_1}\tau\right)\ \cos\left(m_2\omega_{sc_2}\tau\right)\cdots\cos\left(m_n\omega_{sc_n}\tau\right) \qquad \text{(III-7)}$$

where

$$h_{km_1m_2\ldots m_n} = \frac{1}{2\pi j}\int_c f(\omega)\,\omega^k\, I_{m_1}(A_1\omega)\, I_{m_2}(A_2\omega)\cdots I_{m_n}(A_n\omega)\cdot e^{\frac{\sigma^2\omega^2}{2}}\, d\omega \qquad \text{(III-8)}$$

where c is an appropriately chosen contour in the complex plane. Shortly, we will discuss this contour more precisely.

An expansion for two signals is given by

$$R_y(\tau) = \sum_{k=1,3,\ldots}\ \sum_{\substack{m_1=0\\ m_1+m_2=0,2,\ldots}}^{\infty}\ \sum_{m_2=0}^{\infty} \varepsilon_{m_1}\varepsilon_{m_2}\, h^2_{km_1m_2}\cos\left(m_1\omega_{sc_1}\tau\right)\cos\left(m_2\omega_{sc_2}\tau\right)$$

$$+ \sum_{k=0,2,\ldots}\ \sum_{\substack{m_1=0\\ m_1+m_2=1,3,\ldots}}\ \sum_{m_2=0} \varepsilon_{m_1}\varepsilon_{m_2}\, h^2_{km_1m_2}\cos\left(m_1\omega_{sc_1}\tau\right)\cos\left(m_2\omega_{sc_2}\tau\right) \qquad \text{(III-9)}$$

Now consider the clipper amplifier shown in Figure III-1(b) and the expression in equation form in equation (III-10).

$$g(x) = \begin{cases} -a & x \leq -d \\ (a/d)x & |x| \leq d \\ a & x \geq d \end{cases} \qquad \text{(III-10)}$$

From (III-8), the $h_{km_1m_2}$ are given by

$$h_{km_1m_2} = \frac{1}{2\pi J}\int_c f(\omega)\omega^k\, I_{m_1}(A_1\omega)\, I_{m_2}(A_2\omega)\, e^{\left[\frac{\sigma^2\omega^2}{2}\right]}\, d\omega \qquad \text{(III-11)}$$

where $A_1 = \sqrt{2P_1}$, $A_2 = \sqrt{2P_2}$, the A_1's are peak voltages and $\sigma^2 = N_0BG$, with G the AGC power gain.

Let

$$g_+(x) = \begin{cases} g(x) & x \geqslant 0 \\ 0 & x < 0 \end{cases} \quad ; \quad g_-(x) = \begin{cases} 0 & x > 0 \\ g(x) & x \leqslant 0 \end{cases} \tag{III-12}$$

and also let

$$f(\omega) = f_+(\omega) + f_-(\omega) \tag{III-13}$$

with

$$f_+(\omega) = \int_0^\infty g_+(x)\, e^{-\omega X}\, dx \quad ; \quad f_-(\omega) = \int_{-\infty}^0 g_-(x)\, e^{-\omega X}\, dx \tag{III-14}$$

For an odd transfer characteristic (such as our clipper), we have

$$f_{0_+}(\omega) = \phi(\omega) \quad ; \quad f_{0_-}(\omega) = -\phi(-\omega) \tag{III-15}$$

Hence, from equation (III-11), we have

$$h_{km_1m_2} = \frac{1}{(2\pi i)} \int_{c_+} \phi(\omega)\omega^k\, I_{m_1}(\omega A_1)\, I_{m_2}(\omega A_2)\, e^{\frac{\sigma^2\omega^2}{2}}\, d\omega$$

$$- \frac{1}{2\pi i} \int_{c_-} \phi(-\omega)\omega^k\, I_{m_1}(\omega A_1)\, I_{m_2}(\omega A_2)\, e^{\frac{\sigma^2\omega^2}{2}}\, d\omega \tag{III-16}$$

where c_+ and c_- are shown in Figure III-2. Let $-\omega = \omega'$ in the second term of (III-16) so that we get

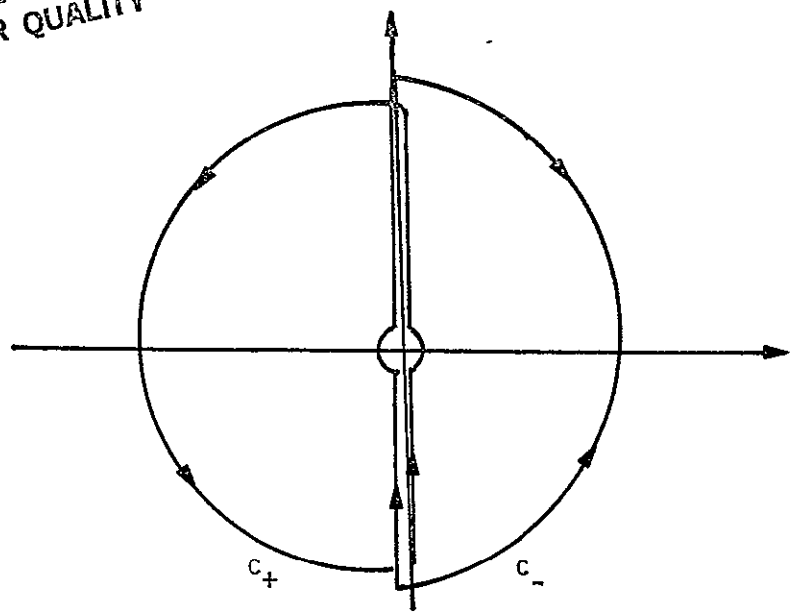

Figure III-2. Complex Integral Contours Used For Evaluating $h_{km_1m_2}$

$$h_{km_1m_2} = \frac{1}{2\pi i}\int_{C_+} \phi(\omega)\omega^k I_{m_1}(\omega A_1) I_{m_2}(\omega A_2) e^{\frac{\sigma^2\omega^2}{2}} d\omega$$

$$- \frac{1}{2\pi i}\int_{C_+} \phi(\omega')(-\omega')^k(-1)^{m_1}(-1)^{m_2} I_{m_1}(\omega' A_1) I_{m_2}(\omega' A_2) e^{\frac{\sigma^2\omega^2}{2}(+)} d\omega' \qquad \text{(III-17)}$$

So when $(-1)^{k+m_1+m_2} = 1$, i.e , $k+m_1+m_2$ is even, then

$$h_{km_1m_2} = 0 \qquad (k + m_1 + m_2 \text{ even})$$

$$h_{km_1m_2} = \frac{2}{2\pi i}\int_{C_+} \phi(\omega)\omega^k I_{m_1}(\omega A_1) I_{m_2}(\omega A_2) e^{\frac{\sigma^2\omega^2}{2}} d\omega$$

$$(k + m_1 + m_2 \text{ odd}) \qquad \text{(III-18)}$$

We now compute $\phi(\omega)$. We have that

$$\phi(\omega) = \int_0^\infty g(x)\, e^{-\omega x}\, dx \qquad \text{(III-19)}$$

$$= \int_0^d \frac{a}{d}\, x\, e^{-\omega x}\, dx + \int_d^\infty a\, e^{-\omega x}\, dx \qquad \text{(III-20)}$$

or finally,

$$\phi(\omega) = \frac{a}{d}\left(\frac{1 - e^{-d\omega}}{\omega^2}\right) \qquad \text{(III-21)}$$

Notice that we can write

$$\phi(\omega) = \lim_{\delta \to 0} \frac{a}{d}\left[\frac{e^{-\delta\omega} - e^{-d\omega}}{\omega^2}\right] \qquad \text{(III-22)}$$

So

$$h_{km_1m_2} = \overbrace{\lim_{\delta\to 0} \frac{2}{2\pi J} \int_{C_+} \frac{a}{d} \frac{e^{-\delta\omega}}{\omega^2}\, \omega^k\, I_{m_1}(\omega A_1)\, I_{m_2}(\omega A_2)\, e^{\frac{\sigma^2\omega^2}{2}}\, d\omega}^{I^{(1)}}$$

$$- \overbrace{\frac{2}{2\pi J} \int_{C_+} \frac{a}{d} \frac{e^{-d\omega}}{\omega^2}\, \omega^k\, I_{m_1}(A_1\omega)\, I_{m_2}(A_2\omega)\, \exp\left(\frac{\sigma_n^2\omega^2}{2}\right) d\omega}^{I^{(2)}} \qquad \text{(III-23)}$$

$$\text{for } k + m_1 + m_2 \quad \text{odd}$$

and

$$h_{km_1m_2} = 0 \qquad \text{for } k + m_1 + m_2 \text{ even.}$$

Note that $h_{km_1m_2} = I^{(1)} - I^{(2)}$. Rotate axis $\pi/2$ radians clockwise by letting $\omega = iz$ so that (see Figure III-3 for the new contour)

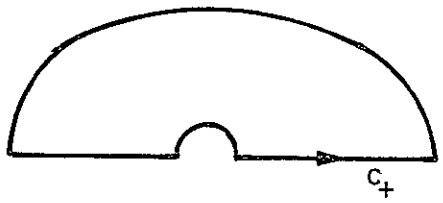

Figure III-3. The Contour c_+ After Rotation

$$I^{(1)} = \frac{1}{\pi 1} \int_{C_+} \frac{a}{d} \frac{e^{-i\delta z}}{-z^2} (iz)^k \, I_{m_1}(A_1 iz) \, I_{m_2}(A_2 1z) \, e^{-\frac{\sigma^2 z^2}{2}} \, idz \qquad \text{(III-24)}$$

or

$$I^{(1)} = \frac{1}{\pi} \int_{C_+} \frac{a}{d} e^{-1\delta z} \, (iz)^{k-2} \, I_{m_1}(A_1 1z) \, I_{m_2}(A_2 1z) \, e^{-\frac{\sigma^2 z^2}{2}} \, dz \qquad \text{(III-25)}$$

Let

$$I_{m_J}(iz) = (i)^{m_J} J_{m_J}(z) \qquad \text{(III-26)}$$

We finally obtain that

$$I^{(1)} = \frac{1}{\pi} \int_{C_+} \left(\frac{a}{d}\right)(1)^{k+m_1+m_2-2} \, z^{k-2} \, e^{-1\delta z} \, J_{m_1}(A_1 z) \, J_{m_2}(A_2 z) \, e^{-\frac{\sigma^2 z^2}{2}} \, dz \qquad \text{(III-27)}$$

Let

$$J_{m_1}(x) = \left(\frac{x}{2}\right)^{m_1} \sum_{\ell=0}^{\infty} \frac{(1z/2)^{2\ell}}{\ell! \, \Gamma(m_1+\ell+1)} \qquad \text{(III-28)}$$

so that

$$I^{(1)} = \frac{a}{\pi d} \sum_{\ell=0}^{\infty} \frac{i^{k+m_1+m_2-2+2\ell} \left(\frac{A_1}{2}\right)^{m_1+2\ell}}{\ell!\, \Gamma(m_1+\ell+1)} \int_{C_+} z^{k+2+m_1+2\ell} J_{m_2}(A_2 z) \exp\left(-i\delta z - \sigma_n^2 \frac{z^2}{2}\right) dz \tag{III-29}$$

To evaluate this expression with $m_2 = 0$, we approximate $J_0(A_2 z)$ by

$$J_0(A_2 z) \cong e^{-\left(\frac{A_2^2}{2}\frac{z^2}{2}\right)} \tag{III-30}$$

to get

$$I^{(1)} \cong \frac{a}{\pi d} \sum_{\ell=0}^{\infty} \frac{i^{k+m_1+m_2-2+2\ell} \left(\frac{A_1}{2}\right)^{m+2\ell}}{\ell!\, \Gamma(m_1+\ell+1)} \int_{C_+} z^{k-2+m_1+2\ell} \exp\left(-i\delta z - \left(\sigma_n^2 + \frac{A_2^2}{2}\right)\frac{z^2}{2}\right) dz \tag{III-31}$$

From (III-31) and (III-28), we have

$$I^{(1)} = \frac{a}{\pi d} \sum_{\ell=0}^{\infty} \frac{i^{(k+m_1+m_2-2+2\ell)} \left(\frac{A_1}{2}\right)^{m_1+2\ell} \pi i^{-k+2-m_1-2\ell}}{\ell!\,\Gamma(m_1+\ell+1) \left(\frac{\sqrt{\sigma_n^2 + \frac{A_2^2}{2}}}{\sqrt{2}}\right)^{k-1+m_1+2\ell}}$$

$$\left\{ \frac{{}_1F_1\left[\frac{k-1+m_1+2\ell}{2}, \frac{1}{2}, \frac{-\delta^2}{2\left(\sigma_n^2 + \frac{A_2^2}{2}\right)}\right]}{\Gamma\left(\frac{3-k-m_1-2\ell}{2}\right)} - \frac{\sqrt{2}\delta}{\sqrt{\sigma_n^2 + \frac{A_2^2}{2}}} \frac{{}_1F_1\left[\frac{k+m_1+2\ell}{2}; \frac{3}{2}; \frac{-\delta^2}{2\left(\sigma_n^2 + \frac{A_2^2}{2}\right)}\right]}{\Gamma\left(\frac{2-k-m_1-2\ell}{2}\right)} \right\} \tag{III-32}$$

where ${}_1F_1(a,b,z)$ is the confluent hypergeometric function.

Define an effective input SNR by

$$\rho_i = \frac{A_1^2}{2\left(\sigma_n^2 + \frac{A_2^2}{2}\right)}$$

or

$$I^{(1)} = \frac{a}{d}\left(\frac{\sigma_n^2 + \frac{A_2^2}{2}}{2}\right)^{\frac{1-k}{2}} \rho_1^{m_1/2} \sum_{\ell=0}^{\infty} \frac{\rho_i^{\ell}(1)^{m_2}}{\ell!\,\Gamma(m_1+\ell+1)}$$

$$\times \left\{ \frac{{}_1F_1\left[\frac{k-1+m_1+2\ell}{2}, \frac{1}{2}, \frac{-\delta^2}{2\left(\sigma_n^2+\frac{A_2^2}{2}\right)}\right]}{\Gamma\left(\frac{3-k-m_1-2\ell}{2}\right)} - \frac{\sqrt{2}\delta \; {}_1F_1\left[\frac{k+m_1+2\ell}{2}; \frac{3}{2}; \frac{-\delta^2}{2\left(\sigma_n^2+\frac{A_2^2}{2}\right)}\right]}{\sqrt{\sigma_n^2+\frac{A_2^2}{2}}\;\Gamma\left(\frac{2-k-m_1-2\ell}{2}\right)} \right\} \tag{III-33}$$

Hence, from (III-23), we have for the coefficients

$$h_{km_10} = \frac{a}{d}\left[\frac{\left(\sigma_n^2 + \frac{A_2^2}{2}\right)}{2}\right]^{\frac{1-k}{2}} \rho_1^{m_1/2} \sum_{\ell=0}^{\infty} \frac{\rho_1^{\ell}}{\ell!\,\Gamma(m_1+\ell+1)}$$

$$\times \left\{ \frac{1 - {}_1F_1\left[\frac{k-1+m_1+2\ell}{2}, \frac{1}{2}, \frac{-d^2}{2\left(\sigma_n^2+\frac{A_2^2}{2}\right)}\right]}{\Gamma\left(\frac{3-k-m_1-2\ell}{2}\right)} + \frac{\sqrt{2}d \; {}_1F_1\left[\frac{k+m_1+2\ell}{2}, \frac{3}{2}; \frac{-d^2}{2\left(\sigma_n^2+\frac{A_2^2}{2}\right)}\right]}{\sqrt{\sigma_n^2+\frac{A_2^2}{2}}\;\Gamma\left(\frac{2-k-m_1-2\ell}{2}\right)} \right\} \tag{III-34}$$

Note that, since $\Gamma(-k) = \pm\infty$, $k \geq 0$ (k an integer), when $\ell > 0$, the first denominator will be either $\pm\infty$ and hence, $h_{km_1 0} = 0$. Also, when $\ell = 0$ and $m_1 + k = 1$, then ${}_1F_1(0,b,z) = 1$, and again the first term drops out. Since $m_1 + k$ must be odd, we see that the first term drops out.

We therefore have

$$h_{km_1 0} = \frac{\sqrt{2}a}{\sqrt{\sigma_n^2 + \frac{A_2^2}{2}}} \left[\frac{\left(\sigma_n^2 + \frac{A_2^2}{2} \right)}{2} \right]^{\frac{1-k}{2}} \rho_1^{m_1/2} \sum_{\ell=0}^{\infty} \frac{\rho_1^{\ell/2}}{\ell! \Gamma(m_1 + \ell + 1)}$$

$$\times \frac{{}_1F_1\left[\frac{(2\ell + k + m_1)}{2} ; \frac{3}{2} ; -\frac{d^2}{2\left(\sigma_n^2 + \frac{A_2^2}{2} \right)} \right]}{\Gamma\left[\frac{(2 - 2\ell - k - m_1)}{2} \right]} \qquad \text{(III-35)}$$

Now note that

$${}_1F_1(y - x, y, -z) = e^{-z} \, {}_1F_1(x, y, z) \qquad \text{(III-36)}$$

so that letting

$$b = \frac{d}{\sqrt{\sigma_n^2 + \frac{A_2^2}{2}}}$$

we finally obtain

$$\left|h_{km_1 0}\right| = \left| \frac{\sqrt{2}a}{d}\, b \left[\frac{\sigma_n^2 + \frac{A_2^2}{2}}{2}\right]^{\frac{1-k}{2}} \rho_i^{m_1/2}\, e^{-b^2/2} \sum_{\ell=0}^{\infty} \frac{\rho_i^{\ell/2}}{\ell!(m_1+\ell)!} \right.$$

$$\left. \times \frac{{}_1F_1\left[\left(\frac{3-2\ell-k-m_1}{2}\right); \frac{3}{2} : \frac{b^2}{2}\right]}{\Gamma\left(\frac{2-2\ell-k-m_1}{2}\right)} \right|_{m_1+k \text{ odd}} \qquad \text{(III-37)}$$

$$= 0 \text{ otherwise}$$

where

$$\rho_1 = \frac{A_1^2}{2\left(\sigma_n^2 + \frac{A_2^2}{2}\right)}, \quad b = \frac{d}{\sqrt{\sigma_n^2 + \frac{A_2^2}{2}}} \qquad \text{(III-38)}$$

In (III-29), we now consider the case $m_2 = 1$ and all m_1 and all k. Consider the approximation

$$J_1\left(A_2 x\right) = \frac{A_2 x}{2}\, e^{-\left(\frac{A_2^2}{3}\right)\frac{x^2}{2}} \qquad \text{(III-39)}$$

See Figure III-4 for a comparison of the approximation. From (III-29), we get

$$I^{(1)} = \frac{a}{\pi d} \sum_{\ell=0}^{\infty} \frac{1^{k+m_1+m_2-2+2\ell}}{\ell!\ \Gamma(m_1+\ell+1)} \left(\frac{A_1}{2}\right)^{m_1+2\ell} \left(\frac{A_2}{2}\right) \int_{C_+'} z^{k-2+m_1+2\ell+1}$$

$$\times \exp\left(-1\delta z - \left(\sigma_n^2 + \frac{A_2^2}{3}\right)\frac{z^2}{2}\right) dz \qquad \text{(III-40)}$$

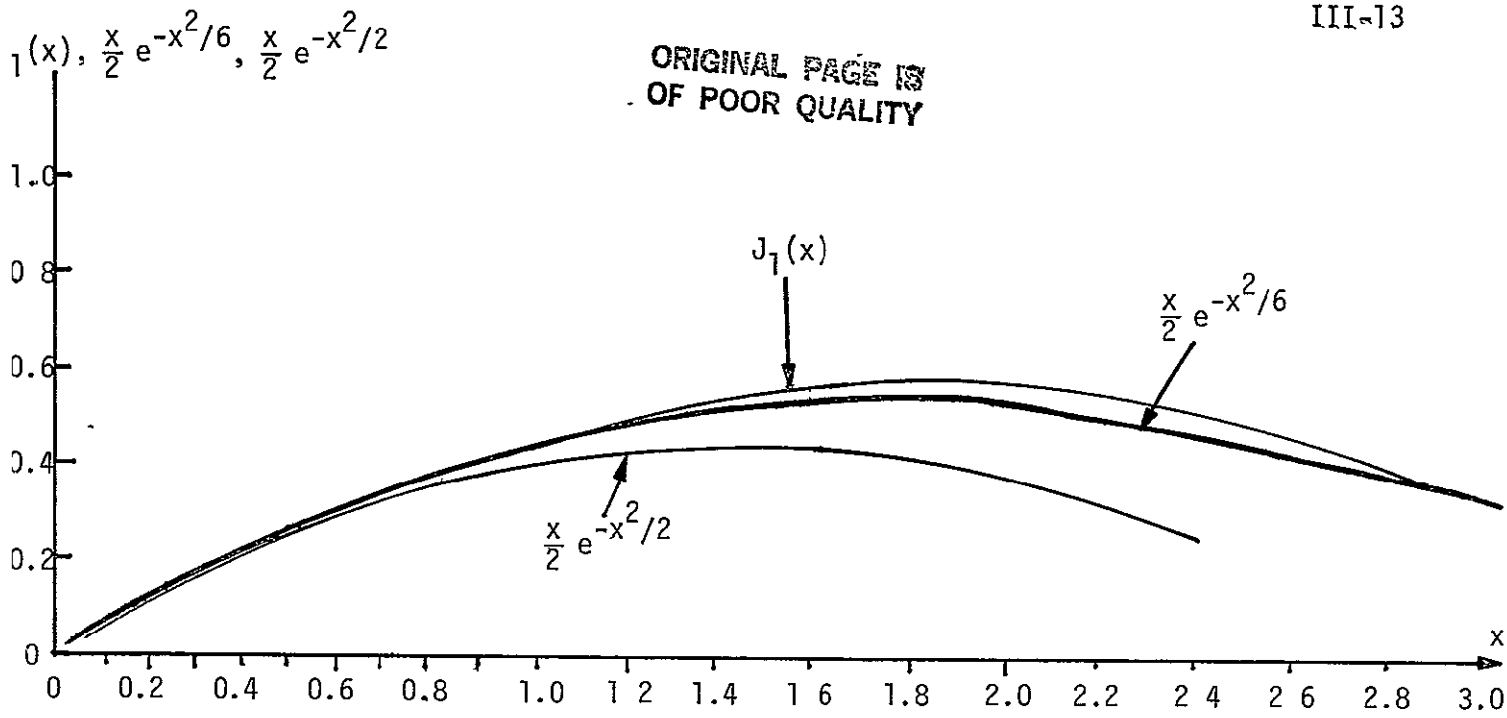

(a) Case of $0 \leq x \leq 3.0$

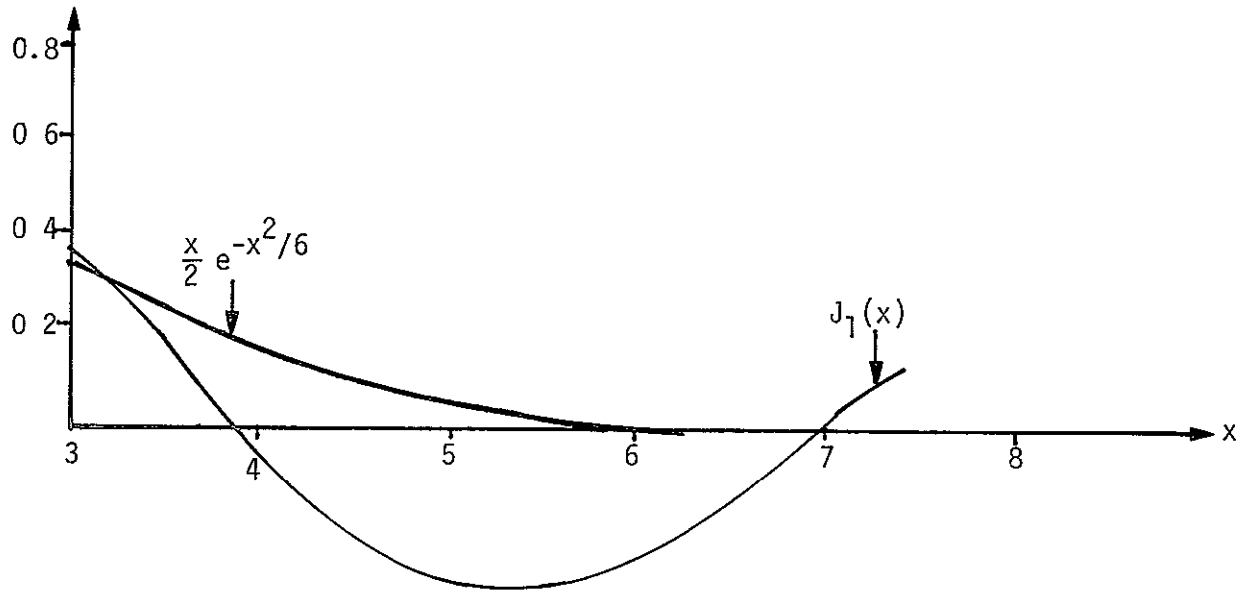

(b) Case of $3.0 \leq x \leq 8.0$

Figure III-4. Comparison of $J_1(x)$ and Its Approximation $\frac{x}{2} e^{-x^2/6}$ and Others

Going through the same calculations as before, using equation (III-28), we obtain the result

$$
{}_1h_{km_1 1} = \left(\frac{a\left(\frac{A_2}{2}\right)}{\pi d}\right) \sum_{\ell=0}^{\infty} \frac{i^{k+m_1+1-2+2\ell}}{\ell!\,\Gamma(m_1+\ell+1)} \frac{\pi i^{-k+1-m_1-2\ell} \left(\frac{A_1}{2}\right)^{m_1+2\ell}}{\left(\frac{\sigma_n^2+\frac{A_2^2}{3}}{2}\right)^{\frac{k+m_1+2\ell}{2}}}
$$

$$
\times \left\{ \frac{{}_1F_1\left[\frac{k+m_1+2\ell}{2}, \frac{1}{2}, \frac{-\delta^2}{2\left(\sigma_n^2+\frac{A_2^2}{3}\right)}\right]}{\Gamma\left(\frac{-k+2-m_1-2\ell-1+1}{2}\right)} - \frac{\delta\sqrt{2}}{\sqrt{\sigma_n^2+\frac{A_2^2}{3}}} \frac{{}_1F_1\left[\frac{k-2+m_1+2\ell+1+2}{2}, \frac{3}{2}, \frac{-\delta^2}{2\left(\sigma_n^2+\frac{A_2^2}{3}\right)}\right]}{\left(\frac{-k+2-m_1-2\ell-1}{2}\right)} \right\}
\tag{III-41}
$$

Letting

$$
\rho_1 = \frac{\frac{A_1^2}{2}}{\left(\sigma_n^2+\frac{A_2^2}{3}\right)} ,
$$

and

$$
\rho_2 = \frac{\frac{A_2^2}{2}}{\left(\sigma_n^2+\frac{A_1^2}{3}\right)} ,
\tag{III-42}
$$

we then have

$$ {}_1h_{km_1 1} = \frac{a}{d}\left(\frac{A_2}{2}\right)\rho_1^{m_1/2}\left(\frac{\sigma_n^2+\frac{A_2^2}{3}}{2}\right)^{-k/2}\sum_{\ell=0}^{\infty}\frac{\rho_1^{\ell}}{\ell!\,\Gamma\ell m_1+\ell+1} $$

$$ \times\left\{\frac{{}_1F_1\left[\frac{k+m_1+2\ell}{2},\frac{1}{2},\frac{-\delta^2}{2\left(\sigma_n^2+\frac{A_2^2}{3}\right)}\right]}{\Gamma\left(\frac{2-k-m_1-2\ell}{2}\right)}-\frac{\sqrt{2}\delta\;\;{}_1F_1\left[\frac{k+m_1+2\ell+1}{2},\frac{3}{2},\frac{-\delta^2}{2\,\sigma_n^2+\frac{A_2^2}{3}}\right]}{\sqrt{\sigma_n^2+\frac{A_2^2}{3}}\;\;\Gamma\left[\frac{-k+1-m_1-2\ell}{2}\right]}\right\} \tag{III-43} $$

Hence, using

$$ h_{km_1 1} = \lim_{\delta\to 0}\;{}_1h_{km_1 1} - {}_1h_{km_1 1}\Big|_{\delta=d} \tag{III-44} $$

along with the fact that

$$ \lim_{\delta\to 0}\;{}_1F_1(a,\,b,\,\delta) = 1 $$

yields from (III-42)

$$ h_{km_1 1} = \frac{a}{d}\left(\frac{A_2}{2}\right)\rho_1^{m_1/2}\left(\frac{\sigma_n^2+\frac{A_2^2}{3}}{2}\right)^{-k/2}\sum_{\ell=0}^{\infty}\frac{\rho_1^{\ell}}{\ell!\,\Gamma(m_1+\ell+1)} $$

$$ \times\left\{\frac{1-{}_1F_1\left[\frac{k+m_1+2\ell}{2},\frac{1}{2},\frac{-\delta^2}{2\left(\sigma_n^2+\frac{A_2^2}{3}\right)}\right]}{\Gamma\left(\frac{2-k-m_1-2\ell}{2}\right)}+\frac{\sqrt{2}\delta\;\;{}_1F_1\left[\frac{k+m_1+2\ell+1}{2},\frac{3}{2},\frac{-\delta^2}{2\left(\sigma_n^2+\frac{A_2^2}{3}\right)}\right]}{\sqrt{\sigma_n^2+\frac{A_2^2}{3}}\;\;\Gamma\left[\frac{-k+1-m_1-2\ell}{2}\right]}\right\} \tag{III-45} $$

Since

$$|\Gamma(n)| = \infty \qquad n=0,-1,-2,\ldots$$

Hence, when $\ell > 0$ $\Gamma(\cdot)\to\infty$ and contributes nothing to $h_{km_1 1}$. Furthermore, when $\ell = 0$ and $m_1+k = 0$, the first term

$$1 - {}_1F_1\left[0, \frac{1}{2}, \frac{-\delta^2}{2\left(\sigma_n^2 + \frac{A_2^2}{3}\right)}\right] = 0$$

Also, when $m_1+k = 2$, the gamma function is ∞ and again we get zero, so that we obtain for h_{km_1}

$$h_{km_1 1} = \frac{a}{d}\left(\frac{A_2}{2}\right)\rho_1^{m_1/2}\left(\frac{\sigma_n^2 + \frac{A_2^2}{3}}{2}\right)^{-k/2} \sum_{\ell=0}^{\infty} \frac{\rho_1^{\ell}}{\ell!\,\Gamma(m_1+\ell+1)} \times \frac{\sqrt{2}\delta \quad {}_1F_1\left[\frac{k+m_1+2\ell+1}{2}, \frac{3}{2}, \frac{-\delta^2}{2\left(\sigma_n^2 + \frac{A_2^2}{3}\right)}\right]}{\sqrt{\sigma_n^2 + \frac{A_2^2}{3}} \qquad \Gamma\left(\frac{-k+1-m_1-2\ell}{2}\right)} \tag{III-46}$$

REFERENCES

1. W. B. Davenport and W. L. Root, An Introduction to the Theory of Random Signals and Noise, McGraw-Hill Book Company, Inc., Chapter 13, 1958.

2. R. J. Helgeson, "PI-PSP BER Degradation Due to PI Baseband Output Limiting Amplifier," TRW IOC #SCTE-50-79-491/RJH, September 5,1979.

3. P. D. Shaft, "Limiting of Several Signals and Its Effect on Communication System Performance," IEEE Transactions on Communications Technology, Vol. COM-13, No. 4, December 1965.

4. P. D. Shaft, "Signal Through Nonlinearities and the Suppression of Undesired Intermodulation Terms," IEEE Transactions on Information Theory, September 1972.

5. M. Gyi, "Some Topics on Limiters and FM Demodulators," Stanford Electron Laboratory, Stanford University, California, Rep SEL-65-056, July 1965.

6 J. K. Holmes, unpublished report on approximate evaluation of some nonlinear systems.

APPENDIX IV

EVALUATION OF AN INTEGRAL USED IN THE CLIPPER PROBLEM

We start with a result due to Middleton [1]:

$$I^{(2)} = \int_c e^{-c^2z^2} z^{2u-1}\, dz = jc^{-2u}\, \Gamma(u)\, e^{-\pi uj}\, \sin\pi u \qquad |\arg c| < \pi/4 \quad \text{(IV-1)}$$

Now

$$\Gamma(z)\Gamma(1-z) = \frac{\pi}{\sin\pi} \quad \text{(IV-2)}$$

so

$$\Gamma(u)\, \sin\pi u = \frac{\pi}{\Gamma(1-u)} \quad \text{(IV-3)}$$

and

$$I^{(2)} = \frac{j\,\pi\, e^{-\pi uj}}{c^{2u}\Gamma(1-u)} \quad \text{(IV-4)}$$

so that

$$\int_{c_+'} \exp(-c^2z^2) z^{2u-1}\, dz = \frac{j\pi\exp(-\pi uj)}{c^{2u}\Gamma(1-u)} \quad \text{(IV-5)}$$

Consider

$$I^{(3)} = \int_{c_1'} z^{u-1}\, J_v(az)\, \exp(-q^2z^2)dz \quad \text{(IV-6)}$$

Now

$$J_v(z) = \left(\frac{z}{2}\right)^v \sum_{k=0}^{\infty} \frac{\left(-\frac{z^2}{4}\right)^k}{k!\Gamma(v+k+1)} \tag{IV-7}$$

so that

$$I^{(3)} = \int_{c_+'} z^{u-1}\left(\frac{za}{2}\right)^v \sum_{k=0}^{\infty} \frac{\left(-\frac{z^2a^2}{4}\right)^k}{k!\Gamma(v+k+1)} e^{-q^2z^2}\, dz \tag{IV-8}$$

$$= \left(\frac{a}{2}\right)^v \sum_{k=0}^{\infty} \frac{(-1)^k\left(\frac{a}{2}\right)^{2k}}{k!\Gamma(v+k+1)} \int_{c_+'} z^{v+2k+u-1}\, e^{-q^2z^2}\, dz \tag{IV-9}$$

Using equation (IV-5), we obtain

$$I^{(3)} = \left(\frac{a}{2}\right)^v \sum_{k=0}^{\infty} \frac{(-1)^k\left(\frac{a}{2}\right)^{2k}}{k!\Gamma(v+k+1)} \cdot \frac{J\pi \exp\left(-J\pi\left[k+\frac{v+u}{2}\right]\right)}{q^2\left[k+\frac{v+u}{2}\right]\Gamma\left(1-k-\frac{u+v}{2}\right)} \tag{IV-10}$$

Now let

$$c_r = c(c+1)(c+2)\cdot\ .(c+r) \tag{IV-11}$$

then

$$\Gamma(\alpha-n) = \frac{\Gamma(\alpha)(-1)^n}{(1-\alpha)_n} \tag{IV-12}$$

so

$$\Gamma\left(1-\left(\frac{u+v}{2}\right)-k\right) = \frac{\Gamma\left(1-\left(\frac{u+v}{2}\right)\right)(-1)^k}{\left[\frac{v+u}{2}\right]_k}\ . \tag{IV-13}$$

Note also that

$$\exp\left(-j\pi\frac{n}{2}\right) = (j)^{-n} \tag{IV-14}$$

Hence, from (IV-10), we find that

$$I^{(3)} = \left(\frac{a}{2}\right)^{v} \sum_{k=0}^{\infty} \frac{\left(\frac{a}{2}\right)^{2k}}{k!\underbrace{\Gamma(v+k+1)}_{\Gamma(v+1)[v+1]_k}} \cdot \frac{1\pi\,1^{-(2k+v+u)}}{\Gamma\left(1-\frac{u+v}{2}\right)} \frac{\left[\frac{v+u}{2}\right]_k}{q^{2k+v+u}} \tag{IV-15}$$

Since

$$\Gamma(\alpha+n) = \Gamma(\alpha)\,(\alpha)_n \tag{IV-16}$$

we have

$$\Gamma(v+k+1) = \Gamma(v+1)[v+1]_k \tag{IV-17}$$

and since

$$i^{-2k} = (-1)^{-k} = (-1)^{k} \tag{IV-18}$$

we have

$$i^{-2k}\left(\frac{a}{2q}\right)^{2k} = \left(\frac{-a^2}{4q^2}\right)^{k} \tag{IV-19}$$

Now using the identity

$$\sum_{k=0}^{\infty} \frac{\left[\frac{v+u}{2}\right]_k \left(\frac{-a^2}{4q^2}\right)^{k}}{k![v+1]_k} \equiv {}_1F_1\left[\frac{v+u}{2}\,,\ v+1\ ;\ \frac{-a^2}{4q^2}\right] \tag{IV-20}$$

$$\int_{c'_+} z^{u-1} J_\nu(az)\, e^{-q^2z^2} dz = \frac{\pi\, i^{1-\nu-u} \left(\frac{a}{2q}\right)^\nu}{\Gamma(\nu+1)\, \Gamma\left(1-\frac{u+\nu}{2}\right) q^u} \cdot {}_1F_1\left[\frac{\nu+u}{2}; \nu+1; \frac{-a^2}{4q^2}\right] \qquad \text{(IV-21)}$$

Now consider

$$I^{(4)} = \int_{c'_+} z^u\, e^{\left[\pm izb_0 - c^2z^2\right]} dz \qquad \text{(IV-22)}$$

now

$$e^{\pm izb_0} = \cos b_0z \pm i \sin b_0z \qquad \text{(IV-23)}$$

and

$$J_{1/2}(x) = \left(\frac{2}{\pi x}\right)^{1/2} \sin x \quad , \quad J_{-1/2}(x) = \left(\frac{2}{\pi x}\right)^{1/2} \cos x \qquad \text{(IV-24)}$$

so

$$e^{\pm ib_0z} = \left(\frac{\pi b_0 z}{2}\right)^{1/2} \left\{J_{-1/2}(b_0z) \pm i\, J_{1/2}(b_0z)\right\} \qquad \text{(IV-25)}$$

Hence, using the above in (IV-22) yields

$$I^{(4)} = \int_{c'_+} z^{u+1/2} \quad e^{-c^2z^2} \sqrt{\frac{\pi b_0}{2}}\, J_{-1/2}(b_0z)\, dz$$

$$\pm i \int_{c'_+} z^{u+1/2}\, e^{-c^2z^2} \sqrt{\frac{\pi b_0}{2}}\, J_{1/2}(b_0z)\, dz \qquad \text{(IV-26)}$$

so

$$I^{(4)} = \sqrt{\frac{\pi b_0}{2}}\ \frac{\pi\, i^{1+1/2-u-3/2}\left(\frac{b_0}{2c}\right)^{-1/2}}{\Gamma\left(\frac{1}{2}\right)\Gamma\left(1-\frac{u+\frac{3}{2}-\frac{1}{2}}{2}\right)c^{u+3/2}}\ {}_1F_1\left[\frac{u+1}{2}\ ;\ \frac{1}{2}\ ;\ \frac{-b_0^2}{2c^2}\right]$$

$$\pm\sqrt{\frac{\pi b_0}{2}}\ (1)\ \frac{\pi\, i^{1-1/2-u-3/2}\left(\frac{b_0}{2c}\right)^{1/2}}{\Gamma\left(\frac{3}{2}\right)\Gamma\left(1-\frac{u+\frac{3}{2}+\frac{1}{2}}{2}\right)c^{u+3/2}}\ {}_1F_1\left[\frac{u+2}{2}\ ;\ \frac{3}{2}\ ;\ \frac{-b_0^2}{4c^2}\right] \qquad \text{(IV-27)}$$

Hence, we finally obtain

$$\int_{c_+'} z^u\, e^{\pm 1 z b_0 - c^2 z^2}\, dz = \frac{\pi 1^{-u}}{c^{u+1}}\left\{\frac{{}_1F_1\left[\frac{u+1}{2}, \frac{1}{2}, \frac{-b_0^2}{4c^2}\right]}{\Gamma\left(\frac{1-u}{2}\right)} \pm \frac{b_0}{c}\,\frac{{}_1F_1\left[\frac{u+2}{2}; \frac{3}{2}; \frac{-b_0^2}{4c^2}\right]}{\Gamma\left(-\frac{u}{2}\right)}\right\} \qquad \text{(IV-28)}$$

$$|\arg c| < \pi/4$$

REFERENCES

1. D. Middleton, "Some General Results in the Theory of Noise Through Nonlinear Devices," Quarterly of Applied Mathematics, Vol. 5, January 1948, pp. 445-448.

2. R. J. Helgeson, "PI-PSP BER Degradation due to PI Baseband Output Limiting Amplifier," TRW IOC #SCTE-50-79-491/RJH, September 5, 1979.

Axiomatix

9841 Airport Boulevard • Suite 912 • Los Angeles, California 90045 • Phone (213) 641 8600

TECHNICAL MEMORANDUM NO. M8105-1

TO: Bill Teasdale DATE: May 11, 1981

FROM: Jim Dodds Copies: NAS 9-16067 "B" Distribution

SUBJECT: Degradation Due To Dither

1.0 INTRODUCTION

In order to reduce the effects of stiction in the Ku-band deployed assembly and the resultant limit cycling, dither is being introduced. This dither is an autonomous sine wave, located at a frequency sufficiently removed from the mechanical assembly resonance to preclude excitation, which keeps the antenna in virtually continuous motion. An heuristic description of dither is given in [1].

Not only must a possible resonance excitation be considered, but the dither frequency cannot be too high or low. At very high frequencies, the mechanical assembly cannot repond and stiction is not affected. At low frequencies, the mechanical assembly excursion is excessive and introduces pointing errors. Hughes has picked a dither frequency of 17 Hz, which does not fall close to any known mechanical resonance. In the following paragraphs, we derive the mechanical motion due to dither and the resultant AM on the sum and difference channel. It is shown that worst-case AM on the sum channel, within the 3 dB beamwidth, is about 0.4 dB; AM on the sum-plus-difference channel is about 5 dB.

2.0 DERIVATION OF ANTENNA RESPONSE

The two axes of the deployed assembly antenna are excited by a 17 Hz sine wave at sufficient current to produce the equivalent of two foot-pounds of torque. The response of the antenna can be derived from the angular equivalent of $F = MA$; $L = I\ddot{\theta}$. The quantity L is torque, equivalent to force, I is the moment of inertia, equivalent to mass, and $\ddot{\theta}$ is angular acceleration. Values of the parameters follow.

$$L = 2 \cos \omega t \quad \text{(foot-pounds)}$$

$$\omega = 2\pi \times 17 \quad \text{(radians)}$$

$$I_\alpha = 0.4 \quad \text{(slug-feet}^2\text{)}$$

$$I_\beta = 0.62 \quad \text{(slug-feet}^2\text{)}$$

The angular excursion, θ, is given by the double integral of $\ddot{\theta}$, as shown below:

$$\theta = -\frac{2L}{\omega^2}\frac{\cos \omega t}{I} = -\frac{1}{(34\pi)^2} \times \frac{2 \cos 34\pi}{I} \quad .$$

The peak-to-peak excursion is

$$\theta = \frac{4}{(34\pi)^2} \times \frac{1}{I}$$

Thus, $\theta_\alpha = 0.000876$ radians, or 0 0502°, and $\theta_\beta = 0.000565$ radians, or 0.0324° The vector sum of these two gives a worst-case peak-to-peak angular excursion of 0.06°. The vector sum is not an unrealistic quantity since the two dither signals are presumably being derived from the same source, and the resultant motion is probably close to being in phase.

3.0 SUM CHANNEL DEGRADATION

In this section, we derive the sum channel degradation based on worst-case 0.060° peak-to-peak antenna motion due to dither. These calculations are based on the approximation to the antenna main lobe pattern given below

$$G(\theta) = 20 \log \frac{\sin k\theta}{k\theta} \text{ , dB}$$

Taking a nominal 3 dB beamwidth of 1.6°, we can solve $20 \log \frac{\sin 0.8k}{0.8k} = 3$ to find $k = 1.74$, with θ in degrees and the $\sin(\cdot)$ function in radians. Now the peak-to-peak gain variation can be computed

from

$$\Delta dB = 20 \log \left[\frac{\sin 1.74\,\theta}{1.74\,\theta} \right] - 20 \log \left[\frac{\sin 1.74\,(\theta - 0.06)}{1.74(\theta - 0.06)} \right] .$$

This is plotted in Figure 1. The points plotted, which we calculated in 0.06° increments, appear to fall on a straight line. Since the computations were done on a calculator with built-in linear regression, it was a simple matter to compute the best straight line fit to the points in the region of interest, 0.06° to 0.80°. In fact, the points are very well correlated to a straight line, with $\rho = 0.999$. The equation is

$$\Delta dB = 0.594\theta - 0\ 030.$$

If we want to maintain the total pointing loss less than 0.3 dB, the maximum allowable θ from the $(\sin x)/x$ approximation is $\theta = 0.26°$ minus one-half the dither amplitude, or 0.23°. That is, the maximum steady state pointing error must be less than 0.23° to maintain the required 0.3 dB maximum loss.

4.0 DIFFERENCE CHANNEL DEGRADATION

The AM on the difference channel can be estimated using the autotrack scale factor and the worst-case antenna motion of 0.060°. The scale factor is defined as

$$K_m = \frac{\Delta G_\Delta}{\Delta\theta} \times \frac{\theta_3}{G_\Sigma}$$

Representative parameters taken from ADL test data are given below:

$K_m = 0.5$
$\Delta\theta = 0.060$, from prior calculation
$\theta_3 = 1.6$, the 3 dB beamwidth
$G_\Sigma = 79.4$, the antenna gain (38 dB) in volts/volt

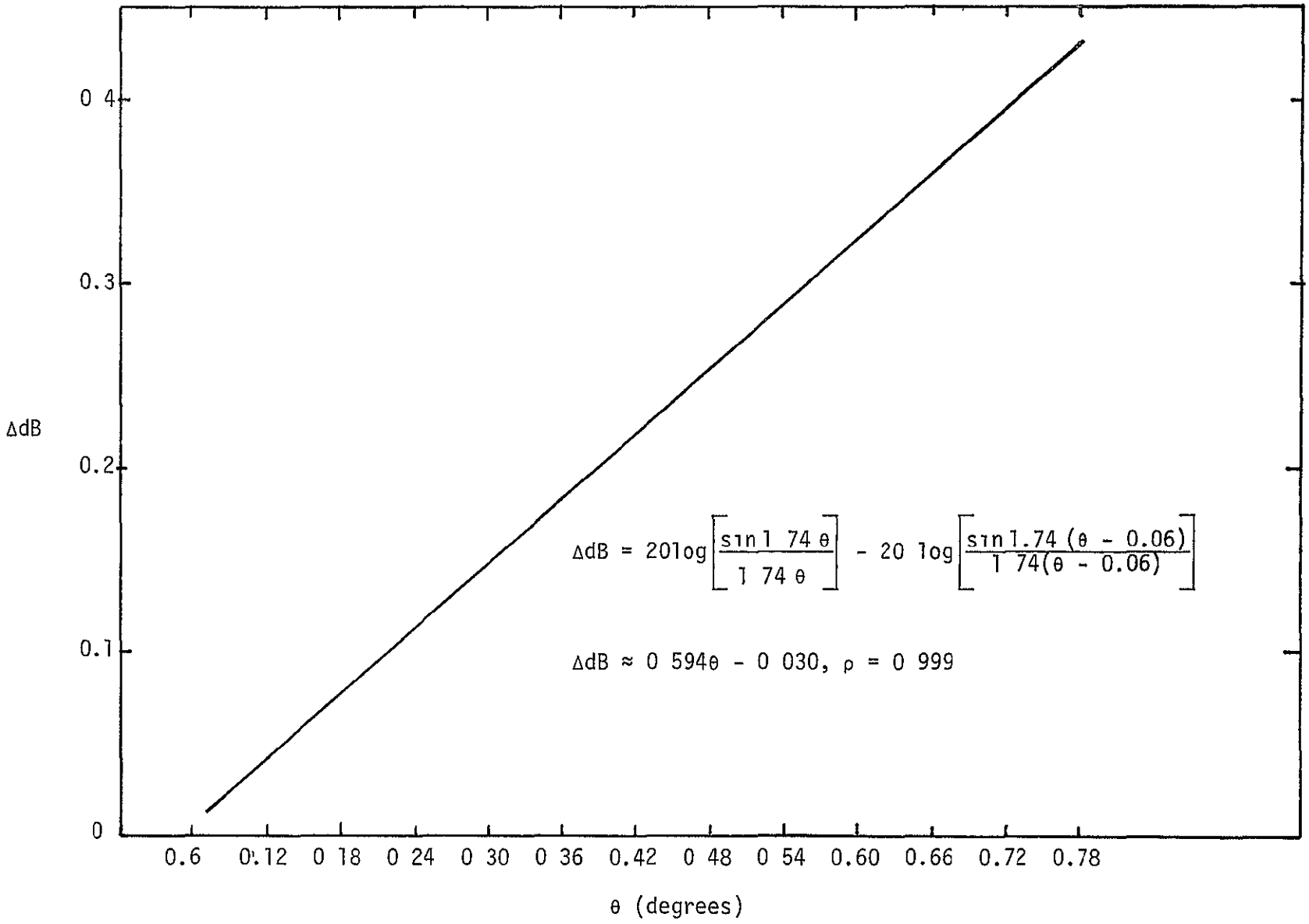

Figure 1 Sum Channel AM due to Dither versus Angle Off Boresight

ΔG_Δ is the difference in Δ channel gain, $G_2 - G_1$, in volts/volt. Using these values, we find that $G_2 - G_1 = 1.49$ volts/volt. In order to convert this to decibels, we need a reference value. From the test data, the difference channel gain at the point of steepest slope appears to be about 6 dB, or 2 volts/volt. Thus, $G_2 = 2 + 1.49 = 3.49$, or 10.86 dB. The AM near boresight on the difference channel is then $10.86 - 6 = 4.86$ dB.

5.0 CONCLUSION

The 17 Hz AM on both channels is insufficient to degrade tracking or communications performance significantly since the angle-tracking filter is so narrow and the 17 Hz is well below the data frequency. However, a minor improvement in steady state angle-track accuracy is required to maintain the 0.3 dB allowable pointing error with dither present.

Axiomatix

9841 Airport Boulevard • Suite 912 • Los Angeles, California 90045 • Phone (213) 641-8600

TECHNICAL MEMORANDUM NO. M8302-1

TO: J. Dodds DATE: February 16, 1983

FROM: R. Iwasaki FILE: 16067"A" Distribution

SUBJECT: Potential Ku-Band Sidelobe Reduction Recommendation

- -

During the recent Ku-band meeting at Hughes, sidelobe acquisitions by both the radar and communication systems were major problems which required many modifications to circumvent limitations in performance. The relatively high (-20 dB) sidelobes are an antenna characteristic that Axiomatix believes may be reduced by relatively simple means which may or may not affect the program schedule, but should at least be brought to the attention of Hughes management as a possible alternative to consider for future STS missions.

First, it is to be emphasized that no major modification is being considered. A simple test is proposed during a currently scheduled antenna pattern measurement that will quickly determine whether or not the change is even feasible. Only one additional pattern cut in the plane of the highest sidelobe is required, which should not impact the tight schedule.

This modification is the second item recommended during Axiomatix's antenna study. The primary fix--the RF fence to minimize mutual-coupling effects in the monopulse feed--reduced the sidelobes from 13-14 dB to the present 20-dB level. At the time, this improvement was considered acceptable but recent experimental tests indicate that a wider acquisition dynamic range is desirable. Although antenna design is still somewhat of an art and therefore unpredictable, based on our antenna design experience which corrected the earlier unacceptable sidelobe problem, Axiomatix feels that an improvement to -22 dB is not unreasonable. This would increase the measured acquisition dynamic range from 17 to 19 dB, thereby eliminating the acquisition threshold setting problem that will exist for missions beyond STS-7.

Axiomatix proposes a test in which a wedge-shaped ridge of heavy-duty aluminum foil is placed along both sides of the feed-support structure, as shown in Figure 1, to minimize the antenna aperture blockage effects which now appear to be the dominant causes of the high sidelobe levels. The rationale for this modification is to reduce the deleterious asymmetrical obstruction of the aperture by allowing some radiation to propagate past the feed, thereby allowing more destructive interference to occur with radiation impinging on the opposite side of the antenna.

The wedge-shaped ridge can be pictured as having polarizing characteristics similar to those of the septum which allows electric fields that are oriented perpendicular to the ridge to be transmitted, whereas the parallel electric fields see an electrical short and are therefore reflected. This behavior is valid even for structures larger than the wavelengths of the electromagnetic radiation and therefore does not depend on any diffraction arguments. The linear polarization, consisting of both RHCP and LHCP components, will then contribute some offsetting aperture illumination versus none with the existing configuration.

Incidentally, this technique is used in radome structural support designs to minimize blockage effects of metallic ribs.

The exact taper of the wedge is somewhat arbitrary because the stowage envelope of the antenna must accommodate the modification but, as a general rule, the longer the taper, the better the performance. If a metallized fiberglass shell is used to shape the wedge, this structure would also serve as a thermal shield which will help stabilize the thermal environment surrounding the sensitive RF mixers, thus reducing the need for the electrical heater.

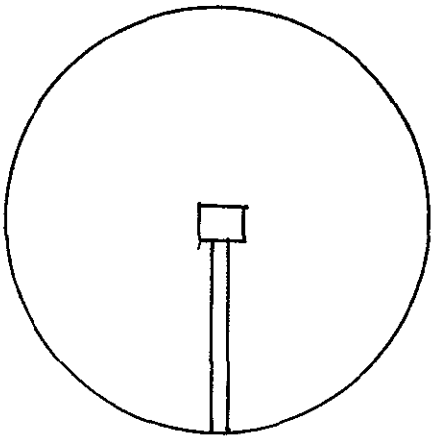

Frontal View of the
Parabolic Antenna

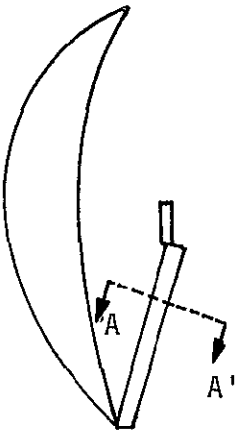

Side View of the
Parabolic Antenna

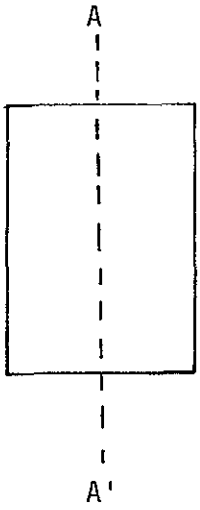

Cross Section of the
Feed Support

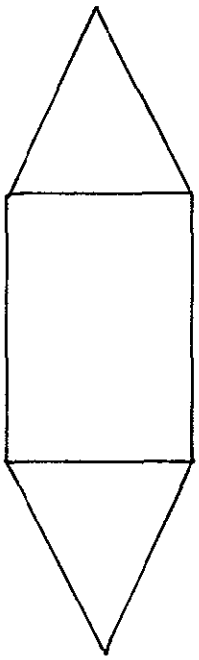

Modified Wedge-Shaped Cross Section
of the Feed Support

Figure 1 The Wedge-Shaped Blockage-Minimization Technique for Sidelobe Reduction

7.0 S-BAND SYSTEM INVESTIGATIONS

Task 2 of Exhibit B was oriented toward the S-band network communication equipment which had already been through the major development stages before this contract effort started, but on-orbit tests with the TDRSS have taken place only in the last few months due to the delayed launch of the TDRS and the initial problems of the satellite achieving synchronous orbit. Therefore, analyses of the S-band network overall system performance were limited to acquisition times with the wide data filter and data off as well as with Shuttle G/T and EIRP calculations. These analyses are presented in this section. It should be pointed out that additional analyses related to problems which developed in ESTL and KSC tests are documented as part of Exhibit A, Task 15, which is presented in Section 4.

Analysis of the Shuttle S-band acquisition times with the wide data filter and data off shows that the acquisition threshold is approximately C/N_0 = 50.5 dB-Hz.

A Shuttle S-band G/T of 29 dB and an EIRP of 15.6 dBW was calculated, as documented in Technical Memorandum No. M8206-3, "Shuttle G/T and EIRP Calculations," dated June 21, 1983. This memorandum was generated in order to eliminate any possible differences of opinion regarding G/T and EIRP.

S-BAND SHUTTLE ACQUISITION TIMES

WITH THE WIDE DATA FILTER AND DATA OFF

Contract No. NAS 9-16067

Prepared for

NASA Lyndon B. Johnson Space Center
Houston, Texas 77058

Prepared by

Axiomatix
9841 Airport Blvd , Suite 912
Los Angeles, California 90045

July 9, 1980

TO: Gaylord Huth

cc: Q. Tu
E. Dodd
B. Batson
B. Teasdale

FROM: J. K. Holmes
641-8600

DATE: July 9, 1980

SUBJECT: S-Band Shuttle Acquisition Times With The Wide Data Filter And Data Off

SUMMARY:

The S-Band Shuttle PN code despreader mean acquisition time is estimated for the case the data is turned off and the high data rate bandpass filters are employed in the despreader.

Based on the available data, acquisition should occur at and above C/No = 50.5 dB-Hz.

ANALYSIS

The intent of this memo is to estimate the mean acquisition time of the Shuttle S-Band and PN code despreader with the high data rate filter switched in and the input data turned off. The only available acquisition time data, however, is for the high data rate mode with the high data rate signal being received Thus to estimate the desired acquisition time we must compute the filtering losses that occur in the pre-detection filters of figure 1 for the case of the high data rate signal in high data rate pre-detection bandpass filters.

After the filtering losses are computed, it is then a simple matter to adjust the measured acquisition times from reference 1 by the filtering loss to yield to the desired results.

The S-Band Shuttle forward link PN code length is 2047 chips and has a rate of 11.232 mega chips/sec. The data is Manchester encoded so that if we assume a random data stream with the probability of a data one and a data zero being 1/2, independent of the previous bits, then the power spectral density is given by

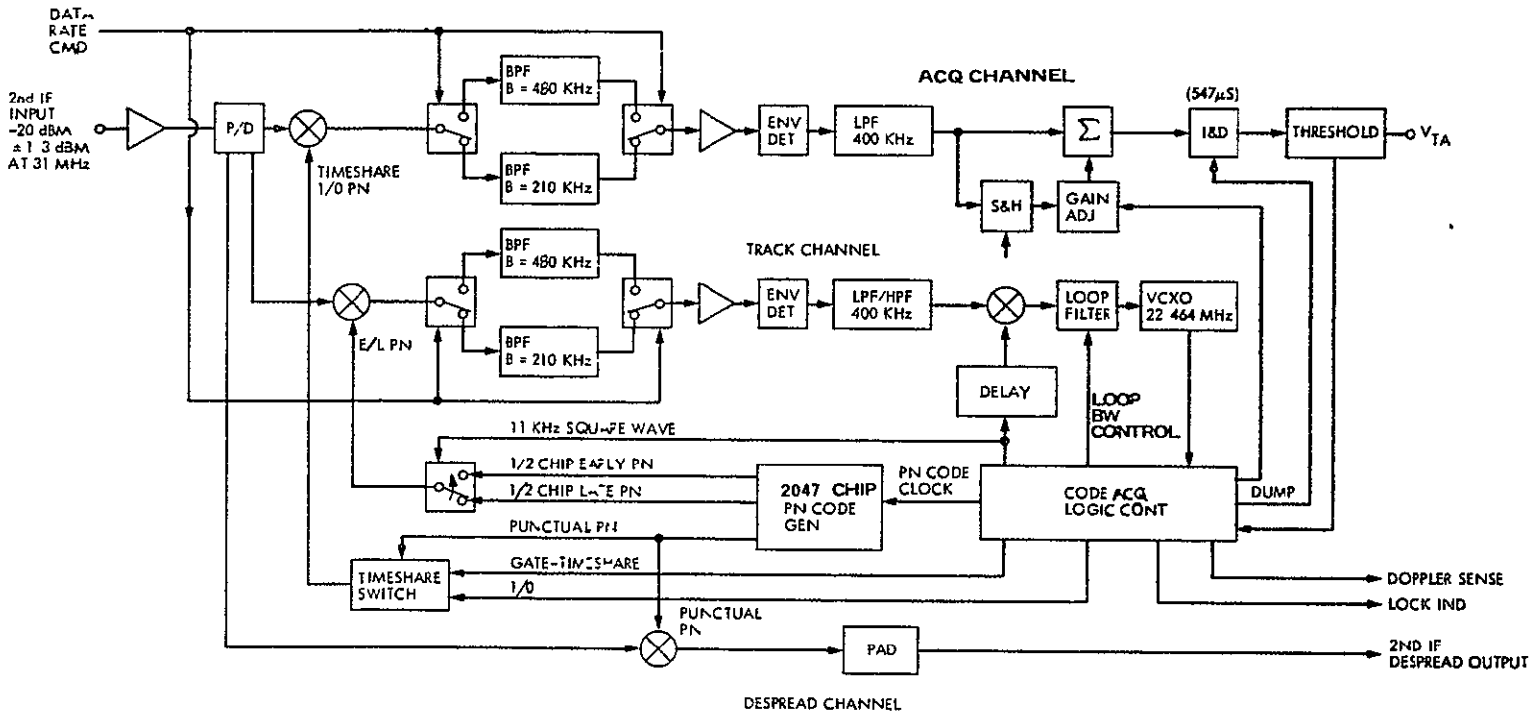

Figure 1 *S*-Band Spread Spectrum Processor Functional Diagram

$$S(f) = (PT)\frac{\sin^4(\pi fT/2)}{(\pi fT/2)^2} \qquad (1)$$

where P is the Manchester data stream power, and T is the Manchester symbol duration.

For zero carrier and code doppler we have that the filtering loss in the bandpass pre-detection filter (assumed to be ideal) is given by

$$L = \int_{\frac{-BW}{2}}^{\frac{BW}{2}} PT\,\frac{\sin^4(\pi fT/2)}{(\pi fT/2)}\,df$$

where BW is the RF bandwidth which is 480 KHZ for the high data rate mode. Numerically evaluating the integral yields L=0 72=-1.43 dB. We conclude that with zero doppler and no data the despreader sensitivity increases by 1.43 dB. Because of the inherent bias in the code loop during acquisition the S-Band Shuttle despreader biased the code loop frequency to -200 chips per second so that a true code doppler of +400,0, and -400 chips per second respectively appears to the acquisition circuitry and the code loop as +600, +200, and -200 chips per second, respectively.

Now at a code doppler of 400 cps, corresponding to about 60 KHZ carrier doppler, the filtering loss is given by

$$L = \int_{\frac{-BW}{2}+60\ KHZ}^{\frac{BW}{2}+60\ KHZ} PT\,\frac{\sin^4(\pi fT/2)}{(\pi fT/2)}\,df$$

which when evaluated numerically is given by L = -1.52 dB

By replotting figure 9 of reference 1 (which is the average code acquisition time versus C/No (dB-Hz).) with the filtering loss subtracted from the abscissa for each acquisition time we obtain figure 2 which is our desired result. Notice from figure 2 that threshold appears to be around 50.5 dB-Hz.

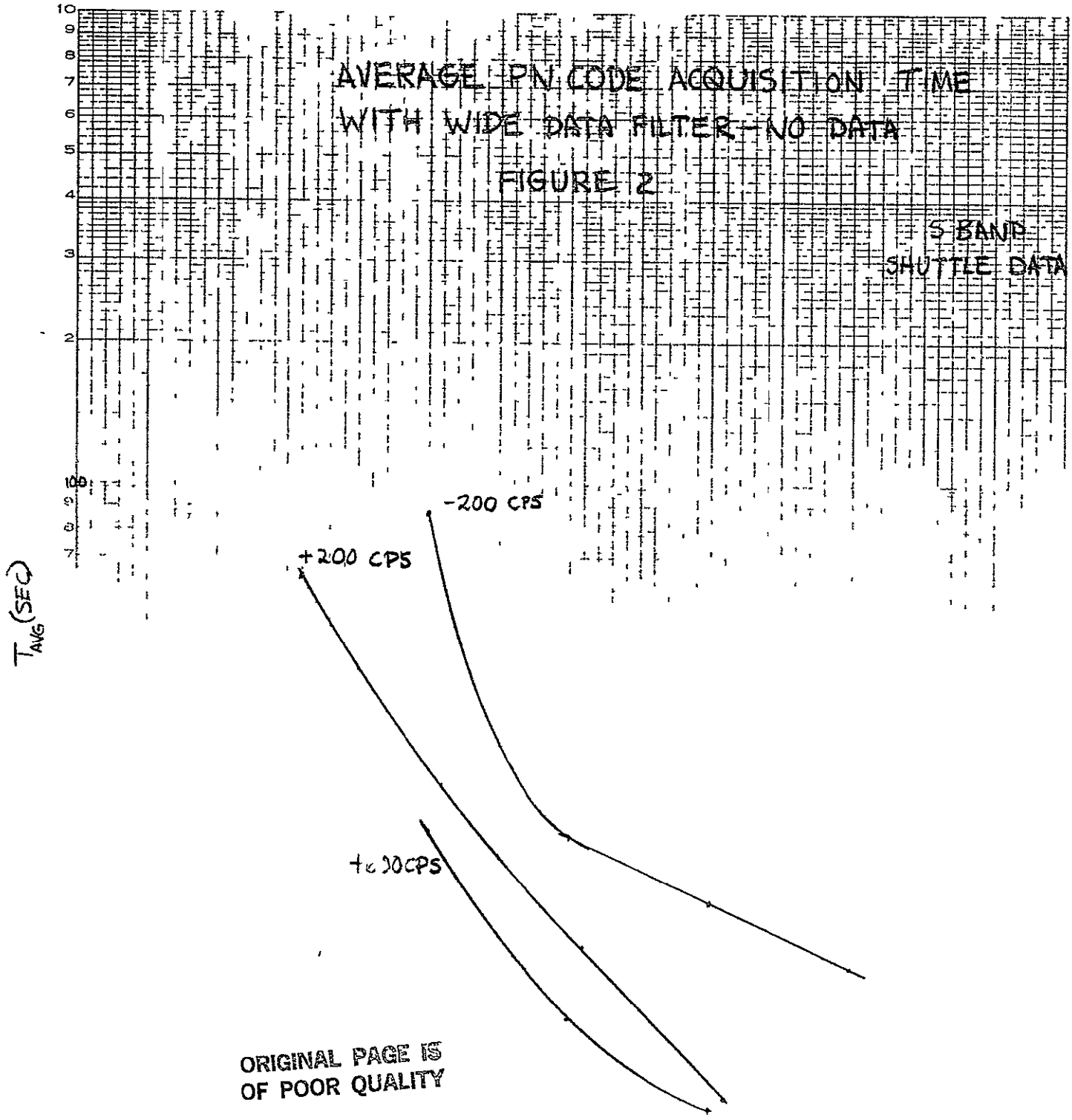

References

(1) J. K. Holmes, "Predicted Mean SSP Code Acquisition Times with the New Algorithm" TRW IOC SCTE-50-76-251/JKH, July 21, 1976.

(2) W.K. Alem, G.K. Huth, J.K. Holmes, and S. Udalov "Spread Spectrum Acquisition and Tracking Performance for Shuttle Communication Links," IEEE Transactions on Communications, Part I, Nov. 1978.

Axiomatix

9841 Airport Boulevard • Suite 912 • Los Angeles, California 90045 • Phone (213) 641-8600

TECHNICAL MEMORANDUM NO. M8206-3

TO: G. Huth DATE: June 21, 1982

FROM: P. Nilsen COPIES: J. Johnson
M. Zealon

SUBJECT: Shuttle G/T and EIRP Calculations

On June 17, 1982, I met with Mike Zealon, Glen Yates and Dick Davis to review the RI methodology for Shuttle S-band G/T and EIRP calculations. Also, we reviewed the RI calculation of RF feedline insertion loss. The RI and Axiomatix methodologies for these calculations were essentially the same, with the minor exception that RI did not include contributions to effective noise temperature beyond the preamp. The formula used by Axiomatix for effective noise temperature, namely,

$$T_{eff} = T_A + (L_1 - 1)T_0 + (NF_{PA} - 1)T_0L_1 + \frac{(L_2 - 1)T_0L_1}{G_{PA}} + \frac{(NF_{XPDR} - 1)T_0L_1L_2}{G_{PA}}$$

where

T_A = antenna temperature (75°K)

L_1 = loss between antenna and preamp (4.34 dB)

L_2 = loss between preamp and transponder (0.5 dB)

NF_{PA} = preamp noise figure (2.6 dB)

G_{PA} = preamp gain (20 dB)

NF_{XPDR} = transponder noise figure (7 dB)

did include the temperature contribution for the cable between the preamp and the transponder as well as the transponder's contribution.

However, we see that, after making these calculations with and without these last two terms, the difference in G/T is only approximately 0.15 dB, with the more precise result being G/T = 31 - 2 = 29 dB for 80% coverage.

The EIRP calculation is given by

$$EIRP = P_T + G_{ANT} - L_T$$

where P_T is the transmitter output power (20 dBW), G_{ANT} is the antenna gain (80%)(2 dB), and L_T is the transmit circuit loss (6.4 dB).

The calculated EIRP is 15.6 dBW for 80% coverage. It should be noted that, in both the EIRP and G/T calculations, the transmission line loss due to VSWR was included in circuit loss values. The VSWR loss was found according to the attached nomograph.

VSWR Nomograph #2

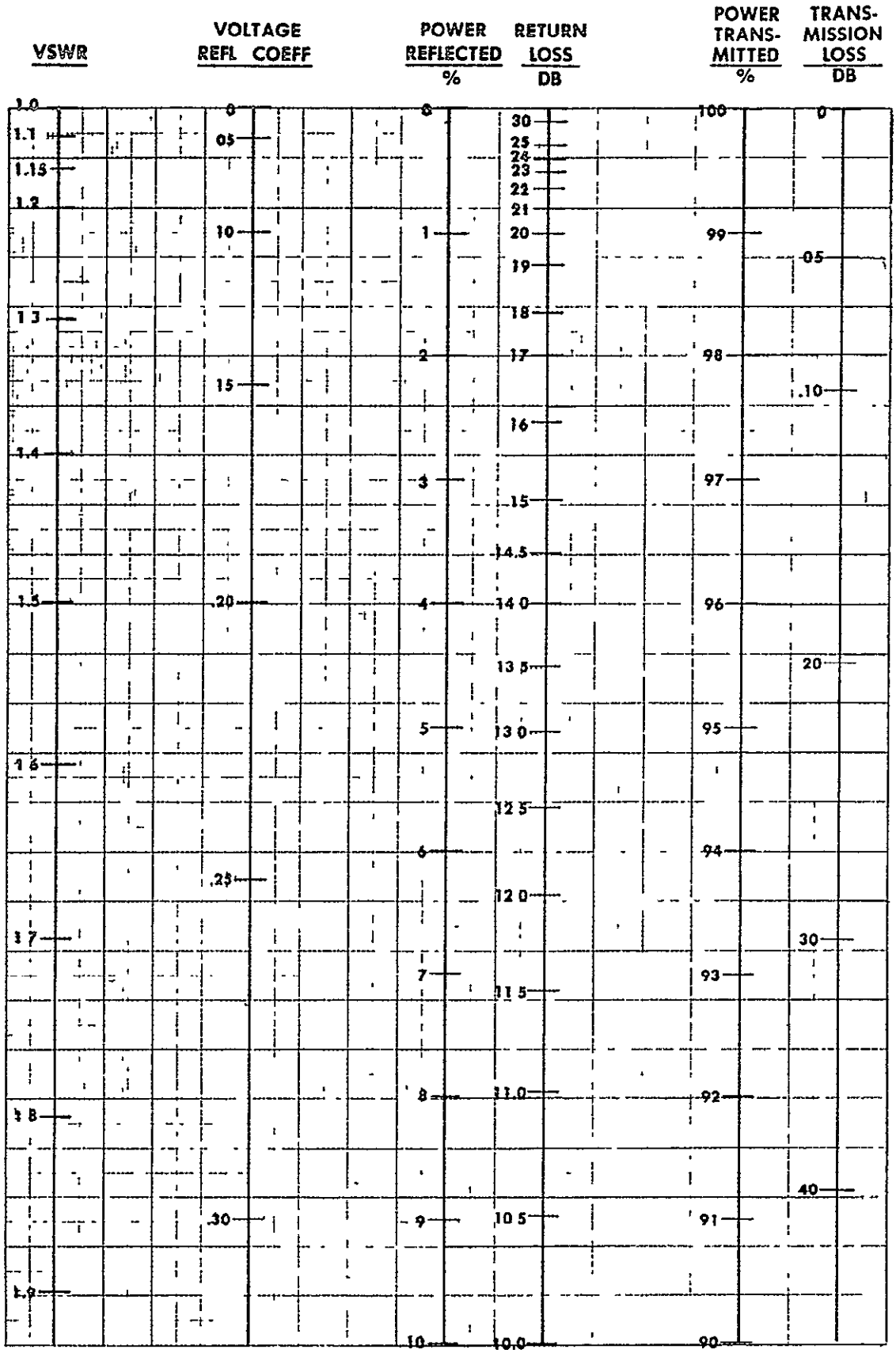

8.0 ORBITER ANTENNA STUDIES AND INVESTIGATIONS

Task 8, Orbiter Antenna Patterns, was composed of two separate areas of investigation. First, were analyses to improve the performance of the S-band quad antennas. Axiomatix was heavily involved in this effort and provided many significant contributions to the improved coverage performance. The second area investigated under this task was to develop techniques by which to determine the actual Orbiter antenna gain and coverage from on-orbit measurements. After an initial investigation, the results were presented in Axiomatix Report No. R8009-1, "The Concept of Maximum-Entropy Filtering and Its Feasibility as a Candidate for Shuttle Antenna-Gain Processing," dated September 5, 1980. Following the review of this report by NASA, Axiomatix was directed on June 1, 1981 to terminate further analysis in this area as there seemed to be little use for on-orbit measurements derived from several ground stations which were calibrated differently.

In order to investigate methods by which the S-and quad antennas would meet the relaxed gain-coverage requirement of 4 dBci over half the sphere, Axiomatix extended many of the concepts used in the switched two-beam quad antenna, taking advantage of the Rockwell-developed basic hardware. The outcome of this study has been the evolution of a new generation of variable-gain, multiple-switched-beam antennas, the principles of which can be applied to the improved Shuttle Orbiter S-band quad antennas.

The switched two-beam quad antenna developed by Rockwell was an improvement over the earlier single-beam quad antenna built by Watkins-Johnson but, due to over-optimistic computer analysis projections of the antenna patterns, the actual performance results were disappointing. The primary limitation of the gain peformance was the selection of only two elements and two beam positions, the minimum required for switched-beam operation. Using the same type of hardware configured in a slightly different manner, Axiomatix developed a two-dimensional cross array that could be electromechanically scanned in both the roll and pitch planes as $2^M x 2^N$ discrete-beam positions, where M and N are the number of double-pole/double-throw electromechanically latching switches in each plane. The advantages of using this type of switch rather than electronic-phase shifters are: (1) high power-handling capabilities, (2) low insertion losses, (3) absence of electrical "holding" power, and (4) the binary nature of the double-throw switch which can readily be converted to a binary code for a specific beam position.

As part of Axiomatix participation in the development of S-band quad antennas, Axiomatix personnel attended the design reviews and technical exchange meetings. In Axiomatix Report No. R8007-2, "S-Band Quad Antenna PDR Evaluation," dated July 23, 1980, recommendations are made to improve the gain-coverage performance since the two-beam approach did not achieve the specification. This report attempted to illuminate the dilemma by suggesting, first, some concave-lens design concepts for the existing randome which would broaden the dipole beams in the array plane, an essential feature to correct the present two-beam coverage deficiencies. If the proposed three-beam scheme was to be used instead of the two-beam design, Axiomatix recommended that a switched four-beam configuration be seriously considered as an alternative system since the hardware and software would be extensively modified for the three-beam scheme. Finally, a novel RF fence design usign the total-reflection concept of critical angle was outlined, which should substantially reduce the amount of mutual coupling and deleterious interaction effects between the two dipole-array cavities for all switched multiple-beam configurations.

Further investigations of the four-beam configuration to simplify the design are presented in Axiomatix Report No. R8106-4, "Simplified Orbiter S-Band Quad Antenna Planar Array Candidate Configurations," dated June 25, 1981. Also, improvements to the lens concept required to broaden the beam of the two-beam design are presented in Axiomatix Report No. R8112-1, "A Protruding Wedge-Shaped Dipole Element Modification For The Orbiter S-Band Quad Antennas," dated December 9, 1981. Finally, the concept of the two-dimensional cross array that would be electromechanically scanned in both the roll and pitch planes at $2^M x 2^N$ discrete-beam positions is developed in Axiomatix Report No. R8112-4, "A Large Switched-Beam Planar Array," dated December 15, 1981, and Axiomatix Report No. R8209-3, "A Variable-Gain Multiple-Switched-Beam-Antenna Configuration," dated September 22, 1982. To implement a variable-gain multiple-switched-beam array, the beam-switching logic must be simple. This switching logic is presented in Axiomatix Technical Memorandum No. M8209-4, "Binary Code Designation of Multiple-Switched-Beam Positions," dated September 30, 1982, as well as in Axiomatix Technical Memorandum No. M8209-5, "Simplification of Antenna Beam-Switching Logic," dated September 30, 1982.

THE CONCEPT OF MAXIMUM ENTROPY FILTERING AND ITS FEASIBILITY AS A CANDIDATE FOR SHUTTLE ANTENNA GAIN PROCESSING

Contract No. NAS 9-16067

Interim Report

Prepared for

Lyndon B Johnson Space Center
Houston, Texas 77058

Prepared by

V. K. Murthy

With Contributions By:

A. Polydoros
C. L. Weber
P. W. Nilsen

Axiomatix
9841 Airport Blvd., Suite 912
Los Angeles, California 90045

Axiomatix Report No. R8009-1
September 5, 1980

1.0 INTRODUCTION

Maximum entropy filtering has been suggested by John Tranter as a candidate approach for filtering the raw antenna gain measurements made during early Shuttle flights. The motivation for this suggestions is the fact that this method has been shown to yield power spectral density (PSD) estimates which have higher resolution than traditional periodogram (Wiener) or weighted periodogram estimators. This advantage is especially true when the measured data is sparse.

The following discussion offers an explanation of maximum entropy filtering and presents several examples. Most important, an explanation of why this technique is not suited to the determination of the Shuttle antenna gain pattern is presented

2.0 DISCUSSION

The expression "maximum entropy" is a misnomer in the sense that one generally maximizes the information, not entropy. However, this expression is used in connection with the channel capacity of a communication system where maximum entropy corresponds to maximum information transmission rate. In statistics and probability theory, the entropy H(X) of a random variable X with probability density function (PDF) f(x) is defined by

$$H(X) = -\int_{-\infty}^{\infty} f(x)\, \ell nf(x)\, dx \qquad (1)$$

The entropy H(X) is closely related to the disorder or uncertainty associated with making a realization X. For that reason, maximizing the entropy is a method for finding the distributions that represent high uncertainty or, equivalently, a state of high ignorance Thus, given a set of constraints, the maximum entropy method provides a candidate distribution which confirms the constraints without assuming anything more.

For example, let the constraints be

$$\int_{0}^{\infty} x\, f(x)\, dx = E(X) = m_0 \quad X \geq 0 \qquad (2)$$

Then the distribution that maximizes (1) subject to (2) is

$$f(x) = \frac{1}{m_0} e^{-x/m_0} \tag{3}$$

Notice that, since constraint (2) specifies m_0, the maximum entropy distribution contains no additional information and is therefore maximally random.

As another example, consider maximizing (1) subject to

$$\left.\begin{aligned} \int_{-\infty}^{\infty} x\, f(x)\, ds &= E(X) = m_0 \\ \int_{-\infty}^{\infty} (x - E(X))^2\, f(x)\, dx &= \sigma_X^2 = \sigma_0^2 \end{aligned}\right\} \tag{4}$$

In this case, the distribution that maximizes (1) subject to (4) is

$$f(x) = \frac{1}{\sqrt{2\pi}\,\sigma_0} \exp\left(-\frac{1}{2\sigma_0^2}(x-m_0)^2\right) \tag{5}$$

Notice that, since m_0 and σ_0 are specified by constraint (4), the maximum entropy distribution given by (5) for this case contains no further information on the underlying PDF of X and is thus maximally random.

Similarly, extending our concepts to a random process, it can be shown that the maximum entropy random process with constraints on only the first and second moments is a Gaussian process. Also, the entropy for a stationary Gaussian process may be shown to be given by

$$H = \frac{1}{\lambda_{\mathscr{D}}} \int_{\mathscr{D}} \log f(\lambda)\, d\lambda \tag{6}$$

where $\mathcal{D}$ is the domain in the frequency space and $\lambda_{\mathcal{D}}$ is the spectral measure of $\mathcal{D}$.

Let X(t) be the stationary Gaussian process in question, with zero mean and with covariance matrix of observations $X(t_1)$, $X(t_2)$,..., $X(t_n)$ sampled at times t_1, t_2,...,t_n given by

$$R_{ij} = E(X_i X_j) = R_{ji}^{t} = r_{i-j}$$

where, for brevity, we write $X(t_i) = X_i$, i=1,2,...,n and

$$r_k = \int_{-\pi}^{\pi} e^{j2\pi\lambda K} \underbrace{f(\lambda)}_{\substack{\text{Discrete} \\ \text{Time PSD}}} d\lambda \tag{7}$$

The maximal entropy spectral density estimate subject to the constraints

$$r_K = r_K^0 \quad , K = 1,2, \ldots ,n \tag{8}$$

is obtained by maximizing (6) subject to (8) and will turn out to be a rational function of $\{r_K^0\}$.

Thus, in general, the maximum entropy principle works if the constraints are practically noiseless or error-free and, if they must be estimated, they should be based on a large data base of observations corresponding to repeated cycles or replications The specification of the constraints could also be based on proven prior knowledge arising from past and cross-sectional experience.

We therefore resort to smoothing procedures for the antenna gain data. The unacceptability of the maximum entropy method of estimating the gain at missing points will be demonstrated for the one-dimensional case.

Assume that

$$f(x_i) = c_i \ , \ i=1,2,\ldots,n \tag{9}$$

$$f(x_i) \geq 0 \tag{10}$$

$$\sum_{i=1}^{N} f(x_i) = 1 \ , \ N > n \tag{11}$$

We will now estimate $f(x_j)$ at the missing points by using the maximum entropy principle, i.e., choose $f(x_j)$ such that

$$H(f) = - \sum_{i=1}^{N} f(x_i) \log f(x_i) \tag{12}$$

is maximized subject to (9), (10) and (11)

From (9), (10) and (11), it follows that it suffices to maximize

$$\tilde{H}(f) = - \sum_{i=n+1}^{N} f(x_i) \log f(x_i) \tag{13}$$

But maximization of (13) subject to (10) and (11) or, equivalently, (11') where

$$\sum_{i=n+1}^{N} f(x_i) = 1 - c \tag{11'}$$

where $c = c_1 + c_2 + .. + c_n$, is attained by

$$f(x_i) = \frac{1 - c}{N - n} \ , \ i=n+1,\ldots,N \tag{14}$$

i.e., uniform distribution for the missing points.

This solution, while mathematically correct, is totally unacceptable for the specific problem at hand since it does not take into account the smoothness properties of the gain function. Furthermore, it is easy to demonstrate by examples that, in most cases, the missing gain distribution between two measured points is not a uniform distribution.

In the next communication, we specifically address the problem of smoothing the gain data in the presence of noise, and establish the rationale, obtain acceptable procedures and develop algorithms for implementation.

3.0 CONCLUSIONS

The maximum entropy filtering technique is not suitable for processing the Shuttle antenna gain measurements. Therefore, it is recommended that no further investigation of this technique be undertaken.

Axiomatix recommends that a more "ad hoc" approach to processing the raw gain measurements be utilized An example of such a technique is the nearest neighbor interpolation to fill in missing data combined with a "pseudo-Kalman" filter for smoothing data from multiple passes and multiple stations. This is the approach which Axiomatix is now pursuing.

S-BAND QUAD ANTENNA PDR EVALUATION

By

Dr. Richard S. Iwasaki

Contract No. NAS 9-16067

Axiomatix Report No. R8007-2
July 23, 1980

S-BAND QUAD ANTENNA PDR EVALUATION

July 15-16, 1980

Dr. Richard S. Iwasaki

Axiomatix

1.0 INTRODUCTION

At the S-Band Antenna Preliminary Design Review (PDR) held at Rockwell/Missile Space Division in Anaheim on July 15-16, 1980, the main issue was the proposed change from the initial switched two-beam configuration to a switched three-beam configuration for the S-band quad antennas. The other major issue of note was the poor antenna patterns of the lower S-band quad antennas. Further work on these antennas cannot proceed until a firm decision is made whether or not to pursue this new approach because of the required alterations in the hardware and software of the system. The meeting concluded with a plan to resolve this issue within ten days after the pertinent system personnel are queried as to the ramifications of the changes.

The other aspects of the S-Band Antenna Program appear to be progressing satisfactorily except for some specification deviations which must be resolved by either waiver or additional engineering adjustments, such as the axial ratios of the quad antennas. However, in light of the major impact of a new three-beam configuration and the obvious inadequacy of the low quad antennas, these latter problems warrant immediate attention.

2.0 TECHNICAL SUMMARY OF THE PDR

From the data supplied during this PDR, it appears that the three-beam approach was analyzed within two weeks of the last technical exchange meeting held May 14, 1980. The implication is that the two-beam approach was deemed unsatisfactory very soon after the preliminary antenna pattern measurements were made and, since completed three-beam patterns were presented, that the decision has been tentatively made and the two-beam approach has been essentially abandoned.

The two-beam approach resulted in a 65% 4.0 dB spherical coverage, for the upper quad antenna (versus the coverage specification of 85%) and a modified two-beam approach which moved the aft beam forward to cover the

actual roll plane (by using a -66° instead of a -90° phase shift) gave a 64% 4.0 dB coverage. The lower quad gave a 35.1% 4.0 dB coverage, indicating serious measurement and/or test antenna design problems.

The corrective measures necessary to improve the two-beam 4.0 dB coverage include broadening the beam to redistribute the peak 6.5 to 7.0 dB gain more evenly over the specified coverage area. The technique attempted by Rockwell MSD was to place a "parasitic" ring on the radome to enhance generation of a third-order mode to put more radiative energy away from the axis. This parasitic ring was intended to function similar to the directional reradiators of the Yagi antenna, but the alternate phasing of the third-order mode greatly complicates the design. The modification did not produce the desired results and it appears that at this point an alternate concept (e.g. three beam) was seriously evaluated.

3.0 POSSIBLE ALTERNATIVE DESIGN MODIFICATIONS

Some possible approaches to broaden the two beams might be considered in the future if the three-beam scheme cannot be realized. One is using a concave-lens configuration on the radome. It was mentioned that Rockwell MSD has experimented with this concept earlier, but the concave surface was on the opposite side away from the dipole, which is not the ideal situation if it is assumed that the dipole radiates quasi-spherical waves and the radome surface is to be in intimate contact with the Thermal Protection System (TPS) tiles. Further, the argument of high cross-polarization levels for broader beams must be evaluated more closely if the beam is selectively broadened, primarily in the array plane where the beam is narrowed by the two-element array.

Another reason for using an inner radome aperture concave surface is the reduction of the cross polarization. The high dielectric constant (ε_r=4) radome behaves as a polarizer in the present dipole configuration,and therefore unequal magnitudes of orthogonal linear polarization (equivalently orthogonal circular polarization) are transmitted through the radome. The reflected components of polarization create the higher VSWR mismatch measurements, which also appear to exceed the desired performance specifications. Impedance matching to decrease the VSWR by design is difficult to achieve within the limited area of the aperture, but the concave inner radome surface will most probably decrease both the VSWR and the cross-polarization levels.

The reason for the selective polarization reflection is the optical principle of reflection at a dielectric interface or, in electromagnetic theory, impedance matching.

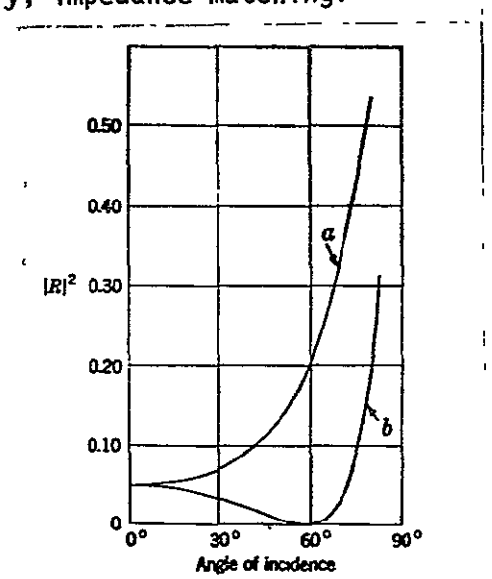

Fraction of incident power reflected from the surface of an infinite dielectric slab vs. angle of incidence: (a) electric vector perpendicular to the plane of incidence, (b) electric vector in the plane of incidence: n = 1.6.

Because of the quasi-spherical phase fronts radiating from the dipole element, the incidence angle varies from the central axis and selective polarization transmission occurs. The same phenomenon also occurs at the outer radome surface where it is in contact with the TPS tiles and should be considered in determining cross polarization effects.

The increased path lengths through the outer edges of the radome also distorts the quasi-spherical phase wave front which is the basis for array theory. In summary, the radome should be analyzed as a polarizing lens system.

By broadening the individual dipole pattern in the array direction, power redistribution can be achieved since the excess power in the peak gain (6.5 to 7.0 dB) is actually being selectively rearranged to reduce the pattern-multiplication factor in the array plane. Therefore, the beam broadening essentially tries to re-establish the symmetrical single-dipole pattern, but uses the two-element phased array to electronically tilt the resultant pattern in the desired directions by switching the appropriate phase shifts.

In order to reduce the gain and broaden the antenna coverage, a concave aperture interface is proposed. Snell's law, which bends the ray closer to the interface normal in a denser medium, is now manipulated to spread the energy outwards since more of the incident spherical wavefront energy is transmitted into the dielectric at divergent angles.

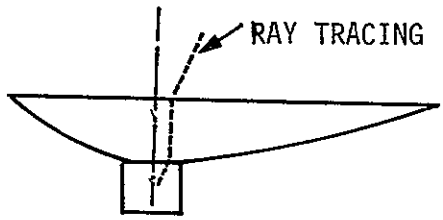

PRESENT PLANAR RADOME

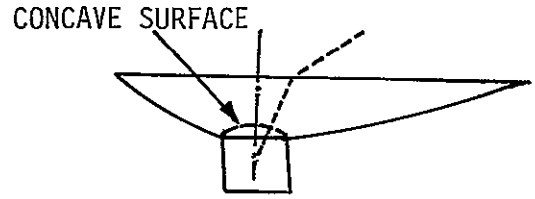

PROPOSED PLANO-CONCAVE RADOME

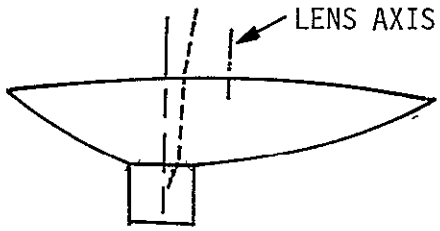

LOWER QUAD CONVEX OUTER SURFACE RADOME

The dielectric radome, presently polyimide E-glass, is machined such that the dielectric interface to the dipole antenna cavity is flush with the cavity aperture. The shape of this radome, since the aperture is indented to accommodate the radome, resembles a convex lens which focusses incident radiation. This effect is even more apparent when the dielectric constant of the dielectric material is higher than anticipated, as the case when the polyimide E-glass replaced the preliminary fiberglass material, especially in the case of the lower quad antenna where the outer radome surface is slightly curved. The net result of this configuration is a plano-convex lens which focusses radiation, or equivalently, increases the gain. This focussing effect of the convex radome surface is further enhanced by the quasi-spherical waves radiating from the dipole element which is located in close proximity to the radome. In order to compensate for this curvature, (if this convex lens shape is indeed found to contribute to the poor lower quad pattern since it is the only difference from the upper quad antenna), a concave inner radome surface will reduce the amount of focussing. Geometric ray

tracing can be useful for determining the overall lens effect. This technique can be extended to produce divergent beam broadening in the lower quad with increased curvature of the inner concave lens surface.

This beam broadening technique need not be symmetrical. In fact, the concave curvature can be tailored to the broadening of the beam in desirable directions. The advantage of this type of modification is that the existing quad antennas can be used and only the dielectric radome, which is readily replaced, is modified.

The lens effect of the radome slightly affects the effective location of the dipole element phase centers. The convex outer radome surface of the lower quad decreases the dipole spacing since the dipoles are not located on the longitudinal axis of the lens, which might contribute to the poor results. For the upper quad with the planar outer radome surface, this effect is less dramatic since, although the "depth" of the phase centers into the Orbiter varies, the dipole spacing remains constant, and the earlier analytical models are still valid.

4.0 RF FENCE DESIGN

Although mutual coupling between dipole elements is not obviously a major problem, it is axiomatic that it exists for adjacent radiators with a common radome. During the recent performance tests, the mutual coupling is indicated by the frequency-swept input return loss measurements where -10 dB was not uncommon. A desirable design goal then is to attempt to minimize this effect as much as possible, especially since the measured performance is unsatisfactory This problem is complicated in the quad antenna design because of the limited space available A technique to surmount these difficulties with minimal effort is suggested here which can be utilized for the switched two-or three-beam case (and even the proposed switched four beam case to be discussed later).

The optical basis for this RF fence is the physical principle of the threshold-critical angle for total reflection which exists for electromagnetic radiation propagating from a dense (high dielectric constant) medium to a less dense one, as is the case of the radome/free-space interface of the S-band antennas The threshold-critical angle θ_c is derived from Snell's low of refraction to be

$$\sin \theta_c = \sqrt{\frac{1}{\varepsilon_r}}$$

where the angle θ_c is measured from the boundary normal and ε_r is the relative dielectric constant of the dense medium; in this case, polyimide E glass with ε_r=4. Thus any radiation incident on this boundary at a greater glancing angle ($\theta \geq \theta_c$) is totally reflected, constituting an RF fence in the classic definition.

The near-field radiation pattern is difficult to characterize. If the radiated waves can be approximated by quasi-spherical waves and geometric ray tracing is employed, this type of concept of RF fence to isolate the two dipole-radiating elements becomes very attractive since there are few readily implemented isolation mechanisms that are frequency independent.

The design criteria for this particular configuration is to have all incident rays greater than 30° from the boundary normal so that total reflection occurs. The separation between the two dipole cavities is small, but the use of the smaller diameter iris or circular aperture provides sufficient room to mill the triangular groove into the radome, restricted primarily by the thickness of the radome and the requirement to retain structural integrity since the groove is prone to fracture. To minimize crack initiation, the production model should have a minimum milling radius at the tip to reduce stress concentrations. The depth of this milling groove is the primary factor in determining the degree of isolation, but even a shallow groove will disrupt surface waves at the radome/ground plane boundary that result in mutual coupling.

5.0 SWITCHED FOUR-BEAM CONFIGURATION

The switched three-beam configuration proposed by Rockwell/MSD attempts to alleviate the apparent design problems associated with obtaining adequate 4.0 dB coverage. By adding the third beam to cover the gap or "cusp" between the initial switched two-beam configuration, the coverage problem is essentially solved, at the expense of added complexity. At the PDR the consensus appeared to favor this approach as the one with the highest probability of successfully meeting the coverage specification. The impact of such an abrupt design change, however, has not yet been fully assessed, and a firm decision to change to the switched three-beam system was delayed until the responsible system and software engineers could be queried.

The implications of such a design change require further examination, at least in principle, to ensure that engineering requirements are optimally satisfied, especially for the added complexity. Besides the appropriate phase shifts, an additional identical RF switch is inserted in series with the switched two-beam configuration to provide the zero phase-shift differential for the broadside array generating the center beam. However, one RF switch position is redundant and unused The question arises whether or not this switch position can be employed in a useful manner, which brings up the point of the feasibility of a switched four-beam configuration with the identical hardware and similar software alterations.

The proposed switched four-beam would have the primary advantage of a larger area coverage with higher gain, taking full advantage of the peak gain which is approximately 6.5 to 7.0 dB (even higher at broadside). The differential gain over the 4.0 dB coverage specification of 2.5 to 3.0 dB over the additional fourth switched beam area may be critical for some marginal communication links, and, if it was available for little extra software development (which has to be revised anyway), the consideration of the switched four-beam approach might be justifiable.

A logical switched-beam configuration might use an arbitrary center line slightly offset from the roll plane (90°) so that one of the two central beams provides adequate coverage in this critical region. The other central beam would then be electronically and mechanically tilted slightly forward Since these inner two beams are closer to broadside, they would have higher gains and narrower beamwidths in the array plane than the outer beams (yet experience some beam broadening for broader coverage than the third broadside center beam of the switched three-beam configuration). The outer two beamwidths can therefore be positioned for the desired coverage, with a bias for more coverage towards the nose of the Orbiter. The additional flexibility provided by the fourth beam simplifies the coverage "filling in" process, an important consideration for the lower quad pattern results where obvious problems exist.

Two switch settings of one RF switch then might be "fore" and "aft" of the imaginary center line and then the other two switch settings of the

other RF switch would be "inner" and "outer", denoting the relative locations of the beam. The appropriate phase shifts for the various beam settings can be readily determined. The availability of the four distinct switched beams from the two serial RF switches is not conceptually unreasonable and makes maximum use of the proposed hardware modification.

6.0 CONCLUSION

There are two possible solutions to the switched-beam S-band quad antenna problem. One is to continue to pursue the original switched two-beam quad-antenna concept which was initially selected for its straightforward simplicity. The problem with the two-beam approach is that the performance specifications have not been achieved since only 65% of the 85% 4.0 dB coverage requirement has been measured. Without new design concepts to broaden the dipole patterns and therefore the coverage, the two-beam effort was abandoned in favor of the more promising three beam scheme which which provides the necessary flexibility at the cost of added system complexity, which is presently being evaluated. Obviously the three beam scheme is more likely to be successful and has nearly attained the desired 85% coverage for the upper quad, according to the 78.5% coverage of the initial three-beam measurements.

This paper has attempted to illuminate the dilemma by suggesting first some concave lens design concepts for the existing radome which would broaden the dipole beams in the array plane, an essential feature to correct the present two beam coverage deficiencies. This concave surface also reduces the reflection and polarizing properties from a dielectric boundary, which minimizes polarization effects and therefore decreases the axial ratio. In the likely event that the more promising proposed switched three-beam scheme is selected instead, it is recommended that a switched four-beam configuration be seriously considered as an alternative system since the hardware and software for the three-beam scheme conversion have to be extensively modified anyway. The addition of another beam position provides higher gain levels in that particular coverage area (2 to 3 dB of communications link margin) and therefore obviously increases the 4.0-dB coverage area. And finally, a novel RF fence design using the total reflection concept of critical angle has been outlined which should substantially reduce the amount of

mutual coupling and deleterious interaction effects between the two dipole-array cavities for all switched multiple-beam configurations.

SIMPLIFIED ORBITER S-BAND QUAD ANTENNA

PLANAR-ARRAY CANDIDATE CONFIGURATIONS

Contract No. NAS 9-16067

Exhibit B

Interim Report

Prepared for

NASA Lyndon B Johnson Space Center
Houston, Texas 77058

Technical Monitor: William Teasdale

Prepared by

Axiomatix
9841 Airport Blvd , Suite 912
Los Angeles, California 90045

Axiomatix Report No. R8106-4
June 25, 1981

A recent presentation of more breadboard evaluation configurations for the Orbiter S-band quad antennas considered the mechanically switched three-element/four-beam system and two electronically phased eight-element/15-beam and 16-element/20-beam systems. The primary reason for proposing these systems is that the current two-element/two-beam system gives only 51%, 4-dBci coverage instead of the 85% coverage specified.

As stated earlier, Axiomatix feels that the present two-element/two-beam configuration has not been optimized since 2 dB excess mainbeam gain indicates that the radiated energy is not uniformly distributed to the 4-dBci level. However, since Rockwell deems any further suggested modifications to the present inadequate system as infeasible, by definition, a configuration change is therefore mandatory if further performance improvement is desired.

Using the available experimental pattern measurements of the existing dipoles, the Axiomatix-proposed three-element/four-beam mechanically switched configuration satisfied the 85%, 4-dBci coverage. However, it appears that even higher gain coverage is desired since the phased-array approach has been suggested. "Are the phased-array configurations proposed truly satisfactory from a practical viewpoint?" then becomes a reasonable question.

Since hardware and software complexity are directly related to the number of elements in the array, we first consider the simplest two-element case. If one element is directly fed and the other has the phase-shifting capability, the array will scan. The two-beam position is implemented by a mechanical switch interchanging a discrete phase shift between the two elements. This is the present S-band quad configuration.

If more than two positions were achievable, higher percentage coverages would be attainable. A multiple-value phase shifter capable of high-power operation was therefore required. But, if more positions are available, it becomes more desirable to have higher gain since little performance improvement occurs with a wide beam, which has a high degree of beam overlap between positions. For this reason, the three-element array was proposed and, with two mechanical switches in series with the appropriate phase shifts, analysis indicates that 85%, 4-dBci coverage is achievable. Since the center element is directly fed, some compensation for the additional switch loss occurs. This configuration satisfied the quad-antenna-coverage specifications, but was unacceptable due to the higher cost and delayed schedules involved. However, if higher gains are desired, it is still not totally impractical to consider using

another mechanical switch in series to obtain eight beam positions with this configuration. Although the 4-dBci percentage coverage will not be substantially improved, the higher (> 4 dBci) gain coverages will be greatly increased. However, the planar-array approach allows more design freedom in achieving the high-percentage-gain coverage.

The emphasis on higher than 4-dBci gain coverage appears to be the motivating factor for suggesting the use of planar arrays. Extending the previous arguments, we find that higher gains from more elements and more beam positions, in both pitch and roll planes, will result in higher percentage, higher gain coverage. There is no question that this is a valid assumption; the questions now really are: "has the gain-percentage coverage performance requirements changed?" and "what is the feasible limitation on the array complexity?"

Application of a two-dimensional planar array creates greater flexibility in gain coverage than simply adding beam positions in a linear array. The beamwidth in the orthogonal dimension is decreased, with a corresponding increase in gain. The simplest configuration for a planar array might be a triangular arrangement, as shown in Figure 1, where the two lower elements are identical to those presently being built.

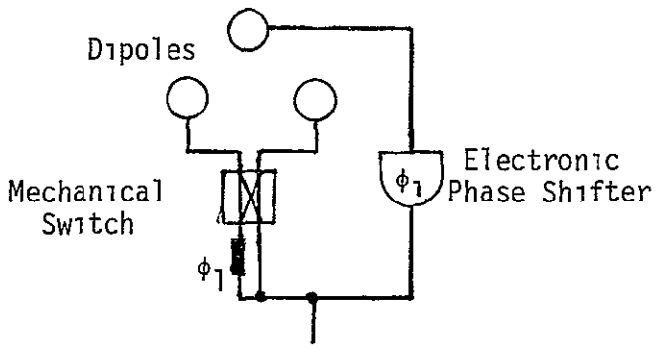

Figure 1. Triangular Planar Array

If two-beam switching can now be incorporated with respect to the third element, is is then possible to generate four beams, with the amount of beam overlap determined by the degree of phase shifting. Note that this particular three-element configuration is most readily implemented by using an electronic phase shifter in the third element, with mechanical switching still feasible between the other two elements.

With the mechanical-switching arrangement used here for explanatory purposes, it is more feasible to consider using a four-beam/four-element array set in a square configuration, as depicted in Figure 2.

Note that a tradeoff exists between the number of beam positions and the number of elements since there is more beam overlap for more beam positions using the wider beamwidths from the smaller number of elements. In order to increase the gain coverage, another possible configuration would be another three-element array superimposed orthogonally on the first three-element array, as shown in Figure 3. The center element is still directly fed, with the four outer elements determining the beam positions by appropriate phase shifting. This configuration is the largest one considered here since any additional elements provide illumination taper and higher gain, but at the expense of considerably higher costs and complexity.

Using the earlier arguments for the linear array, it is now possible to consider a four-beam planar array using the earlier switched two-beam concept in both orthogonal directions with two mechanical switches, as illustrated in Figure 3(a). The gain coverage is substantially higher than before because of the narrower beamwidth in the orthogonal direction. Similarly, since the three-element linear array was suitable for four beam positions, it is feasible to consider 16 beam positions using a total of four mechanical switches, as shown in Figure 3(b). Since the center element is directly fed and each orthogonal linear array is fed in parallel, the switch losses are not as significant.

The phase-shifting mechanism has not really been specified except that, since mechanical switches have been utilized in the present configuration, it has been retained in principle. Mechanical switching is preferable to electronic switching because it has low-loss characteristics and possesses the required high-power-handling capabilities. In addition, being the bistate "latching type," no holding current (as in the case of PIN diode phase shifters) is required. Since rapid scanning is not a critical factor, the mechanical switch is suitable for these applications. The only situation wherein the

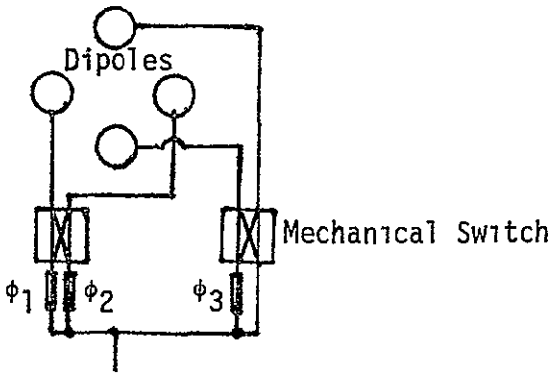

Figure 2. Square Planar Array

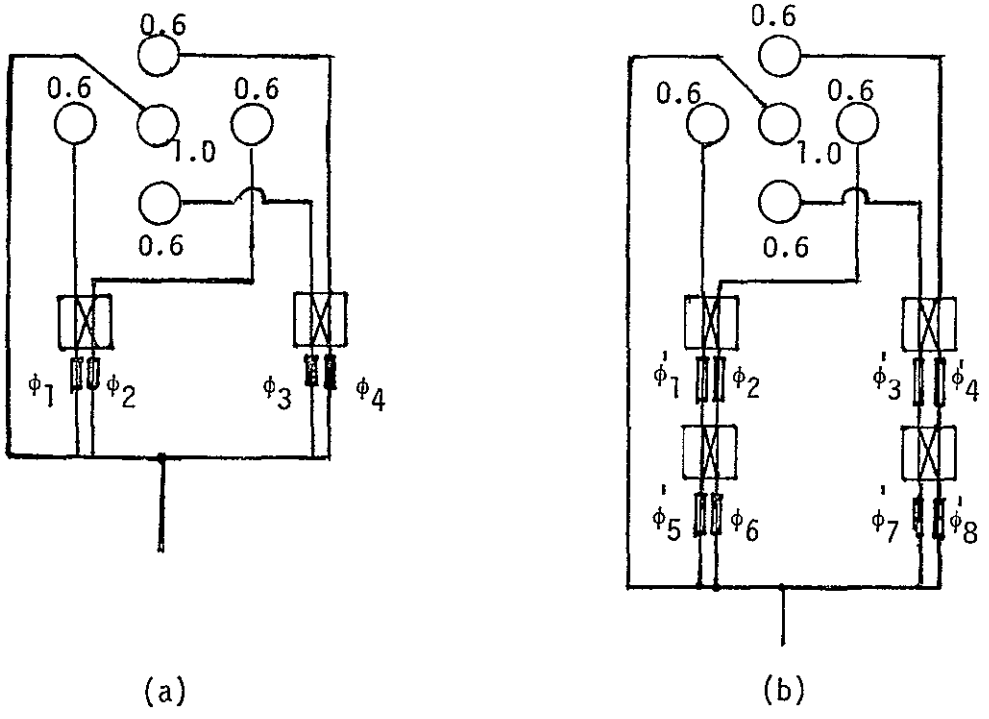

Figure 3. Five-Element Planar Array

electronic-phase shifting might be seriously considered in the planar arrays discussed here is for the triangular three-element array.

In conclusion, if higher gain levels at 85% coverage are desired for the S-band quad-antenna system, a five-element/16-beam mechanically switched system is proposed. The microwave circuit losses would be about the same (1.8 dB) as the three-element/four-beam linear-array system proposed earlier since the switching systems are in parallel and therefore identical. The only additional new component is a power splitter used to distribute the power in the orthogonal direction, which is easily incorporated into the input stripline. Because the number of beam positions is nearly identical to the eight-element (4x2) phased array proposed by Rockwell, it is anticipated that the 85% gain coverage would also be about 6.5 dB. However, since the microwave circuit losses are significantly lower (1.8 dB versus 3.6 dB) because mechanical switches are used, the overall 85% gain coverage should be accordingly higher. Also, since there are no electronic-phase shifters, no electrical "holding" power (24W - 48W in the electronic-phase configurations proposed) is a definite advantage in space operations. This configuration also has the advantage that, since only three linear elements form the beam, the beamwidth is quite large so that extreme pointing accuracy is not required, and there is a great deal of pointing margin before a communication link is lost.

Although it is considered somewhat impractical, by adding another switch in series with both feed lines (which adds only 0.2 dB more circuit loss), it is conceivable to have a 64-beam/five-element array which will definitely have the highest gain-percentage coverage--if that is indeed the primary operational requirement.

A PROTRUDING WEDGE-SHAPED DIPOLE ELEMENT MODIFICATION FOR THE ORBITER S-BAND QUAD ANTENNAS

Interim Report

Contract NAS 9-16067, Exhibit B

Contract Monitor: William Teasdale

Prepared for

NASA Lyndon B. Johnson Space Center
Houston, Texas 77058

Prepared by

R. Iwasaki

Axiomatix
9841 Airport Blvd., Suite 912
Los Angeles, California 90045

Axiomatix Report No. R8112-1
December 9, 1981

1.0 INTRODUCTION

A meeting was held at the Rockwell facility in Anaheim on November 24, 1981 to discuss some alternative R&D modifications for the Shuttle Orbiter S-band quad antennas. The present 4-dBci gain percentage coverage of approximately 50% is substantially below the 85% specification, with the coverage at one frequency, 2.217 GHz, measured to be 38%. This frequency sensitivity is somewhat disconcerting since the production flight models are fabricated identically, but there is optimism that the coverage degradation might be "tuned" out by mechanical adjustments. The cause of the frequency sensitivity is not known and therefore cannot be easily remedied without extensive testing. The low-percentage coverage problem, however, is more amenable to improvement and, after extensive discussions, a preliminary modification program, funded internally by Rockwell, was formulated, with the antenna measurements to be conducted at JSC. This interim report attempts to document the results of this meeting such that the approach and justifications are clearly delineated.

2.0 PROBLEM

The prototype S-band quad antennas have a 4-dBci percentage coverage of only 50% instead of the desired 85% coverage. The selection of the two-element/two switched-beam quad configuration early in the program arose from some unrealistic projections on reducing circuit losses as well as misunderstanding the interpretation of the data, specifically the gain levels. Since the configuration cannot be readily altered, the obvious question is: can any suitable modifications be suggested which might improve the percentage coverage? The extent of improvement is difficult to assess, of course, but some ideas were aired that appeared to have a valid basis for improving the percentage coverage, off-axis axial ratios and radiation efficiency.

3.0 RECOMMENDATIONS

The flush-mounted dipole elements appear to have an intrinsic limitation on the off-axis axial ratios because of the small electric field component radiated normal to the plane of the aperture. In order to circumvent this problem, a protruding-antenna concept was introduced

which extends the radiating elements to the thermal tile interface, or even beyond, by recessing the tile. This radical departure from the present conventional design will indeed improve the axial ratio if properly implemented.

The radiating-element design was addressed next. The existing crossed-dipole design was found to be the most suitable because the circular polarization characteristic could be readily controlled and the criterion of minimal modification was satisfied. Shaping of the radome, as described earlier, was deemed unfeasible and the related concept of a dielectric rod antenna was similarly dismissed due to the difficulty in controlling the propagation modes and, therefore, the radiation properties.

The "wedge" dipole concept, basically a curved dipole as sketched with dashed lines on the present dipole configuration in Figure 1, was then introduced. This design attempts to broaden the beam of the individual crossed-dipole elements and, therefore, the array beamwidth by physically altering the radiation pattern of the dipole by geometric means. Generally, dipoles are not considered in a three-dimensional manner. The idea here is to exploit the maximum radiation intensity normal to the radiating current by imposing a symmetric angular relationship to the crossed-dipole elements, thereby broadening the beam. The basis for this idea is that the peak gain of the array is approximately 6.5 dBci, as illustrated in Figure 2, and this excess gain can be usefully employed by spreading out the energy by broadening the beam, as depicted in Figure 3. Any increase in the beamwidth is substantial with regard to the percentage coverage since the area about the perimeter increases rapidly for relatively small beamwidth additions.

The iris aperture restriction, which earlier broadened the beam by decreasing the aperture area, was discussed. It was felt that this planar iris would affect the wege dipole design by maintaining the same aperture fields which determine the final radiation pattern. Incorporation of the protruding-antenna concept, however, permitted extension of the wedge dipole past the circular iris into the radome, as sketched in Figure 4, which appeared to be a reasonable compromise of the conflicting requirements. Therefore, the basis of the modification program was conceived.

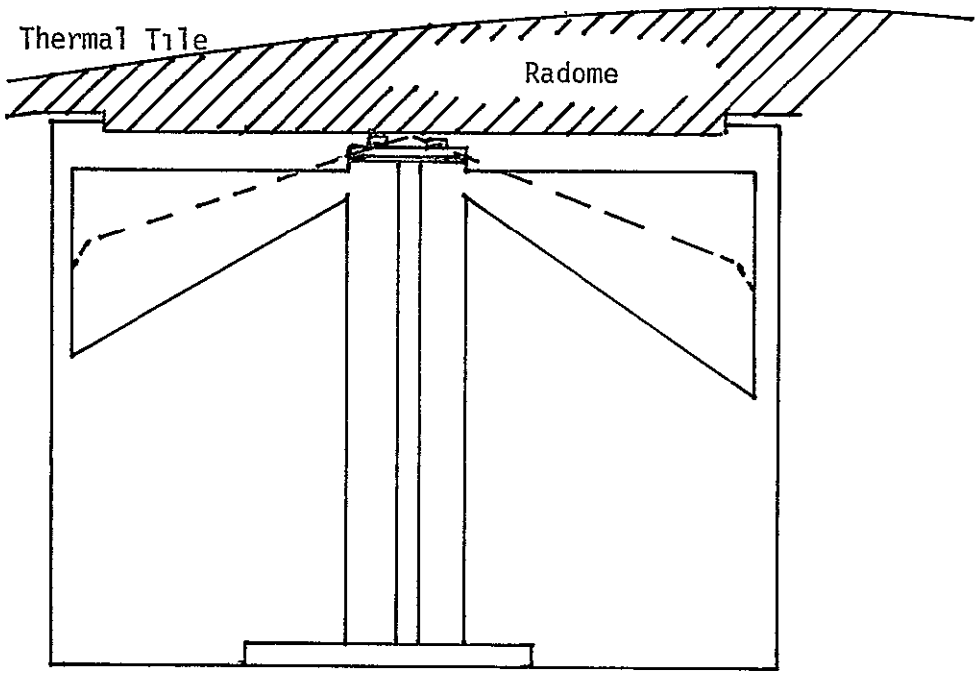

Figure 1. Present Dipole-Element Configuration

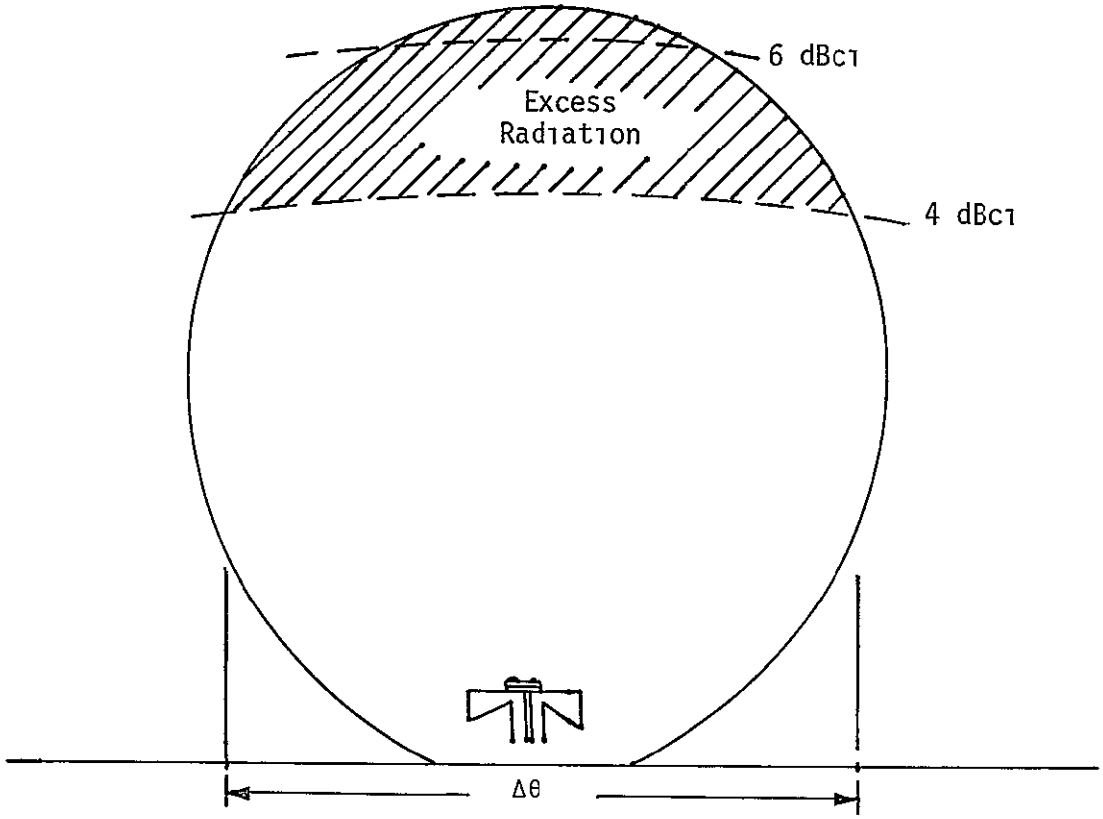

Figure 2. Excess Radiation (> 4 dBc1) to be Redistributed

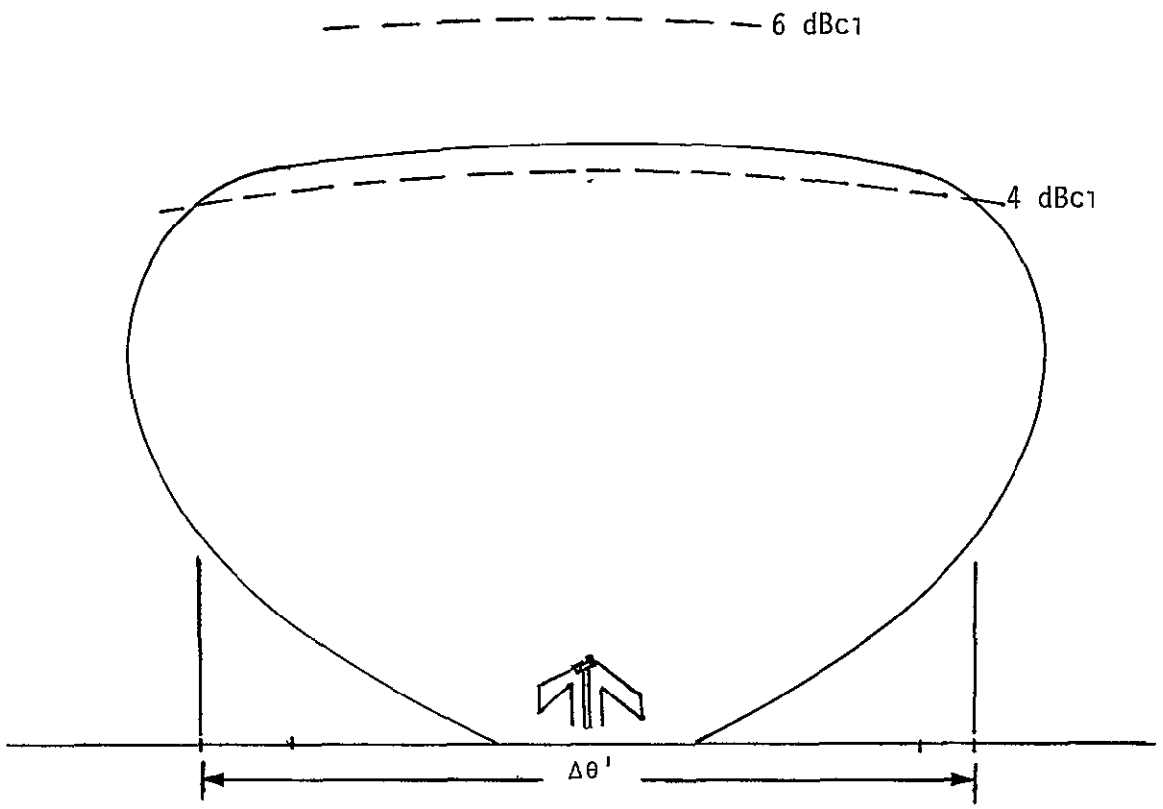

Figure 3. Redistributed Radiation by Beam Broadening

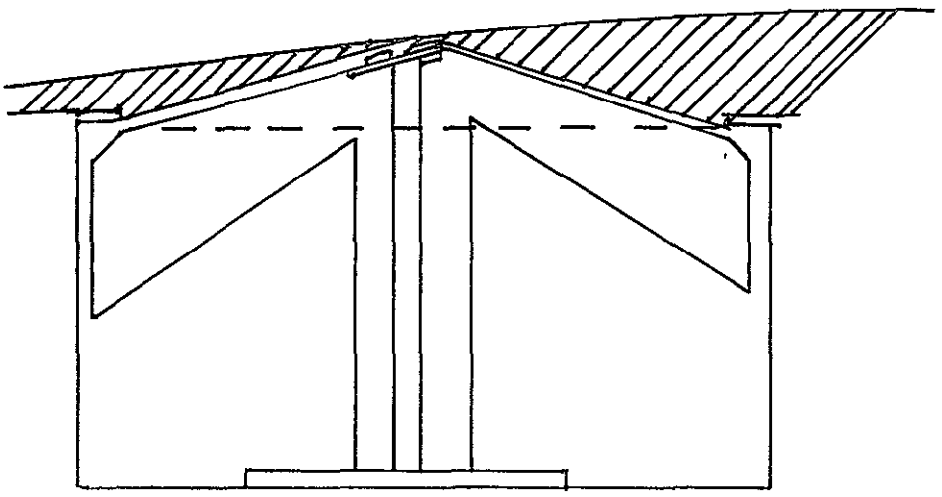

Figure 4. Proposed Wedge-Shaped Protruding Dipole

The angular relationships of the wedge dipole cannot be easily assessed but, using the previous gain values and standard dipole radiation equations, an angle of 30° is free space is not unreasonable. If too large a wedge angle is used, it is conceivable that the peak gain would be reduced below 4 dBci, which is counterproductive. However, an R&D effort could establish the optimum angle using this baseline design wedge-dipole concept once it was demonstrated. The effects of the radome, however, must be considered since some refraction might occur. The angular interface, using geometric optics, now has a tendency to further broaden the beam and, thus, this lens phenomena must be compensated for by reducing the free-space baseline angle. Therefore, an angle of 20° is not unreasonable for any initial R&D attempt to verify the concept.

The limitation on the percentage coverage measurement is that only JSC has the facilities to measure and analyze the data. Rockwell, however, can measure the principal plane dipole-element patterns, then analytically use pattern multiplication to predict the array beamwidths. This assumption allows Rockwell to assess the modification results in a preliminary manner to determine if the percentage coverage was indeed improved.

Since the dipole shape would be modified, the other recommendation made to Rockwell was to correct what was felt to be a design deficiency in the shorting strap of the crossed dipoles. There was a failure in the connecting solder joint during earlier vibration acceptance tests which was attributed to a "blind" connection where inspection was not feasible. By separating the crossed shorting straps onto two separate discs, visual inspection was made possible, avoiding a recurrence of the problem. However, it was noted that the positions of the shorting straps were above the plane of the crossed dipoles, which creates an uneven radiation pattern since the radiating current is "stepped," especially in the critical central region where the current density is highest. Although it was felt that the shorting strap functioned only as a bridge to connect the dipole elements, it would, by definition, affect the radiation pattern since it carries current. Therefore, it was suggested that the dipole connection points be indented, as shown in Figure 5, to accommodate the shorting strap on the same level as the dipoles to retain the classical dipole configuration. The wedge design of the dipole complicates this indented dipole strapping arrangement, but it might be modified as shown in Figure 6 to incorporate the angular configuration.

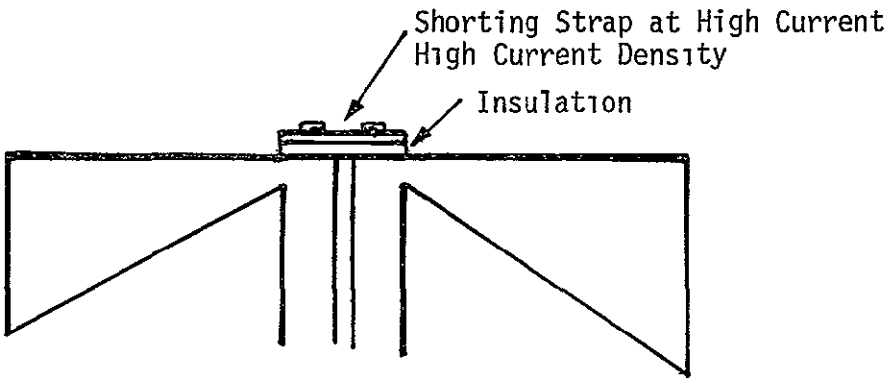

(a) Present Configuration with Stepped Shorting Strap

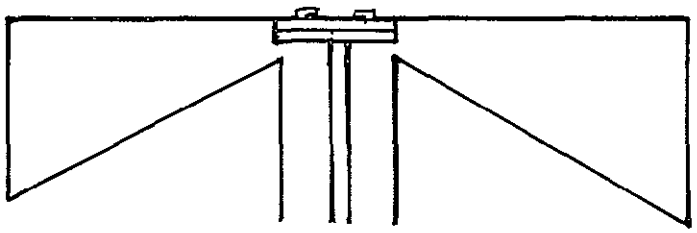

(b) Proposed Indented Shorting Strap

Figure 5. Indented Shorting-Strap Concept

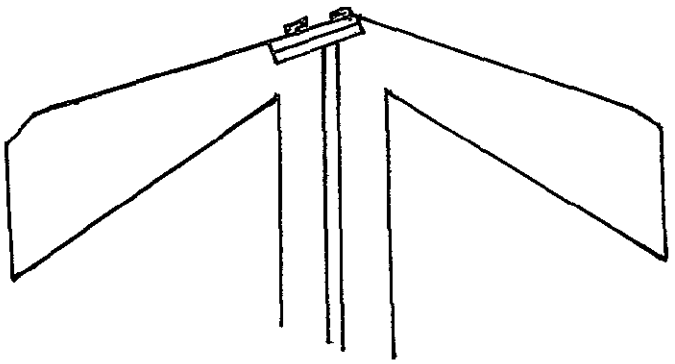

Figure 6. Indented Shorting Strap for Wedge Dipole

4.0 CONCLUSIONS

Although it is somewhat late to introduce new concepts which attempt to improve the gain percentage coverage performance of the Orbiter S-band quad antennas, it is still feasible in that the modifications required to upgrade the design, once it has been satisfactorily demonstrated, has been intentionally restricted to be minimal. At the present time, there are definite questions as to the reproducibility of pattern coverage results, even though they do not satisfy the existing gain percentage coverage specification. Rather than simply accepting the present design and, therefore, the inadequate performance, these possible modifications have been introduced which may ameliorate the poor performance. Simply tuning to obtain impedance matching for selective frequencies in order to reduce losses is often unsatisfactory if large discrepancies in predicted performance arise unexpectedly. It should be noted that antenna development is not a textbook problem and the antenna performance is often dictated by minor modifications to correct obvious deficiencies which result from the initial design.

The wedge-dipole design which has been introduced here will most certainly broaden the beamwidth and, therefore, increase the gain percentage coverage. In retrospect, this wedge dipole is a descendent of the earlier radome lens concepts since it physically implements the ray bending that was to be achieved by refraction effects from a concave lens surface. In fact, some design compensation must be incorporated for the radome lens effect since it has a tendency to broaden the beam even further It must be recognized that this modification has the specific goal of increasing the gain percentage coverage by broadening the existing antenna pattern at the cost of reducing the peak gain. If gain was the essential criterion, as might be required for some marginal communication links, other more complex solutions would be required.

A LARGE SWITCHED-BEAM PLANAR ARRAY

Interim Report

Contract No. NAS9-16067, Exhibit B

Technical Monitor: William Teasdale

Prepared for

NASA Lyndon B. Johnson Space Center
Houston, Texas 77058

Prepared by

Dr. Richard S. Iwasaki

Axiomatix
9841 Airport Blvd., Suite 912
Los Angeles, California 90045

Axiomatix Report No. R8112-4
December 15, 1981

There has been a recent emphasis on high-gain antennas for both the Shuttle Orbiter S-band quad antennas and the Centaur vehicle. An earlier Axiomatix report (R8106-4, June 25, 1981) outlined a two-dimensional switched-beam array using five elements. However, since high gain is of interest, this report continues the development of larger switched-beam arrays. Although the basis of these concepts utilizes electromechanical switches, this technique is by no means limited by this constraint since PIN diode phase shifters can also be readily substituted. The justification for this report is to expand the available options by describing the use of switched beams rather than phased arrays for applications where high power and no electrical holding current are desired at relatively slow switching rates. Since the switches are utilized in parallel, little overall loss (0.2 dB for a switch and discrete phase element) occurs. A systems trade-off using PIN diode phase shifters can then be made using the baseline configurations for comparison purposes.

The next step in increasing the gain beyond the basic three-element linear array described earlier is to add two additional outer elements with the appropriate illumination taper. The five-element array is sketched in Figure 1 with the additional switching arrangement. Note that there is no additional loss compared to the three-element array since the switches are incorporated in parallel. The primary difference in the new set of switching circuits is that the discrete phase shifts are twice those of the corresponding three-element set to account for the elements being at the extremes of the array.

The proposed Centaur biconical array is now composed of three elements, but higher gain can be achieved (with no additional circuit loss) by adding this second set of switching circuits. The beam position which is described by a binary code, as described in an earlier report, is identical for both the three-element and five-element arrays since the switch positions are the same for both sets of switches.

This concept of extending the linear array can be continued further by adding additional pairs of outer elements but, for explanatory purposes, a large planar array will be developed using the five-element linear array as a basis.

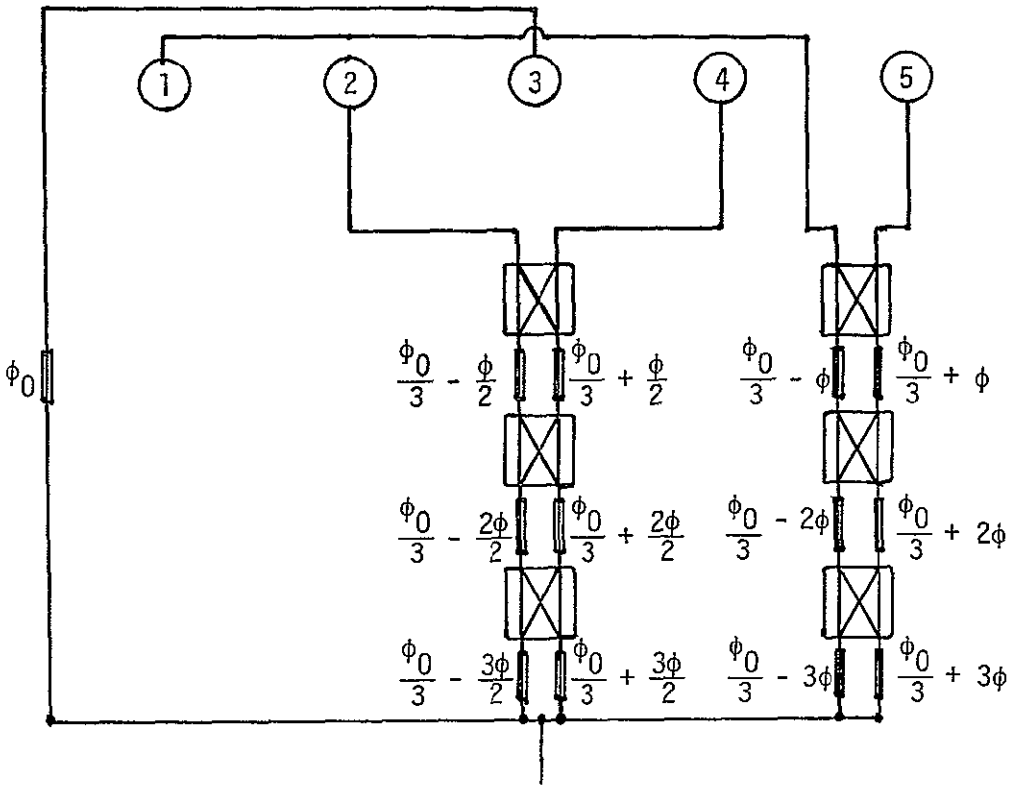

Beam	Element 1	Element 2	Element 3	Element 4	Element 5
1	$\phi_0 - 6\phi$	$\phi_0 - 3\phi$	ϕ_0	$\phi_0 + 3\phi$	$\phi_0 + 6\phi$
2	$\phi_0 - 4\phi$	$\phi_0 - 2\phi$	ϕ_0	$\phi_0 + 2\phi$	$\phi_0 + 4\phi$
3	$\phi_0 - 2\phi$	$\phi_0 - \phi$	ϕ_0	$\phi_0 + \phi$	$\phi_0 + 2\phi$
4	ϕ_0	ϕ_0	ϕ_0	ϕ_0	ϕ_0
-	ϕ_0	ϕ_0	ϕ_0	ϕ_0	ϕ_0
5	$\phi_0 + 2\phi$	$\phi_0 + \phi$	ϕ_0	$\phi_0 - \phi$	$\phi_0 - 2\phi$
6	$\phi_0 + 4\phi$	$\phi_0 + 2\phi$	ϕ_0	$\phi_0 - 2\phi$	$\phi_0 - 4\phi$
7	$\phi_0 + 6\phi$	$\phi_0 + 3\phi$	ϕ_0	$\phi_0 - 3\phi$	$\phi_0 - 6\phi$

Figure 1 Seven-Beam/Five-Element Switched-Beam Array

The last planar array described was a five-element array sketched in Figure 2. Note that the central element is directly fed, and the four outer elements have circuit losses of 0.6 dB (0.2 dB per switch) for a 49-beam (i.e., 7 x 7) configuration with redundant broadside beams. A 225-beam (i.e., 15 x 15) configuration would have only 0.8 dB of loss but, for the present, let us only use three switches in parallel as the baseline design.

There is a definite trade-off between the gain desired and the number of beam positions since these two parameters constitute the gain percentage coverage. Naturally, the higher the gain, the more complex the system, but the number of beam positions can be approximately doubled by adding only another switch (and 0.2 dB of loss) to each set of switches This feature is especially important when the gain percentage coverage is emphasized since, effectively, the percentage coverage is directly related to beam positions

To continue with the large planar array development, if two of the five-element linear arrays are orthogonally positioned, a nine-element planar array with extremely high gain is developed by the two-dimensional pattern multiplication concept. Again, note that no additional circuit losses are involved since the radiated power is redistributed and the switching sets are in parallel The essential features of this nine-element array are sketched in Figure 3 Again, the beam position is determined by a binary switching code which, for this two-dimensional case with three switches in each arm, is composed of six binary numbers for the 49 beam positions (assuming redundant broadside beams). The 225-beam configuration is correspondingly characterized by eight binary numbers.

The next step in increasing the gain involves filling in the array, as shown in Figure 4, with another four elements. This 13-element configuration still has 49 beam positions with no additional circuit loss even though four more elements are incorporated The addition of these four additional elements, however, greatly increases the complexity since these elements are shared by the two orthogonal linear arrays so that the appropriate phase shifts must be computed by an algorithm. For example, if the phase shifts for a given beam position are characterized by $(\phi_0 \pm m\phi)(\phi_0 \pm n\phi)$, the phase shifts for these four elements are then described by $\left[\phi_0 \pm (\pm m \pm n)\phi\right]$ so that the complexity is substantially increased.

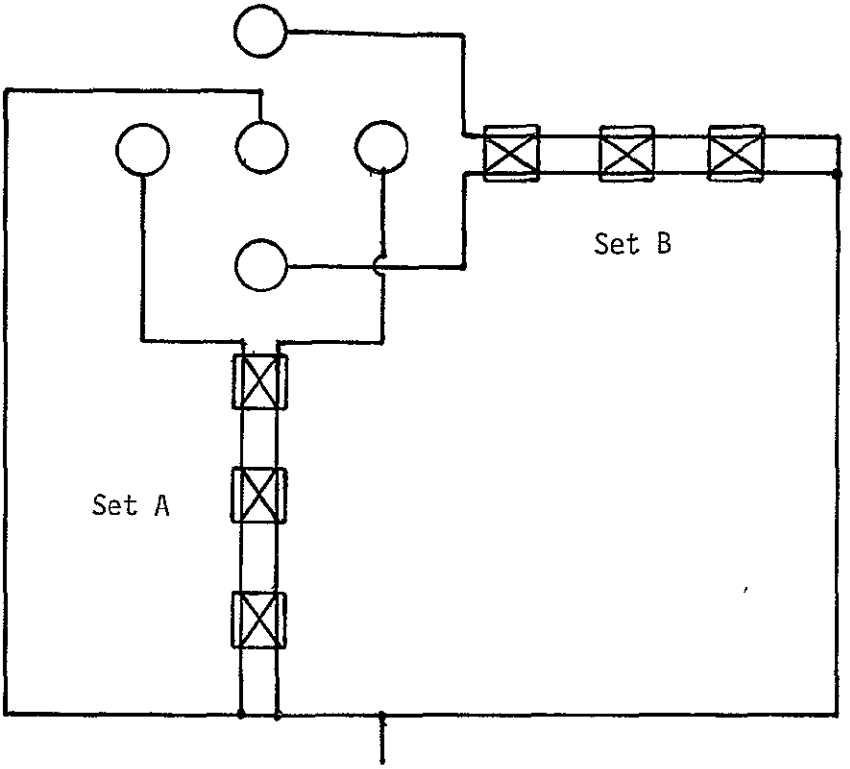

Figure 2. 49-Beam/Five-Element Switched-Beam Array

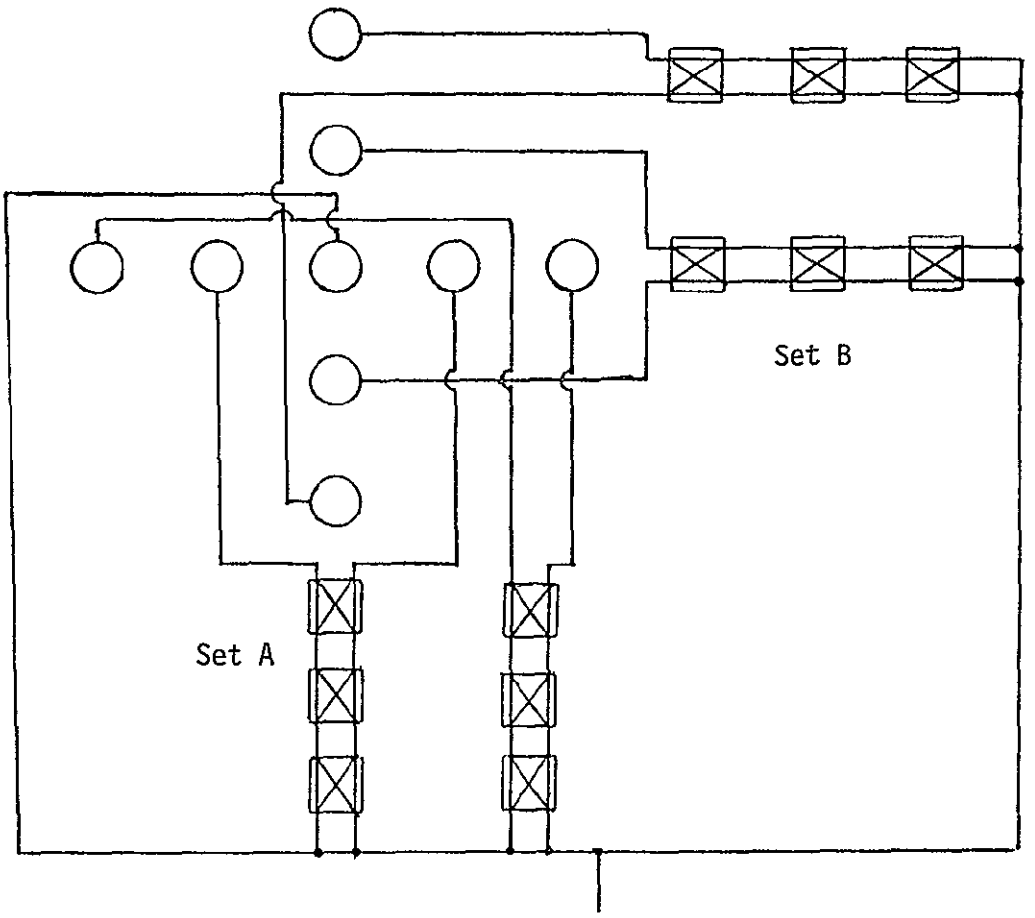

BEAM	B1	B2	B3	B4	B5	B6	B7
A1	A1B1	A1B2	A1B3	A1B4	A1B5	A1B6	A1B7
A2	A2B1	A2B2	A2B3	A2B4	A2B5	A2B6	A2B7
A3	A3B1	A3B2	A3B3	A3B4	A3B5	A3B6	A3B7
A4	A4B1	A4B2	A4B3	A4B4	A4B5	A4B6	A4B7
A5	A5B1	A5B2	A5B3	A5B4	A5B5	A5B6	A5B7
A6	A6B1	A6B2	A6B3	A6B4	A6B5	A6B6	A6B7
A7	A7B1	A7B2	A7B3	A7B4	A7B5	A7B6	A7B7

Figure 3. 49-Beam/Nine-Element Switched-Beam Array

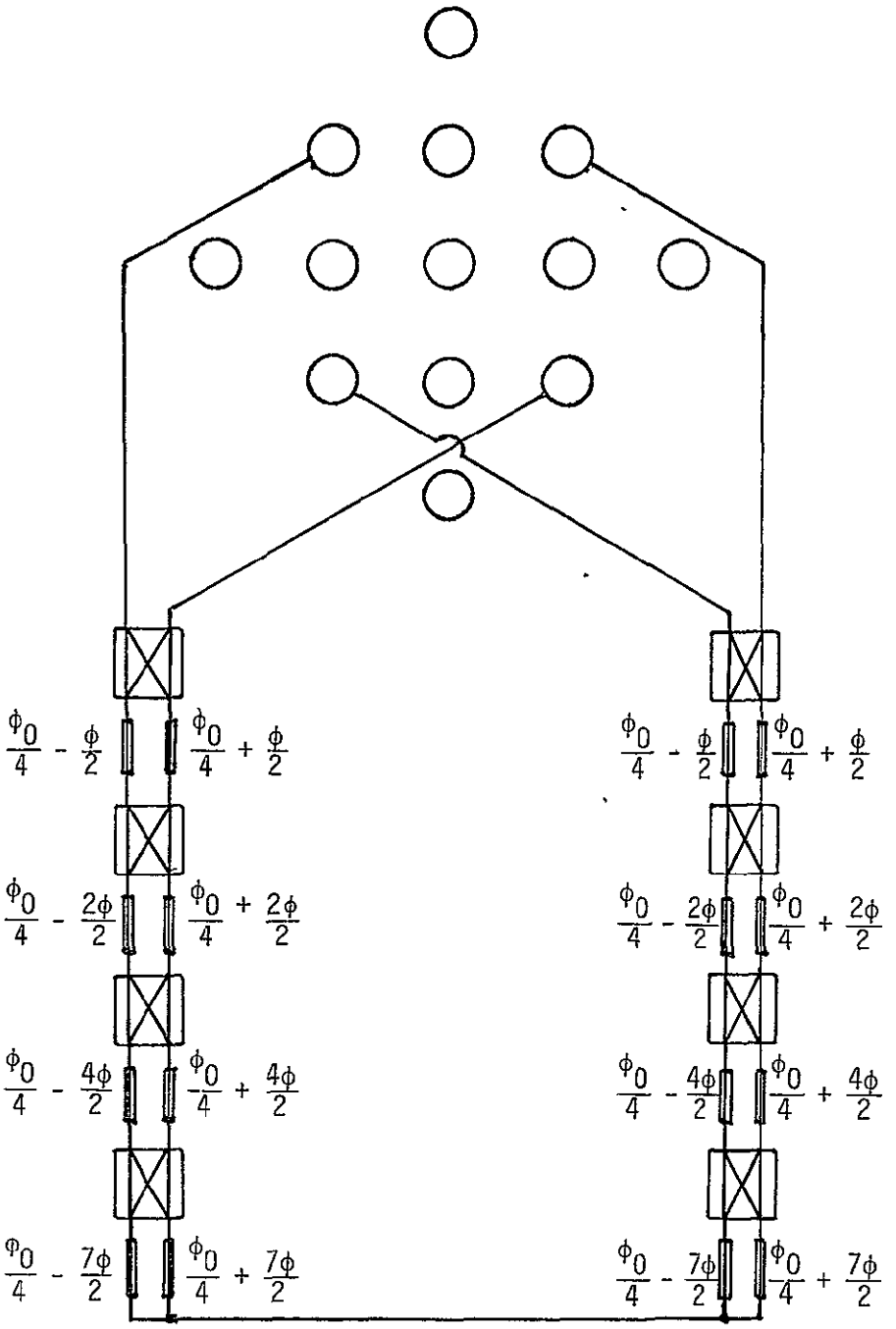

Figure 4 49-Beam/13-Element Switched-Beam Configuration

Note that the set of switches required to fill in the array is one more than that used for the other sets; in this case, four switches instead of three because of the (m+n) factor which doubles the number of phase shift increments required. For example, for beam position A1B1 which, for element 2 of both sets, is $(\phi_0 - 3\phi)(\phi_0 - 3\phi)$, the mutually adjacent fill-in element should then have a phase shift of $(\phi_0 - 6\phi)$, which requires four switches for integral values of ϕ. Because of the added complexity, however, a system analysis is required to justify filling in the array to obtain the higher gain values.

In summary, techniques to implement a large switched-beam planar array have been described. Higher gain has been achieved by adding more switches and elements to increase the effective aperture. The circuit losses remain constant except for any incurred for redistributing the power, which should be small. The primary value of this approach is the large number of beam positions available, which approximately doubles for every switch added to a set, at a cost of only 0.2 dB of additional loss per switch and discrete phase element. For two orthogonal three-switch sets, for example, 49 beams are achievable. Even more dramatic are two orthogonal four-switch sets which can generate 225 beam positions. With the capability of precise pointing, the peak gain of the array can be fully utilized and the net gain percentage coverage is thus accordingly higher. Another advantage is that the switches are electromechanical latching switches which can handle high-power levels and require no electrical holding currents. The discrete phase shifts are lengths of cable or microstrip sections which are not temperature-dependent. Finally, the selection of a particular beam position can be reduced to a six-binary-number sequence for the three-switch set (49 beams) and an eight-binary-number sequence for the four-switch set (225 beams), thereby simplifying the software required for implementation.

These advantages should be compared with comparable electronic phased arrays with PIN diode phase shifters to select beam positions. This electromechanical switched-beam approach is used on the Shuttle S-band quad antennas for two-beam positions, but its capabilities for large planar arrays were not fully investigated or appreciated previously. The intent of this series of interim reports has been to discuss and develop the necessary techniques to exploit this technology as an alternative option in selecting future antenna configurations for the high-gain percentage coverage applications required for the new generation of communication requirements for space vehicles.

ADDENDUM
TO
"A LARGE SWITCHED-BEAM PLANAR ARRAY"

Further consideration of the 49-beam/13-element switched-beam array has resulted in an improved version which completely eliminates the software problem of determining the proper phase settings for the four "fill-in" elements. The improved configuration is shown in Figure 5, where again there are only two switch sets to consider. The modification which permits this simplification is feeding the "fill-in" elements off of switch set A, which determines the proper phase shifts for one orientation. Switch set B then determines the proper phase shifts for the orthogonal orientation. The primary advantage of this configuration is that the two switch sets designated B have identical binary codes so that the beam position notation is greatly simplified. Fewer switches (six versus eight) are required but, because of the power distribution, additional circuit loss is encountered (although, because of the weighting factors, the actual amount is small).

This improved version of the 13-element array completes the basis for the development of a large planar switched-beam array since the basic mechanism is clearly outlined. Further modifications for even larger arrays can be developed from the techniques outlined, but the conceptual feasibility has been demonstrated for this new type of array.

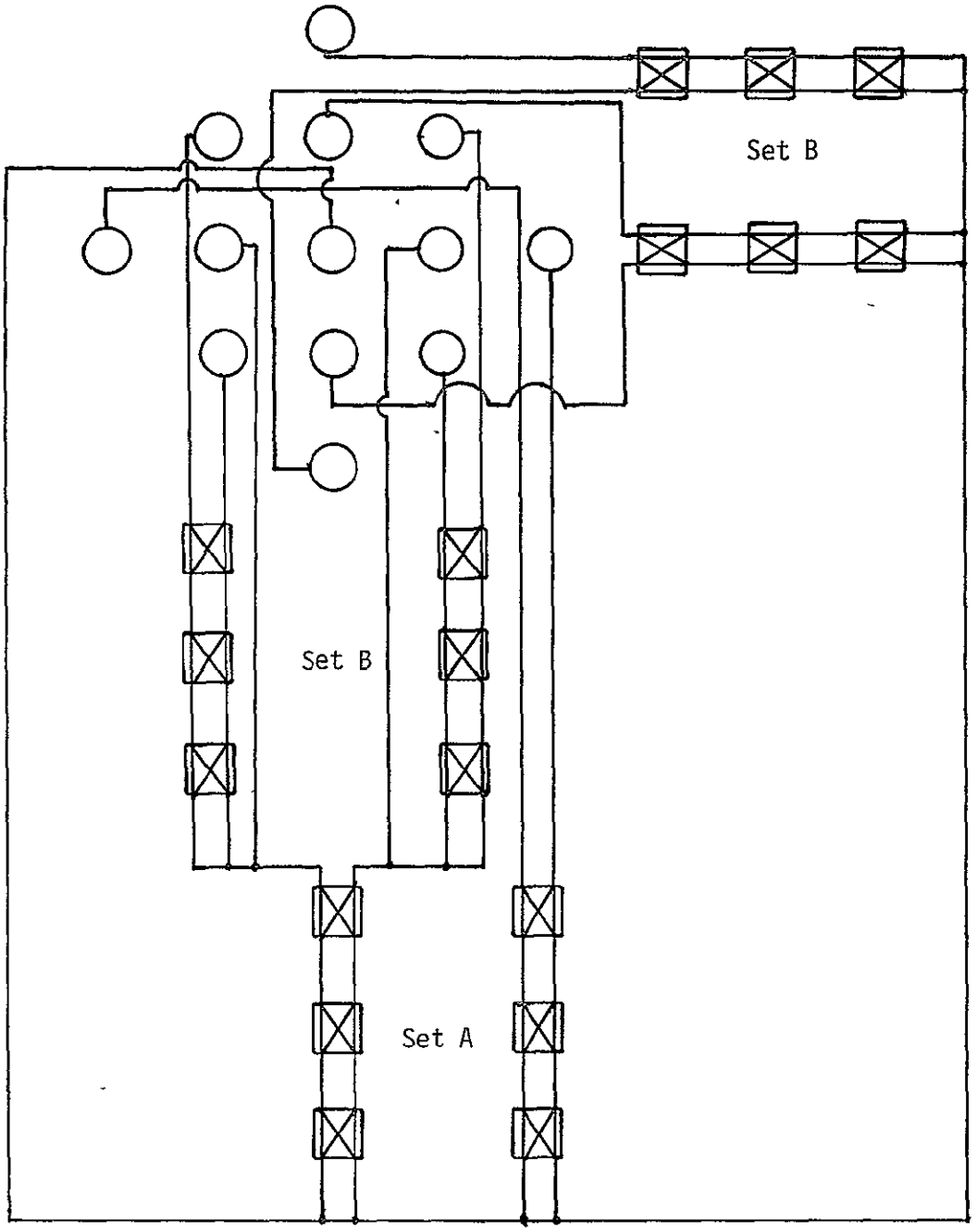

Figure 5. Improved 49-Beam/13-Element Switched-Beam Array

A VARIABLE-GAIN MULTIPLE-SWITCHED-BEAM-ANTENNA CONFIGURATION

Interim Report

Contract No NAS9-16067, Exhibit B

Technical Monitor William Teasdale

Prepared for

NASA Lyndon B. Johnson Space Center
Houston, Texas 77058

Prepared by

Axiomatix
9841 Airport Blvd., Suite 912
Los Angeles, California 90045

Axiomatix Report No. R8209-3
September 22, 1982

1.0 INTRODUCTION

The difficulty of achieving the original percentage coverage gain specification of 85% 4 dBci, which has been relaxed to 50% 4 dBci, became apparent during the Shuttle Orbiter S-band quad antenna program. The purpose of this specification was to ensure that adequate communication link margins were available about the Orbiter. As a result of monitoring the S-band antenna program under NASA Contract NAS 9-16067, Axiomatix extended many of the concepts used in the switched two-beam quad antenna, taking advantage of the Rockwell-developed basic hardware. The outcome of the study has been the evolution of a new generation of variable-gain multiple-switched-beam antennas whose principles can be applied to the improved Shuttle Orbiter S-band quad antennas and Centaur biconical arrays, as well as to proposed future Space Station antenna systems.

This switched two-beam quad antenna developed by Rockwell was an improvement over the earlier single-beam quad antenna built by Watkins-Johnson but, due to overoptimistic computer analysis projections of the antenna patterns, the actual performance results were disappointing. The primary limitation of the gain performance was the selection of only two elements and two beam positions, the minimum required for switched-beam operation. Using the same type of hardware configured in a slightly different manner, Axiomatix developed a two-dimensional cross array that could be electromechanically scanned in both the roll and pitch planes at $2^M \times 2^N$ discrete beam positions, where M and N are the number of double-pole/double-throw electromechanical latching switches in each plane. The advantages of using this type of switch rather than electronic phase shifters are: (1) high power-handling capabilities, (2) low insertion losses, (3) absence of electrical "holding" power, and (4) the binary nature of the double-throw switch which can readily be converted to a binary code for a specific beam position.

Higher gain can be achieved by adding additional radiating elements to the basic configuration, the only complexity being a doubling of the differential phase shifts of the outer elements. The binary code for the beam positions remains the same since the switching configuration used for the inner elements is identical to that of the outer elements.

Since it is possible to physically switch out various combinations of radiating elements to form an antenna pattern of the desired shape using this same electromechanical switch, an even more unique feature arises from this switched-beam configuration in that low, medium and high gains can be independently attained in each plane by simply activating two switches, with the beam

position remaining constant and without phase transients. This variable-gain capability in both planes greatly relieves the tracking requirement since the pattern shape can be adjusted to accommodate the relative motion between the antenna system and the "target" vehicle. For example, if a free flyer was passing the Shuttle Orbiter (i.e., being in a lower orbit), the low/high-gain configuration combination would result in an elongated pattern which follows the path of the free flyer, thus eliminating the tracking function.

The variable-gain multiple-switched-beam antenna takes advantage of the trade-off between gain and percentage coverage. If high gain is required, the full antenna-array aperture is utilized, and this switched-beam array can position the narrow beam anywhere in its sector of coverage. If high gain is not required, the outer radiating elements are switched out and the larger resultant beamwidth associated with the lower gain relaxes the tracking requirement. Finally, if low gain from an omnidirectional antenna is needed for a nearby target, only the central radiating element is used by switching out the inner two elements, which also automatically removes the outer elements, as will be shown later.

2.0 MULTIPLE BEAMS

The Rockwell proposal to develop an improved S-band quad antenna using the Axiomatix "cross" five-element configuration prompted a more detailed evaluation of the design. As a result, the switched-beam phase relationships were reexamined and a significantly better scheme evolved, one which was not immediately obvious. Since a similar switched-beam scheme has also been proposed for the Centaur vehicle, documenting the results herein is considered appropriate.

This modified configuration avoids the "double-angle broadside gap" previously described in Axiomatix Report No. R8112-4, where the two adjacent near-broadside beams were pointed $\pm\phi$ for an angular separation of 2ϕ. In order to avoid this problem, it was suggested that the one-beam position be sacrificed while having a redundant broadside beam. With this improved phase relationship scheme, the beams are equispaced and separated by the same angle, $\phi' = 2\phi/3$, without losing a beam position. Note that the near-broadside beams are now $\pm \phi/3$. The only design criteria is then the selection of the number of beams in each plane and, therefore, the number of switches required.

In order to dramatically demonstrate the desirability of adding another switch in series, which doubles the number of beam positions at the cost of only 0.2 dB additional loss, the phase relationships for the two-, three- and four-switch configurations are shown in Figures 1 - 3 for four, eight and 16 beams in each plane, respectively. It should be noted that a similar switching arrangement exists in the orthogonal plane so that various combinations of beam positions, up to a maximum of 256, are possible for four switches in each plane for each of the four quad antennas. Although this might be considered "overkill the points to be emphasized are that the simple addition of another switch in each circuit greatly increases the potential advantages of switched-beam technology by doubling the number of beams, and the resultant availability of a large number of beam positions easily compensates for the unpredictable performance which has plagued the quad antenna program due to the curved Orbiter shape.

The high-gain version of the switched-beam array is shown in Figure 4, where two additional elements create a five-element linear array whose phase lationships for the 16 beam positions are observed to be similar to the three-element array except that the differential phase shifts for the outer elements are doubled. The binary code for the beam position is identical since the switching configuration for the five-element array is directly related to the

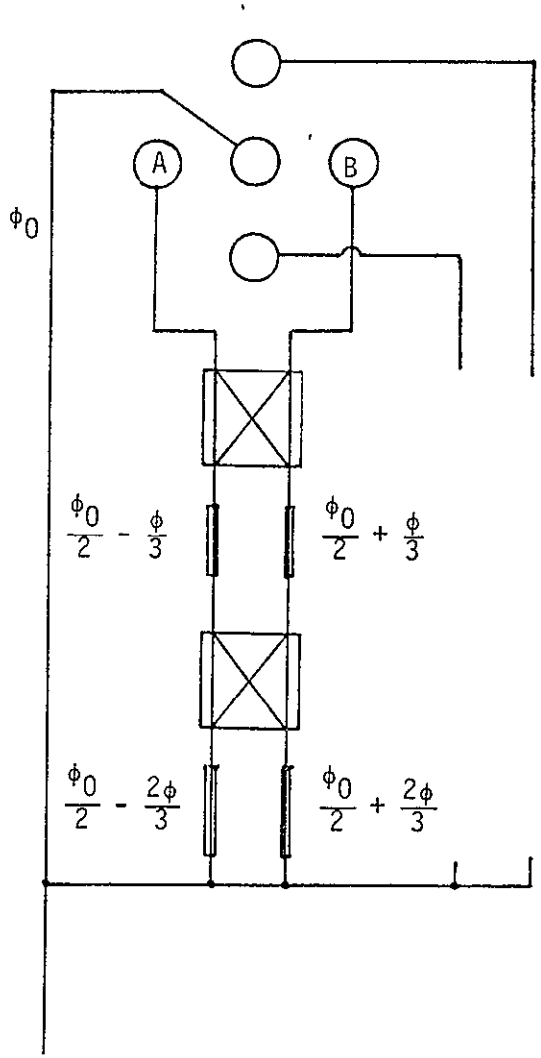

Beam	Element A	Element B
1	$\phi_0 - \phi$	$\phi_0 + \phi$
2	$\phi_0 - \frac{\phi}{3}$	$\phi_0 + \frac{\phi}{3}$
3	$\phi_0 + \frac{\phi}{3}$	$\phi_0 - \frac{\phi}{3}$
4	$\phi_0 + \phi$	$\phi_0 - \phi$

Figure 1. Two-Switch/Four-Beam Configuration

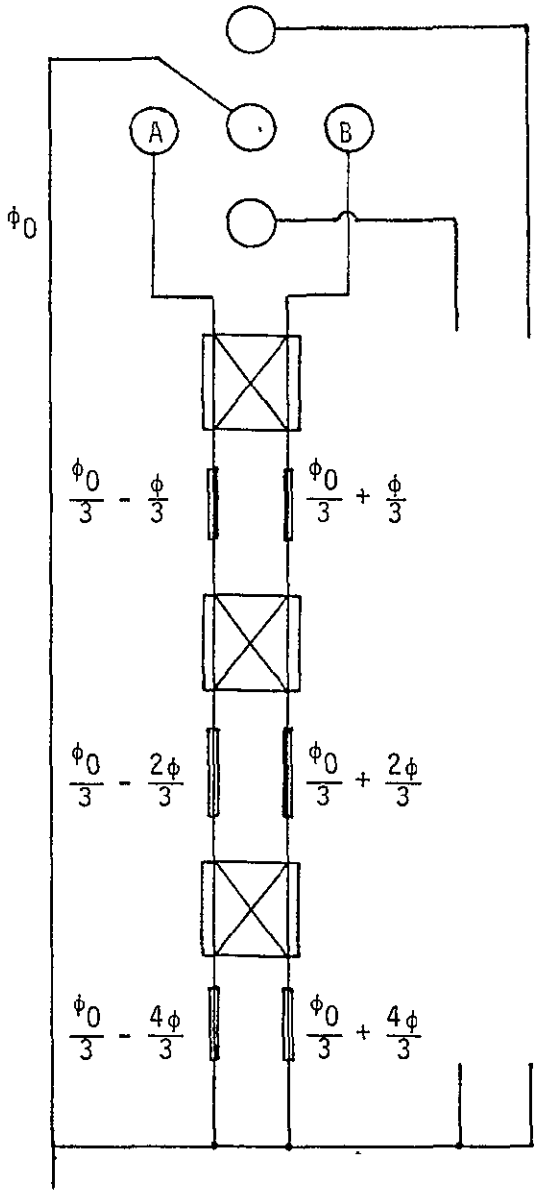

Beam	Element A	Element B
1	$\phi_0 - \frac{7\phi}{3}$	$\phi_0 + \frac{7\phi}{3}$
2	$\phi_0 - \frac{5\phi}{3}$	$\phi_0 + \frac{5\phi}{3}$
3	$\phi_0 - \phi$	$\phi_0 + \phi$
4	$\phi_0 - \frac{\phi}{3}$	$\phi_0 + \frac{\phi}{3}$
5	$\phi_0 + \frac{\phi}{3}$	$\phi_0 - \frac{\phi}{3}$
6	$\phi_0 + \phi$	$\phi_0 - \phi$
7	$\phi_0 + \frac{5\phi}{3}$	$\phi_0 - \frac{5\phi}{3}$
8	$\phi_0 + \frac{7\phi}{3}$	$\phi_0 - \frac{7\phi}{3}$

Figure 2. Three-Switch/Eight-Beam Configuration

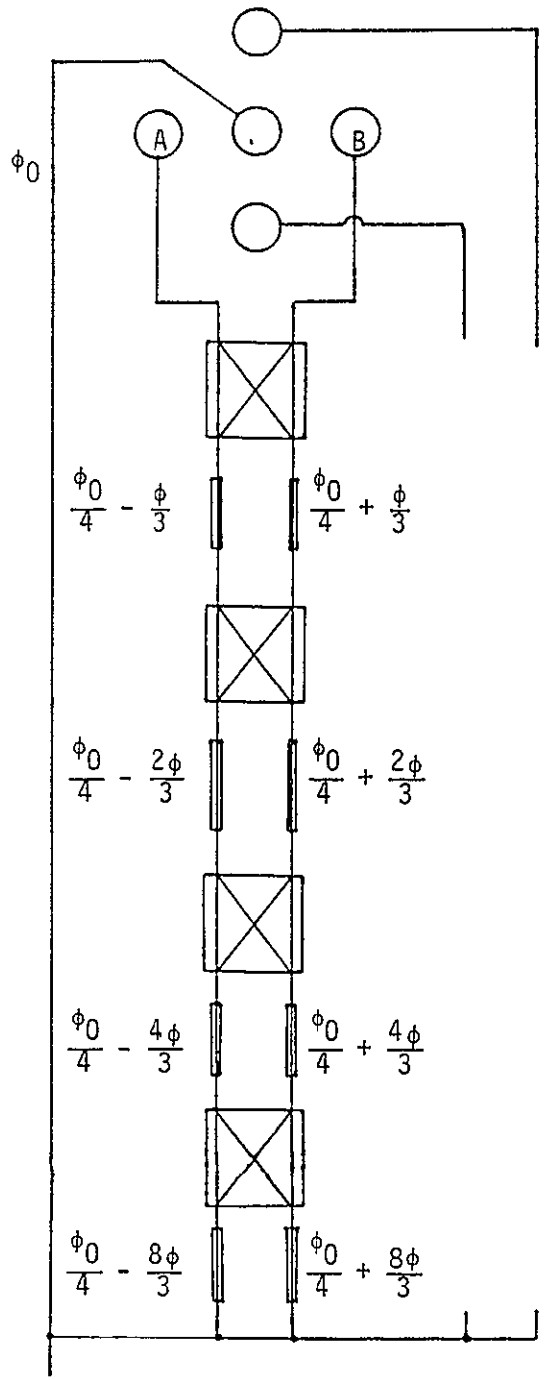

Beam	Element A	Element B
1	$\phi_0 - 5\phi$	$\phi_0 + 5\phi$
2	$\phi_0 - \frac{13\phi}{3}$	$\phi_0 + \frac{13\phi}{3}$
3	$\phi_0 - \frac{11\phi}{3}$	$\phi_0 + \frac{11\phi}{3}$
4	$\phi_0 - 3\phi$	$\phi_0 + 3\phi$
5	$\phi_0 - \frac{7\phi}{3}$	$\phi_0 + \frac{7\phi}{3}$
6	$\phi_0 - \frac{5\phi}{3}$	$\phi_0 + \frac{5\phi}{3}$
7	$\phi_0 - \phi$	$\phi_0 + \phi$
8	$\phi_0 - \frac{\phi}{3}$	$\phi_0 + \frac{\phi}{3}$
9	$\phi_0 + \frac{\phi}{3}$	$\phi_0 - \frac{\phi}{3}$
10	$\phi_0 + \phi$	$\phi_0 - \phi$
11	$\phi_0 + \frac{5\phi}{3}$	$\phi_0 - \frac{5\phi}{3}$
12	$\phi_0 + \frac{7\phi}{3}$	$\phi_0 - \frac{7\phi}{3}$
13	$\phi_0 + 3\phi$	$\phi_0 - 3\phi$
14	$\phi_0 + \frac{11\phi}{3}$	$\phi_0 - \frac{11\phi}{3}$
15	$\phi_0 + \frac{13\phi}{3}$	$\phi_0 - \frac{13\phi}{3}$
16	$\phi_0 + 5\phi$	$\phi_0 - 5\phi$

Figure 3. Four Switch/16-Beam Configuration

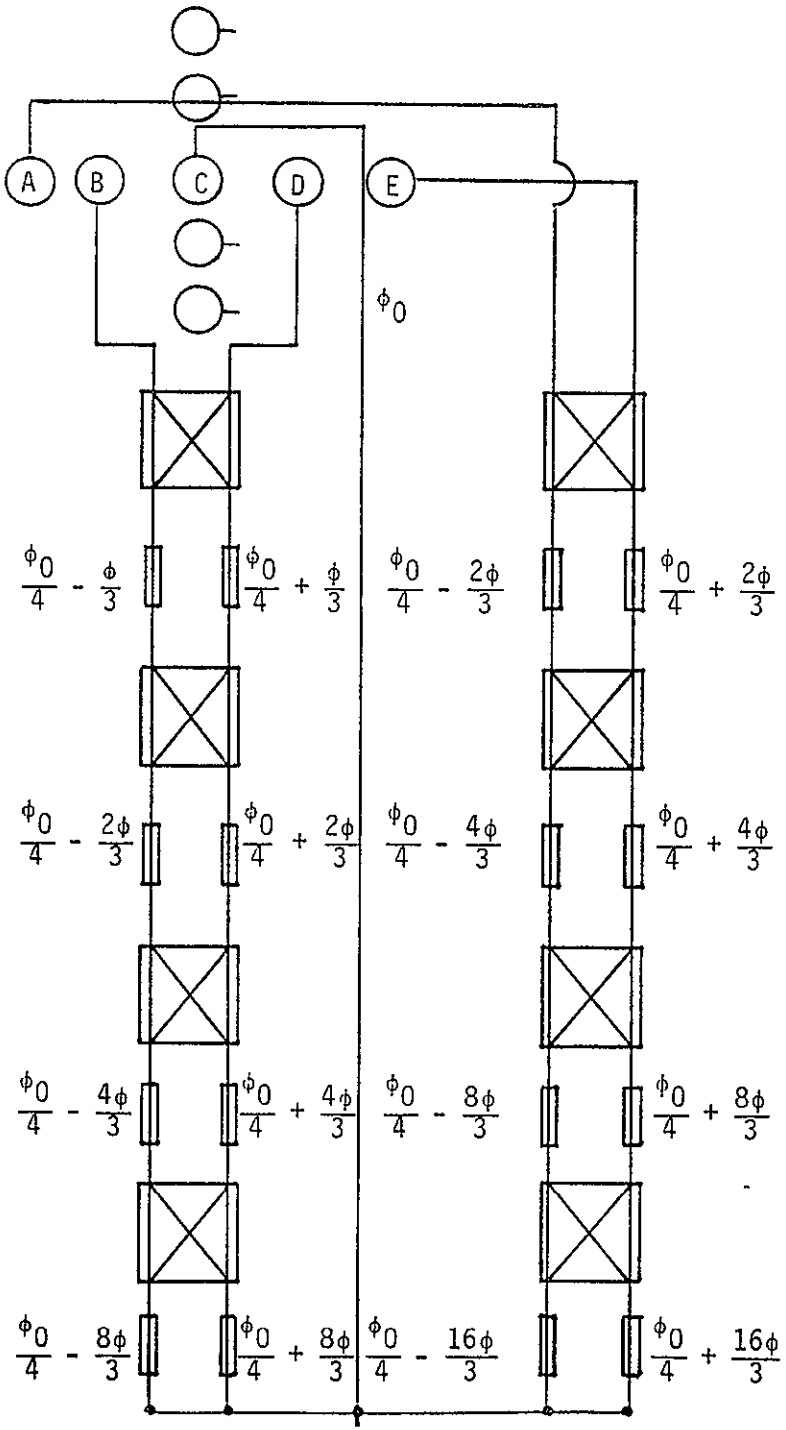

Beam	Element A	Element B	Element D	Element E
1	$\phi_0 - 10\phi$	$\phi_0 - 5\phi$	$\phi_0 + 5\phi$	$\phi_0 + 10\phi$
2	$\phi_0 - \frac{26\phi}{3}$	$\phi_0 - \frac{13\phi}{3}$	$\phi_0 + \frac{13\phi}{3}$	$\phi_0 + \frac{26\phi}{3}$
3	$\phi_0 - \frac{22\phi}{3}$	$\phi_0 - \frac{11\phi}{3}$	$\phi_0 + \frac{11\phi}{3}$	$\phi_0 + \frac{22\phi}{3}$
4	$\phi_0 - 6\phi$	$\phi_0 - 3\phi$	$\phi_0 + 3\phi$	$\phi_0 + 6\phi$
5	$\phi_0 - \frac{14\phi}{3}$	$\phi_0 - \frac{7\phi}{3}$	$\phi_0 + \frac{7\phi}{3}$	$\phi_0 + \frac{14\phi}{3}$
6	$\phi_0 - \frac{10\phi}{3}$	$\phi_0 - \frac{5\phi}{3}$	$\phi_0 + \frac{5\phi}{3}$	$\phi_0 + \frac{10\phi}{3}$
7	$\phi_0 - 2\phi$	$\phi_0 - \phi$	$\phi_0 + \phi$	$\phi_0 + 2\phi$
8	$\phi_0 - \frac{2\phi}{3}$	$\phi_0 - \frac{\phi}{3}$	$\phi_0 + \frac{\phi}{3}$	$\phi_0 + \frac{2\phi}{3}$
9	$\phi_0 + \frac{2\phi}{3}$	$\phi_0 + \frac{\phi}{3}$	$\phi_0 - \frac{\phi}{3}$	$\phi_0 - \frac{2\phi}{3}$
10	$\phi_0 + 2\phi$	$\phi_0 + \phi$	$\phi_0 - \phi$	$\phi_0 - 2\phi$
11	$\phi_0 + \frac{10\phi}{3}$	$\phi_0 + \frac{5\phi}{3}$	$\phi_0 - \frac{5\phi}{3}$	$\phi_0 - \frac{10\phi}{3}$
12	$\phi_0 + \frac{14\phi}{3}$	$\phi_0 + \frac{7\phi}{3}$	$\phi_0 - \frac{7\phi}{3}$	$\phi_0 - \frac{14\phi}{3}$
13	$\phi_0 + 6\phi$	$\phi_0 + 3\phi$	$\phi_0 - 3\phi$	$\phi_0 - 6\phi$
14	$\phi_0 + \frac{22\phi}{3}$	$\phi_0 + \frac{11\phi}{3}$	$\phi_0 - \frac{11\phi}{3}$	$\phi_0 - \frac{22\phi}{3}$
15	$\phi_0 + \frac{26\phi}{3}$	$\phi_0 + \frac{13\phi}{3}$	$\phi_0 - \frac{13\phi}{3}$	$\phi_0 - \frac{26\phi}{3}$
16	$\phi_0 + 10\phi$	$\phi_0 + 5\phi$	$\phi_0 - 5\phi$	$\phi_0 - 10\phi$

Figure 4. Five Element/16-Beam Configuration

three-element array. Note that, since the additional four switches for the outer array are in parallel, negligible additional switching insertion loss occurs. And, if four more elements are added in the orthogonal plane, high gain can be attained in that plane also, and the total number of possible beam positions is then 256.

3.0 VARIABLE GAIN

Further progress in the switched-beam-array technology has resulted in the conceptual development of a variable-gain antenna which can be adjusted for particular mission requirements. For example, on the Centaur five-element biconical array, there may be occasions when high gain is unneeessary for a distant target and it is desirable to have a wider beamwidth with medium gain in order to simplify tracking. In this case, a scheme to switch out the two outer elements has been developed using the same double-pole/double-throw electromechanical latching switches, as shown in Figure 5. Further, extension of the variable-gain technique applies for the low-gain or omnidirectional mode where only the central element radiates. Thus, by adding two switches, it is possible to have low-, medium- and high-gain capabilities with the same array, with very little additional insertion loss.

For the improved version of the Shuttle Orbiter S-band quad antennas, this technique can similarly be used for variable-gain capabilities in both dimensions, as shown in Figure 6. Thus, it is possible to alter the pattern to a desirable shape, such as using high gain in one dimension and low gain in the other in order to form an elongated beam that accommodates a moving target and therefore satisfies the tracking function without any antenna switching.

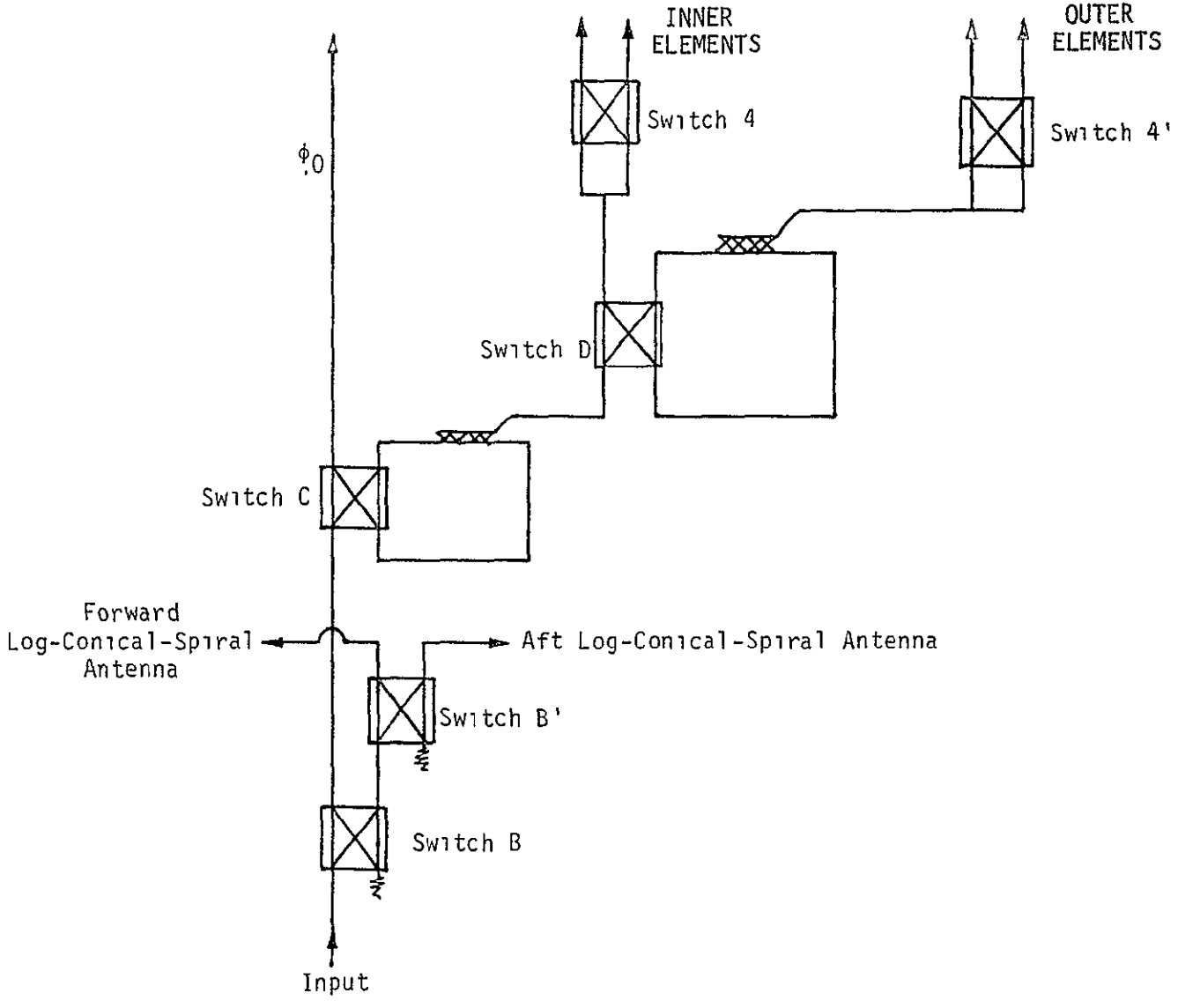

Figure 5 Multimode Antenna-Switching Arrangement

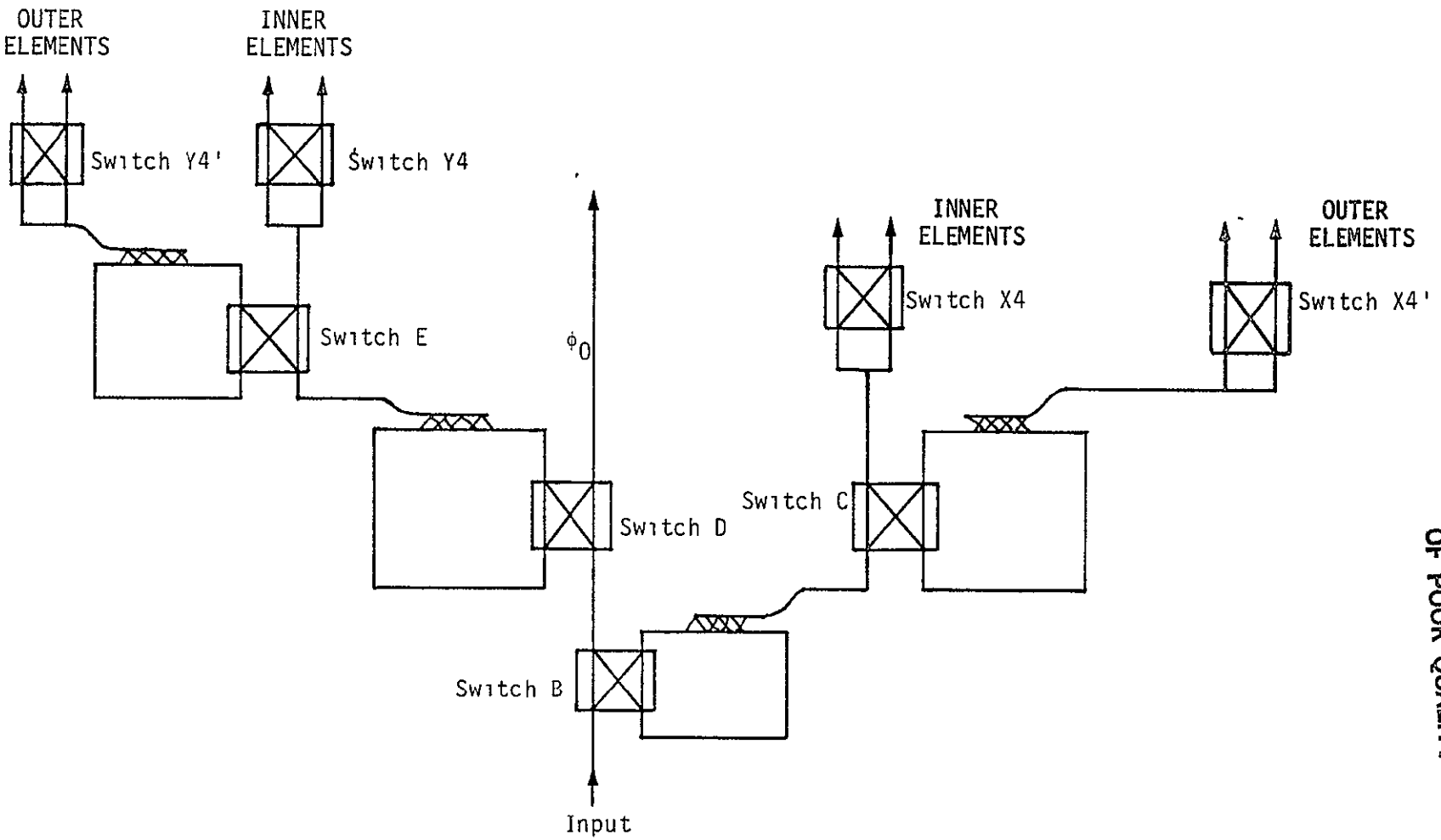

Figure 6. Two-Dimensional Multimode Antenna-Switching Arrangement

Axiomatix

9841 Airport Boulevard • Suite 912 • Los Angeles, California 90045 • Phone (213) 641-8600

TECHNICAL MEMORANDUM NO. M8209-4

TO: Don Eggers DATE: September 30, 1982

FROM: Richard Iwasaki FILE: NAS 9-16067"B"

SUBJECT: Binary Code Designation of Multiple-Switched-Beam Positions

---

One of the important considerations in implementing a variable-gain multiple-switched-beam array is the simplicity of obtaining a desired beam position. It was noted earlier that the electromechanical double-throw switches have a binary nature which can be described by a binary code. For four switches, a beam position in one plane can be characterized by a unique four-digit binary number and, for the two-dimensional case, by eight binary digits in sequence In actuality, only 16 memory locations need to be allocated for this selection process since the orthogonal plane can use the identical binary codes.

As an example, Figure 1 shows the switching arrangement necessary to achieve beam position 4. Using the notation that a "0" represents a "straight-through" switching position and a "1" denotes a "cross-over" switching position and the binary code begins with the switch closest to the radiating elements, the binary code for beam position 4 is 1010. Note that the switching arrangement is identical for the inner and outer elements so that, if the high-gain, five-element array is used, no modifications will be required Table 1 lists the remaining binary codes for the other beam positions

For the two-dimensional cross array, the beam position is specified first by the X-plane beam position, then by the Y-plane beam position, as depicted in Figure 2, which has a total of 256 beam positions. If the cross-hatch beam position designated by 4,15 is desired, the appropriate binary code is simply 10100100, where the first four digits characterize beam position 4 in the X-plane and the last four digits characterize beam position 15 in the Y-plane.

Copies NAS9-16067"B" Distribution
H. Ellis, RI
S. Wong, RI

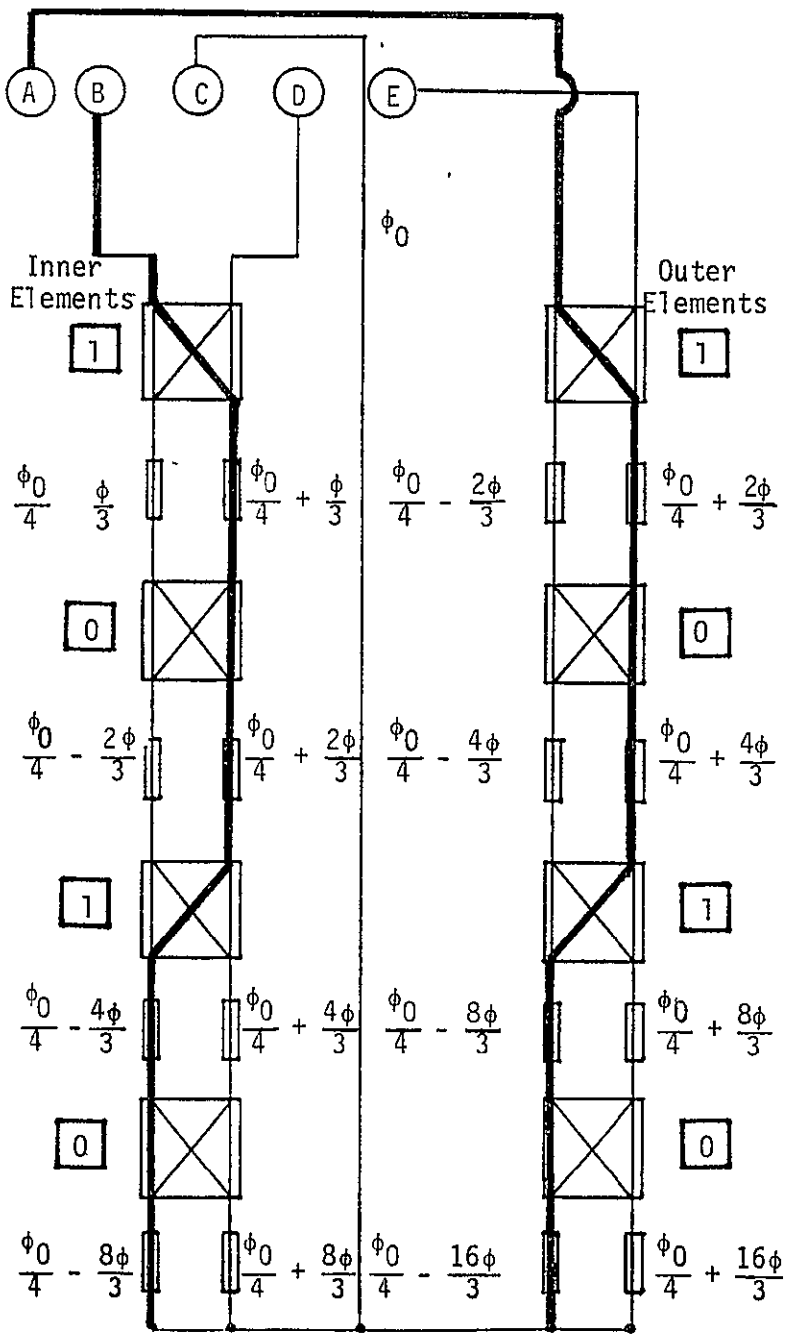

Beam	Element A	Element B	Element D	Element E	Binary Code
1	$\phi_0 - 10\phi$	$\phi_0 - 5\phi$	$\phi_0 + 5\phi$	$\phi_0 + 10\phi$	
2	$\phi_0 - \frac{26\phi}{3}$	$\phi_0 - \frac{13\phi}{3}$	$\phi_0 + \frac{13\phi}{3}$	$\phi_0 + \frac{26\phi}{3}$	
3	$\phi_0 - \frac{22\phi}{3}$	$\phi_0 - \frac{11\phi}{3}$	$\phi_0 + \frac{11\phi}{3}$	$\phi_0 + \frac{22\phi}{3}$	
4	$\phi_0 - 6\phi$	$\phi_0 - 3\phi$	$\phi_0 + 3\phi$	$\phi_0 + 6\phi$	1010
5	$\phi_0 - \frac{14\phi}{3}$	$\phi_0 - \frac{7\phi}{3}$	$\phi_0 + \frac{7\phi}{3}$	$\phi_0 + \frac{14\phi}{3}$	
6	$\phi_0 - \frac{10\phi}{3}$	$\phi_0 - \frac{5\phi}{3}$	$\phi_0 + \frac{5\phi}{3}$	$\phi_0 + \frac{10\phi}{3}$	
7	$\phi_0 - 2\phi$	$\phi_0 - \phi$	$\phi_0 + \phi$	$\phi_0 + 2\phi$	
8	$\phi_0 - \frac{2\phi}{3}$	$\phi_0 - \frac{\phi}{3}$	$\phi_0 + \frac{\phi}{3}$	$\phi_0 + \frac{2\phi}{3}$	
9	$\phi_0 + \frac{2\phi}{3}$	$\phi_0 + \frac{\phi}{3}$	$\phi_0 - \frac{\phi}{3}$	$\phi_0 - \frac{2\phi}{3}$	
10	$\phi_0 + 2\phi$	$\phi_0 + \phi$	$\phi_0 - \phi$	$\phi_0 - 2\phi$	
11	$\phi_0 + \frac{10\phi}{3}$	$\phi_0 + \frac{5\phi}{3}$	$\phi_0 - \frac{5\phi}{3}$	$\phi_0 - \frac{10\phi}{3}$	
12	$\phi_0 + \frac{14\phi}{3}$	$\phi_0 + \frac{7\phi}{3}$	$\phi_0 - \frac{7\phi}{3}$	$\phi_0 - \frac{14\phi}{3}$	
13	$\phi_0 + 6\phi$	$\phi_0 + 3\phi$	$\phi_0 - 3\phi$	$\phi_0 - 6\phi$	
14	$\phi_0 + \frac{22\phi}{3}$	$\phi_0 + \frac{11\phi}{3}$	$\phi_0 - \frac{11\phi}{3}$	$\phi_0 - \frac{22\phi}{3}$	
15	$\phi_0 + \frac{26\phi}{3}$	$\phi_0 + \frac{13\phi}{3}$	$\phi_0 - \frac{13\phi}{3}$	$\phi_0 - \frac{26\phi}{3}$	
16	$\phi_0 + 10\phi$	$\phi_0 + 5\phi$	$\phi_0 - 5\phi$	$\phi_0 - 10\phi$	

Figure 1. Switching Arrangement for Beam Position 4

Table 1. Binary Codes for the 16 Beam Positions

Beam Position	Binary Code			
1	0	0	0	0
2	1	1	0	0
3	0	1	1	0
4	1	0	1	0
5	0	0	1	1
6	1	1	1	1
7	0	1	0	1
8	1	0	0	1
9	0	0	0	1
10	1	1	0	1
11	0	1	1	1
12	1	0	1	1
13	0	0	1	0
14	1	1	1	0
15	0	1	0	0
16	1	0	0	0

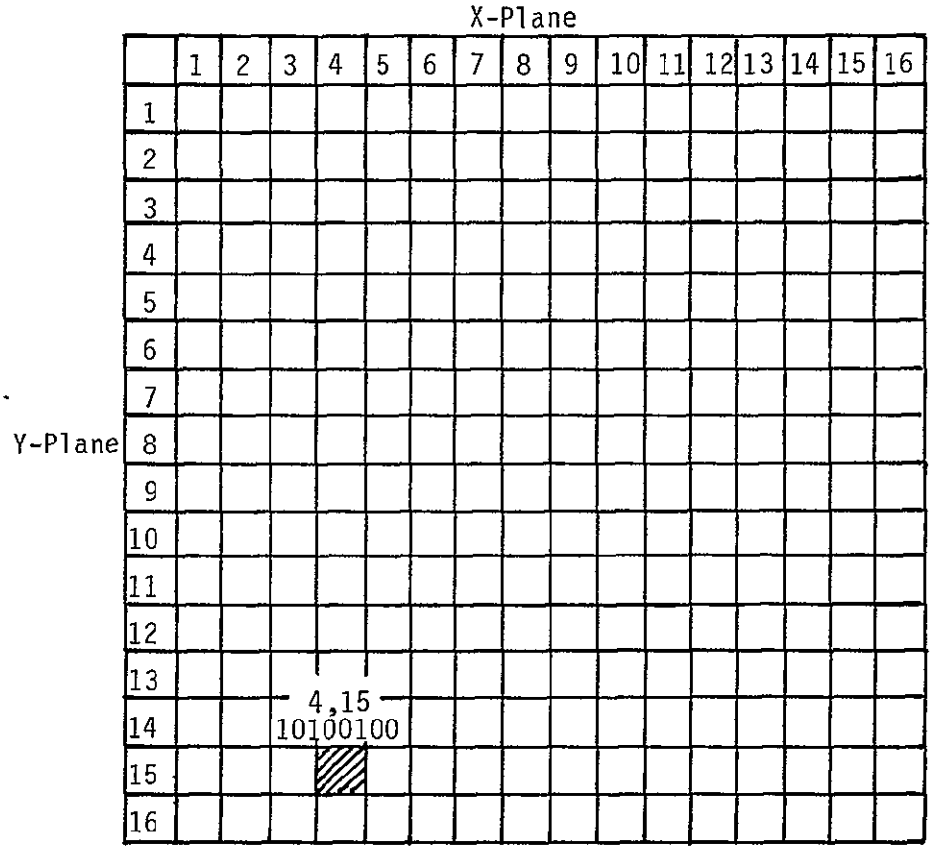

Figure 2. 256-Beam-Position Selection Using Binary Codes

Axiomatix

9841 Airport Boulevard • Suite 912 • Los Angeles, California 90045 • Phone (213) 641-8600

TECHNICAL MEMORANDUM NO. M8209-5

TO: Richard Iwasaki DATE: September 30, 1982

FROM. Jim Dodds FILE· NAS 9-16067"B"

SUBJECT: Simplification of Antenna Beam-Switching Logic

The switched-beam array described in Axiomatix Technical Memorandum No. M8209-4 requires that the beam position be mapped into a binary code in order to control a set of phase-shifting elements. This can be effected by using one of the following methods: (1) a microprocessor to access one of 16 memory locations, each of which contains a four-bit code, (2) a programmable logic array or, (3) hard-wired logic. The format of the conversion from four input bits to four output bits is particularly simple in this application and can be implemented with the EXCLUSIVE-OR gates, as can be shown by inspection, or by using Karnaugh maps.

Table 1 of M8209-4 is reproduced below, with the ordinal beam positions represented by four-bit binary sequences b_0, b_1, b_2, b_3. The binary output is represented as a four-bit code a_0, a_1, a_2, a_3.

INPUT					OUTPUT			
Beam Position	Binary Code				Binary Code			
	b_0	b_1	b_2	b_3	a_0	a_1	a_2	a_3
1	0	0	0	0	0	0	0	0
2	0	0	0	1	1	1	0	0
3	0	0	1	0	0	1	1	0
4	0	0	1	1	1	0	1	0
5	0	1	0	0	0	0	1	1
6	0	1	0	1	1	1	1	1
7	0	1	1	0	0	1	0	1
8	0	1	1	1	1	0	0	1
9	1	0	0	0	0	0	0	1
10	1	0	0	1	1	1	0	1
11	1	0	1	0	0	1	1	1
12	1	0	1	1	1	0	1	1
13	1	1	0	0	0	0	1	0
14	1	1	0	1	1	1	1	0
15	1	1	1	0	0	1	0	0
16	1	1	1	1	1	0	0	0

The phase shift logic can be implemented as shown below for both the X-plane and Y-plane logics, with $a_0 = b_3$, $a_1 = b_2 \oplus b_3$, $a_2 = b_1 \oplus b_2$ and $a_3 = b_0 \oplus b_1$. As can be seen, only three mod-2 (EXCLUSIVE-OR) adders are needed per plane.

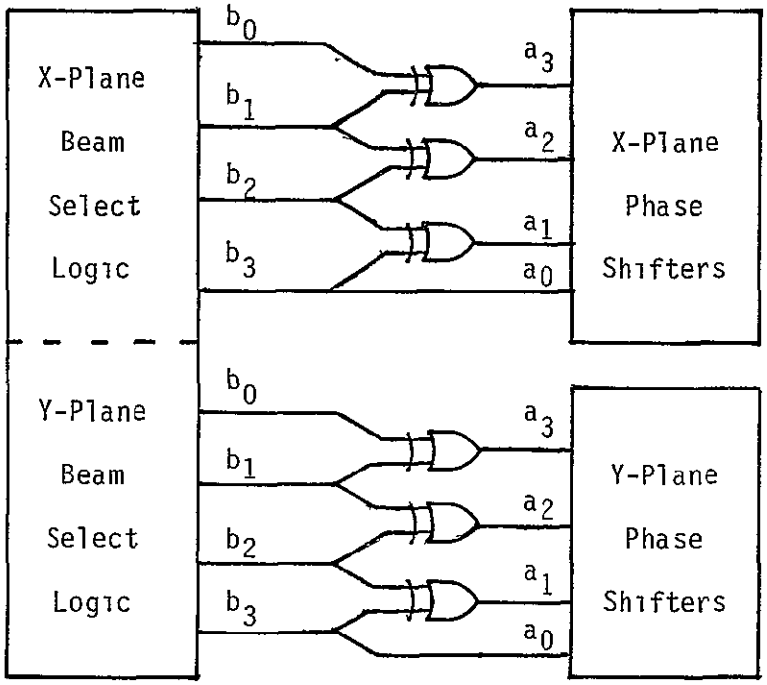

Copies NAS 9-16067 "B" Distribution
Haynes Ellis, RI
Sam Wong, RI

9.0 PAYLOAD COMMUNICATIONS INVESTIGATIONS

The major thrust of Axiomatix investigations of payload communications centered on the payload signal processor (PSP) bit-synchronizer problem. During ESTL tests, it was found that the TRW PSP bit synchronizer would false lock under high SNR conditions. This pnenomenon was subsequently duplicated at RI, ADL and TRW.

Axiomatix efforts to analyze this problem included numerous conversations with Brett Parrish of JSC, Larry Stein and Rich Helgeson of TRW, and Mike Rueterman of RI, as well as attendance at meetings and hardware demonstrations. Axiomatix has analyzed the algorithm lock-detector-threshold parameter for optimality over SNR's ranging from low to high as well as carefully evaluating the entire algorithm. A recommendation was made to change both the threshold parameter and the filter bandwidths, computer simulations later indicated an improvement in performance with the new parameter values.

The technical memoranda which follow document the analyses performed and meetings attended by Axiomatix personnel on this problem.

Axiomatix

9841 Airport Boulevard • Suite 912 • Los Angeles, California 90045 • Phone (213) 641-8600

TECHNICAL MEMORANDUM NO. M8206-1

TO: G. Huth DATE: June 18, 1982

FROM: J. Holmes

SUBJECT: PSP Bit Synchronizer NRZ False-Lock Status--Interim Report

REFERENCES: (1) Telephone Conversations with Brett Parrish (NASA/JSC), Larry Stein (TRW), and Rich Helgeson (Consultant)

(2) Abbreviated Flow Chart for the PSP Bit Synchronizer Algorithm, by Brett Parrish

- -

1.0 INTRODUCTION

During recent ESTL tests, it was found that the TRW PSP bit synchronizer would false lock under high SNR conditions. This phenomenon was subsequently duplicated at RI, ADL and TRW Axiomatix has begun to analyze the problem. This effort has included numerous conversations with Brett Parrish of JSC, Larry Stein and Rich Helgeson of TRW, and Mike Reuterman of RI, as well as attendance at meetings and hardware demonstrations. Axiomatix is analyzing the algorithm threshold parameter for optimality over SNR's ranging from low to high as well as carefully evaluating the entire algorithm. This interim report documents the findings to date concerning this problem.

2.0 STATUS SUMMARY

(1) Brett Parrish has determined that the summation used in the filter computation of the mid-phase filter* overflows at high SNR such that the algebraic sign of the phase update control changes and therefore provides a stable lock point at nominally 180° away from the true-lock point (a half-bit error) Brett has also demonstrated at JSC that, by prohibiting the overflow and associated algebraic sign change, the false-lock condition at ~180° will not occur This fact has been verified by Rich Helgeson with the TRW program simulation

*FSTB2+PRTB2 doesn't have overflow protection on page 2 of Brett's brief algorithm.

(2) Rich Helgeson and others have determined that a "lack-of-a-transition" detector must be added (on page 2 of the brief flow chart). This is because, for example, if the data were turned off, no transitions would occur so that it is impossible for the lock detector to enter the out-of-lock state and, therefore, to return to the acquisition mode. According to Larry Stein, this detector, which counts nontransitions, can be implemented without a great deal of trouble. Most probably, it is also a problem when the subcarrier or the carrier drops out temporarily.

(3) The offset in both the true-lock and false-lock points can be attributed to the fact that, at high SNR, the A/D converter outputs its maximum value of ±3 (in binary-twos complement) so that 64 samples of the maximum value limit at about two thirds of the way across a presum, or about 43 samples. The remaining samples are, in effect, discarded. Although this problem is disconcerting, the author does not believe that it must be fixed immediately, if at all, since the main effect is to induce a static phase (or timing) error at either the true-lock or false-lock point. Larry Stein has indicated that it is possible to fix the problem by allowing only 16 samples per presum to accumulate, then scaling the sum of the presums so that it will not overflow in an eight-bit register

(4) Manchester data does not produce false phase lock Possibly, this is because, with NRZ data and a ~180° error offset, the sum of the mid-phase signal can roll over and change sign, providing a stable ~180° error whereas, in the Manchester case, there is always a transition at (true) mid-phase so that, at least for transition densities not equal to zero or 100%, Manchester data is tested for ~180° false lock in the algorithm and would be rejected

(5) The automatic gain control (AGC) used for the A/D converter is done in a 5-MHz bandwidth, but the input is then filtered by a 250-kHz filter which makes this signal poorly AGC'd since the signal component will increase at high SNR's in such a way as to produce a level larger than the A/D range.

(6) It appears that the "very small timing error" test performed in the bit synchronizer algorithm (which is indicated on page 3 of Brett's short algorithm just below the NTSPC transition count from the last phase correction)

is not required and could be eliminated if necessary in order to implement the changes required in items (1) and (2). This check bypasses a phase update correction if the error is small enough; otherwise, it does nothing.

2.0 CONCLUSIONS

It is the opinion of the author (and others) that it is important to fix only items (1) and (2) in order that the bit synchronizer will not exhibit false lock, namely, change the mid-phase summation of FSTB2 and PRTB2 so that it will not roll over to the opposite algebraic sign, then add a nontransition counter to limit the number of nontransitions which can occur before the algorithm declares that the loop is out of lock Neither "fix" appears to be a major problem. It would be desirable to fix item (3), the saturation in the presum, but this item is not related to false-lock avoidance. Also, item (5) is not an important item and probably should not be changed if its space in the microprocessor is not needed.

Any additional comments, observations or corrections should be indicated to the author so that a revised memorandum can be written prior to the next meeting at TRW scheduled for early July.

Distribution:
R. Helgeson, Consultant
J. Johnson, NASA/JSC
S. May, TRW
B. Parrish, NASA/JSC
T. Pederson, TRW
M Reuterman, Rockwell

Axiomatix

9841 Airport Boulevard • Suite 912 • Los Angeles, California 90045 • Phone (213) 641 8600

TECHNICAL MEMORANDUM NO. M8206-4

TO: G. Huth DATE: June 30, 1982

FROM: J. Holmes

SUBJECT: PSP NRZ Lock Detector and Loop Control Signal
Phase Error Range of Operation at High SNR--Interim Report

1.0 INTRODUCTION

This is the second technical memorandum/interim report that concerns the PSP bit synchronizer false-lock problem. The causes of the false lock are considered based on analyzing the bit synchronizer and lock detector, but not considering the DC bias removal algorithm It appears that, at least at high SNR, the lock detector constant (6.5) should be increased. In order to enable us to choose the best value of the lock detector constants, an analysis is continuing and documentation will be forthcoming.

2.0 SUMMARY

The error control signal and the lock detector test for the PSP S-band bit synchronizer has been analyzed at high SNR for the 8-kbps data rate case by hypothesizing various fixed phase errors and evaluating the inphase and midphase filter outputs. It is to be noted that DC bias removal was not considered in this analysis.

It was found that the lock detector indicates an in-lock condition anywhere within a phase error of zero to about ±75° (±21% of a bit, which is considered too large) Furthermore, the lock detector will indicate an in-lock condition between about 104° and somewhat less than 130° (and between -104° and ~ -130°) and also between 150° and 210°.

The error control signal of the bit synchronizer loop pushes the loop in the wrong direction when the phase error is between 90° and 150°, which is due to the unprotected overflow of the midphase addition.

This control signal reversal causes the false-lock condition The in-lock indication between a phase error of 150° and 210° can be removed by prohibiting the saturation of the presums.

It is expected that the above two problems will occur at the other data rates as well, although they have not yet been analyzed in detail.

3.0 RECOMMENDATIONS

Based on this preliminary study, it is felt that, at least at high SNR, the lock detector constant of 6.5 is too small and should be increased since this value allows large timing errors (±21%) to be declared in lock. It might be desirable to provide different constants for different data rates as well as for low or high SNR conditions. Further analysis aimed at recommending values for this constant is currently underway.

Also, overflow protection must be provided for the midphase summation and the presums should be modified to prevent limiting.

4.0 ANALYSIS

We consider the lock detector test given in [1] as

$$AVIN > 6.5|AVMI| \tag{1}$$

where AVIN and AVMI are lowpass filtered versions of the inphase and midphase summers, respectively. Basically, the idea of the lock detector test given by (1) is to announce when the PSP bit synchronizer loop is in or out of lock.

In Figure 1, a simplified block diagram illustrates some details of the bit synchronizer loop. First note that all presums and adders outside the microprocessor are combined with two's-complement arithmetic with overflow protection. Internally, the inphase (AVIN) signal is formed with two's-complement combining with overflow protection, whereas the midphase combining is done with two's-complement combining without overflow protection!

The loop uses a filtered version of the output error to correct the timing of the loop, with the addition of a rate-aiding component which attempts to remove small doppler errors (rate tracking).

In order to analyze the lock detector, it is necessary to analyze the value of AVIN, AVMI and TRIND, which is the variable that indicates whether a positive, negative or lack of transition has just occurred We now consider various phase error angles Table 1 lists the data rate, samples per presum, fractions of a bit for a presum, samples per bit, and whether or not the number of samples saturates the presum.

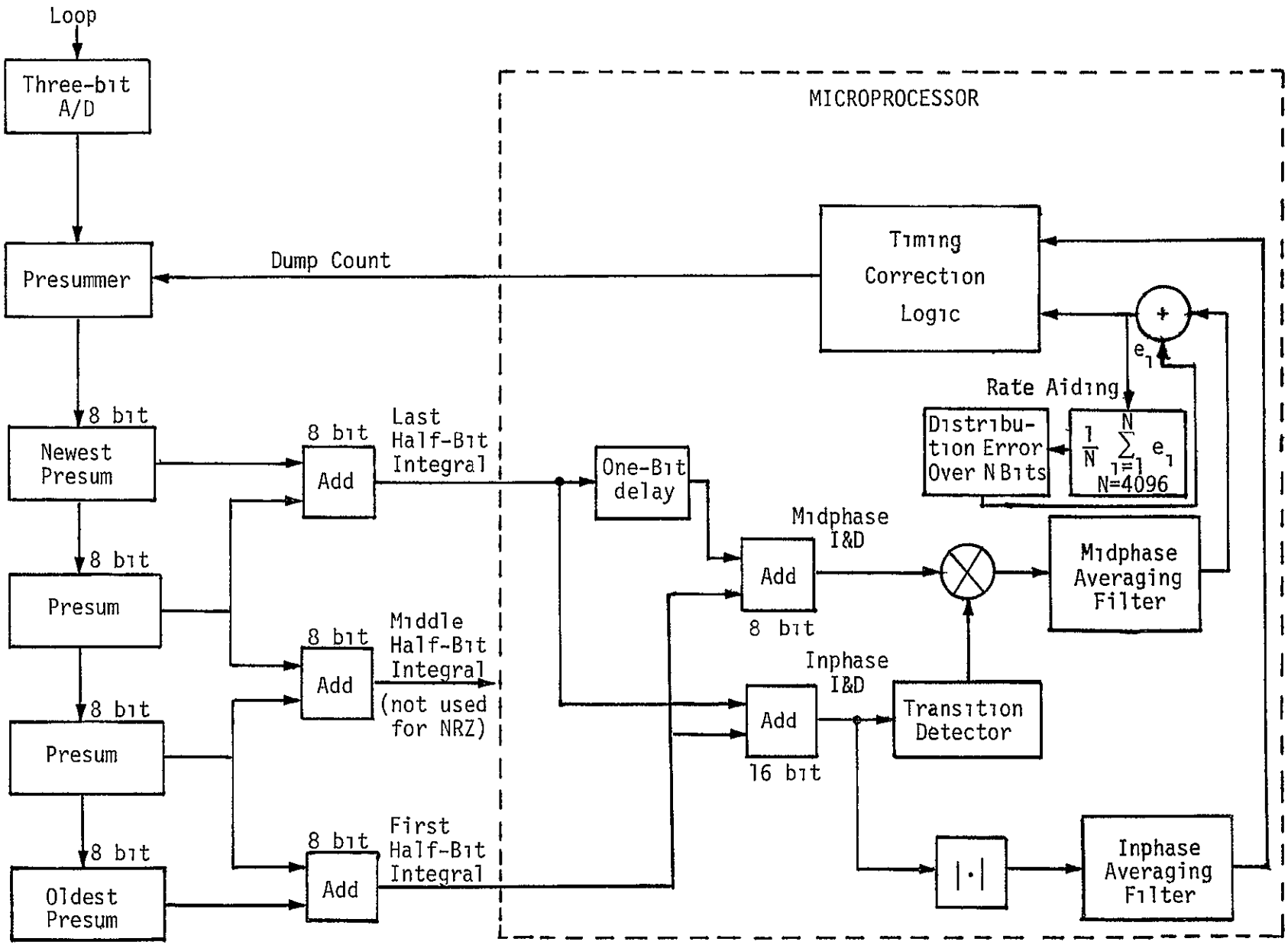

Figure 1. PSP Data Transition Tracking Loop for NRZ Data

Table 1. Samples Per Bit Versus Data Rate Matrix

R_b	Samples/ Sum	Fraction of a Bit	Samples/ Bit	Presum Saturated?
16 kbps	16	1/4	64	No
8 kbps	32	1/4	128	No
4 kbps	64	1/4	256	Yes
2 kbps	64	1/8	512	Yes
1 kbps	64	1/16	1024	Yes

4 1 $\phi = 0°$, 8 kbps

Denote $\boxplus$ as two's-complement addition (or subtraction) with overflow protection and $\boxplus$ as two's-complement addition without overflow protection. Based on Figure 2 and Table 1, we can write

$$AVIN^{(n+1)} = L_I AVIN^{(n)} + |96 \boxplus 96| \tag{2}$$

since the two's complement has a maximum of 127 and a minimum of -128. Therefore,

$$AVIN^{(n+1)} = 127 \sum_{i=0}^{n} L_I^i \tag{3}$$

Solving (3) yields

$$AVIN^{(n+1)} = 127\left[\frac{1 - L_I^{n+1}}{1 - L_I}\right] \tag{4}$$

For large n, $AVIN^{(n)}$ converges to

$$AVIN^{(n)} \rightarrow \frac{127}{1 - L_I}$$

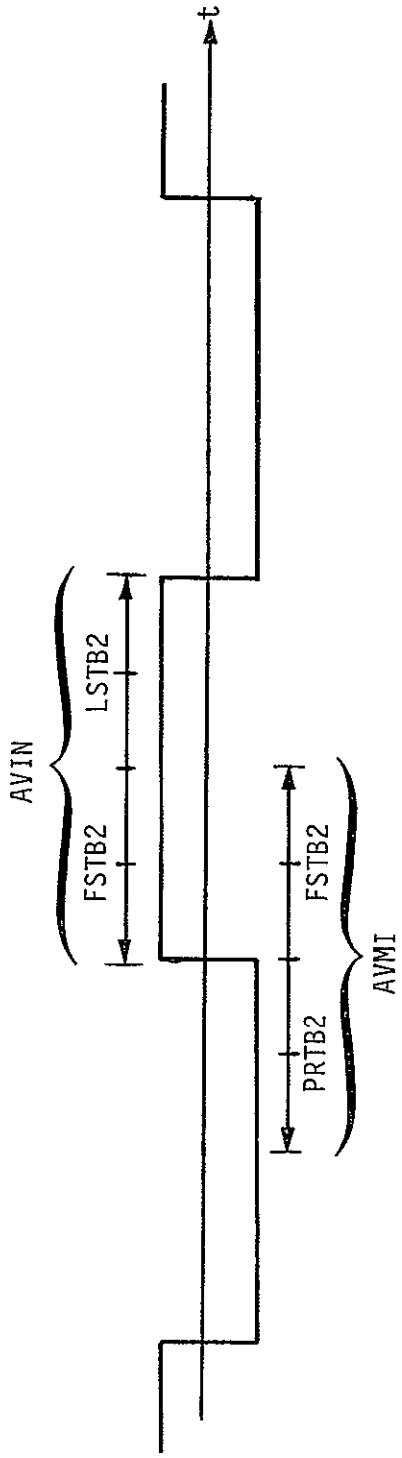

Figure 2 Phase Error Relationship for $\phi = 0°$ (Zero Timing Error)

For the lowpass filter defined by (2), $L_I = 0.99$ so that

$$AVIN^{(n)} \rightarrow 12700 \text{ or } 12800 \tag{5}$$

or an average of

$$AVIN^{(n)} = 12750 \tag{6}$$

The bit transition decision variable (TRIND) takes on the value of 1, -1 or 0 according to whether the bit goes from negative to positive, positive to negative, or does not change. Now consider the midphase integration (AVMI) for the situation depicted in Figure 2. We have (TRIND = 1)

$$AVMI^{(n+1)} = L_M\, AVMI^{(n)} + |FSTB2 + LSTB2| \tag{7}$$

Now, when centered at zero phase error, the value of FSTB2 = 127 and PRTB2 = -128 so that we have

$$AVMI^{(n+1)} = L_M\, AVMI^{(n)} = (-128 \boxplus 127) \tag{8}$$

Solving (8) yields ($-128 \boxplus 127 = -1$)

$$AVMI^{(n)} = -\frac{\left(1 - (L_M)^n\right)}{1 - L_M}, \quad L_M = 0.95 \tag{9}$$

Hence, for large n, we have

$$AVMI^{(n)} \rightarrow \frac{-1}{1 - L_M} = -20 \tag{10}$$

The lock detector makes the comparison

$$AVIN \overset{?}{>} |AVMI| \tag{11}$$

which, in our present case, leads to

$$12{,}750 \overset{?}{>} 20(6.5) = 130 \tag{12}$$

Consequently, the loop is declared in lock.

4.2 $\phi = 45°$, 8 kbps

Consider Figure 3, which illustrates a 45° phase error (1/8-bit timing error). We find that

$$AVIN^{(n+1)} = L_I\, AVIN^{(n)} + |96 \boxplus (96 \boxplus 96)| \tag{13}$$

or

$$AVIN^{(n+1)} = L_I\, AVIN^{(n)} + 127 \tag{14}$$

where, for convenience, we have assumed a positive bit in the AVIN interval* Solving, we obtain

$$AVIN^{(n)} \longrightarrow 12700 \tag{15}$$

Since TRIND = 1, we have

$$AVMI^{(n+1)} = L_M\, AVMI^{(n)} + [(-96 \boxplus -96) \boxplus (-48 + 48 \boxplus 96)] \tag{16}$$

or

$$AVMI^{(n+1)} = L_M\, AVMI^{(n)} - 32 \tag{17}$$

Solving, we obtain

$$AVMI^{(n)} \rightarrow \frac{-32}{0.05} = 640 \tag{18}$$

*We use this assumption in what follows.

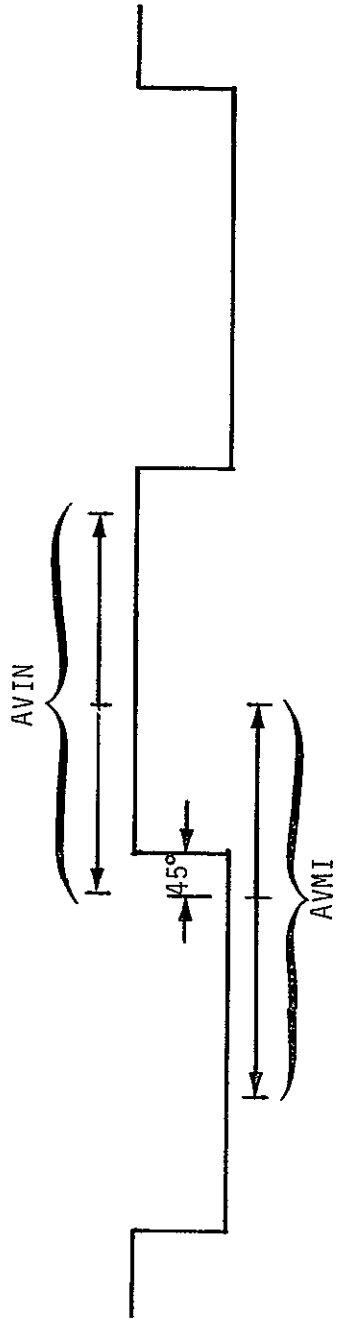

Figure 3 Phase Error Relationship for $\phi = 45°$ (1/8 of a Bit)

The bit synchronizer lock detector comparison is given by

$$12700 \overset{?}{>} 640\ (6.5) \quad = \quad 4160 \tag{19}$$

so the lock detector again declares an in-lock condition.

4.3 $\phi = 67.5°$, 8 kbps

Now consider Figure 4, which illustrates the case when $\phi = 67.5°$. For the inphase component, we have

$$AVIN^{(n+1)} = L_I\ AVIN^{(n)} + |((-72+24) \boxplus 96) \boxplus (127)| \tag{20}$$

or

$$AVIN^{(n+1)} = L_I\ AVIN^{(n)} + |127| \tag{21}$$

or solving

$$AVIN^{(n)} \rightarrow 12700 \tag{22}$$

The midphase recursion relationship is given by (TRIND = 1)

$$AVIN^{(n+1)} = L_M\ AVMI^{(n)} + [-128 \boxplus (-72+24) \boxplus 96] \tag{23}$$

This yields

$$AVMI^{(n+1)} = L_M\ AVMI^{(n)} - 80 \tag{24}$$

Solving, we obtain

$$AVMI^{(n)} \rightarrow \frac{-80}{0.05} = -1600 \tag{25}$$

The lock detector test is given by

$$12700 \overset{?}{>} (1600)(6.5) \quad = \quad 10,400 \tag{26}$$

Hence, the lock detector declares that the bit synchronizer loop is still in lock.

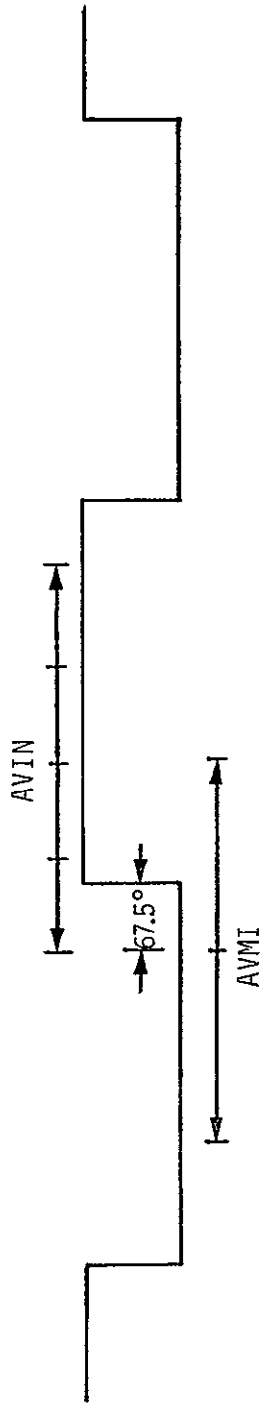

Figure 4 Phase Error Relationship for $\phi = 67.5°$ (0.188 of a Bit)

4.4 $\phi = 75°$, 8 kbps

Figure 5 illustrates the case in which the phase error is 75°. Again it can be shown that

$$AVMI^{(n)} \longrightarrow 12700 \tag{27}$$

and, further, that TRIND = 1 so that, for the midphase signal, we have

$$AVMI^{(n+1)} = L_M\, AVMI^{(n)} + |-128 \boxplus ((-80+16) \boxplus 96)| \tag{28}$$

which can be evaluated to be

$$AVMI^{(n+1)} = L_M\, AVMI^{(n)} - 96 \tag{29}$$

Therefore, for large n, we have

$$AVMI^{(n)} \longrightarrow \frac{-96}{0.05} = -1920 \tag{30}$$

Checking the lock detection equation, we have

$$12700 \overset{?}{>} 1920\ (6.5) = 12480 \tag{31}$$

which indicates that the lock detector is almost ready to declare the bit synchronizer out of lock! It can be shown that the out-of-lock condition for a positive transition occurs at 76°

4.5 $\phi = 90°$, 8 kbps

Now we consider the case when $\phi = 90°$, as shown in Figure 6. It can again be shown that

$$AVIM^{(n)} \longrightarrow 12700 \tag{32}$$

so we now consider the midphase component We have

$$AVMI^{(n+1)} = L_M\, AVMI^{(n)} + [(-96 \boxplus -96) \boxplus (-96 \boxplus 96)] \tag{33}$$

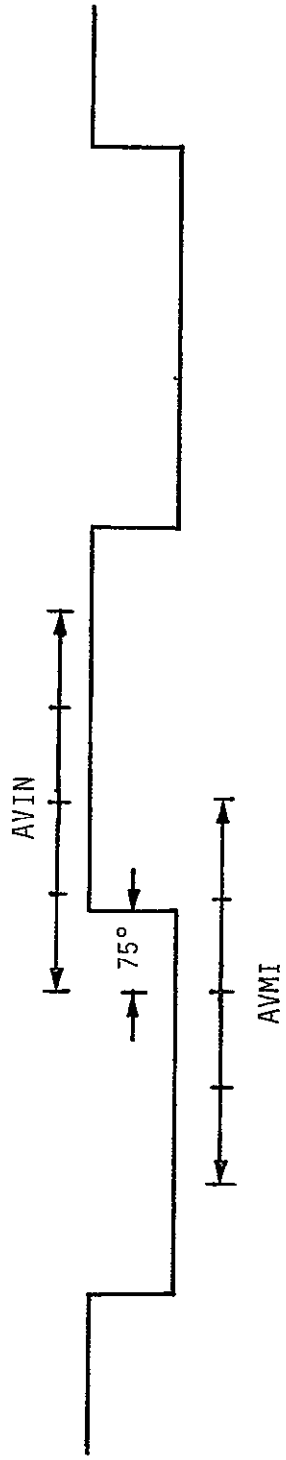

Figure 5 Phase Error Relationship for $\phi = 75°$ (0.21 of a Bit)

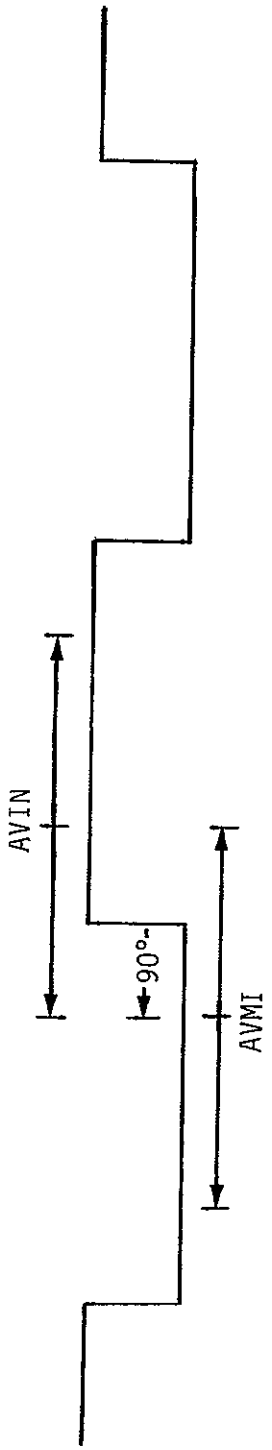

Figure 6 Phase Error Relationship for $\phi = 90°$ (1/4 of a Bit)

so that

$$AVMI^{(n+1)} = L_M\, AVMI^{(n)} + [-128] \tag{34}$$

Solving, we find that

$$AVMI^{(n)} \rightarrow \frac{-128}{0.05} = -2560 \tag{35}$$

Checking the lock detector function, we obtain

$$12700 \overset{?}{>} (2560)(6.5) = 16640 \tag{36}$$

and the lock detector still declares that the loop is out of lock.

4.6 $\phi = 135°$, 8 kbps

We now consider the case when $\phi = 135°$. Consider Figure 7. We have that (TRIND = 1)

$$AVIN^{(n+1)} = L_I\, AVIN^{(n)} + |(-96 \boxplus 0) \boxplus (96 \boxplus 96)| \tag{37}$$

or

$$AVIN^{(n+1)} = L_I\, AVIN^{(n)} + 31 \tag{38}$$

Solving, we obtain

$$AVIN^{(n)} \rightarrow +3100 \tag{39}$$

Now $AVIN^{(n)}$ satisfies

$$AVMI^{(n+1)} = L_M\, AVMI^{(n)} + ((-96 \boxplus -96) \boxplus (-96 \boxplus 0)) \tag{40}$$

or

$$AVMI^{(n+1)} = L_M\, AVMI^{(n)} + (-128 \boxplus -96) \tag{41}$$

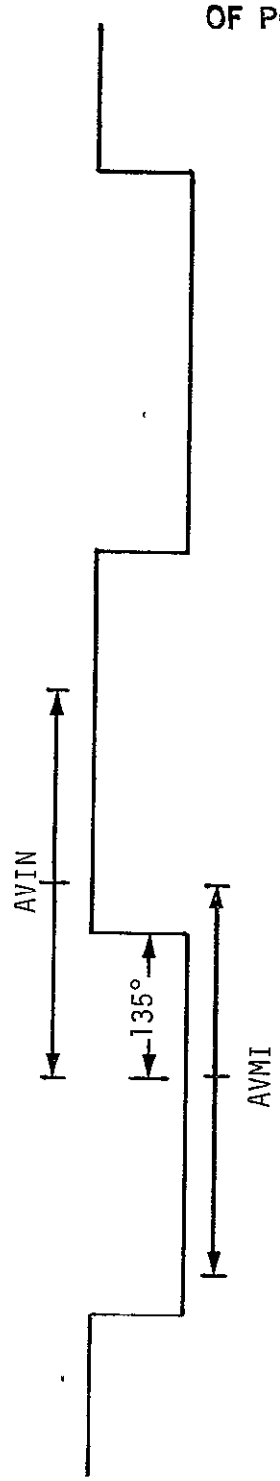

Figure 7 Phase Error Relationship for $\phi = 135°$ (0 375 of a Bit)

Simplifying, we have

$$AVMI^{(n+1)} = L_M\, AVMI^{(n)} + 32 \tag{42}$$

Solving (42) produces -128 $\boxplus$ -96 = +32 since the subtraction is not protected. In the limit, we have

$$AVMI^{(n)} \rightarrow \frac{32}{0.05} = 640 \tag{43}$$

The lock detector test yields

$$3100 \overset{?}{>} 6.5\ (640) = 4160 \tag{44}$$

which implies that the loop is declared out of lock at $\phi = 135°$! Additionally, the error control increases the phase error since the algebraic sign of the correction is now positive. In fact, a little reflection will indicate that the error signal is positive between $90^{+°}$ and 135°; furthermore, the lock detector is satisfied in a region between 104° and ~130°.

4.7 $\phi = 145°$, 8 kbps

Consider the case when $\phi = 145°$, which is illustrated in Figure 8. Considering AVIN, we have that

$$AVIN^{(n+1)} = L_I\, AVIN^{(n)} + \left|\left(-96 \boxplus \left(96\ \frac{55-35}{90}\right)\right) \boxplus (96 \boxplus 96)\right| \tag{45}$$

or

$$AVIN^{(n+1)} = L_I\, AVIN^{(n)} + |-117 + 127| \tag{46}$$

so that

$$AVIN^{(n+1)} = L_I\, AVIN^{(n)} + 10 \tag{47}$$

Solving, we obtain

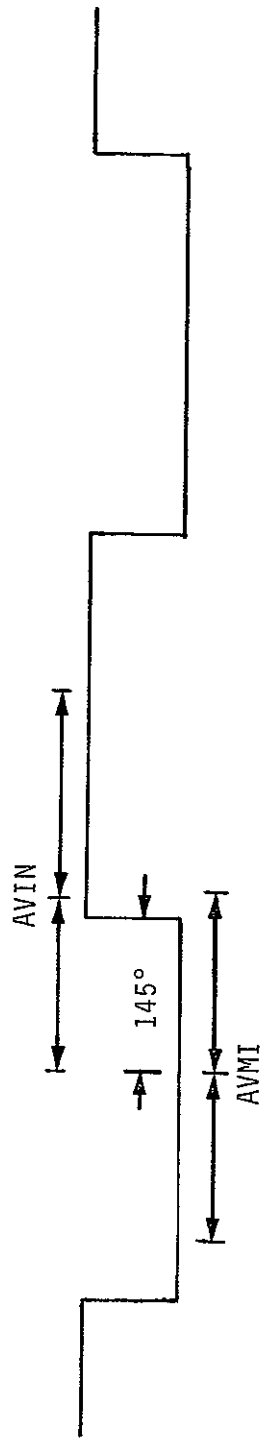

Figure 8. Phase Error Relationship for $\phi = 145°$ (0.4 of a Bit)

$$AVIN^{(n)} \rightarrow \frac{10}{0.01} = 1000 \tag{48}$$

Since TRIND = 1, we have

$$AVMI^{(n+1)} = L_M\, AVMI^{(n)} + \left((-96 \boxplus -96) \boxplus \left(-96 \boxplus -96\ \frac{55-35}{90}\right)\right) \tag{49}$$

Evaluating, we obtain

$$AVMI^{(n+1)} + L_M\, AVMI^{(n)} + 11 \tag{50}$$

so that

$$AVMI^{(n)} \rightarrow \frac{11}{0.05} = 220 \tag{51}$$

The lock detector test produces

$$1000 \overset{?}{>} (220)(6\ 5) = 1430 \tag{52}$$

which indicates that the loop is out of lock.

4.8 $\phi = 150°$, 8 kbps

In the same manner as that computed above, we find that

$$AVIN^{(n)} \rightarrow 100 \quad , \quad TRIND = 0 \quad ; \quad AVMI^{(n)} \rightarrow 0 \tag{53}$$

so that there is no update signal, however, the lock detector signal is satisfied and declares that the loop is in lock.

4.9 $\phi = 158°$, 8 kbps

In the same manner, we can show that

$$AVIN^{(n)} \rightarrow 100 \quad ; \quad TRIND = 0 \quad , \quad AVMI^{(n)} \rightarrow 0 \tag{54}$$

and again there is no update signal and the lock detector test declares a locked condition. It appears that $AVMI^{(n)}=0$ out to $\phi = 180°$ and beyond to 210°

beyond which the lock detector is not satisfied, but the control is to push the error back to $\phi = 180°$, where the lock detector again declares that the loop is in lock. This would explain a false-lock mode in both the coherent and noncoherent tests. The coherent test would yield a very stable false lock whereas the noncoherent test would not appear to be as stable.

5.0 CONCLUSIONS

We have considered the case in which the data rate is 8 kbps and the input SNR is very large; therefore, the signal level into the A/D converter yields a signal which is either +3 or -3 (seven-level output). The result found in this case was that the lock detector indicates an in-lock condition up to a phase error of ±75° (±20% of a bit). Furthermore, the lock detector will indicate an in-lock condition between about 104° and less than 130°. Again, in the region 150° to 210°, the lock detector declares an in-lock condition.

It was further determined that the error control signal changes its algebraic sign when the phase error is between 90° and 150°, so that phase false lock potential exists in the region between ~150° and ~210°.

Based on the error control and lock detector functions, it appears that false lock could occur if the signal was turned off, then turned back on when the phase error was between 90° and 250°. By symmetry, the loop is also pushed in the wrong direction between -90° and -135°.

By preventing the midphase adder from overflowing, it appears that the loop will no longer produce a control signal in the wrong direction. The only remaining point is that, since the lock detector will be satisfied only in the region between 150° to 210°, drift would tend to pull the loop in. But, by removing saturation this lock detector false indication would be prohibited, thus causing the loop to enter the acquisition mode and hasten acquisition.

References

1. Abbreviated Flow Chart for the PSP Bit Synchronizer Algorithm, by Brett Parrish
2. J. K. Holmes, "PSP Bit Synchronizer NRZ False-Lock Status--Interim Report," Axiomatix Technical Memorandum No. M8206-1, June 18, 1982

Distribution

R. Helgeson, Consultant
J. Johnson, NASA/JSC
S. Mayo, TRW
B. Parrish, NASA/JSC
T. Pederson, TRW
M. Reuterman, Rockwell

Axiomatix

9841 Airport Boulevard • Suite 912 • Los Angeles, California 90045 • Phone (213) 641 8600

TECHNICAL MEMORANDUM NO. M8207-2

TO: B. Parrish, J. Johnson DATE: July 23, 1982

FROM: J. Holmes, P. Nilsen

SUBJECT: Recommendations on PSP Bit Synchronizer Design Changes

---

Axiomatix has been involved in a review and analysis of the PSP bit synchronizer false-lock problem. This has entailed the following effort:

(1) Attending technical discussions, meetings/telecons

(2) Witnessing laboratory tests

(3) Analyzing algorithms and hardware performance

Axiomatix has not yet completed this activity, especially with respect to (3) above However, Axiomatix does feel it appropriate to make certain design change recommendations in light of its findings to date. The design changes which Axiomatix recommends at this time are considered by Axiomatix as the minimum changes required in order to achieve a viable, satisfactorily performing payload communication capability. These changes are as follows

(a) Correct the microprocessor midphase addition overflow (and sign change)

(b) Modify or reparameterize the lock dectector algorithm

(c) Add a bit transition counter.

Without these changes, there appears to be a reasonable probability that, given certain operational situations which result in signal strength fluctuations, i.e., antenna pattern modulation of signal amplitude, the bit synchronizer will false lock and data will be lost. Furthermore, the present lock detector does not reliably indicate this condition. Also, the present PSP design may necessitate the SSO crew reinitializing the PSP several times in order to achieve initial acquisition. At present, the only reliable indication of successful PSP bit synchronizer acquisition is the successful frame synchronizer indication.

In addition to the three design issues ((a)-(c)) cited previously, there are several other related design issues which have surfaced during the investigation which have the potential to affect communication performance. These are:

(d) Saturation of the PSP A/D converter due to a gain change made between the 250-kHz filter and the A/D converter

(e) Saturation of the presum integrators

(f) Potential DC bias-removal algorithm problems.

Axiomatix has analyzed the second item (e) and feels that the present presum design, while being undesirable, does not cause the false-lock problem to occur; however, correction of this problem is a relatively simple software change. Because the DC bias-removal algorithm (f) has been substantially changed, we feel that this should be reviewed by all interested parties in order to verify the accuracy of the new algorithm. We also believe that the gain between the 250-kHz lowpass filter and the A/D converter (d) should be reduced to the original design value or changed to a new, more nearly optimum value in order to avoid clipping the signal plus noise.

Axiomatix

9841 Airport Boulevard • Suite 912 • Los Angeles, California 90045 • Phone (213) 641-8600

TECHNICAL MEMORANDUM NO. M8208-1

TO: P. Nilsen

FROM: J. K. Holmes

DATE. August 9, 1982

DISTRIBUTION: R. Helgeson
G. Huth
J. Johnson
S. Mayo
B. Parrish
M. Reutermann

SUBJECT: Observations of NRZ and Biphase-L PSP False Lock at Rockwell

---

Both NRZ and biphase-L false lock induced by RF power interrupts were observed at the PSP tests conducted at Rockwell ADL. Details of this observation are provided herein.

Testing of the PSP false-lock phenomenon was observed at Rockwell (Downey) on August 2-3 by the author, representing Axiomatix, Mike Reutermann, Michelle Knowlden, Pete Berndsen and Barry Mathias of Rockwell (who actually performed the tests), Sal Mayo of TRW, and Jack Rivers and Bob Vermillion of NASA

Both NRZ and biphase-L false lock was observed at high SNR (-60 to -80 dBm). Three types of simulated RF dropouts were used, as follows:

(1) Fast switching between two antenna ports with negligible differential signal level, except for the approximate 3 ms switch time

(2) Slow switching from antenna port to dummy load and back to the antenna dwelling on the load for about one second

(3) Manual attenuation to simulate an antenna fade, with maximum attenuation held for about one second

The last two switching procedures were used since the first did not induce false lock. Biphase-L false lock was different from NRZ false lock in that it was data-pattern dependent and NRZ was not Also, both lock detector and frame synchronization discretes are low in biphase-L false lock. Practically speaking, since data would tend to be more or less random, the biphase-L false-lock problem may not be "real" although it should be verified with actual payload data. Table 1 summarizes the differences between NRZ and biphase-L false lock. Some of the test data are included at the end of this memorandum.

Table 1. False-Lock Summary

NRZ	Biphase-L
1. Only at high SNR (-60 to -80 dBm) (At 16 kbps, need > -80 dBm)	1. Only at high SNR (-60 to -80 dBm) (At 16 kbps, may need > -80 dBm)
2. Not data-pattern dependent (ability to false lock)	2. Data-pattern dependent (ability to false lock)
3. In false lock: Bit synchronization - high Frame synchronization - low	3. In false lock: Bit synchronization - low Frame synchronization - low
4. Changing data pattern does not break false lock	4 Changing data pattern breaks false lock
5. False locks at all data rates	5 False locks only at 1 and 16 kbps (2 kbps not yet tested, does not false lock at 4 or 8 kbps)
6. False locks on switching from antenna to load to antenna and when using the attenuator to increase attenuation to simulate a fade	6. False locks when switching from antenna to load to antenna and when increasing the attenuation by means of an attenuator to simulate a fade
7. Not dependent on having wire on PSP clock pin to cause false lock	7. Not dependent on having wire on PSP clock pin to cause false lock

7-29-82 THURS!

PSP S/N 201

MODE	DATA RATE	DENSITY	RF SLOW INTERRUPT	RF FAST INTERRUPT	DATA INTERRUPT	REMARKS
NRZ-L	8kbps	100% 10101010		2 FALSE LOCKS		CHANNEL 1 - GROUND LOOP PROBLEM
NRZ-L	4kbps	50% 10000010		FALSE LOCK 1/6 TIMES		GND LOOP PROBLEM CABLE DISCONNECT NO MORE FALSE LOCKS
NRZ-L	4kbps	25% 10000000		NO FALSE LOCKS		
NRZ-L	1kbps	25% 10000000		4 FALSE LOCKS / 37 TRIES		PHOTO #2
NRZ-L	1kBps	50% 10000010		1 FALSE LOCK/5 TRIES		PHOTO #3
NRZ-L	1kBps	100% 1010010		1 FALSE LOCK/3 TRIES		
NRZ-L	1KBPS	25% 11110000		FALSE LOCK 1ST TRY		PHOTO #4
NRZ-L	1KBPS	25% 11110000	FALSE LOCK 1ST TRY USED RF ATTEN			LOOP STRESS = 1.67 CAP ON CONNECT
"	"	"	FALSE LOCK AFTER 16 TRIES			UNCAPPED
"	"	"	FALSE LOCK AFTER 31 TRIES			CAPPED T/C: SOMETIMES WHEN REACQUIRING F/S WOULD JUMP IN AND OUT - W SIGNAL LEVEL?
"	"	"	NO FALSE LOCKS >60 TRIES			CAPPED

ORIGINAL PAGE IS OF POOR QUALITY

WORK AROUND TEST

RE INITIALIZE → RECONFIGURE : 11 TIMES NO	FALSE LOCK	1KB/S :	11110000	25%		
4 → " : " " NO	" "	1KB/S :	10000000	25%		
PWR DWN→UP → " : 17 " NO	" "	4KB/S :	10000000	25%		

	RATE	DENSITY	~~SLOW INTERRUPT~~	~~FAST INTERRUPT~~ RF ATTENUATOR	~~TYPE~~ IN NO TRIALS	LEVEL IN DBM	
	1KB/S	87.5% FOFO	TELEMETRY DATA INTERRUPT FOR 3SEC BATTERY POTENTIOMETER NO TRANSIENTS		7/20	-80	1 A
					7/20	-80	
BI-Φ-L		87.5% FOFO	4 4		15/20	-70	
		87.5% FOFO	| |		5~~5~~/20	-70	SCOPE WIRES DISCONNECTED
	GOOD	75% AOAO	| |		0/20	-70	
		75% AOAO	| |		0/20	-80	
		87.5% EOEO	| |		7/20	-70	
		87.5% EOEO	| |	REPEAT	3/20	-70	WIRES DISCONNECTED
		87.5% EOEO	| |		8/20	-70	SCOPE WIRES CONNECT
		87.5% EOEO		RF ATTENUATOR	10/20	-70	WITH SCOPE WIRES
		87.5% EOEO		4 4	5/20	-70	NO WIRES
BI-Φ-L	GOOD	75% AOAO		4 4	0/20	-70	NO WIRES
		87.5% EOEO		4 4	4/20	-70	4 4
	GOOD	75% AOAO		4 4	0/20	-70	4 4
		87.5% EOEO		4 4	3/20	-70	4 4
	GOOD	75% OSOS			0/20	-70	4 4

	RATE	DENSITY	~~SLOW INTERRUPT~~	~~FAST INTERRUPT~~ RF ATTENUATOR	~~TYPE~~ IN MA TRIALS	LEVEL IN DBM	
	1KB/S	87.5% FOFO	TELEMETRY DATA BATTERY POTENTIOMETER NO TRANSIENTS	INTERRUPT FOR 3SEC	7/20	-80	1A
					7/20	-80	
BI-Φ-L		87.5% FOFO	4 4		15/20	-70	
		87.5% FOFO	| |		5~~5~~/20	-70	SCOPE WIRES DISCONNECTED
	GOOD	75% AOAO	| |		0/20	-70	
		75% AOAO	| |		0/20	-80	
		87.5% EOEO	| |		7/20	-70	
		87.5% EOEO	| |		3/20	-70	WIRES DISCONNECTED
		87.5% EOEO	| |		8/20	-70	SCOPE WIRES CONNECT
		87.5% EOEO		RF ATTENUATOR	10/20	-70	WITH SCOPE WIRES
		87.5% EOEO		4 4	5/20	-70	NO WIRES
BI-Φ-L	GOOD	75% AOAO		4 4	0/20	-70	NO WIRES
		87.5% EOEO		4 4	4/20	-70	4 4
	GOOD	75% AOAO		4 4	0/20	-70	4 4
		87.5% EOEO		4 4	3/20	-70	4 4
	GOOD	75% 0505			0/20	-70	4 4

REPEAT

Axiomatix

9841 Airport Boulevard • Suite 912 • Los Angeles, California 90045 • Phone (213) 641-8600

TECHNICAL MEMORANDUM NO. M8208-2

TO: P. Nilsen DATE: August 27, 1982

FROM: J. K. Holmes

SUBJECT: Recommended Changes to the Tracking Mode of the PSP Bit Synchronizer Lock Detector for NRZ Data

REFERENCE: B. Parrish, "PSP Bit Synchronization Algorithm Flowchart Summary for the NRZ Mode," JSC document, undated (about July 1982)

- -

1.0 INTRODUCTION

This technical memorandum documents the recommended parameter value changes which were previously transmitted to TRW by telephone. The recommendations are to narrow the in-phase and midphase filter bandwidths and to change the lock detector test ratio in the NRZ mode of the PSP bit synchronizer lock detector By making these changes, it is believed that the problem of the lock detector not indicating loss of lock, sometimes not until minutes after the signal is removed, will be eliminated. These recommended changes will require only that the bit synchronizer algorithm parameters be modified, and no algorithm or hardware changes will be involved.

2.0 RECOMMENDED CHANGES

It is recommended that both the in-phase and midphase filters be reduced in bandwidth so as to increase their respective output signal-to-noise ratios (SNR's) and thereby improve the reliability of the lock detector test. Specifically, it is recommended that (1) the L-value of the in-phase filter be changed from 0.99 to 0.999 (if feasible to implement digitally) so that the "gain" goes from 100 to 1000 and, (2) the L-value of the midphase filter be changed from 0.95 to 0.995 so that this "gain" goes from 20 to 200. With the narrow bandwidth digital filters, it is possible to change the in-lock bit synchronizer test from

$$AVIN \overset{?}{>} 6\ 5|AVMI|$$

to

$$AVIN \overset{?}{>} 50|AVMI|$$

The result of this change would be to greatly improve the probability of declaring that the bit synchronization loop is out of lock when the signal is removed. Presently, the loop can display an in-lock condition, sometimes until minutes after the signal has been removed. This would be confusing to flight operation personnel.

The analysis which led up to the recommendations of narrowing the digital filters and changing the in-lock test is based on a rather involved analysis, which will be the subject of a future memorandum.

DISTRIBUTION

R. Helgeson, Consultant
J. Johnson, JSC
S. Mayo, TRW
B. Parrish, JSC
T. Pederson, TRW
M. Reutermann, RI

Axiomatix

9841 Airport Boulevard • Suite 912 • Los Angeles, California 90045 • Phone (213) 641-8600

TECHNICAL MEMORANDUM NO. M8209-2 DATE: September 3, 1982

TO: P. Nilsen

FROM: J. K. Holmes

COPIES: NAS 9-16067"B" File
R. Helgeson, Consult.
J. Johnson, JSC
S. Mayo, TRW
B. Parrish, JSC
T. Pederson, TRW
M. Reutermann, RI

SUBJECT: PSP Bit Synchronizer Lock Detector Parameter Value Changes for the NRZ Data-Tracking Mode

REF. (1) Technical Memorandum No. M8208-2
(2) B. Parrish, "PSP Bit Synchronization Algorithm Flowchart Summary for the NRZ Mode," JSC document, undated (about July 1982)

- -

1.0 INTRODUCTION

This memorandum makes a "final" recommendation for the PSP bit synchronizer lock detector parameters in the NRZ data mode based on the current state of the microprocessor available memory and processing rate. Due to the lack of additional memory storage space, Rich Helgeson has pointed out that, with the present schedule and memory constraints, it is feasible only to reparameterize the lock detector algorithm at this time.

The recommended recursive L parameters of the respective one-pole in-phase and midphase filters are given by

$$L_I = \frac{254}{256} = 0.9922$$

$$L_M = \frac{248}{256} = 0.9688$$

and the lock detector test becomes

$$AVIN \overset{?}{>} 13*|AVMI|$$

for NRZ data.

2.0 BASIS OF NEW RECOMMENDATION

Based on a recent telecon with Rich Helgeson, it was determined that it was impossible to implement the desired values of L = 0.999 for the in-phase filter and L = 0.995 for the midphase filter of the bit synchronizer lock detector

recommended in ref. 1. Basically, the allowable values of the recursive filter parameter L must be of the form

$$L = \frac{n}{256} \qquad (1)$$

where n is an even integer less than 256. Based on this constraint, the maximum recursive filter L value is then L = 254/256 = 0.9922 and, hence, 0.999 cannot be achieved.

In ref. 1, it was recommended that the lock detector for the NRZ case have separate in-phase and midphase lock detector filters which are much narrower than the bit synchronizer loop in-phase and midphase filters; however, in light of the above-mentioned limitations, it is recommended that both the loop and the lock detector use the same filters. Thus, the in-phase and midphase filters should be modified from

$$L_I = \frac{252}{256} = 0.984375$$

$$L_M = \frac{242}{256} = 0.9453$$

with the lock detector test in tracking specified by

$$AVIN \overset{?}{>} 6\ 5*|AVMI|$$

to

$$L_I = \frac{254}{256} = 0.9922$$

$$L_M = \frac{248}{256} = 0.9688$$

with the lock detector test in tracking now being specified by

$$AVIN \overset{?}{>} 13*|AVMI|$$

where the coefficient 13 is close to the desired value of 15 and is a simple shift of one digit, resulting in a multiply-by-two of the current value of 6.5.

The above changes should provide the same probability of detection value when in lock as those of the existing parameters but, in addition, they will decrease the probability that the lock detector declares that the signal is present when it is not. As a result, the lock detector light should not remain on for long periods of time when the signal drops out; this is a problem in the original algorithm.

Axiomatix

9841 Airport Boulevard • Suite 912 • Los Angeles, California 90045 • Phone (213) 641 8600

TECHNICAL MEMORANDUM NO. M8210-1

TO: P. Nilsen DATE: October 4, 1982

FROM: J. Holmes FILE: NAS 9-16067"B"

SUBJECT: PSP Lock Detector Performance in the Tracking Mode for NRZ and Biphase Data

---

1.0 SUMMARY

In this technical memorandum, we analyze the lock detector performance of the Shuttle PSP (in tracking only) and recommend improvements and/or modifications to minimize the time required to indicate out-of-lock status when the input signal is removed. Because of microprocessor limitations in both memory size and speed, it was determined that the digital filters used for the inphase and midphase bit synchronizer tracking loop and lock detector must be the same, forcing a compromise of sorts. Consequently, with this constraint and the fact that only a limited number of one-pole digital-filter-recursion parameters were available in the microcode, the following results were obtained.

- NRZ Data

  A. Present parameters

  Inphase parameter: $L_I = 252/256 = 0.9844$
  Midphase parameter: $L_M = 242/256 = 0.9453$
  Lock detector criteria: $AVIN \overset{?}{>} 6.5\ |AVMI|$

  B. Recommended parameters

  Inphase parameter. $L_I = 254/256 = 0.9922$
  Midphase parameter: $L_M = 248/256 = 0.9688$
  Lock detector criteria· $AVIN \overset{?}{>} 13\ |AVMI|$

- Manchester Data

  A. Present parameters

  Inphase parameter. $L_I = 252/256 = 0.9844$
  Midphase parameter· $L_M = 252/256 = 0.9844$
  Lock detector criteria: $AVIN \overset{?}{>} 5\ |AVMI|$

B. Recommended parameters

Inphase parameters: $L_I = 254/256 = 0.9922$
Midphase parameter: $L_M = 254/256 = 0.9922$
Lock detector criteria: $AVIN \stackrel{?}{>} 15\ |AVMI|$

The mean time to indicate out-of-lock with the new parameters when the signal is removed reduces to one-half the time in the NRZ case and about one-tenth the time in the Manchester (biphase-L) case, compared to existing parameters. Since the analysis and system modeling were very involved, approximations were made in the analysis; however, it is believed that the answers are representative of the actual system performance.

During the course of this work, numerous helpful discussions were held with Rich Helgeson (consultant) and Brett Parrish (NASA/JSC) concerning the operation of this bit synchronizer. In addition, observations of the false-lock phenomena on the actual hardware were observed at both Rockwell and TRW.

2.0 INTRODUCTION

Shuttle-launched payloads will communicate with the Space Shuttle Orbiter payload communications system over a range of tens of nautical miles. Command data is transmitted to the payloads while telemetry data are received at the Orbiter on multiple S-band frequency channels. Figure 1 illustrates the Space Shuttle Orbiter receiver block diagram for payload signals, which is part of the Payload Interrogator (PI). The PI sends a 1.024-MHz subcarrier PSK modulated by either NRZ or biphase signals at date rates of either 1, 2, 4, 8 or 16 kbps. Signals from the PI are sent to either the NASA PSP, the DOD PSP or the Ku-band signal processor (KuSP). This memo is concerned with the performance of the NASA PSP which performs subcarrier demodulation, bit and frame synchronization, as well as matched-filter detection of the data, as shown in Figure 2.

This memo concentrates on PSP bit synchronizer lock detector performance during tracking. Performance specifications of the PSP bit synchronizer loop require less than 1.5 dB implementation loss over a signal level corresponding to an E_b/N_0 range of 2 - 11 dB at the minimum average bit transition density of 12.5% (64 bit transitions in 512 bit periods). Acquisition must occur within four seconds with 0.9 probability for E_b/N_0 values and data formats listed in the specification amendment of March 25, 1982, shown as Appendix D in this memo. A more detailed (but still simplified) block diagram of the original

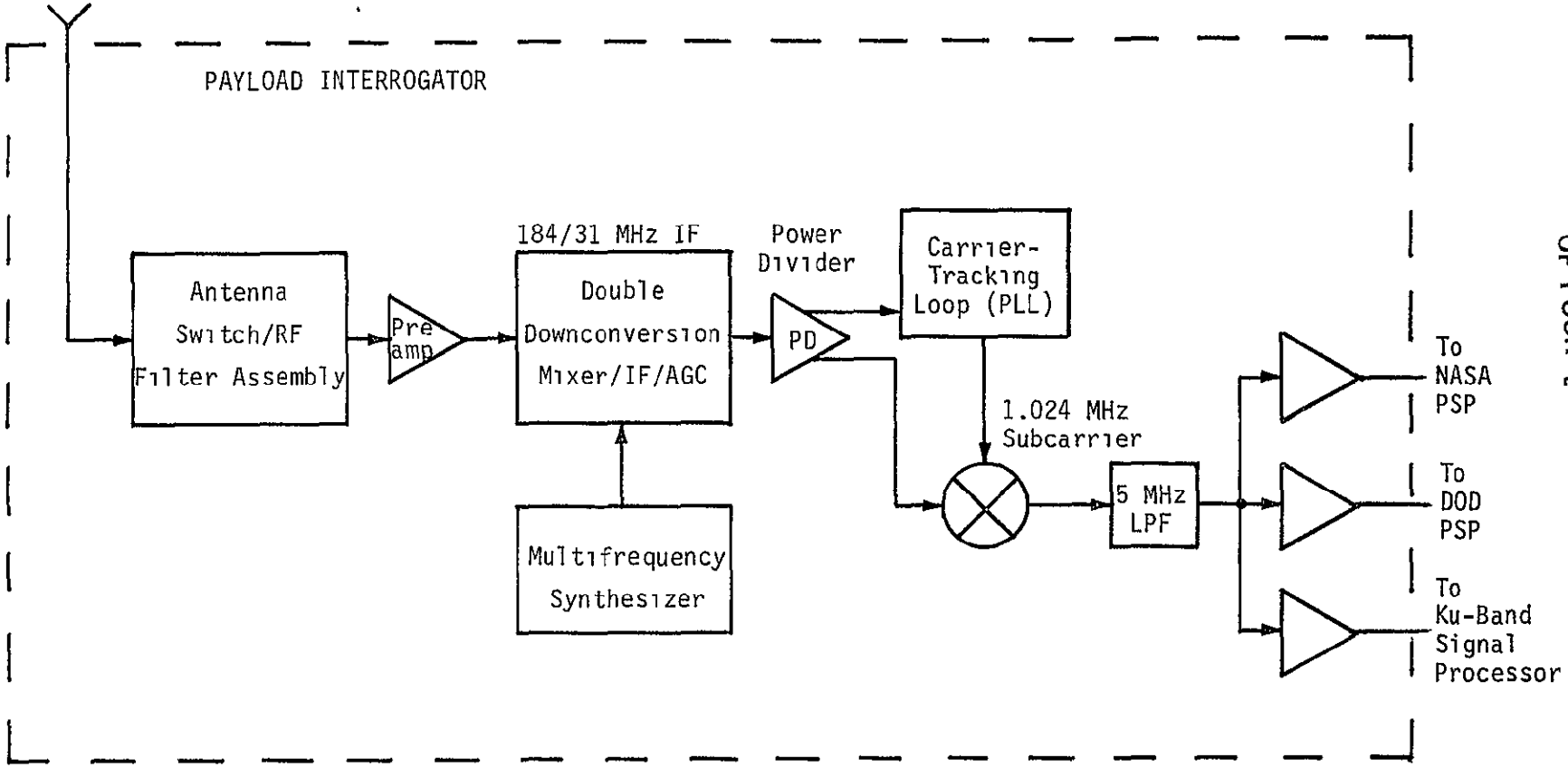

Figure 1 Shuttle Payload Communications Receiver

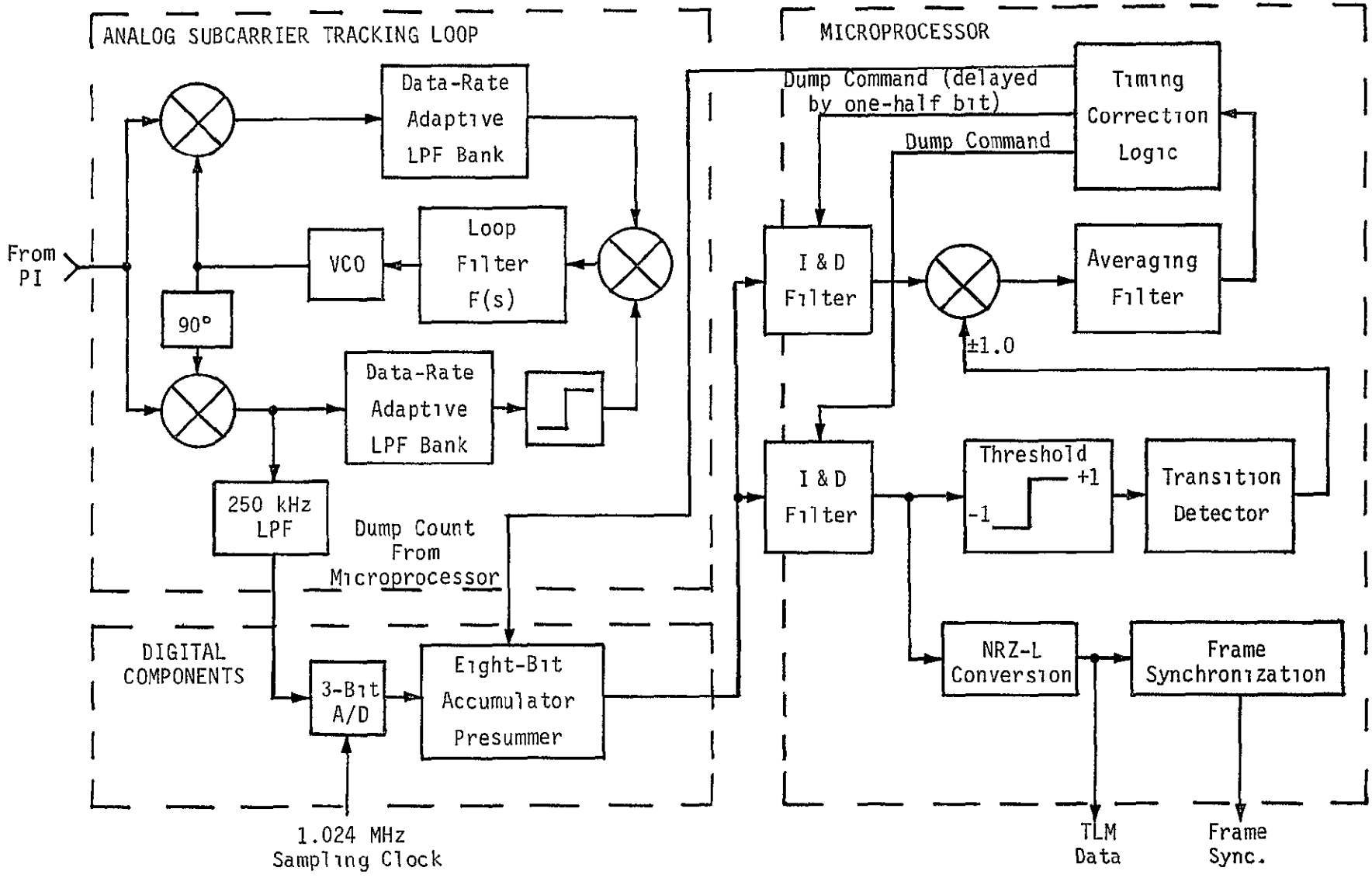

Figure 2 NASA PSP Configuration

bit synchronizer is shown in Figures 3 and 4. Basically, the data is demodulated by the 1.024-MHz subcarrier (Costas) loop and is sampled at 1.024 Msamples per second, with each sample being quantized to three bits. These samples are stored in presums that are added together in eight-bit registers to form the last, middle, and first half-bit integrals, as depicted in Figure 5.

The inphase averaging filter is driven by the magnitude of the sum of the first and last half bits, and the midphase filter is driven by the sum of the first half bit and the previous last half bit (delayed one bit)--all multiplied by the transition indicator [1,2].

3.0 THE THREE-BIT QUANTIZER

In order to proceed with our analysis, certain assumptions were made so that the analysis would be manageable. First, the effect of the second-order tracking component was neglected because it was designed for a very limited correctional capability. Second, the DC restoration algorithm was not modeled because the new algorithm was not available at the time of the analysis for this writing and, also, it was felt that, in tracking, the DC restoration was not an important factor in the loop operation. In addition, the scaling algorithm was not incorporated since it does not have a major effect at low SNR's. Finally, it was assumed that the revised algorithm for acquisition and tracking will not cause either limiting or register rollover due to unprotected registers This has been verified by simulation, calculation and laboratory measurements. An abbreviated flowchart is presented in Appendix A which was constructed by Brett Parrish, NASA/JSC.

Table 1 lists the number of samples per bit at each data rate with the new microcode.

Table 1. Samples Per Bit at Each Data Rate

R_b	Samples/Bit	Samples/Presum (Current System)	Samples/Presum (Proposed System)
16	64	16	16
8	128	32	16
4	256	64	16
2	512	64	16
1	1024	64	16

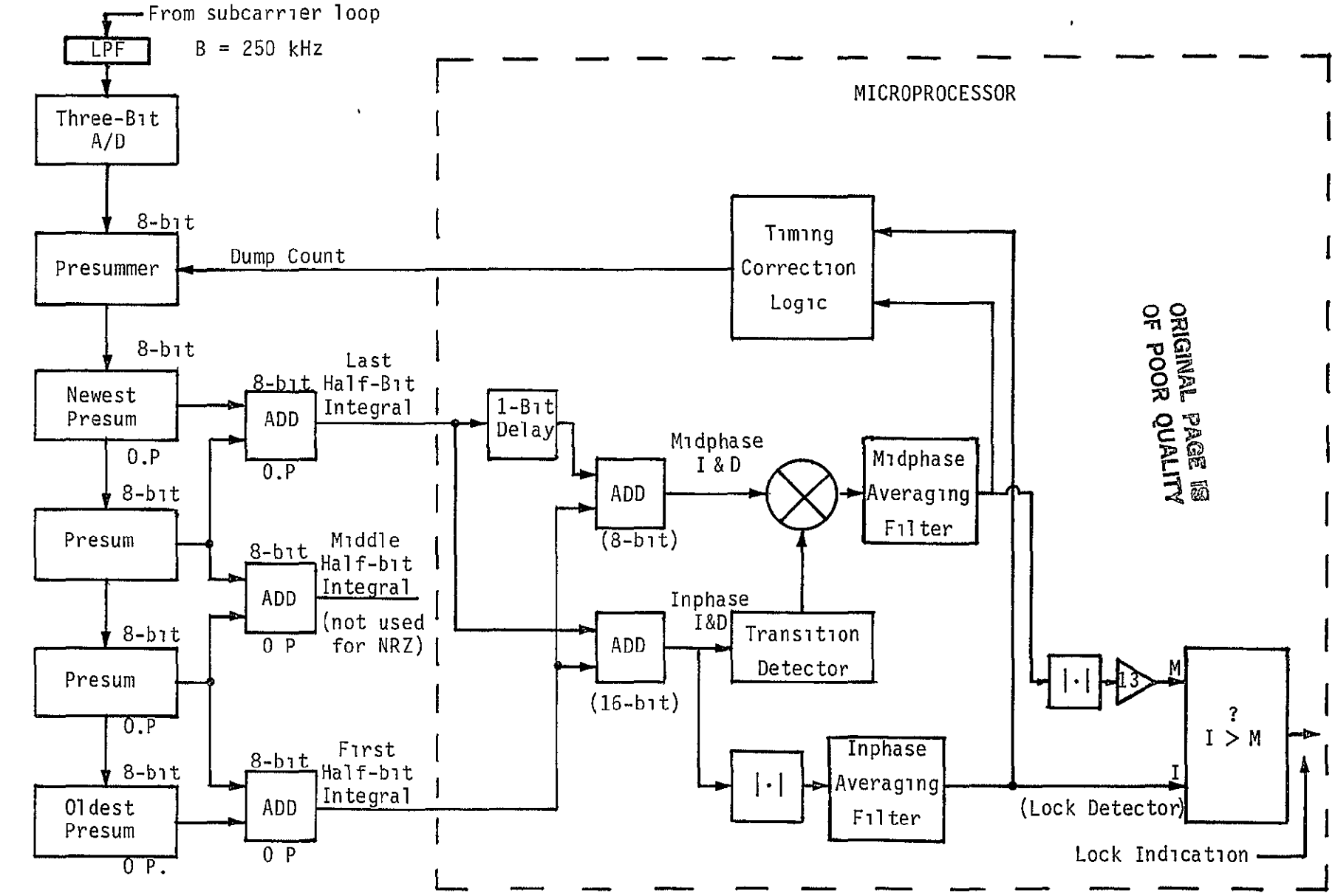

Note· O P. = overflow protection

Figure 3. PSP Data-Transition Tracking Loop and Lock Detector for NRZ Data in the Tracking Mode

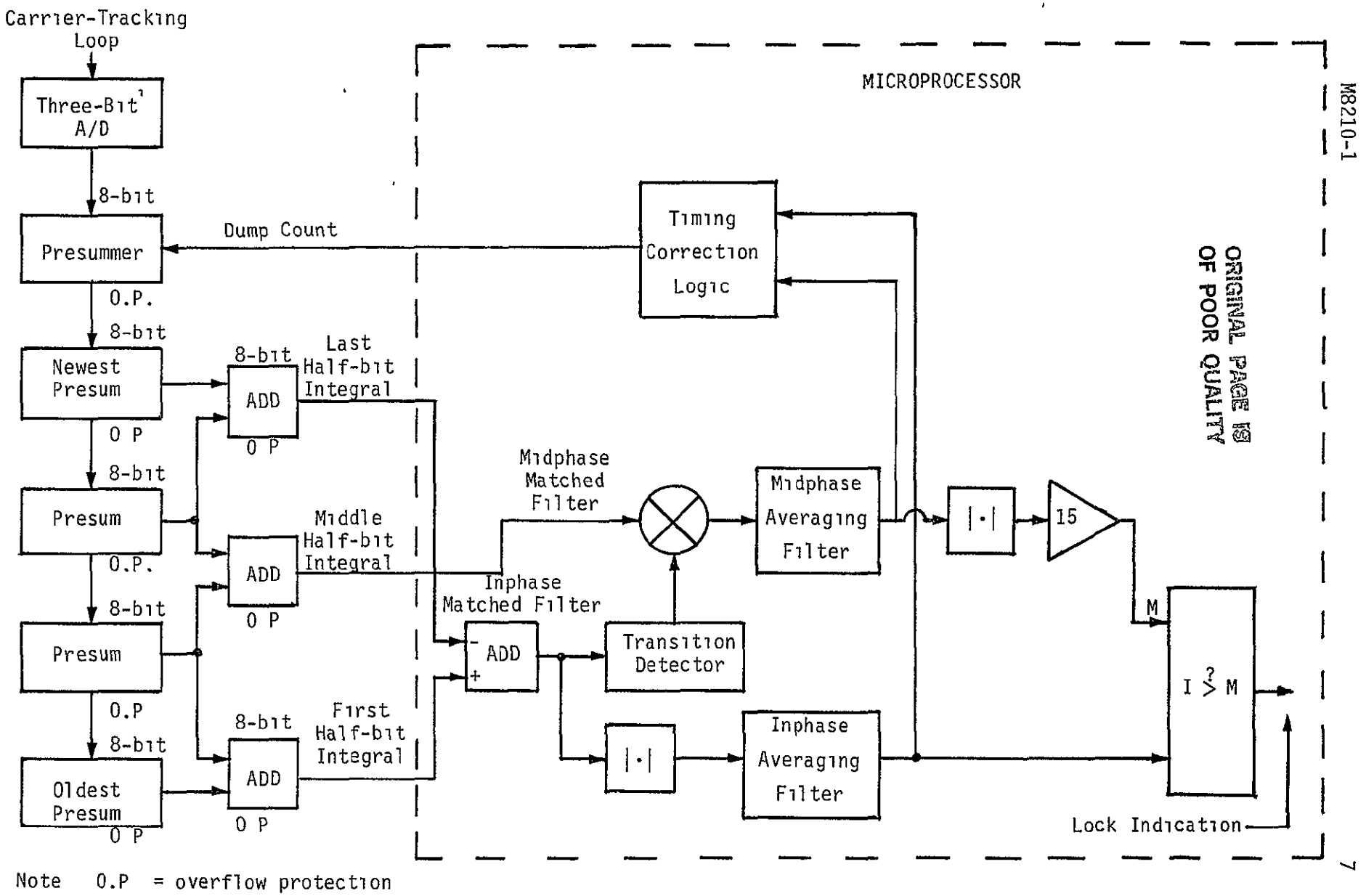

Figure 4 PSP Data-Transition Tracking Loop and Lock Detector for Biphase Data in the Tracking Mode

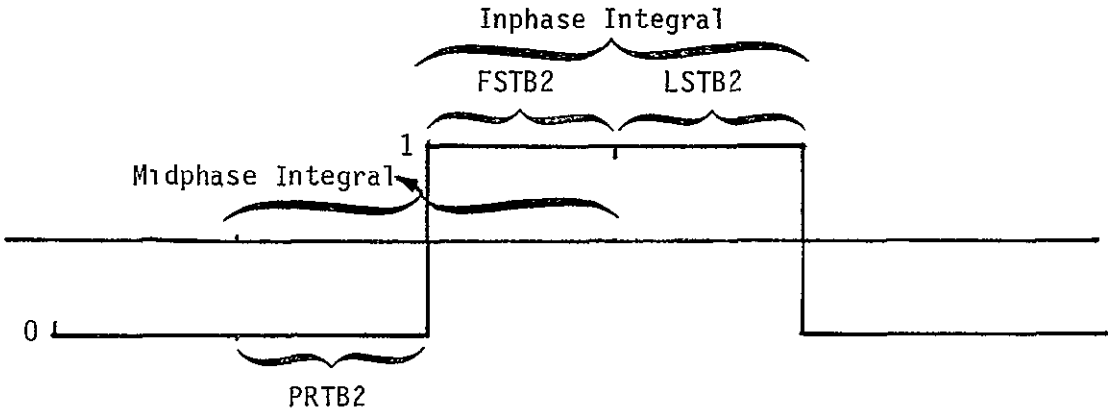

NOTE: FSTB2 - first half-bit
LSTB2 - last half-bit
PRTB2 - previous last half-bit

(a) NRZ Data

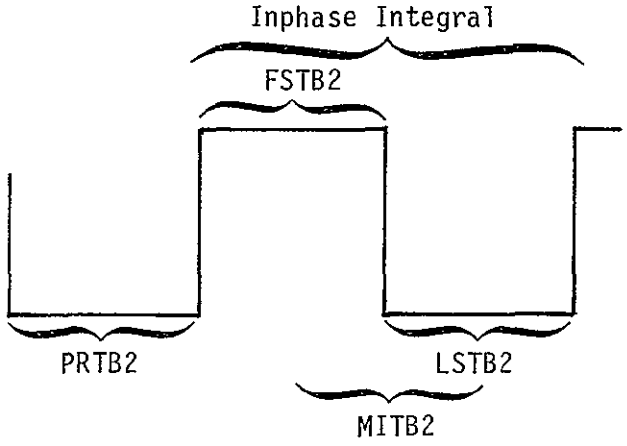

(b) Biphase Data

Figure 5 Time Blocks in One Bit Period for NRZ and Biphase Data

Let N denote the number of samples per bit which is either 64, 128, 256, 512 or 1024, as indicated in Table 1. The sample rate is 1.024 Msps and the baseband signal plus noise is filtered to 250 kHz. In Figure 6, a model of the deadzone A/D converter is illustrated. Notice that, if the signal were less than one-half of a cell in peak amplitude, there would be zero output. Consequently, AGC action is necessary to keep the peak amplitude greater than one-half of the cell size. The analog baseband signal to the A/D converter is given by

$$y(t) = A\,d(t) + n(t) \qquad 0 \leq t < T \qquad (1)$$

where A is the signal amplitude, d(t) is the baseband NRZ data signal, and n(t) is modeled as bandlimited white Gaussian noise. Each bit integral is approximated by the sampling of $y(t)$ over one bit time to yield

$$\text{FSTB2} + \text{LSTB2} = \sum_{i=1}^{N} d_i + \sum_{i=1}^{N} n_i + \sum_{i=1}^{N} q_i \qquad (2)$$

Based on the new implementation, we assume that saturation cannot occur in any of the registers. In (2), d_i is the ith sample of d(t), n_i is the ith sample of n(t), and q_i is the ith sample of q(t), where q(t) is the quantization noise introduced by the A/D sampling process. Although q_1 is not generally independent of d_i and n_i, we will assume that it is in order to simplify the following analysis. Now we determine the level of the signal and the thermal noise out of the 250-kHz lowpass filter We have

$$\frac{E_b}{N_0} = \frac{P}{N_0 B}\left(\frac{B}{R}\right) \qquad (3)$$

where B is the lowpass filter noise bandwidth and R is the data rate, $R = 1/T$, with T being the bit duration. The signal power to noise power is then given by

$$\text{SNR} = \frac{E_b}{N_0}\frac{R}{B} \qquad (4)$$

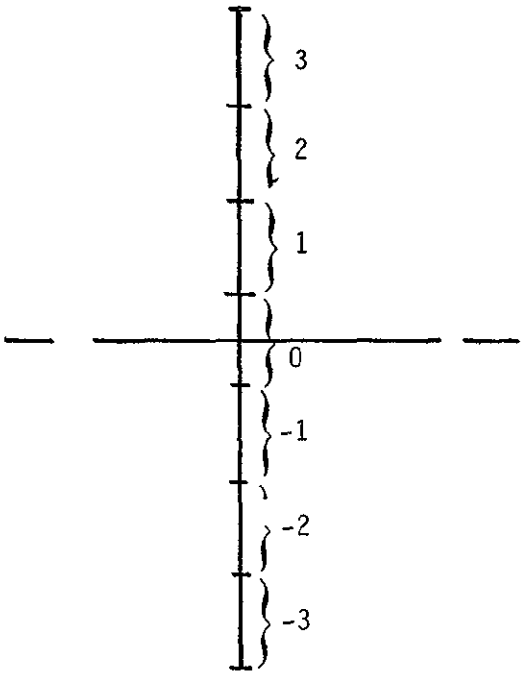

Figure 6 Model for the Deadzone A/D Converter

For example, at $\mathcal{R}$ = 8 kHz and E_b/N_0 = 4 dB, we have

$$SNR = 1.58 \frac{8 \times 10^3}{250 \times 10^3} = -13 \text{ dB} \tag{5}$$

Thus, we tend to have rather negative sample SNR's. Now the sample signal voltage to noise standard deviation is given (from (4))

$$\frac{|d_1|}{\sigma} = \sqrt{\frac{E_b}{N_0}\frac{R}{B}}, \quad \sigma^2 = N_0 B \tag{6}$$

When the loop is at the correct timing position, (2) becomes

$$FST2 + LSTB2 = \pm N\sqrt{\frac{E_b}{N_0}\frac{R}{B}}\,\sigma + \sum_{i=1}^{N} n_i + \sum_{i=1}^{N} q_i \tag{7}$$

the ± sign is determined by the algebraic sign of d(t), $t\varepsilon(0,T)$. Now, since the samples are taken at a sample rate of 1.024 Msps and since the lowpass filter preceding the sampling is 250 kHz wide, the noise samples are not independent. Hence, we assume that sample pairs are independent and each sample has the same value in the pair. Using this mode, we have

$$FSTB2 + LSTB2 = \pm N\sqrt{\frac{E_b}{N_0}\frac{R}{B}}\,\sigma + 2\sum_{i=1}^{N/2} n_i + 2\sum_{i=1}^{N/2} q_i \tag{8}$$

where, since we have assumed that the noise samples are pairwise independent, we make the same assumption for the quantization samples

Letting n denote the noise sample sum in (8) produces

$$n = 2\sum_{i=1}^{N/2} n_i \tag{9}$$

$$E[n] = 0 \tag{10}$$

$$Var[n] = 4\sum_{i=1}^{N/2}\sum_{j=1}^{N/2} E\left[n_i n_j\right] = 2N\sigma^2 \tag{11}$$

If we let n_q denote the quantization noise, we have

$$n_q = 2 \sum_{i=1}^{N/2} q_i \tag{12}$$

Hence, by symmetry,

$$E[n_q] = 0 \tag{13}$$

$$\mathrm{Var}[n_q] = 4 \sum_{i=1}^{N/2} \sum_{j=1}^{N/2} E[q_i q_j] = 2N \, \mathrm{Var}(q_i) = \sigma_q^2 \tag{14}$$

If we model the quantization noise as having a uniform distribution and let L denote the width of the quantization cell, then the quantization noise is given by

$$\sigma_q^2 = \frac{1}{L} \int_{-L/2}^{L/2} x^2 \, dx = \frac{L^2}{12} \tag{15}$$

and

$$E[n_q] = 0 \tag{16}$$

If we let the load factor* be denoted by LF, then the optimum LF should be about 2.28. From Figure 6 and the definition of the load factor, we have

$$2.28 = \frac{3L}{\sigma} \tag{17}$$

or

$$L = 0.77 \, \sigma \tag{18}$$

From (15), we obtain

$$\sigma_q^2 = 0.05 \, \sigma^2 \tag{19}$$

*The A/D converter load factor is the ratio of peak output to RMS noise input.

For arbitrary load factors, we obtain

$$\sigma_q^2 = 0.0092\ (LF)^2\ \sigma^2 \tag{20}$$

Using (10), (11), (15) and (16) in

$$FSTB2 + LSTB2 = \pm N \sqrt{\frac{E_b}{N_0}\frac{R}{B}}\,\sigma + 2\sum_{i=1}^{N/2} n_1 + 2\sum_{i=1}^{N/2} q_1 \tag{21}$$

yields for the mean and variance

$$E[FSTB2 + LSTB2] = \pm N \sqrt{\frac{E_b}{N_0}\frac{R}{B}}\,\sigma \tag{22}$$

and

$$Var[FSTB2 + LSTB2] = 2N\sigma^2 + 0.1N\sigma^2 = 2.1N\sigma^2 \tag{23}$$

Since the magnitude of the inphase term is recursively filtered, we now investigate the statistics of $|FSTB2 + LSTB2|$ that are needed before we can analyze the filtered version. Let x denote FSTB2 + LSTB2 Since the major noise is thermal noise, we shall approximate FSTB2 + LSTB2 as a Gaussian random variable with mean μ and variance $\sum^2$. From [3], it can be shown that

$$E\left[|x|\right] = \sqrt{\frac{2}{\pi}}\,\sum \exp\left(\frac{-\mu^2}{\sum^2}\right) + |\mu|\ \mathrm{erf}\left(\frac{|\mu|}{\sqrt{2}\Sigma}\right) \tag{24}$$

where

$$\mathrm{erf}(x) = \frac{2}{\sqrt{\pi}}\int_0^x e^{-t^2}\,dt \tag{25}$$

and where

$$\mu = \pm N \sqrt{\frac{E_b}{N_0}\frac{R}{B}}\,\sigma \tag{26}$$

$$\sum^2 = 2.1N\sigma^2 \tag{27}$$

Now consider the variance of $|x|$. We have

$$\mathrm{Var}\left[|x|\right] = E\left[|x|^2\right] - E^2\left[|x|\right]$$

or

$$\mathrm{Var}\left[|x|\right] = \Sigma^2 + \mu^2 - \Sigma^2\left[\sqrt{\frac{2}{\pi}}\, e^{-\mu^2/\Sigma^2} + \frac{\mu}{\Sigma}\,\mathrm{erf}\left(\frac{\mu}{\sqrt{2}\Sigma}\right)\right]^2 \qquad (28)$$

When $(\mu/\Sigma)^2 = 4$ dB, we have

$$\mathrm{Var}\left[|x|\right] = \Sigma^2 + \mu^2 - (1.05\mu)^2 \cong \Sigma^2 \qquad (29)$$

Hence, for $(\mu/\Sigma)^2 \geqslant 4$ dB, we have that

$$\mathrm{Var}\left[|x|\right] \cong \mathrm{Var}[x] \quad ; \quad E\left[|x|\right] \cong |E[x]| \quad \text{for } \frac{\mu^2}{\Sigma^2} \geqslant 4 \text{ dB} \qquad (30)$$

Hence, if we assume that $d(t)$ is $+1$ in every bit interval*, we have $E\left[|x|\right] \cong E[x]$.

Now note that

$$N = \frac{R_s}{R} = \frac{B}{R}\frac{R_s}{B} \qquad (31)$$

with R_s the same rate and R the data rate. Hence,

$$\mu = N\sqrt{\frac{E_b}{N_0}\frac{R}{B}}\,\sigma \qquad (32)$$

or

$$\mu = N\sqrt{\frac{E_b}{N_0}\frac{R_s}{BN}}\,\sigma \qquad (33)$$

Since $R_s/B = 4$, we have

$$\mu = 2\sqrt{N}\sqrt{\frac{E_b}{N_0}}\,\sigma \qquad (34)$$

*Henceforth, we assume that μ is always positive and drop the magnitude signs for simplicity.

It is worthwhile to compare the performance of an analog matched filter with the digital version that we have just analyzed. The digitized SNR is given by

$$SNR_D = \frac{E^2[FSTB2 + LSTB2]}{Var(FSTB + LSTB2)} \tag{35}$$

or

$$SNR_D = \frac{4N \frac{E_b}{N_0} \sigma^2}{2.1\ N\ \sigma^2} = 1.9 \frac{E_b}{N_0} \tag{36}$$

Since the ideal analog matched filter would yield an SNR of $2.0(=E_b/N_0)$, we see that, within our approximations, the sampling and quantization noise have produced a loss of 0.2 dB.

4.0 BIT SYNCHRONIZER DIGITAL FILTER OUTPUT STATISTICS WITH SIGNAL PRESENT--NRZ DATA

We now present some of the main elements of the bit synchronizer and lock detector algorithms. An abbreviated flowchart developed by Brett Parrish is included in Appendix B.

Basically, two one-pole recursive filters are used in the bit synchronizer and lock detector. The first is AVIN, the inphase bit integral filter (Figures 4 and 5); the second is AVMI, the midphase bit integral (Figure 4). The former is defined by

$$AVIN^{(n+1)} = L\ AVIN^{(n)} + \overbrace{\left|FSTB2^{(n)} + LSBT2^{(n)}\right|}^{x(n)} \tag{37}$$

where n denotes the nth bit time The midphase filter has an output given by

$$AVMI^{(n'+1)} = L\ AVMI^{(n')} + \left(FSTB2^{(n')} + PRTB2^{(n')}\right) TRIND^{(n')} \tag{38}$$

where the n' denotes the n'th bit transition. Figure 4 illustrates FSTB2,

LSTB2 and PRTB2. The term TRIND takes on the value 0, 1 or -1 according to whether no bit transition occurs or whether a positive or negative transition occurs. Therefore, the last term of (38) is a proportional measure of the bit timing error whenever a bit transition occurs.

To determine if the bit synchronizer should be in the tracking or acquisition mode, a lock detector is utilized by making the following comparison:

$$\text{AVIN} \overset{?}{>} 6.5\ |\text{AVMI}| \tag{39}$$

so that, when AVIN is larger than 6.5 AVMI, the lock detector declares that the bit synchronizer loop is in lock.

Consider AVIN first. Using the approximations of (30), we have that

$$\text{AVIN}^{(n+1)} \cong L_I \text{AVIN}^{(n)} + \overbrace{n^{(n)} + n_q^{(n)} + \begin{cases} 2\sqrt{N}\left(1 - \frac{2|j|}{N}\right)\sqrt{\frac{E_b}{N_0}}\,\sigma & \text{with probability } p_t \\ 2\sqrt{N}\sqrt{\frac{E_b}{N_0}}\,\sigma & \text{with probability } (1 - p_t) \end{cases}}^{x^{(n)}} \tag{40}$$

where p_t is the bit transition probability. The term j is the number of samples in which the timing is in error so that j/N is the discrete measure of phase error. Note that, when no bit transition occurs, there is no signal loss, however, when a transition does occur, the signal component is reduced by the factor $(1 - 2|j|/N)$, with j being the number of samples (out of N samples) in error. For convenience in the analysis, we shall approximate the discrete timing error by a continuous phase error and let

$$\frac{j}{N} = \frac{\phi}{2\pi} \tag{41}$$

where ϕ is the continuous-valued phase error. Using (41) in (40) leads to

$$x^{(n)} = n^{(n)} + n_q^{(n)} + 2\sqrt{N}\sqrt{\frac{E_b}{N_0}}\,\sigma\, X^{(n)} \tag{42}$$

and

$$\text{AVIN}^{(n+1)} = L_I \text{AVIN}^{(n)} + x^{(n)} \tag{43}$$

with

$$x^{(n)} = \begin{cases} \left(1 - \frac{\phi}{\pi}\right) & \text{with probability } p_t \\ 1 & \text{with probability } \left(1 - p_t\right) \end{cases} \tag{44}$$

where p_t is the bit transition probability. Since the phase error is normally quite small, we will approximate ϕ by a zero-mean Gaussian random variable with variance σ_ϕ^2.

First, we compute $E\left[x^{(n)}\right]$. We have from (44) that

$$E\left[x^{(n)}\right] = 2\sqrt{N}\sqrt{\frac{E_b}{N_0}}\,\sigma\left[\left(1 - \frac{E[|\phi|]}{\pi}\right) p_t + \left(1 - p_t\right)\right] \tag{45}$$

For a Gaussian random variable, it can be shown that

$$E[|\phi|] = \sqrt{\frac{2}{\pi}}\,\sigma_\phi \tag{46}$$

Using (46) in (45) produces

$$E\left[x^{(n)}\right] = 2\sqrt{N}\sqrt{\frac{E_b}{N_0}}\,\sigma\left[1 - \frac{\sqrt{\frac{2}{\pi}}\,\sigma_\phi}{\pi}\,p_t\right] \tag{47}$$

To evaluate the variance of $x^{(n)}$, we first compute $E\left[\left(x^{(n)}\right)^2\right]$. Using (42), we have

$$E\left[\left(x^{(n)}\right)^2\right] = E\left[\left(n^{(n)}+n_q^{(n)}\right)^2\right] + 4E\left[\left(n^{(n)}+n_q^{(n)}\right)\sqrt{N}\sqrt{\frac{E_b}{N_0}}\,\sigma\,x^{(n)}\right] + 4N\frac{E_b}{N_0}\,\sigma^2\,E\left[X^2\right] \tag{48}$$

Evaluating, we obtain (since the second term is equal to zero)

$$E\left[\left(x^{(n)}\right)^2\right] = 2.1N\sigma^2 + 4N\frac{E_b}{N_0}\,\sigma^2\left\{\left(1 - \frac{2}{\pi}\sqrt{\frac{2}{\pi}}\,\sigma_\phi + \frac{\sigma_\phi^2}{\pi^2}\right) p_t + \left(1 - p_t\right)\right\} \tag{49}$$

or

$$E\left[\left(x^{(n)}\right)^2\right] = 2.1N\sigma^2 + 4N\frac{E_b}{N_0}\sigma^2\left\{1 - \left[\left(\frac{2}{\pi}\right)^{3/2}\sigma_\phi - \frac{\sigma_\phi^2}{\pi^2}p_t\right]\right\} \quad (50)$$

Now

$$E^2\left[x^{(n)}\right] = 4N\frac{E_b}{N_0}\sigma^2\left[1 - \left(\frac{2}{\pi}\right)^{3/2}\sigma_\phi\, p_t + \frac{2}{\pi^3}\sigma_\phi^2\, p_t^2\right] \quad (51)$$

Since

$$\mathrm{Var}\left[x^{(n)}\right] = E\left[\left(x^{(n)}\right)^2\right] - E^2\left[x^{(n)}\right] \quad (52)$$

we obtain

$$\mathrm{Var}\left[x^{(n)}\right] = 2.1N\sigma^2 + 4\frac{E_b}{N_0}N\sigma^2\left(\frac{\sigma_\phi}{\pi}\right)^2\left[p_t - \frac{2}{\pi}p_t^2\right],\ 1 > p_t > 0 \quad (53)$$

It follows from (A-5) and (A-13) that $(0 < p_t < 1)$

$$\mathrm{Var}\left[AVIN^{(n)}\right] = \frac{2.1N\sigma^2 + 4\frac{E_b}{N_0}N\sigma^2\left(\frac{\sigma_\phi}{\pi}\right)^2\left[p_t - \frac{2}{\pi}p_t^2\right]}{1 - L_I^2} \quad (54)$$

and

$$E\left[AVIN^{(n)}\right] = \frac{2\sqrt{N}\sqrt{\frac{E_b}{N_0}}\sigma\left[1 - \sqrt{\frac{2}{\pi}}\frac{\sigma_\phi}{\pi}p_t\right]}{1 - L_I} \quad (55)$$

Now we consider the inphase one-pole digital filter The output of this filter is characterized by the following recursion, as indicated in (38)

$$AVMI^{(n'+1)} = AVMI^{(n')}L_M + (FSTB2^{(n')}+PRTB2^{(n')})TRIND^{(n')} \quad (56)$$

recall that n denotes the nth bit and n' denotes the n'th bit transition. Only where $p_t = 1$ does $n = n'$. In the following analysis, we will model $TRIND^{(n')}$ as a perfect estimator of the algebraic sign of the bit transition*. Bit transitions from -1 to +1 produce a value of TRIND = 1 and bit transitions from +1 to -1 produce a value of TRIND = -1. Again writing the sum of (FSTB2 + PRTB2)TRIND in the form of thermal noise, quantization noise and loop phase error control signal, we have as our recursion (positive bit transitions considered)

$$AVMI^{(n'+1)} = L_M AVMI^{(n')} + n_T^{(n)} - 2J\sqrt{\frac{E_b}{N_0}\frac{R}{B}}\,\sigma \quad (57)$$

where $\sqrt{E_b/N_0\ R/B}\ \sigma$ is the signal level out of the A/D converter and, therefore, the input signal level to the midphase recursive one-pole filter, and we have let $n_T^{(n')} = n^{(n')} + n_q^{(n')}$ for convenience.

From (31) and the fact that $R_s/B = 4$, we have the alternate form

$$AVMI^{(n'+1)} = L_M AVMI^{(n')} + n_{n'} - 4\left(\frac{J}{N}\right)\sqrt{\frac{E_b}{N_0}}\sqrt{N}\,\sigma \quad (58)$$

Further equating the discrete phase error J/N to the continuous equivalent phase error $\phi/2\pi$, we can express (58) in the form

$$AVMI^{(n'+1)} = L_M AVMI^{(n')} + \overbrace{n_T^{(n')} - \frac{2\phi}{\pi}\sqrt{\frac{E_b}{N_0}}\sqrt{N}\,\sigma}^{x^{(n')}} \quad (59)$$

Since the rightmost two terms are of zero-mean value, we see from (A-5) that

$$E\left[AVMI^{(n'+1)}\right] = 0 \quad (60)$$

Now consider the second moment We have

*Since we are dealing with low bit-error rates, this assumption causes a negligible error in the results.

$$E\left[\left(x(n')\right)^2\right] = E\left[\left(n_T(n') - \frac{2\phi}{\pi}\sqrt{\frac{E_b}{N_0}}\sqrt{N}\sigma\right)^2\right] = E\left[\left(n_T(n')\right)^2\right] + \frac{4}{\pi^2}\frac{E_b}{N_0}N\sigma^2\sigma_\phi^2 \quad (61)$$

From (61) and (A-13), it follows that

$$\mathrm{Var}\left[\mathrm{AVMI}^{(n')}\right] = \frac{2\,1N\sigma^2 + 4\,\frac{E_b}{N_0}N\sigma^2\left(\frac{\sigma_\phi}{\pi}\right)^2}{1 - L_M^2} \quad (62)$$

Also, from (60) and (A-5), it follows that

$$E\left[\mathrm{AVMI}^{(n')}\right] = 0 \quad (63)$$

5.0 BIT SYNCHRONIZER DIGITAL FILTER OUTPUT STATISTICS WITH NOISE ONLY--NRZ DATA

In the last section, we characterized the output of the inphase and midphase filters when signal and noise were present and $E_b/N_0 \geq 4$ dB. At lower values of E_b/N_0, the inphase model estimate becomes poorer and one is forced to reconsider the problem when the signal is not present. Since the SNR in the 5-MHz filter bandwidth is, at most, -12 dB at the highest data rate, decreasing the signal will have a negligible effect on the noncoherent AGC gain. We neglect this negligible gain change between no signal and the 4-dB E_b/N_0 value.

Since there are no additional approximations in the midphase case, we may let E_b/N_0 equal zero in (62) and (63) to obtain for the NRZ noise-only statistics

$$\mathrm{Var}\left[\mathrm{AVMI}^{(n')}\right] = \frac{2\,1\,N\,\sigma^2}{1 - L_M^2} \quad (64)$$

and

$$E\left[\mathrm{AVMI}^{(n')}\right] = 0 \quad (65)$$

Now consider the inphase digital filter output statistics. From (37) with $E_b/N_0 = 0$, we have that

$$x^{(n)} = \left| n^{(n)} + n_q^{(n)} \right| \tag{66}$$

since it is no longer possible to employ the approximations of (30), i.e.,

$$E\left[n^{(n)} + n_q^{(n)}\right] \cong E\left[\left|n^{(n)} + n_q^{(n)}\right|\right], \quad Var\left[\left|n^{(n)} + n_q^{(n)}\right|\right] = Var\left[n^{(n)} + n_q^{(n)}\right] \tag{67}$$

If we again model the thermal noise plus quantization noise as Gaussian, we then have

$$E\left[x^{(n)}\right] = 2 \int_0^\infty \frac{x\, e^{-x^2/2\Sigma^2}}{\sqrt{2\pi}\,\Sigma} \tag{68}$$

where Σ^2 is the variance of $\left(n^{(n)} + n_q^{(n)}\right)$. Evaluating (68) and using (27) leads us to

$$E\left[\left|n^n + n_q^{(n)}\right|\right] = \sqrt{\frac{2}{\pi}}\,\Sigma = \sqrt{\frac{2}{\pi}}\sqrt{2.1\,N\sigma^2} \tag{69}$$

as is clear from (24). Further, the variance is given by (28) with $\mu = E[x^n] = 0$ and Σ defined by (27) so that

$$Var\left[n^{(n)} + n_q^{(n)}\right] = \left(1 - \frac{2}{\pi}\right)\left(2.1\,N\sigma^2\right) \tag{70}$$

It then follows that

$$E\left[AVIN^{(n)}\right] = \frac{\sqrt{\frac{2}{\pi}}\sqrt{2\ 1\,N\sigma^2}}{1 - L_I} \tag{71}$$

and

$$Var\left[AVIN^{(n)}\right] = \frac{\left(1 - \frac{2}{\pi}\right) 2\ 1\,N\sigma^2}{1 - L_I^{\,2}} \tag{72}$$

6.0 BIT SYNCHRONIZER DIGITAL FILTER OUTPUT STATISTICS WITH SIGNAL PRESENT--BIPHASE DATA

The biphase inphase digital recursive filter input when no timing error exists is identical to the NRZ data case. When a timing error exists, the output differs somewhat. We have that

$$AVIN^{(n+1)} = L_I AVIN^{(n)} + |FSTB2 - LSTB2| \tag{73a}$$

Assuming that $E_b/N_0 \geq 4$ dB allows us to write (when $|j|/N \leq 1/4$)

$$AVIN^{(n+1)} \cong L_I AVIN^{(n)} + \overbrace{n^{(n)} + n_q^{(n)} + X^{(n)}}^{x^{(n)}} \tag{73b}$$

where

$$x^{(n)} = 2\sqrt{N}\sqrt{\frac{E_b}{N_0}}\,\sigma\left(1 - \frac{4|j|}{N}\right) \quad \text{with probability } (1 - p_t) \tag{74}$$

and

$$x^{(n)} = 2\sqrt{N}\sqrt{\frac{E_b}{N_0}}\,\sigma\left(1 - \frac{2|j|}{N}\right) \quad \text{with probability } p_t \tag{75}$$

Again approximating the discrete variable j/N by the continuous-phase error ϕ (i.e., $|j|/N = |\phi|/2\pi$), we have

$$x^{(n)} = 2\sqrt{N}\sqrt{\frac{E_b}{N_0}}\,\sigma\left(1 - \frac{2|\phi|}{\pi}\right) \quad \text{with probability } (1 - p_t)$$

and (76)

$$x^{(n)} = 2\sqrt{N}\sqrt{\frac{E_b}{N_0}}\,\sigma\left(1 - \frac{|\phi|}{\pi}\right) \quad \text{with probability } p_t$$

Averaging $x^{(n)}$ of (73), we obtain

$$E\left[x^{(n)}\right] = 2\sqrt{N}\sqrt{\frac{E_b}{N_0}}\,\sigma\left(1 - \frac{2}{\pi}\sqrt{\frac{2}{\pi}}\,\sigma_\phi - \frac{1}{\pi}\sqrt{\frac{2}{\pi}}\,\sigma_\phi\, p_t\right) \tag{77}$$

so that

$$E\left[AVIN^{(n)}\right] = \frac{2\sqrt{N}\sqrt{\frac{E_b}{N_0}}\sigma\left(1 - \frac{2}{\pi}\sqrt{\frac{2}{\pi}}\sigma_\phi - \frac{1}{\pi}\sqrt{\frac{2}{\pi}}\sigma_\phi p_t\right)}{1 - L_I} \tag{78}$$

Evaluating $E\left[\left(x^{(n)}\right)^2\right]$, we obtain

$$E\left[\left(x^{(n)}\right)^2\right] = 2\,1N\sigma^2 + 4N\frac{E_b}{N_0}\sigma^2\left[\left(1 - \frac{4}{\pi}\sqrt{\frac{2}{\pi}}\sigma_\phi + \frac{4\sigma_\phi^2}{\pi^2}\right) + \left(\frac{2}{\pi}\sqrt{\frac{2}{\pi}}\sigma_\phi - \frac{3\sigma_\phi^2}{\pi^2}\right)p_t\right] \tag{79}$$

It follows from (77) and (79) that

$$Var\left[x^{(n)}\right] = 2.1N\sigma^2 + 4N\frac{E_b}{N_0}\sigma^2\left[\frac{4}{\pi}\sqrt{\frac{2}{\pi}}\sigma_\phi p_t + \frac{(4\pi-8)}{\pi^3}\sigma_\phi^2 - \frac{(3\pi+8)}{\pi^3}\sigma_\phi^2 p_t^2 - \frac{2}{\pi^3}\sigma_\phi^2 p_t^2\right] \tag{80}$$

Therefore,

$$Var\left[AVIN^{(n)}\right] = \frac{2.1N\sigma^2 + 4N\frac{E_b}{N_0}\sigma^2\left[\frac{4}{\pi}\sqrt{\frac{2}{\pi}}\sigma_\phi p_t + \frac{(4\pi-8)}{\pi^3}\sigma_\phi^2 - \frac{(3\pi+8)}{\pi^3}\sigma_\phi^2 p_t^2 - \frac{2}{\pi^3}\sigma_\phi^2 p_t^2\right]}{1 - L_I^2} \tag{81}$$

Now we consider $AVMI^{(n)}$, the midphase filter output In the biphase case, the integral over the transition is for a duration of one-half a bit time, not a whole bit time, as in the NRZ case.

The midphase filter is specified by

$$AVMI^{(n+1)} = L_M * AVMI^{(n)} + \overbrace{MITB2*TRIND}^{x^{(n)}} \tag{82}$$

Now the signal-plus-noise component, again neglecting bit errors, is given by

$$x^{(n)} = n^{(n)} + n_q^{(n)} - 2J\sqrt{\frac{E_b}{N_0}\frac{R}{B}}\sigma \quad , \; J=1,-1,2,-2,.. \quad \left(\frac{|J|}{N} \leq \frac{1}{4}\right) \tag{83}$$

By (31), we have

$$\frac{R}{B} = \frac{R_s}{NB} = \frac{4}{N} \tag{84}$$

so that (83) becomes

$$x^{(n)} = n^{(n)} + n_q^{(n)} - \frac{2J}{N}(2\sqrt{N})\sqrt{\frac{E_b}{N_0}}\,\sigma \tag{85}$$

If we again approximate the discrete timing error j by an approximately equivalent zero-mean Gaussian phase error ϕ. We use (41) in (85) to obtain

$$x^{(n)} = n^{(n)} + n_q^{(n)} - 2\frac{\phi}{\pi}\sqrt{N}\sqrt{\frac{E_b}{N_0}}\,\sigma \tag{86}$$

Again, since ϕ is assumed to be zero mean, we obtain

$$E\left[x^{(n)}\right] = 0 \tag{87}$$

so that

$$E\left[AVMI^{(n)}\right] = 0 \tag{88}$$

To obtain the second moment and, therefore, the variance, consider $\left(n^{(n)} = n^{(n)} + n_q^{(n)}\right)$

$$E\left[\left(x^{(n)}\right)^2\right] = E\left[\left(n_T^{(n)} - 2\frac{\phi}{\pi}\sqrt{N}\sqrt{\frac{E_b}{N_0}}\,\sigma\right)^2\right] = E\left[\left(n_T^{(n)}\right)^2\right] + 4E\left[n_T^{(n)}\frac{\phi}{\pi}\sqrt{N}\sqrt{\frac{E_b}{N_0}}\,\sigma\right] + 4\frac{E\left[\phi^2\right]}{\pi^2}N\frac{E_b}{N_0}\sigma^2 \tag{89}$$

The second term is zero if $n_T^{(n)}$ and ϕ are uncorrelated Since ϕ depends on at least 20 or more bits, the correlation is very small; hence, we assume zero for the second term.

Hence, (89) becomes (since $E[\underline{x}(n)] = 0$) ($N' = N/2$)

$$\mathrm{Var}[x(n)] = 1.05\,N\sigma^2 + \frac{4N\sigma_\phi^2}{\pi^2}\frac{E_b}{N_0}\sigma^2 \tag{90}$$

From (A-13), we obtain

$$\mathrm{Var}[\mathrm{AVMI}^{(n)}] = \frac{1.05\,N\sigma^2 + \frac{4N\sigma_\phi^2}{\pi}\frac{E_b}{N_0}\sigma}{1 - L_M^2} \tag{91}$$

Thus, (88) and (91) characterize the discrete one-pole filter output when the distribution is assumed to be normal.

7.0 BIT SYNCHRONIZER DIGITAL FILTER OUTPUT STATISTICS WITH NOISE ONLY--BIPHASE DATA

In this section, we determine the one-pole digital filter output statistics for the noise-only case with biphase data. Since the inphase $[\mathrm{AVIN}^{(n)}]$ filter has the same statistics for noise only with both NRZ and biphase data, we therefore obtain from (71) and (72)

$$E[\mathrm{AVIN}^{(n)}] = \frac{\sqrt{\frac{2}{\pi}}\sqrt{2.1\,N\sigma^2}}{1 - L_I} \tag{92}$$

and

$$\mathrm{Var}[\mathrm{AVIN}^{(n)}] = \frac{\left(1 - \frac{2}{\pi}\right)2.1\,N\sigma^2}{1 - L_I^2} \tag{93}$$

Now the midphase filter statistics with noise can be obtained from (88) and (91) with E_b/N_0 set equal to zero:

$$E[\mathrm{AVMI}^{(n)}] = 0 \tag{94}$$

and

$$\mathrm{Var}[\mathrm{AVMI}^{(n)}] = \frac{1.05\,N\sigma^2}{1 - L_M^2} \tag{95}$$

8.0 PROBABILITIES OF THE LOCK DETECTOR TEST

From (29), we see that the current lock detector test is based on comparing the inphase filter output with 6.5 times the magnitude of the midphase filter output. If the inphase filter output is larger, lock is then declared; otherwise, an out-of-lock condition is indicated. We consider the slightly more general test

$$\text{AVIN} \overset{?}{>} r\ |\text{AVMI}| \tag{96}$$

where r is a real-valued number greater than zero. Let p_n denote the probability that the inequality of (64) is satisfied so that

$$p_n = P\left(\text{AVIN}^{(n)} > r\ \text{AVMI}^{(n)}\right) \tag{97}$$

Denote the probability density* of $\text{AVMI}^{(n)}$ and $\text{AVIN}^{(n)}$, respectively, by $p_n\left(\text{AVMI}^{(n)}\right)$ and $p_I\left(\text{AVIN}^{(n)}\right)$; then we obtain

$$p_n = \int_0^\infty p\left(\left|\text{AVMI}^{(n)}\right|\right) \int_{r\left|\text{AVMI}^{(n)}\right|}^\infty p\left(\text{AVIN}^{(n)}\right) d\left|\text{AVMI}^{(n)}\right| d\ \text{AVIN}^{(n)} \tag{98}$$

Let u = AVMI and y = AVIN, then, from (54), (55), (62) and (63) and using the Gaussian assumption, we have

$$p(u) = \frac{1}{\sqrt{2\pi}\ \sigma_{MI}} e^{-u^2/2\sigma_{MI}^2} \qquad \forall u \tag{99}$$

and

$$p(y) = \frac{1}{\sqrt{2\pi}\ \sigma_{IN}} e^{-y^2/2\sigma_{IN}^2} \qquad \forall y \tag{100}$$

*We assume that $\text{AVMI}^{(n)}$ and $\text{AVIN}^{(n)}$ have continuous-density functions by virtue of the assumption that the filter outputs are Gaussian.

where $\mathrm{Var}[\mathrm{AVIN}(n)] = \sigma_{IN}^2$, $\mathrm{Var}[\mathrm{AVMI}(n)] = \sigma_{MI}^2$, $E[\mathrm{AVIN}(n)] = \mu_{IN}$ and $E[\mathrm{AVMI}(n)]=0$. If we let $x = |u|$, we then have

$$p(x) = \frac{2}{\sqrt{2\pi}\,\sigma_{MI}} e^{-x^2/2\sigma_{MI}^2} \qquad x \geq 0 \qquad (101)$$

so that $x = |\mathrm{AVMI}|$. Using (96) and (97) in (94) yields

$$p_n = \int_0^\infty \frac{2}{\sqrt{2\pi}\,\sigma_{MI}} e^{-x^2/2\sigma_{MI}^2} \int_{rx}^\infty \frac{1}{\sqrt{2\pi}\,\sigma_{IN}} e^{\frac{-(y-\mu_{IN})^2}{2\sigma_{IN}^2}} dy\,dx \qquad (102)$$

A change of variables leads to

$$p_n = \int_0^\infty \frac{1}{\sqrt{2\pi}\,\sigma_{MI}} e^{-x^2/2\sigma_{MI}^2} \mathrm{ERFC}\left[\frac{rx - \mu_{IN}}{\sqrt{2}\,\sigma_{IN}}\right] dx \qquad (103)$$

where

$$\mathrm{ERFC}(t) = \frac{2}{\sqrt{\pi}} \int_t^\infty e^{-t^2} dt \qquad (104)$$

First consider the NRZ case. The original parameters for the one-pole digital filter were

$$L_I = \frac{252}{256} = 0.9844 \quad , \quad L_M = \frac{242}{256} = 0.9453 \quad ; \quad \mathrm{AVIN} \overset{?}{>} 6.5\ |\mathrm{AVMI}| \qquad (105)$$

and the new recommended values, to be discussed below, are

$$L_I = \frac{254}{256} = 0\ 9922 \quad ; \quad L_M = \frac{248}{256} = 0\ 9688 \quad ; \quad \mathrm{AVIN} \overset{?}{>} 13\ |\mathrm{AVMI}| \qquad (106)$$

The most desirable fix to the lock detector would utilize new narrower band filters for the lock detector which would be distinct from the loop inphase

and midphase filters; however, the modified version (corrections, etc.) of the microprocessor does not have excess memory or the speed necessary to implement the additional lock detector filters. Consequently, single filters will be a compromise between the lock detector and the bit synchronizer loop requirements. It should be noted that Richard Helgeson has tried these NRZ parameters values (from (106)) and found them to be quite satisfactory. The Manchester mode of the bit synchronizer had original parameters of

$$L_I = \frac{252}{256} = 0.9844 \quad ; \quad L_M = \frac{252}{256} = 0.9844 \quad ; \quad AVMI \overset{?}{>} 5 \ |AVMI| \tag{107}$$

The new recommended values are

$$L_I = \frac{254}{256} = 0.9922 \quad ; \quad L_M = \frac{254}{256} = 0.9922 \quad ; \quad AVIN \overset{?}{>} 15 \ |AVMI| \tag{108}$$

Note that L_I applies to both the AVIN and AVMI filters.

As mentioned previously, these filter L values were compromises since they were constrained to be of the form N/256, where N is an even positive integer. Various values of r were tried for the new parameter values. Due to the approximations in the analysis and the computer program involved, it was determined that, for given "L" values, p_n would saturate at around four 0.9999z, where z is the fifth digit and is between 1 and 9. Consequently, by narrowing the digital filters and increasing r, it was possible to keep the probability p_n high (0.9999z) when the signal was present and simultaneously reduce the probability p_n when only noise was present. This will reduce the time to indicate lost lock due to signal dropout. In other words, the detection probability could be maintained and the false alarm reduced, thereby reducing the mean time to indicate the out-of-lock condition when the signal drops out

The results for the NRZ and biphase cases are indicated in Tables 2 and 3, with P_d denoting the value of p_n when the signal is present and P_{FA} is the value of p_n when the signal is absent for all data rates. Equation (103) was used to evaluate these probabilities.

Table 2. NRZ Data

$\frac{E_b}{N_0}$ (dB)		Performance with Original Parameters	Performance with Recommended Parameters
P_d	4	0.999921	0.999940
	6	0.999921	0.999940
	7	0.999921	0.999940
P_{FA}	Noise Only	0 98850	0.9478

Table 3. Biphase Data

$\frac{E_b}{N_0}$ (dB)		Performance with Original Parameters	Performance with Recommended Parameters
P_d	4	0.999940	0.998923
	6	0 999940	0.999921
	7	0 999940	0.999954
P_{FA}	Noise Only	0.98783	0.769926

In order to determine the mean time to indicate the out-of-lock state when the signal is not present, we must evaluate

$$\overline{T}_{OL} = T_M\left[1 - P_{FA} + 2\left(1 - P_{FA}\right)P_{FA} + 3\left(1 - P_{FA}\right)P_{FA}^{\,2} + \ldots\right] \quad (109)$$

where P_{FA} is the false-alarm probability and T_M is the "memory time" of the inphase digital filter output*.

From (108),

$$\overline{T}_{OL} = \left(1 - P_{FA}\right)T_M\left[1 + 2\,P_{FA} + 3\,P_{FA}^{\,2} + \ldots\right] \quad (110)$$

*The memory is approximately $T_b/(1 - L_I)$.

and, since

$$1 + 2\alpha + 3\alpha^2 + 4\alpha^3 + \cdots = \frac{1}{(1-\alpha)^2} \tag{111}$$

we have the simple result:

$$\overline{T}_a = \frac{T_M}{1 - P_{FA}} \tag{112}$$

Evaluating $\overline{T}_{OL}$ for the four cases of Tables 2 and 3 yields the results presented in Table 4 for both the NRZ and biphase cases.

Table 4 Mean Time to Indicate Out of Lock (Noise Only)

Case	$\overline{T}_{OL}$ (Seconds)				
	16 kbps	8 kbps	4 kbps	2 kbps	1 kbps
NRZ - Original Parameters	0.348	0.696	1 392	2.784	5 568
NRZ - Recommended Parameters	0.154	0.307	0.614	1 228	2 456
Biphase - Original Parameters	0 329	0.657	1.314	2.628	5.256
Biphase - Recommended Parameters	0.0348	0.070	0 139	0.278	0.556

Thus, we see that the recommended parameters for the filters and lock detector reduce the time to indicate the out-of-lock condition to one-half of the original case for the NRZ mode and about one-tenth for the Manchester mode

It should be emphasized that the loop performance could have been considerably improved if separate filters were utilized for the lock detector since they would have been made narrower Due to the changes and additions in the microprogram for saturation, etc., however, the additional room for the extra filters was not available. Furthermore, the constants relating AVIN and |AVMI| were constrained to be of the form $2^n \times 6.5$, where n = 1, -1, 2, -2, etc for the NRZ mode and, for the biphase mode, were constrained to be 5, 10, or 15. Consequently, only approximately optimal values could be used It should

also be emphasized that, because the DC bias-removal and scaling algorithms were unavailable, their effects could not be included in the analysis presented here. It is believed they will not affect the analysis during tracking; however, when the signal is removed, the DC bias-removal algorithm could conceivably cause the lock detector to indicate the out-of-lock state more quickly.

REFERENCES

1. S. Houston, D. Martin and L. Stine, "Microprocessor Bit Synchronizer for Shuttle Payload Communications," IEEE Trans. on Comm., Vol. COM-26, No. 11, November 1978.

2. B. Parrish, "PSP Bit Synchronizer Algorithm Flowchart Summary for the NRZ Mode," JSC Document, undated (about July 1982).

3. Jack K. Holmes, Coherent Spread Spectrum Systems, Chapter 12, Wiley-Interscience, 1982.

4. R. J Helgeson, "PSP Bit Synchronizer False-Lock Problem," a presentation to the Shuttle S-Band Meeting of September 15, 1982.

5 SCTE Payload Signal Processor Preliminary Design Data Package, Vol I, TRW internal report.

APPENDIX A

EVALUATION OF THE MEAN AND VARIANCE OF THE RECURSIVE ONE-POLE DIGITAL-FILTER OUTPUT

In this appendix, we derive the steady-state mean and variance of the recursive one-pole digital filter used for both the inphase and midphase filters. Let $z^{(n)}$ be the value of the filter output at time n. We then have

$$z^{(n+1)} = L\, z^{(n)} + x^{(n)} \qquad 0 < L < 1 \qquad \text{(A-1)}$$

where $x^{(n)}$ is the nth bit sample of the input digital matched-filter output. In (36), we showed that its SNR is $1.9\ E_b/N_0$. Solving (A-1), we obtain

$$z^{(n+1)} = \sum_{i=0}^{n} x_i\, L^{n-i} \qquad \text{(A-2)}$$

To obtain the mean $E\left[z^{(n)}\right]$, we average both sides of (A-1) to achieve

$$E\left[z^{n+1}\right] = L_I\, E\left[z^{(n)}\right] + E\, x^{(n)} \qquad \text{(A-3)}$$

In steady state,

$$E\left[z^{(n)}\right] = E\left[z^{(n+1)}\right] \qquad \text{(A-4)}$$

so that (A-3) yields

$$E\left[z^{(n)}\right] = \frac{E\left[x^{(n)}\right]}{1 - L} \qquad \text{(A-5)}$$

Now we consider the variance of $z^{(n)}$. First, we square and take the ensemble average of (A-1) to yield

$$E\left[\left(z^{(n+1)}\right)^2\right] = L^2\, E\left(z^{(n)}\right)^2 + 2L\, E\left[x^{(n)} z^{(n)}\right] + E\left[\left(x^{(n)}\right)^2\right] \qquad \text{(A-6)}$$

In steady state,

$$E\left[\left(z^{(n+1)}\right)^2\right] = E\left[\left(z^{(n)}\right)^2\right] \tag{A-7}$$

so that

$$E\left[\left(z^{(n)}\right)^2\right] = \frac{2L\,E\left[x^{(n)}\right]\,E\left[z^{(n)}\right] + E\left[\left(x^{(n)}\right)^2\right]}{1 - L^2} \tag{A-8}$$

By definition,

$$\mathrm{Var}\left(z^{(n)}\right) = E\left[\left(z^{(n)}\right)^2\right] - E^2\left[z^{(n)}\right] \tag{A-9}$$

Therefore,

$$\mathrm{Var}\left[z^{(n)}\right] = \frac{2L\,E\left[x^{(n)}\right]E\left[z^{(n)}\right] + E\left[\left(x^{(n)}\right)^2\right]}{1 - L^2} - \frac{E^2\left[x^{(n)}\right]}{(1 - L)^2} \tag{A-10}$$

or

$$\mathrm{Var}\left[z^{(n)}\right] = \frac{2(1-L)\,L\,E^2\left[x^{(n)}\right] + (1-L)^2\,E\left[\left(x^{(n)}\right)^2\right] - \left(1-L^2\right)E^2\left[x^{(n)}\right]}{(1 - L^2)(1 - L)^2} \tag{A-11}$$

After simplifying, we obtain

$$\mathrm{Var}\left[z^{(n)}\right] = \frac{E\left[\left(x^{(n)}\right)^2\right] - E^2\left[x^{(n)}\right]}{1 - L^2} \tag{A-12}$$

or, finally,

$$\mathrm{Var}\left[z^{(n)}\right] = \frac{\mathrm{Var}\left[x^{(n)}\right]}{1 - L^2} \tag{A-13}$$

Equations (A-5) and (A-13) constitute the main results of this appendix

APPENDIX B

ORIGINAL PSP BIT SYNCHRONIZER ALGORITHM

The following documentation is a slightly updated form of an abbreviated flowchart of the PSP bit synchronizer algorithms for NRZ and biphase-L data. They are not considered to be exact and can be compared to the "final version" given in Appendix C. The NRZ algorithm includes a transition check which was not in the original algorithm, plus the changes of the lock detector. The biphase-L algorithm has not been updated due to the lack of a complete algorithm; however, the lock detector portion does have the new parameters. This flowchart was developed at Johnson Space Center by Brett Parrish independently of any flowcharts that TRW might have used in the development of their bit synchronizer program. The PSP bit synchronizer "machine-code" program (as supplied by TRW) was disassembled and flowcharts were generated from it.

B 1 NOMENCLATURE

Each bit of incoming data is sampled at a rate of 1.024 MHz and integrated (summed) in hardware. At the end of the bit period, the hardware interrupts the bit synchronizer computer (which is caught in a loop at program location PEXEC) and the "bit-time interrupt" routine is performed.

The bit-time interrupt routine polls the hardware for three partial integrals, as shown in Figure B.1 (assume that the bit synchronizer is locked). When the bit synchronizer is locked, the hardware takes 1.024×10^6/DATA RATE = Ns samples per bit.

The current microcode program utilizes DMPNM, as described below. The new program was modified to avoid saturation but, due to time limitations, has not been introduced in the discussion to follow. Whenever a phase correction is required, the software changes the nominal dump count by a small amount $\pm e$.

$$\underset{\text{(nominal)}}{\text{DMPNM}} + \underset{(\Delta\phi)}{\text{DMPCP}} + \underset{\text{(rate tracking)}}{\text{DMPCD}} = \text{DMPCU}$$

where

DMPCU = current value of dump count to be output to hardware (number of samples/4 to be taken during the next bit period)

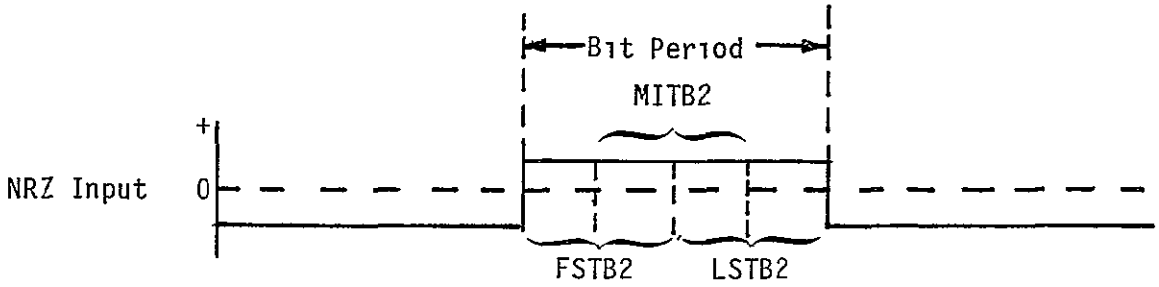

NOTES FSTB2 - first half-bit integral
MITB2 - middle half-bit integral (used in biphase mode only)
LSTB2 - last half-bit integral
PRTB2 - last half-bit integral of previous bit

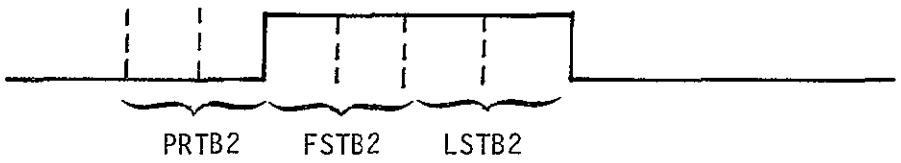

NOTES For NRZ data formats, the software implements two filters:

$|FSTB2 + LSTB2| \rightarrow$ inphase filter

$(PRTB2 + FSTB2) * TRIND \rightarrow$ midphase filter

TRIND is the transition indicator and has a value of +1 or -1 or 0 The MITB2 value is not used in the NRZ mode

Figure B 1 Half-Bit Integrals Used in the Algorithm

DMPNM = nominal dump count = Ns/4

DMPCP = dump count correction due to phase-tracking loop

DMPCD = dump count correction due to data-rate tracking loop

Bit-time interrupt routine (executed after hardware integrates over one bit period):

1. Outputs previous bit decision to frame synchronizer circuit
2. Takes current LSTB2 and puts it in PRTB2
3. Inputs FSTB2 from hardware
4. Inputs MITB2 from hardware
5. Inputs LSTB2 from hardware
6. Outputs new DMPCU to hardware
7. Sets DMPCU equal to DMPNM
8. Set NDATR flag
9. Returns to PEXEC loop in main routine.

B.2. NRZ Algorithm

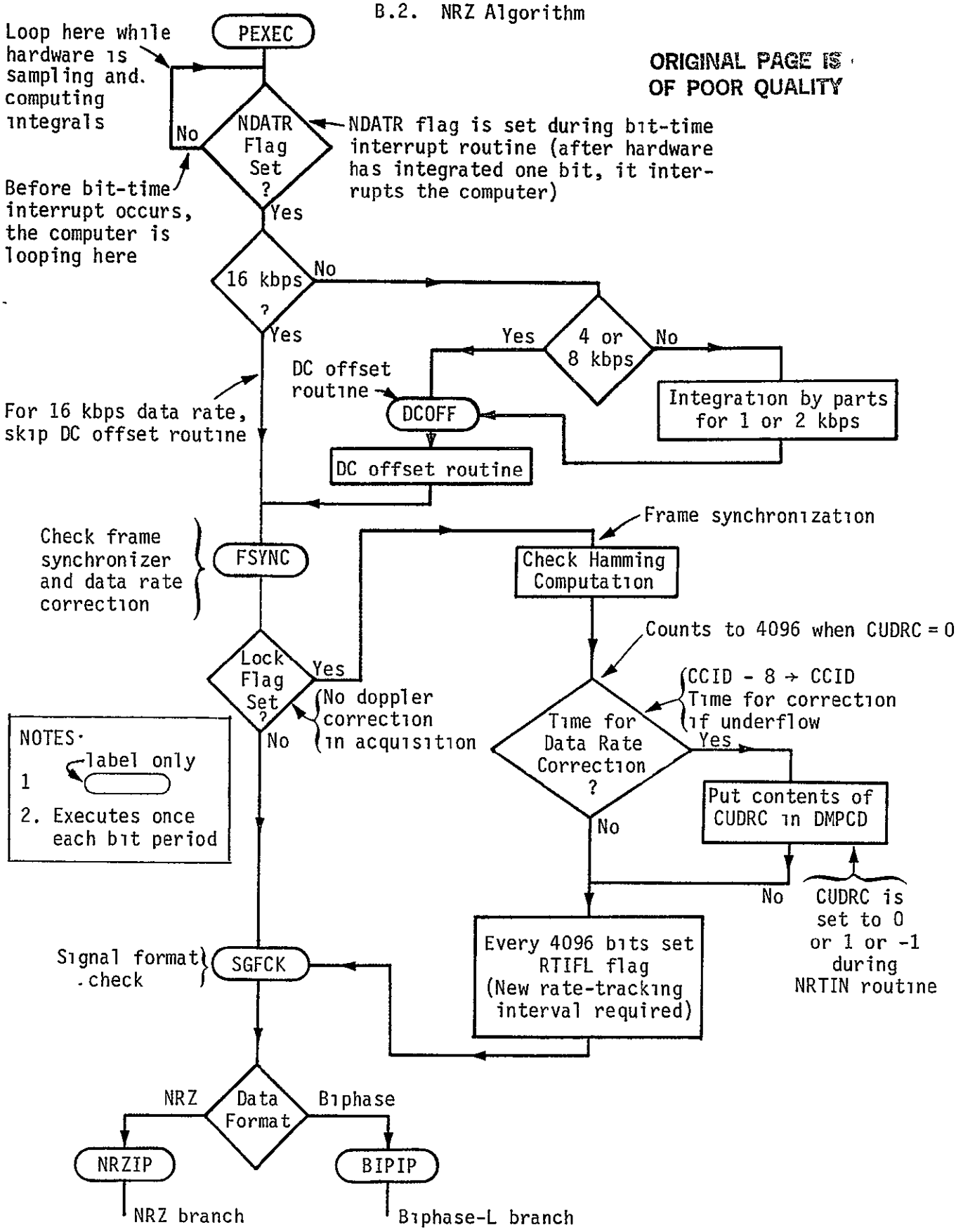

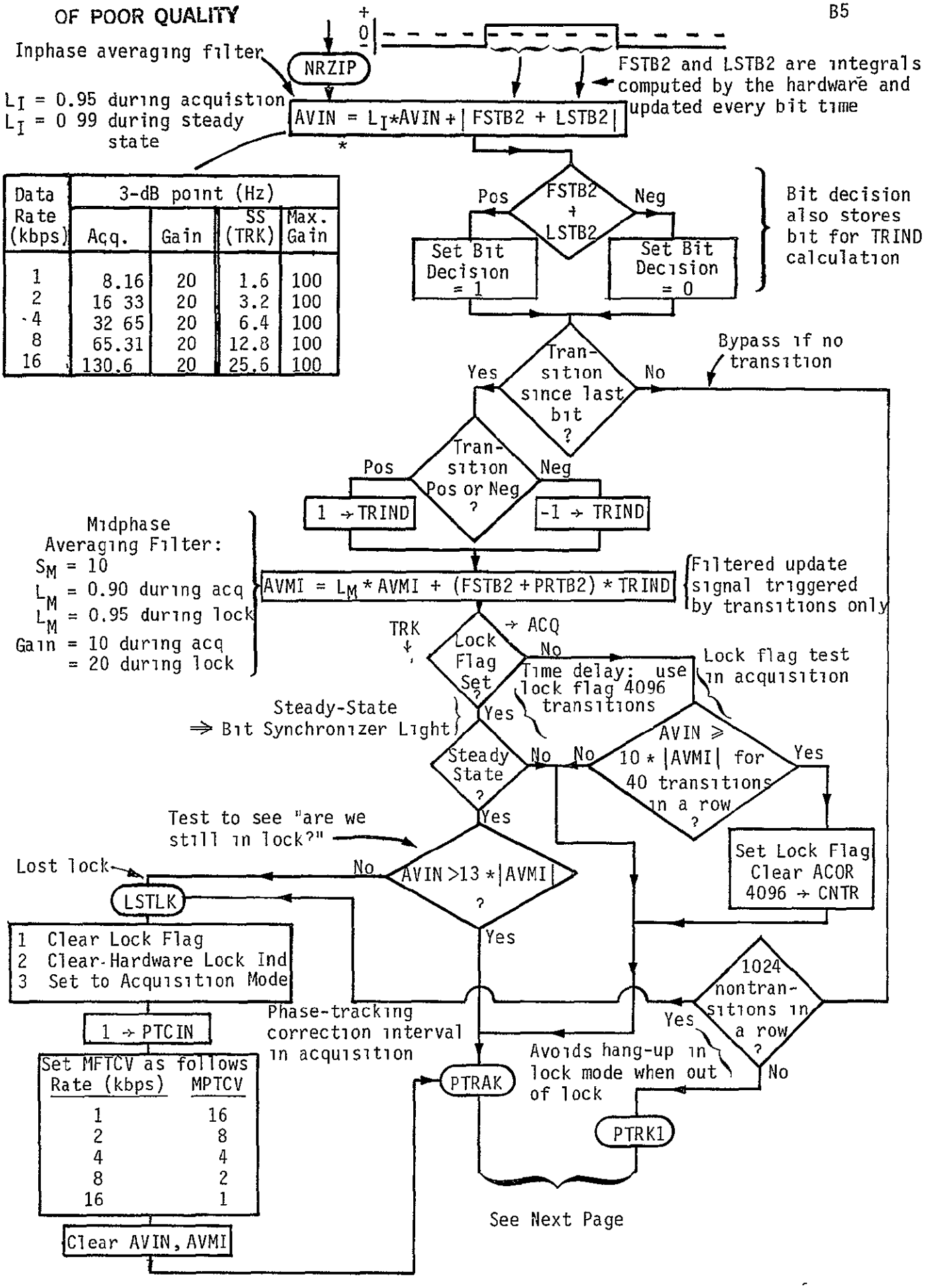

Data Rate (kbps)	3-dB point (Hz) Acq.	Gain	SS (TRK)	Max. Gain
1	8.16	20	1.6	100
2	16 33	20	3.2	100
4	32 65	20	6.4	100
8	65.31	20	12.8	100
16	130.6	20	25.6	100

Rate (kbps)	MPTCV
1	16
2	8
4	4
8	2
16	1

See Next Page

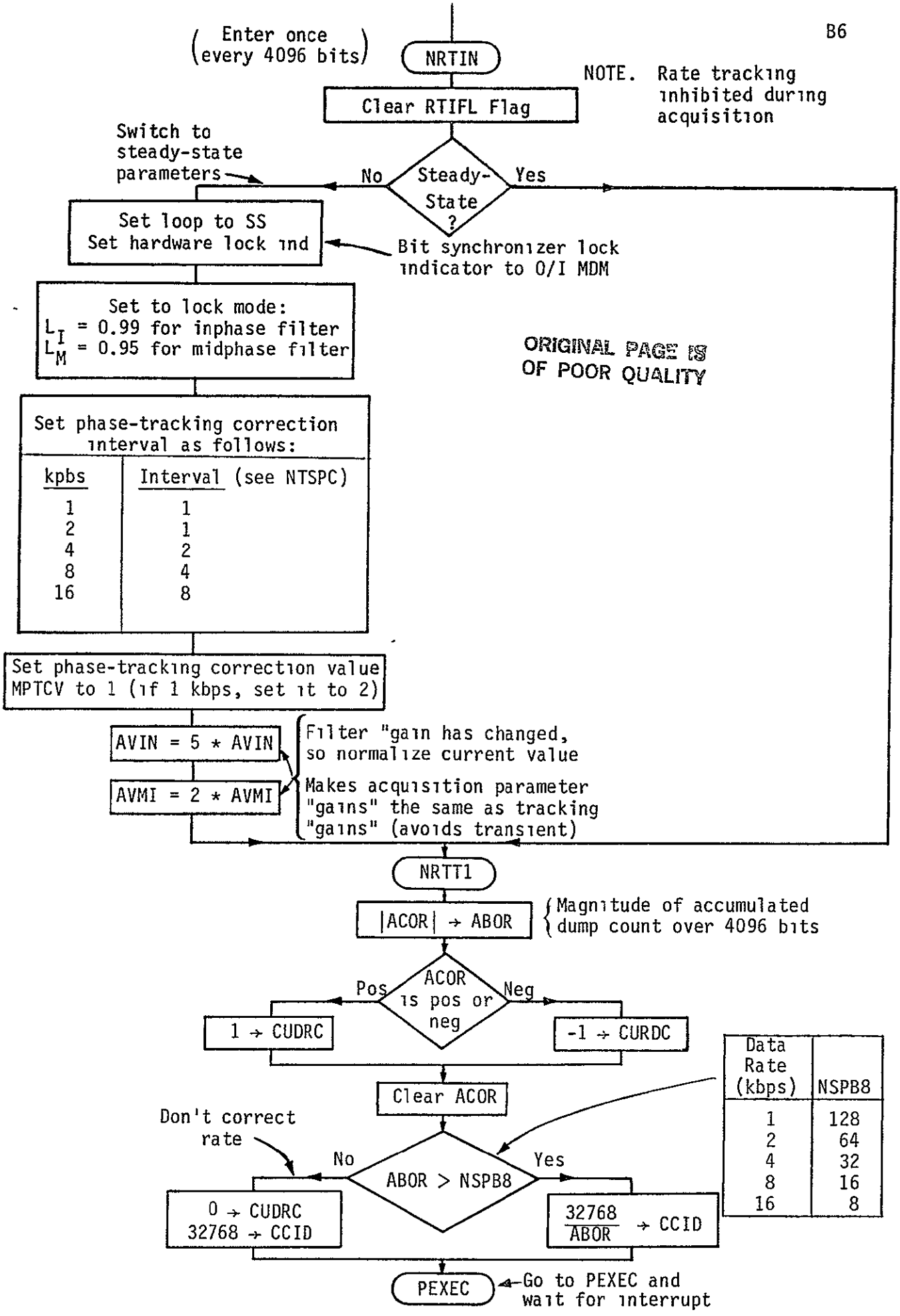
Enter once every 4096 bits
NRTIN
NOTE. Rate tracking inhibited during acquisition
Clear RTIFL Flag
Switch to steady-state parameters
No
Steady-State ?
Yes
Set loop to SS
Set hardware lock ind
Bit synchronizer lock indicator to O/I MDM
Set to lock mode:
L_I = 0.99 for inphase filter
L_M = 0.95 for midphase filter
ORIGINAL PAGE IS OF POOR QUALITY
Set phase-tracking correction interval as follows:
kpbs | Interval (see NTSPC)
1 | 1
2 | 1
4 | 2
8 | 4
16 | 8
Set phase-tracking correction value MPTCV to 1 (if 1 kbps, set it to 2)
AVIN = 5 * AVIN
AVMI = 2 * AVMI
Filter "gain has changed, so normalize current value
Makes acquisition parameter "gains" the same as tracking "gains" (avoids transient)
NRTT1
|ACOR| → ABOR
Magnitude of accumulated dump count over 4096 bits
Pos
ACOR is pos or neg
Neg
1 → CUDRC
-1 → CURDC
Clear ACOR
Don't correct rate
No
ABOR > NSPB8
Yes
0 → CUDRC
32768 → CCID
32768 / ABOR → CCID
Data Rate (kbps) | NSPB8
1 | 128
2 | 64
4 | 32
8 | 16
16 | 8
PEXEC
Go to PEXEC and wait for interrupt

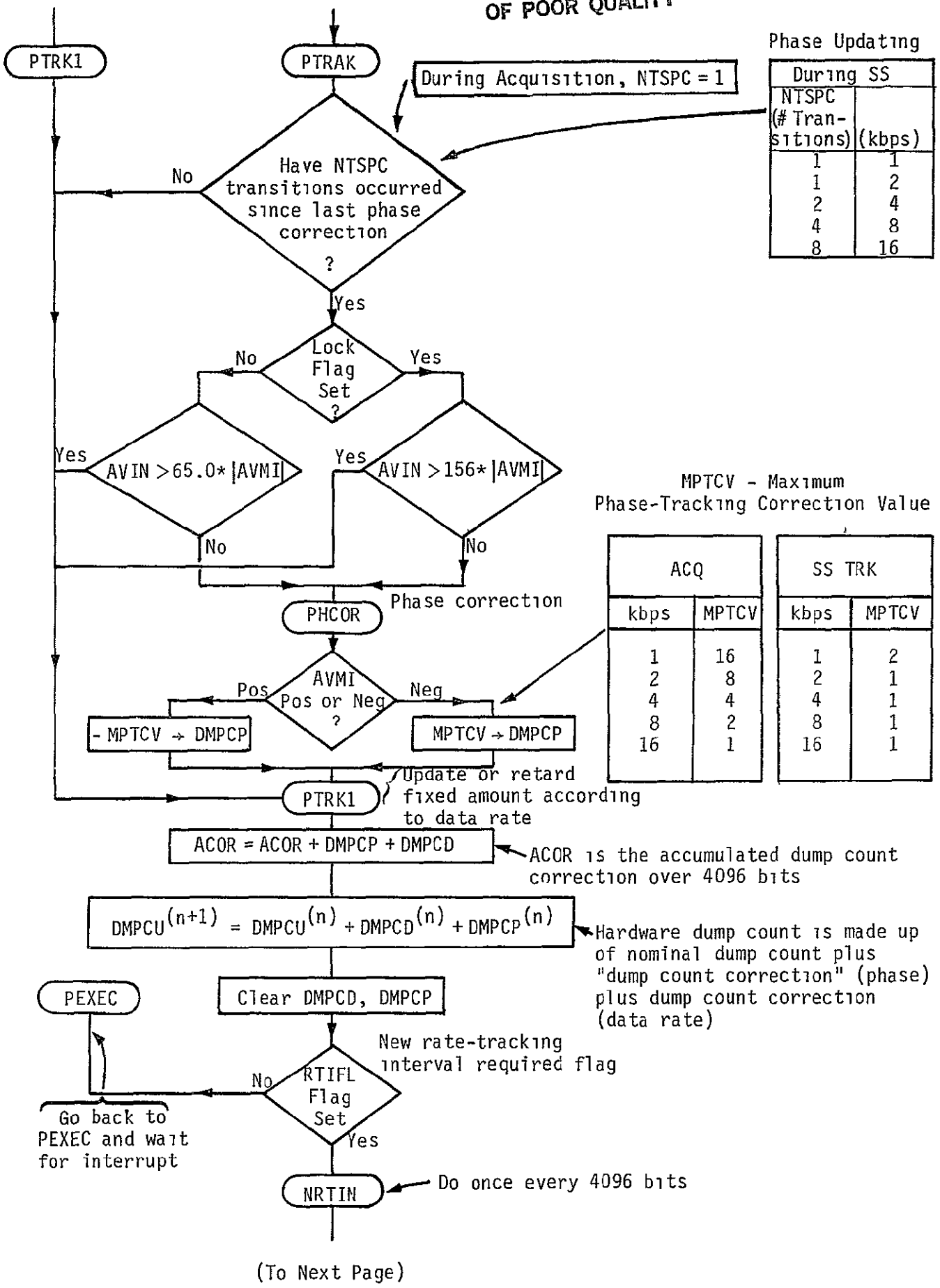

Phase Updating

During SS	
NTSPC (# Transitions)	(kbps)
1	1
1	2
2	4
4	8
8	16

MPTCV - Maximum Phase-Tracking Correction Value

ACQ		SS TRK	
kbps	MPTCV	kbps	MPTCV
1	16	1	2
2	8	2	1
4	4	4	1
8	2	8	1
16	1	16	1

Bit Time Interrupt Routine (Executed after hardware integrates one bit)

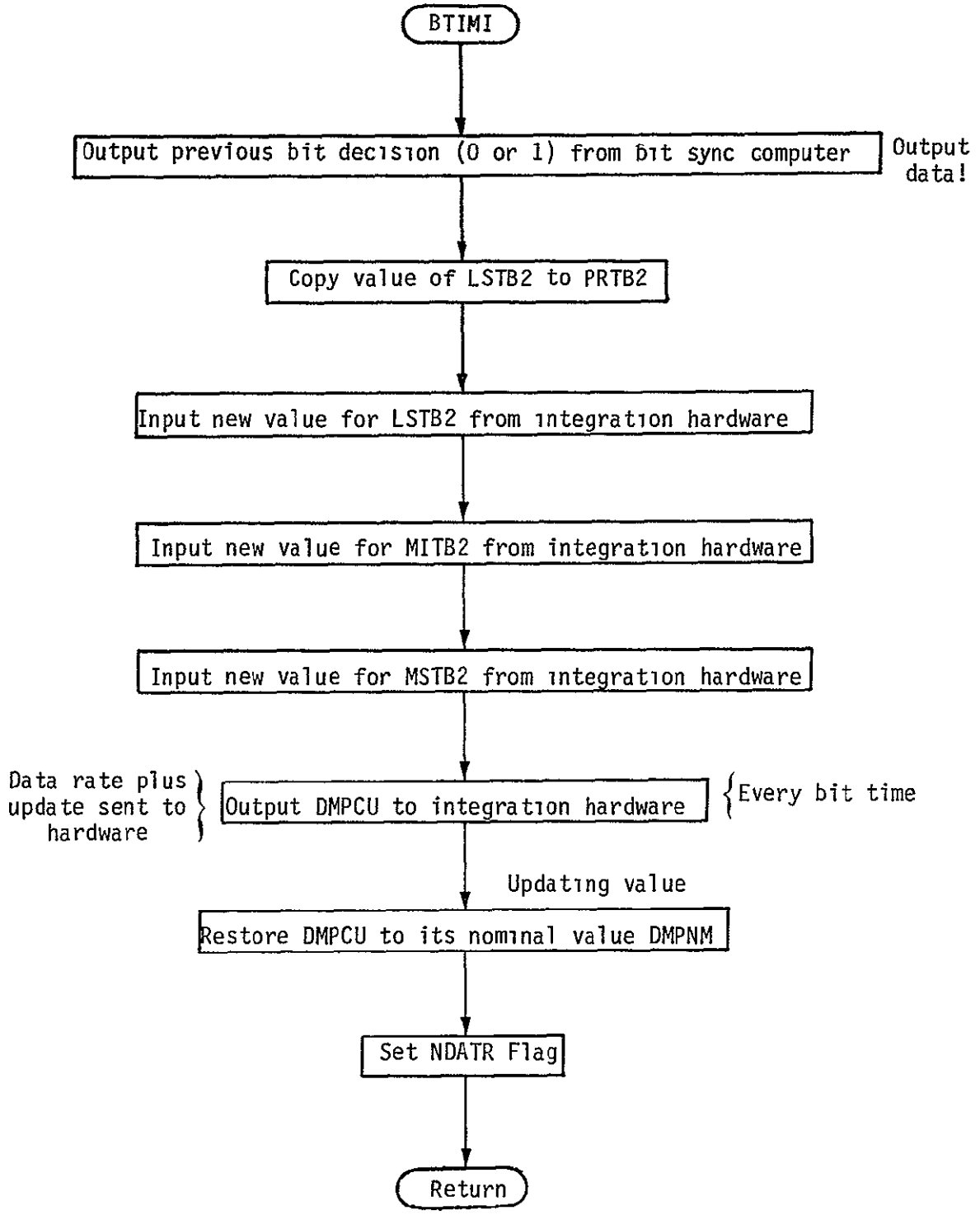

B.3. Biphase-L Algorithm

(Executes once each bit period)

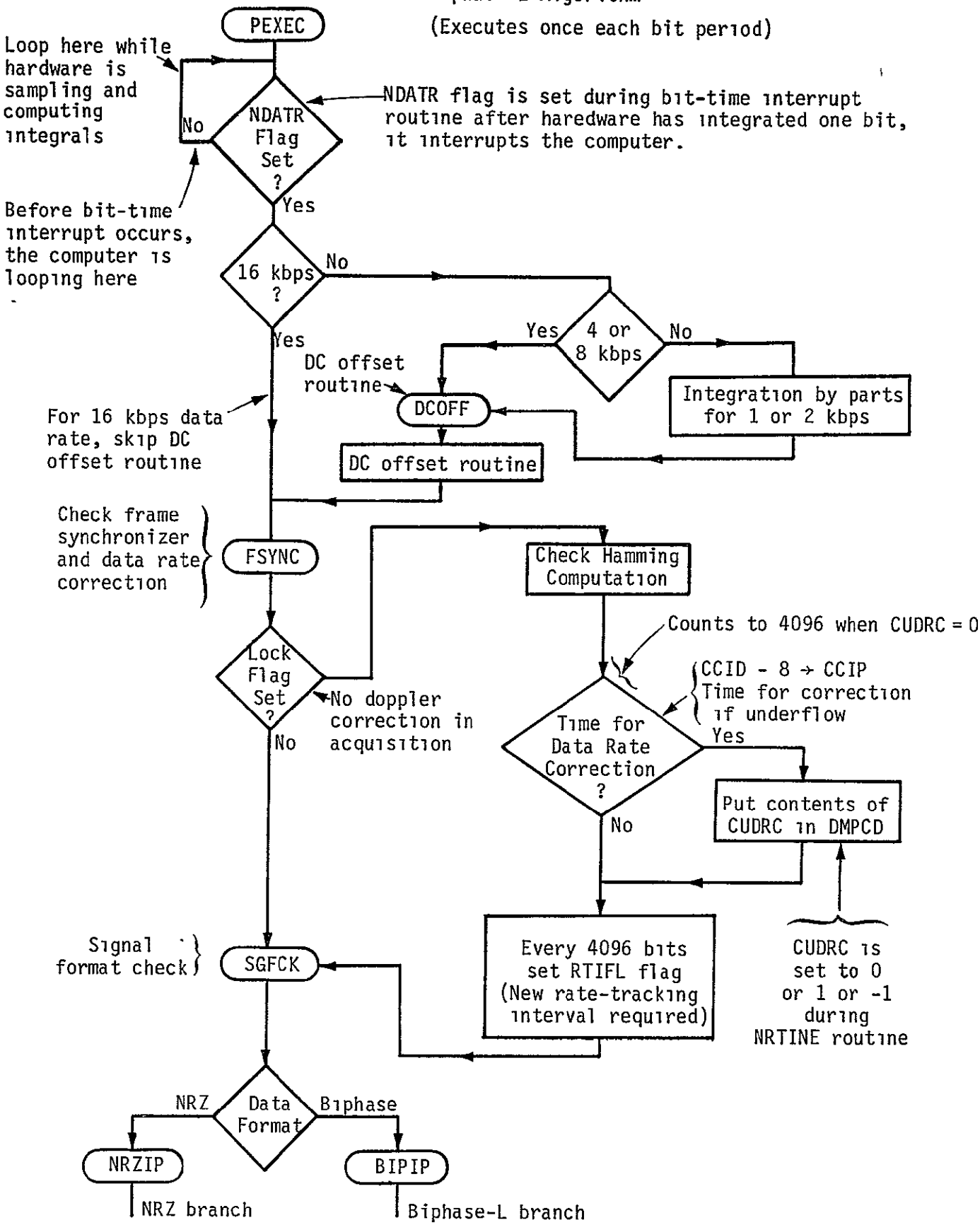

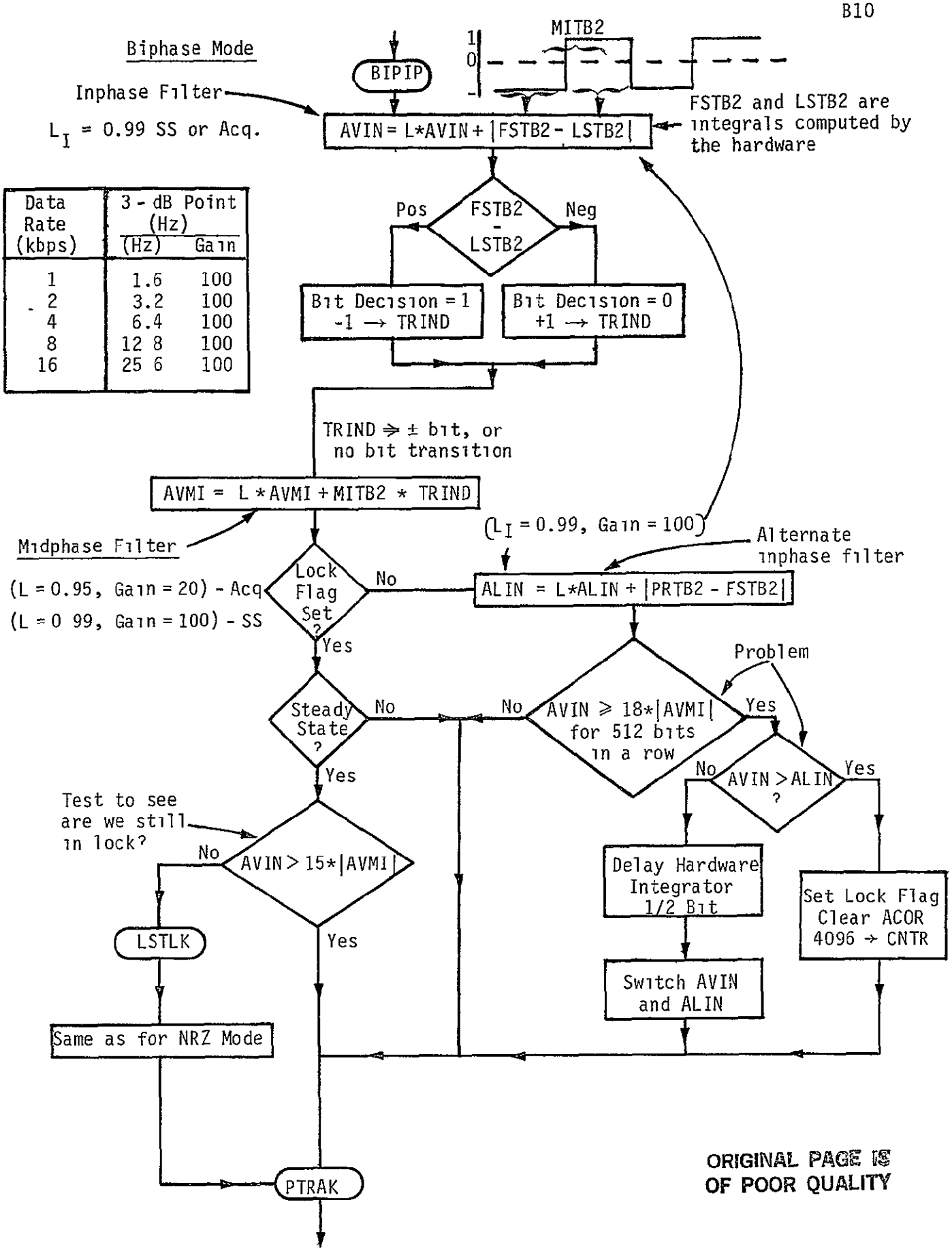

Data Rate (kbps)	3 - dB Point (Hz) (Hz)	Gain
1	1.6	100
2	3.2	100
4	6.4	100
8	12 8	100
16	25 6	100

ORIGINAL PAGE IS
OF POOR QUALITY

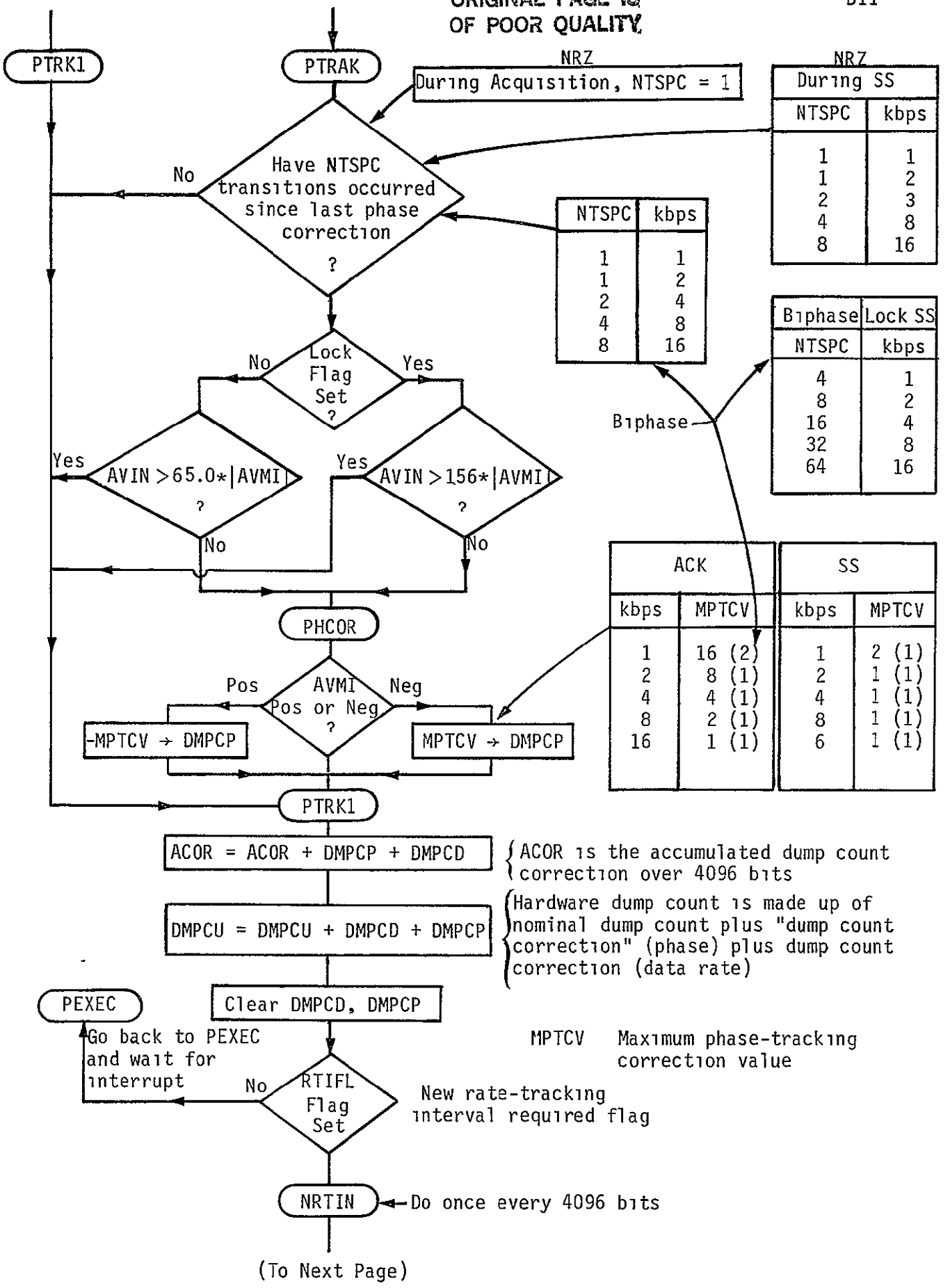

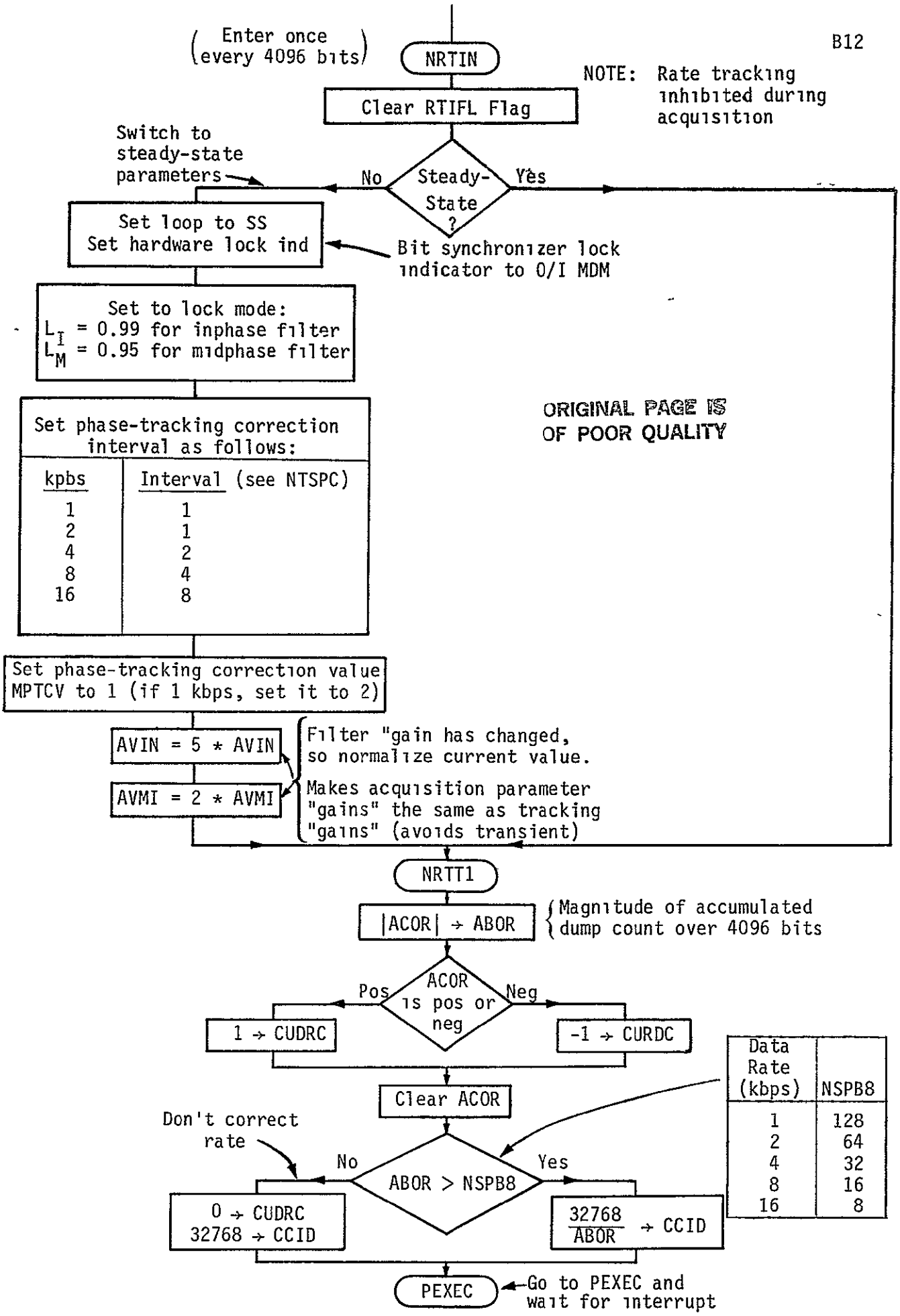

Bit Time Interrupt Routine (Executed after hardware integrates one bit)

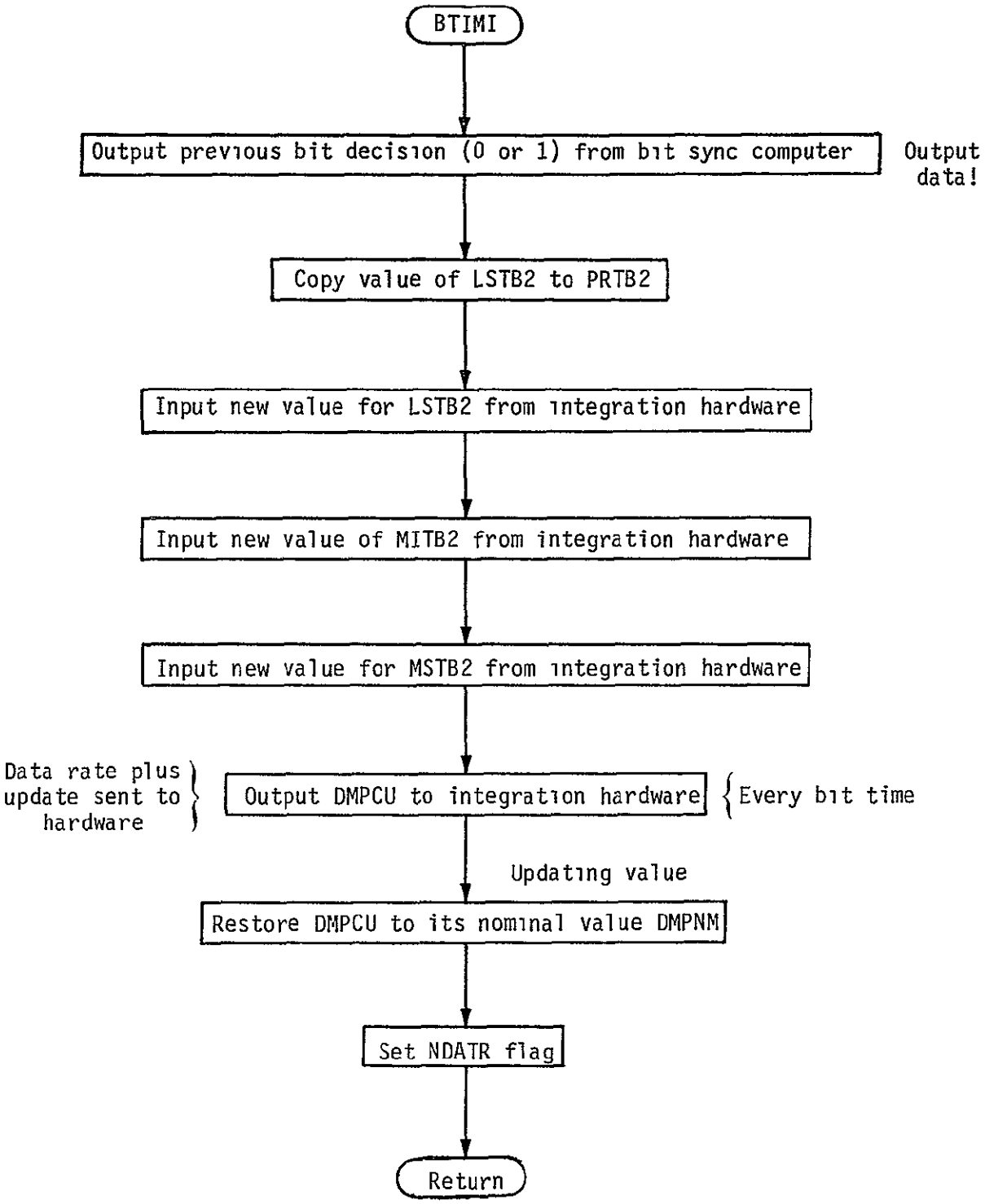

APPENDIX C

NEW PSP BIT SYNCHRONIZER ALGORITHM

This new algorithm was made available to the author by Brett Parrish. The changes in the original algorithm leading to this algorithm were made primarily by Rich Helgeson and Brett Parrish. This program is current as of October 22, 1982.

Power-up Routine

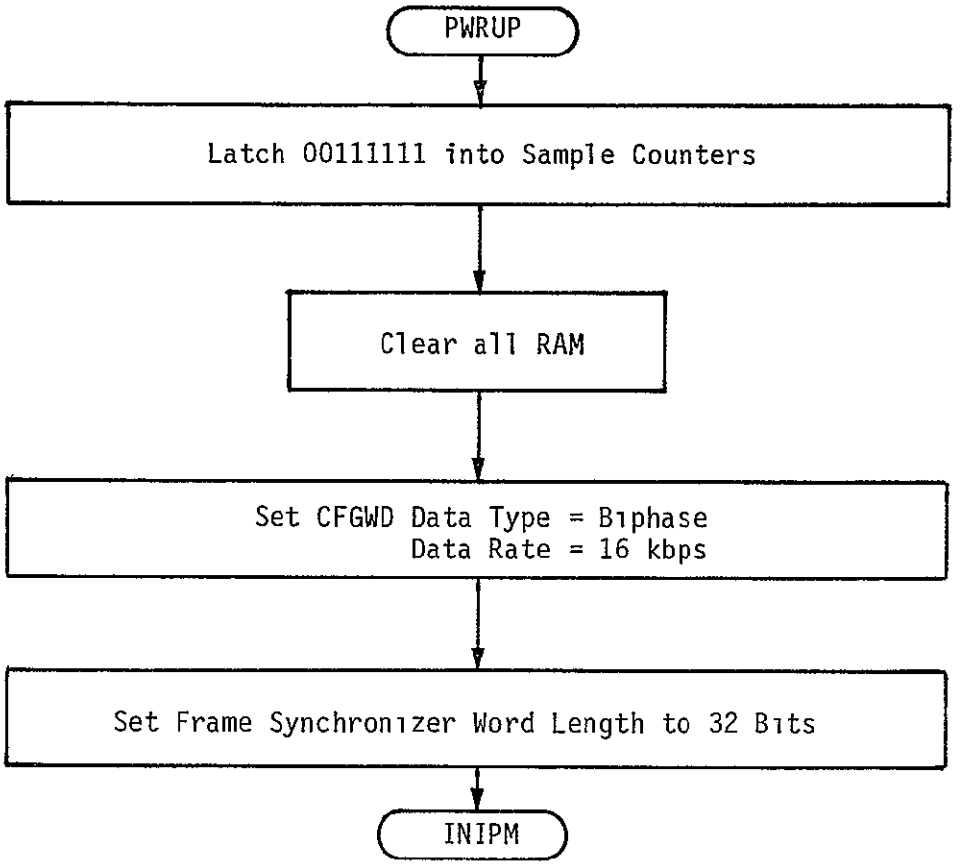

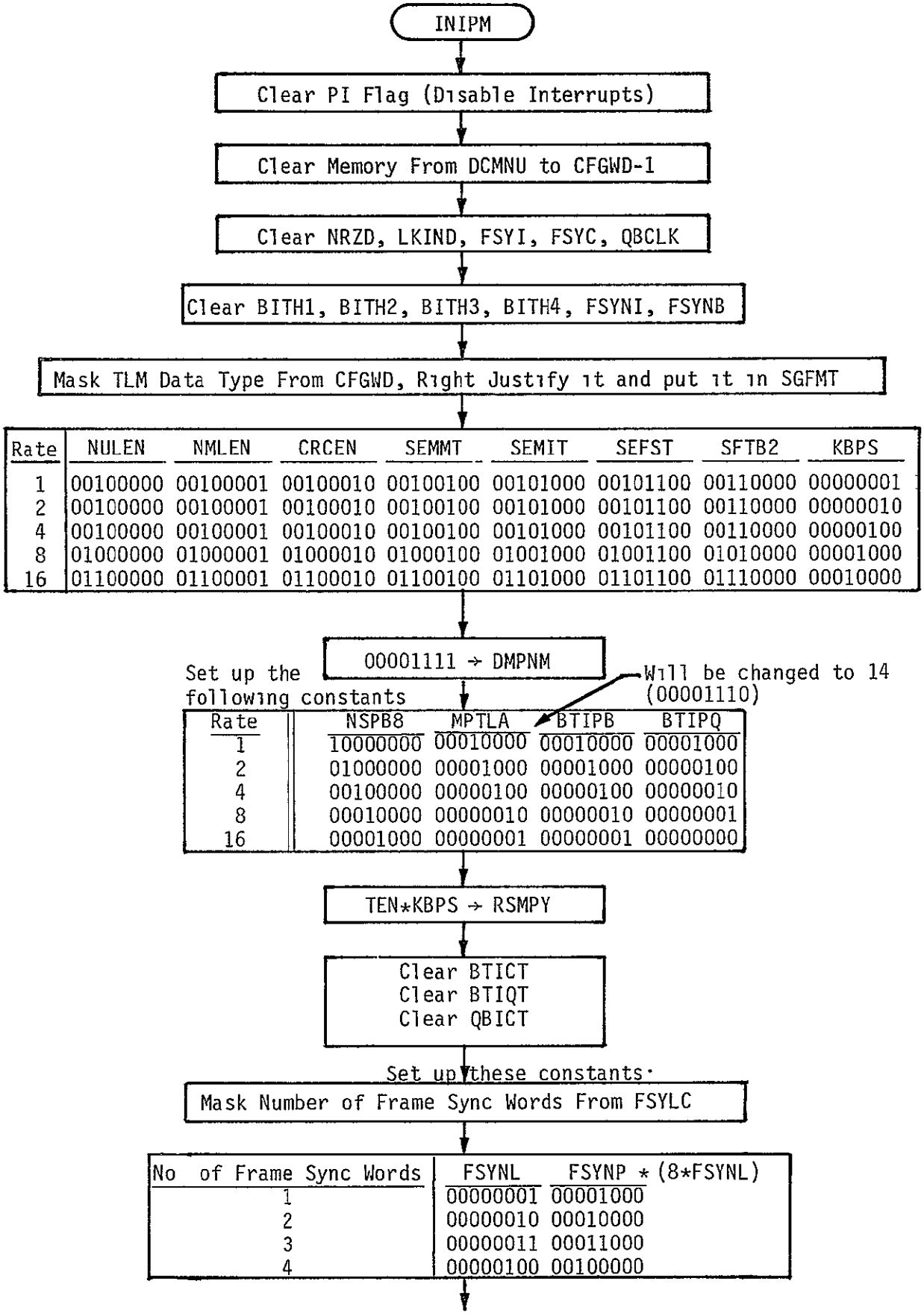

Rate	NULEN	NMLEN	CRCEN	SEMMT	SEMIT	SEFST	SFTB2	KBPS
1	00100000	00100001	00100010	00100100	00101000	00101100	00110000	00000001
2	00100000	00100001	00100010	00100100	00101000	00101100	00110000	00000010
4	00100000	00100001	00100010	00100100	00101000	00101100	00110000	00000100
8	01000000	01000001	01000010	01000100	01001000	01001100	01010000	00001000
16	01100000	01100001	01100010	01100100	01101000	01101100	01110000	00010000

Rate	NSPB8	MPTLA	BTIPB	BTIPQ
1	10000000	00010000	00010000	00001000
2	01000000	00001000	00001000	00000100
4	00100000	00000100	00000100	00000010
8	00010000	00000010	00000010	00000001
16	00001000	00000001	00000001	00000000

No of Frame Sync Words	FSYNL	FSYNP * (8*FSYNL)
1	00000001	00001000
2	00000010	00010000
3	00000011	00011000
4	00000100	00100000

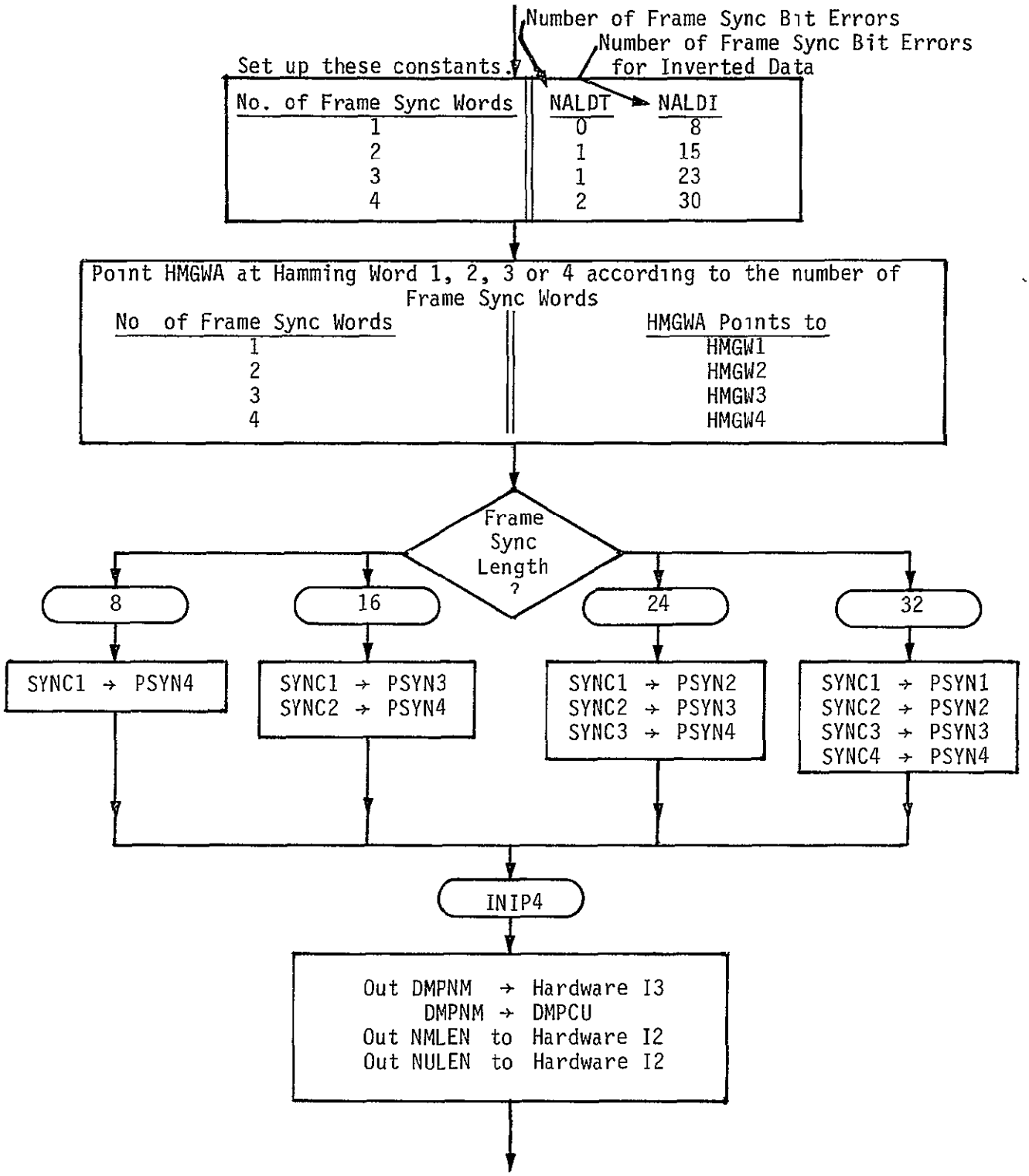

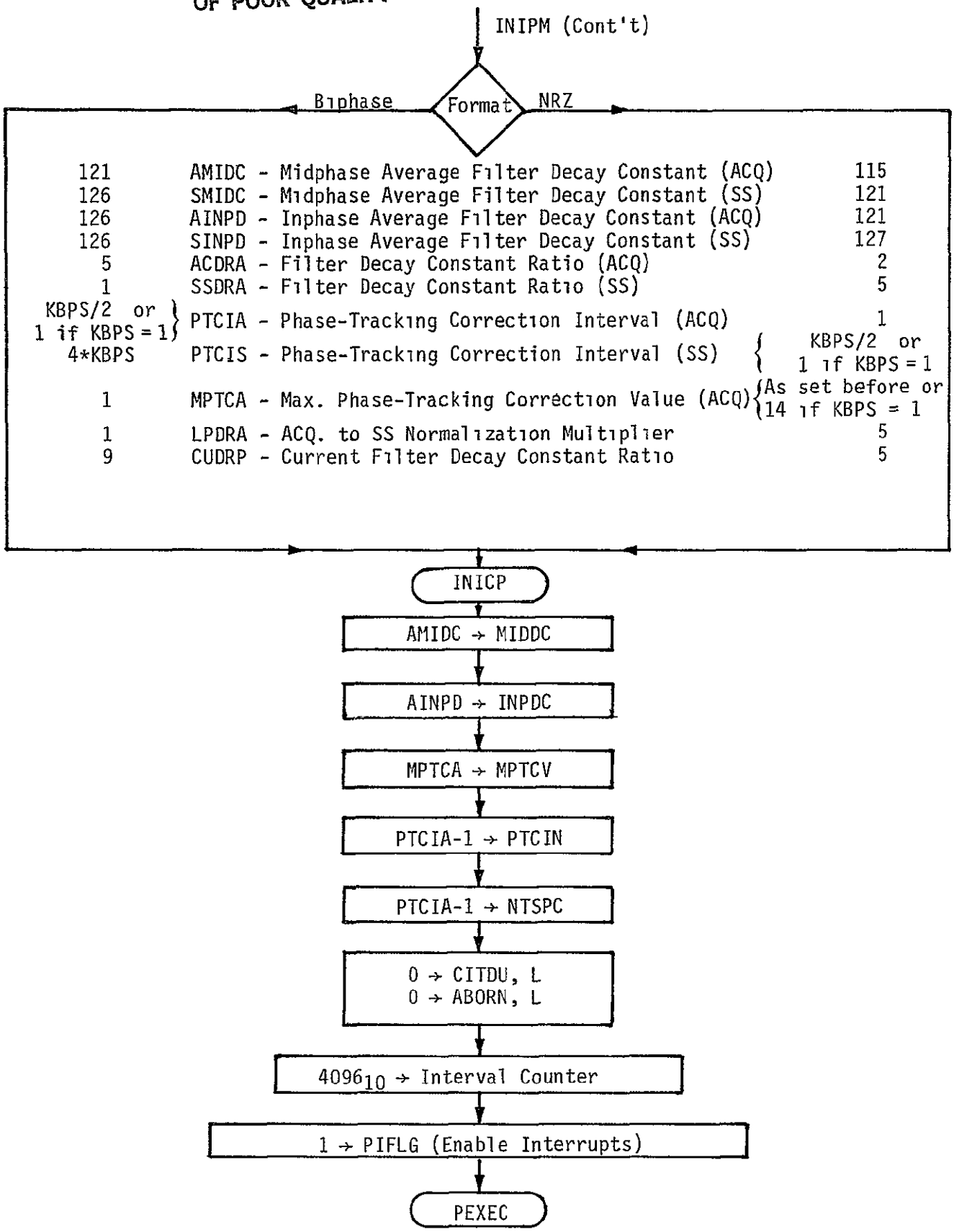

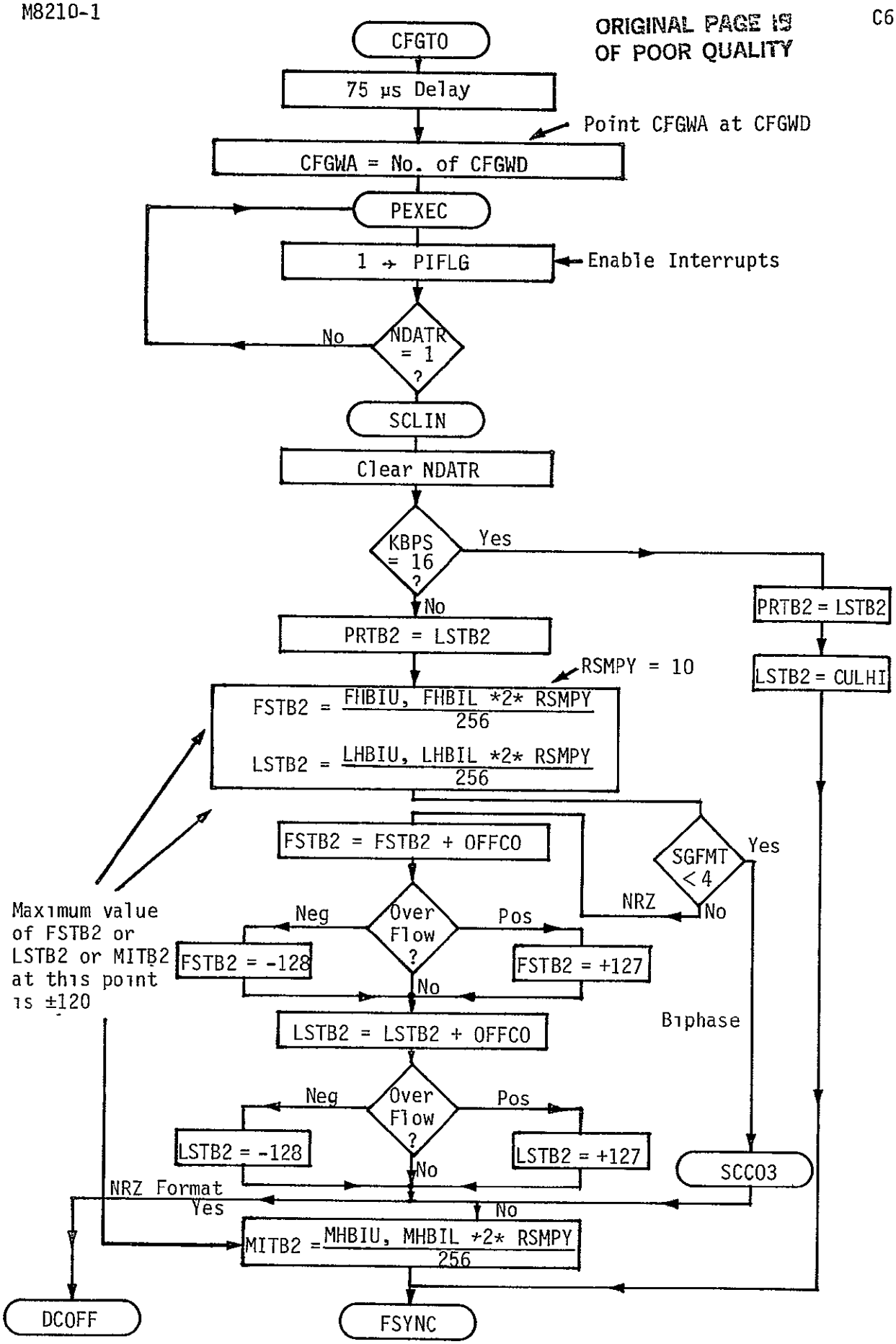

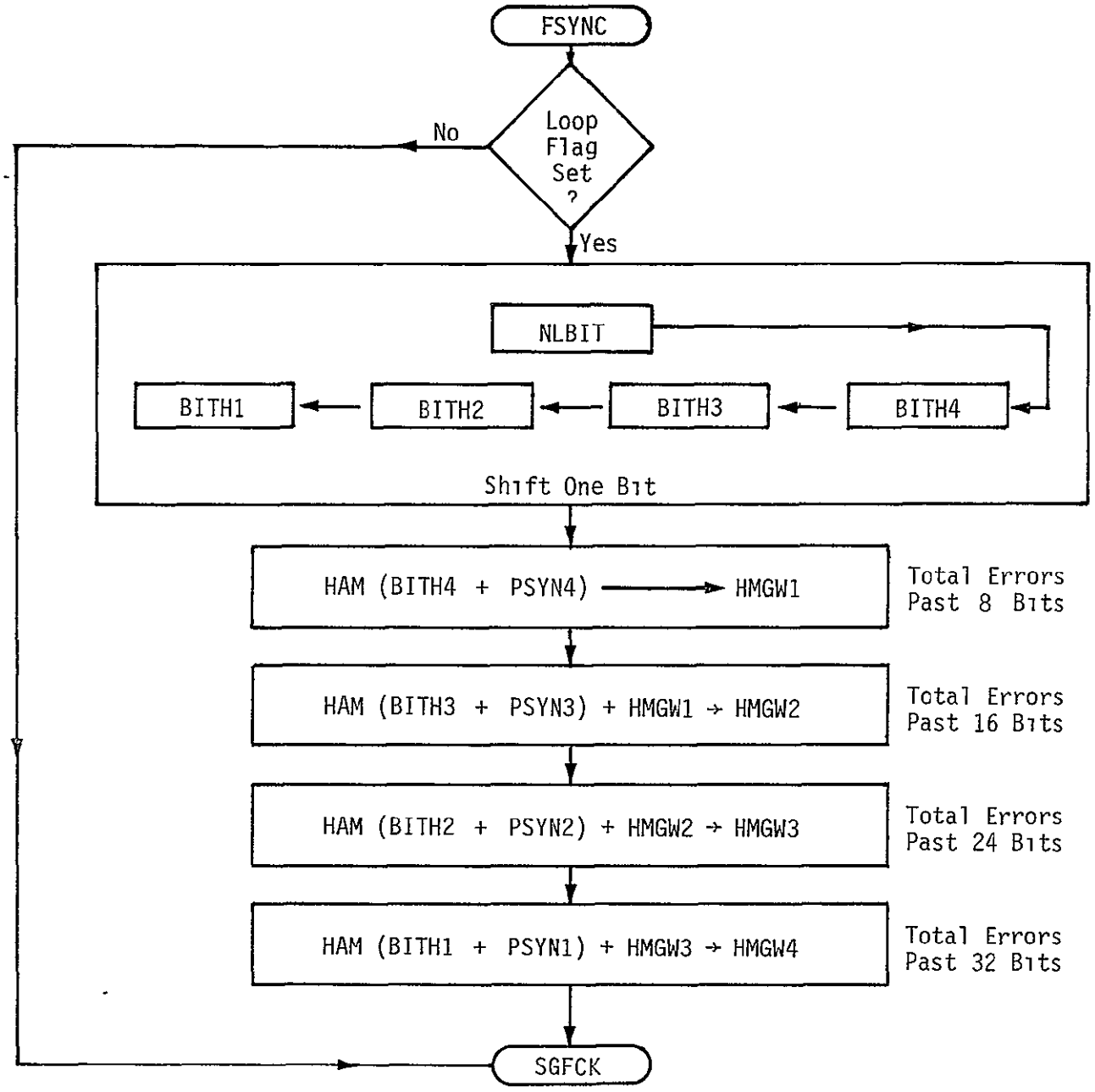

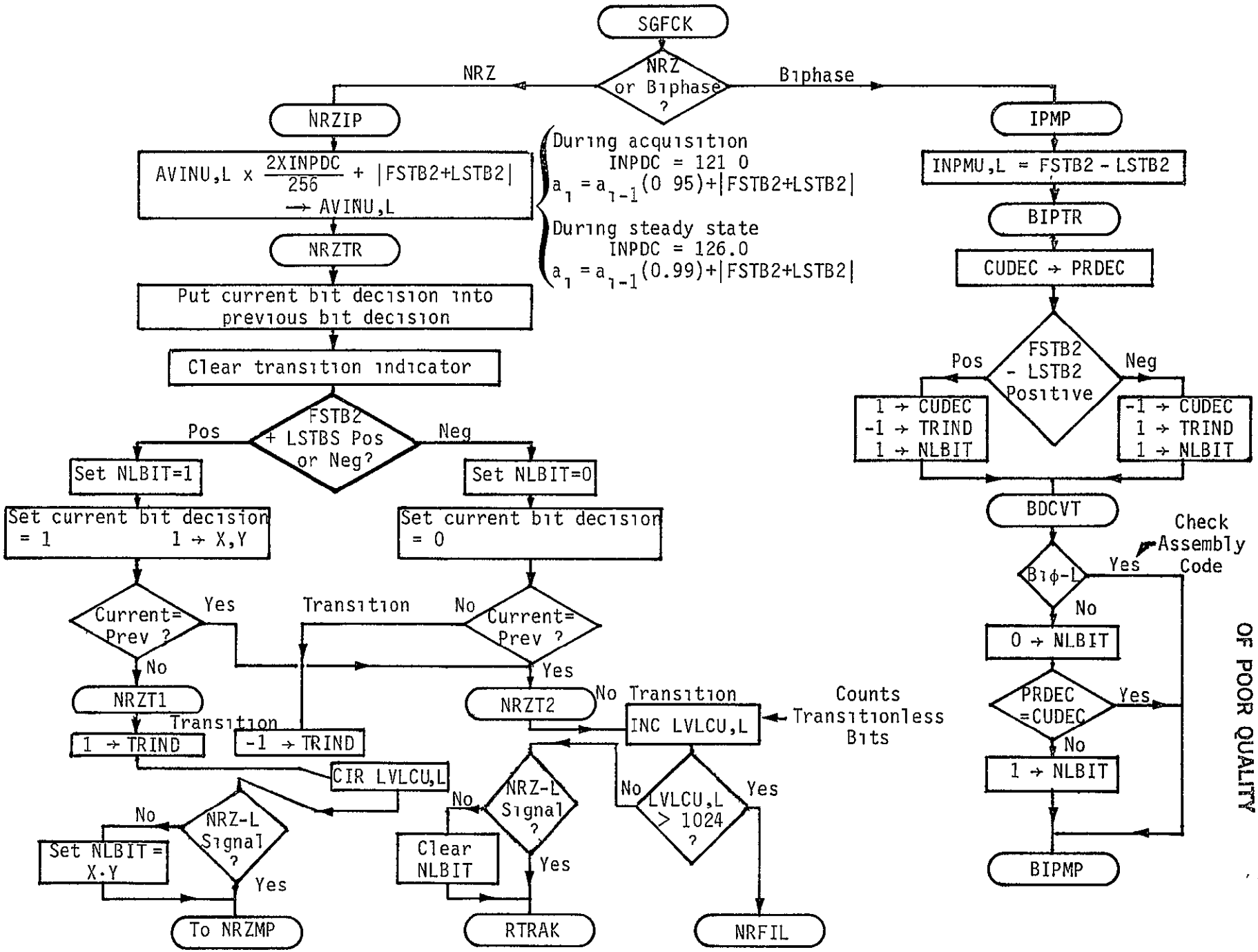

M8210-1

ORIGINAL PAGE IS OF POOR QUALITY

C8

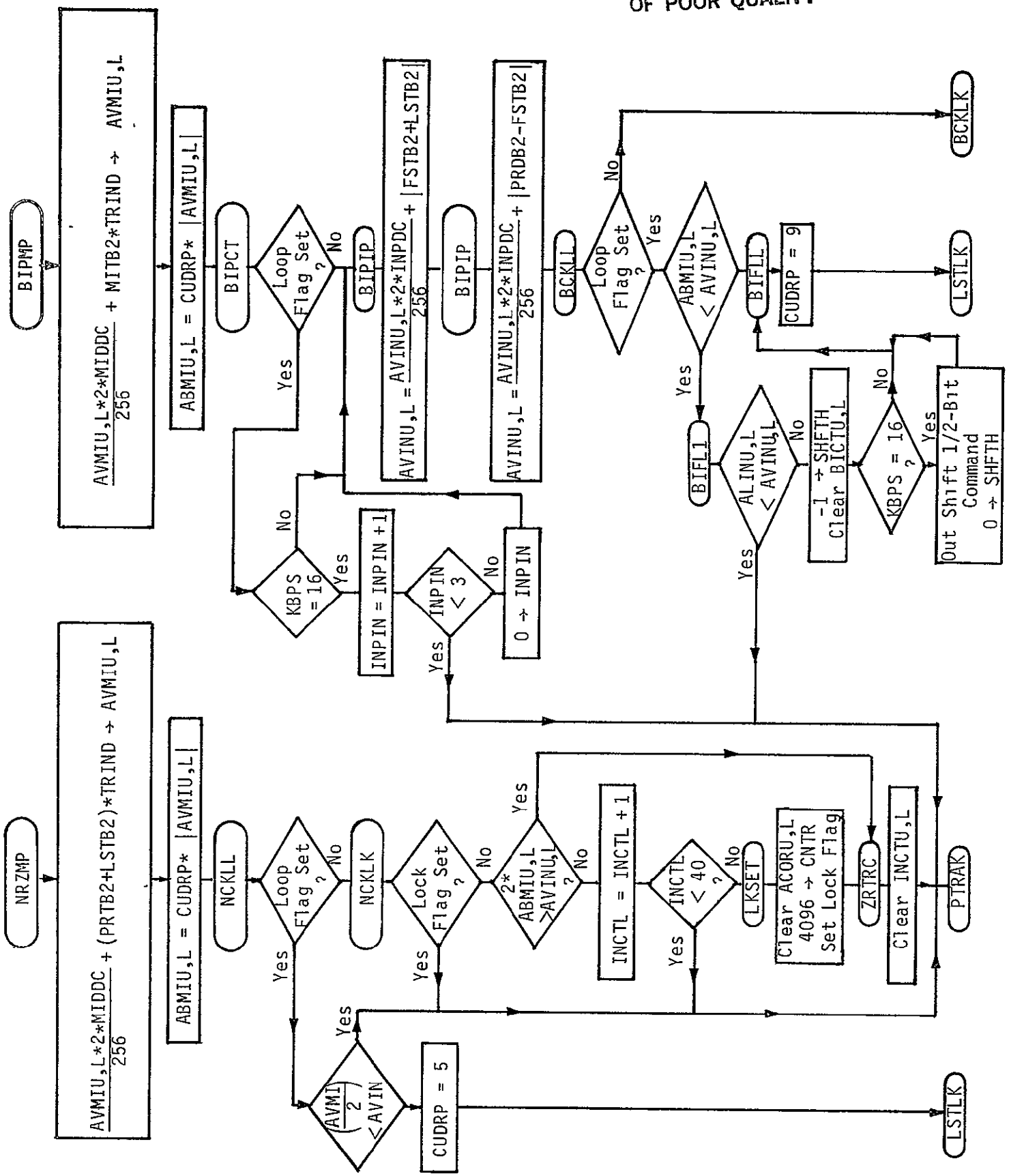

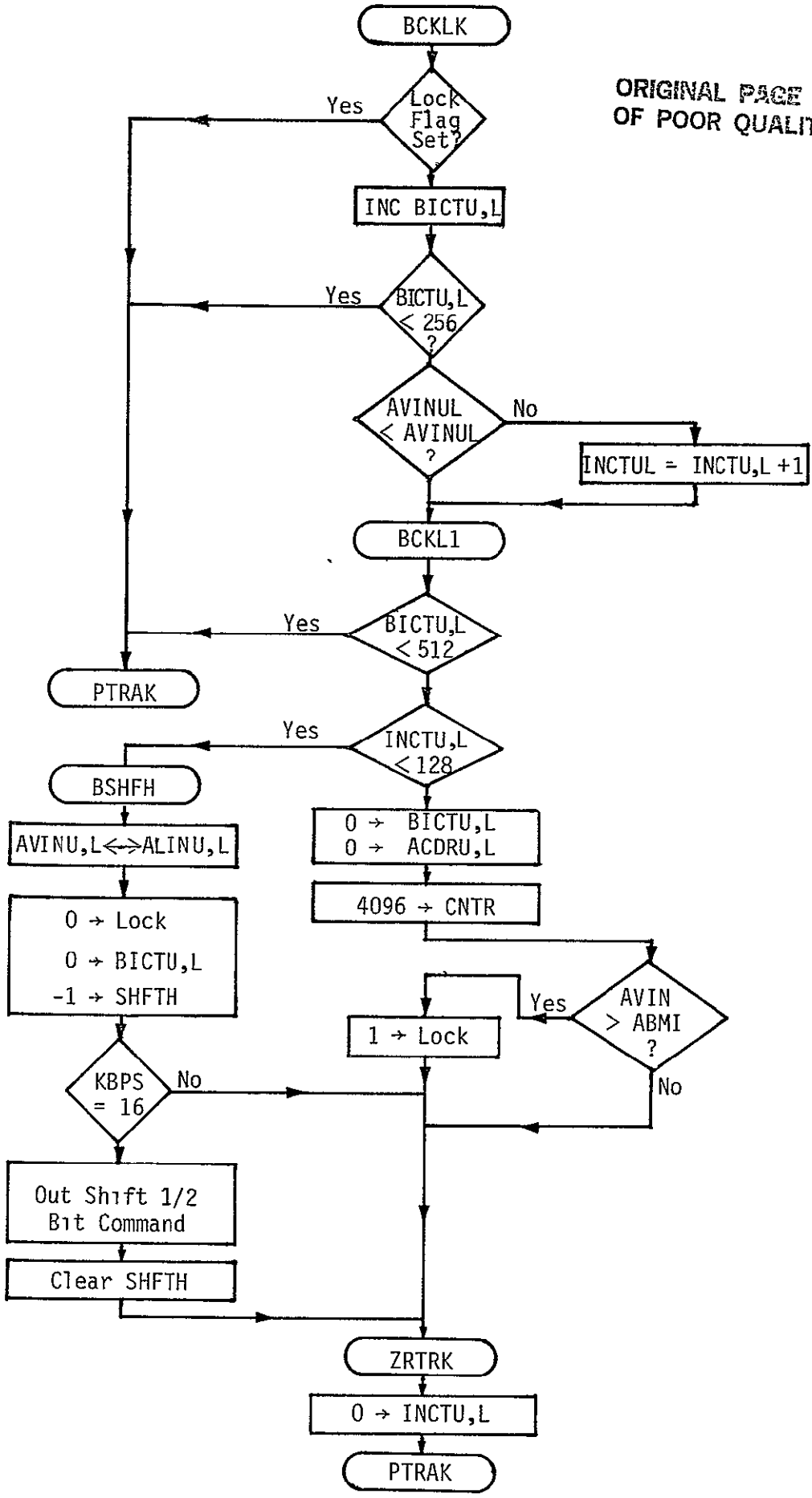

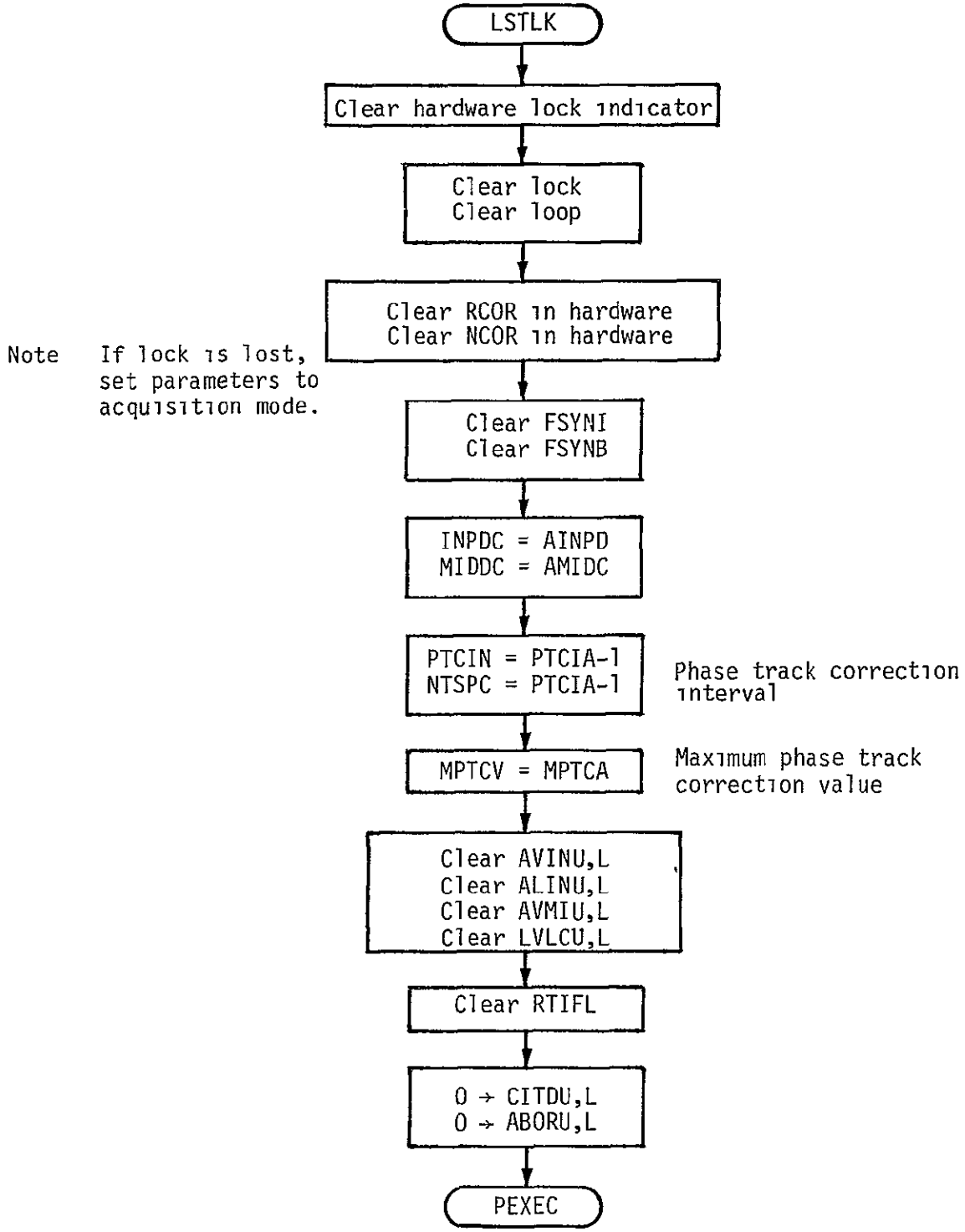

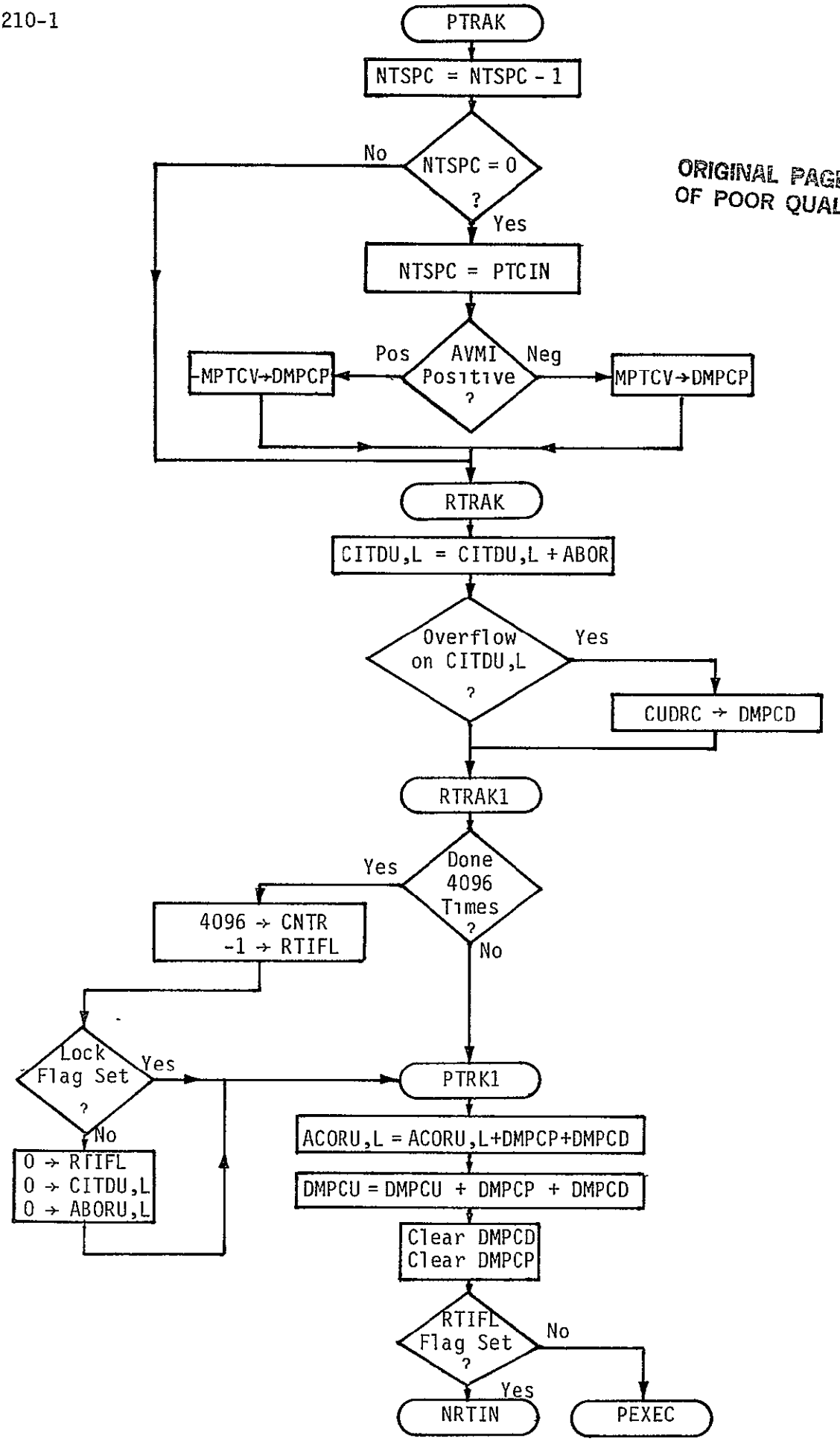

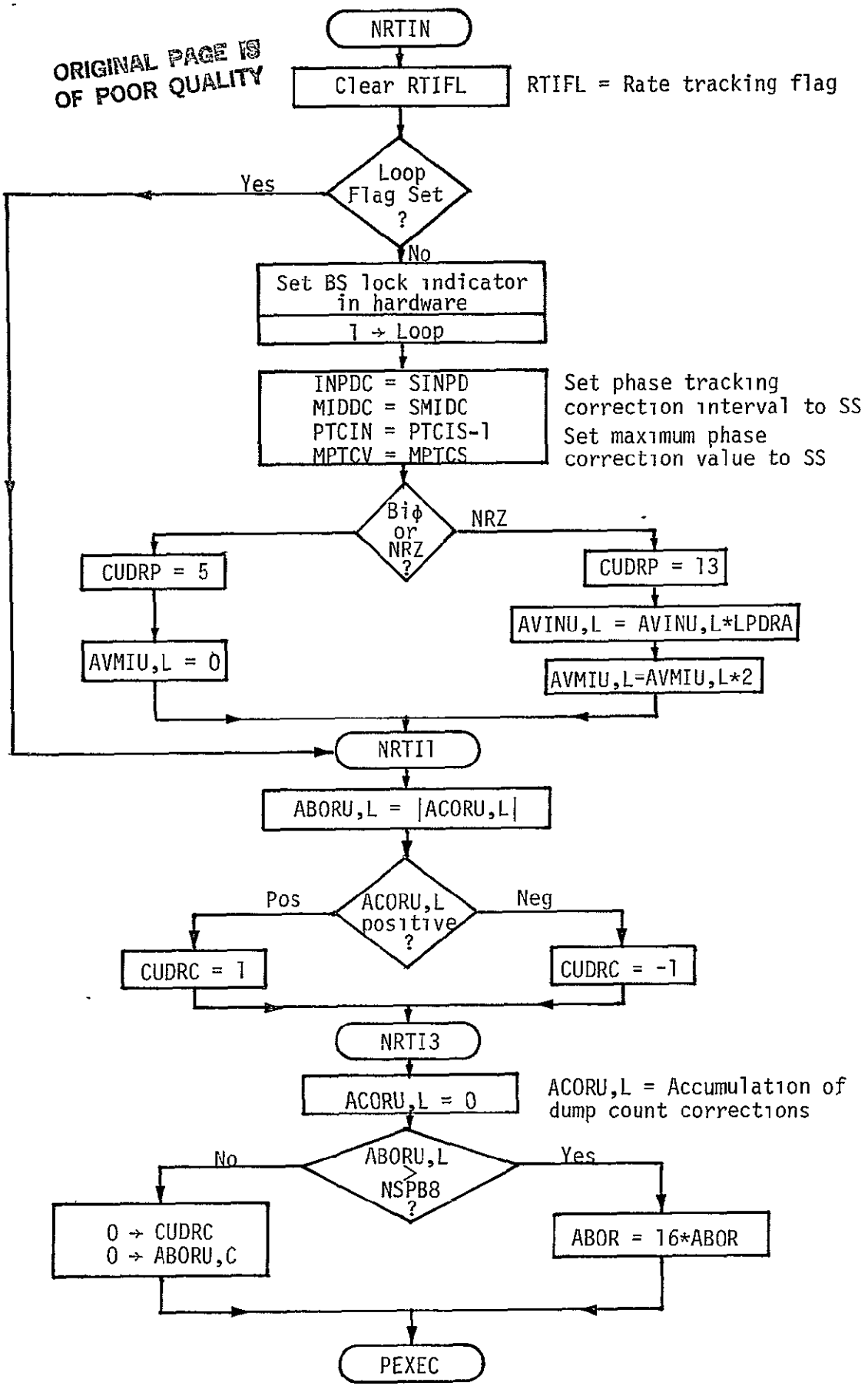

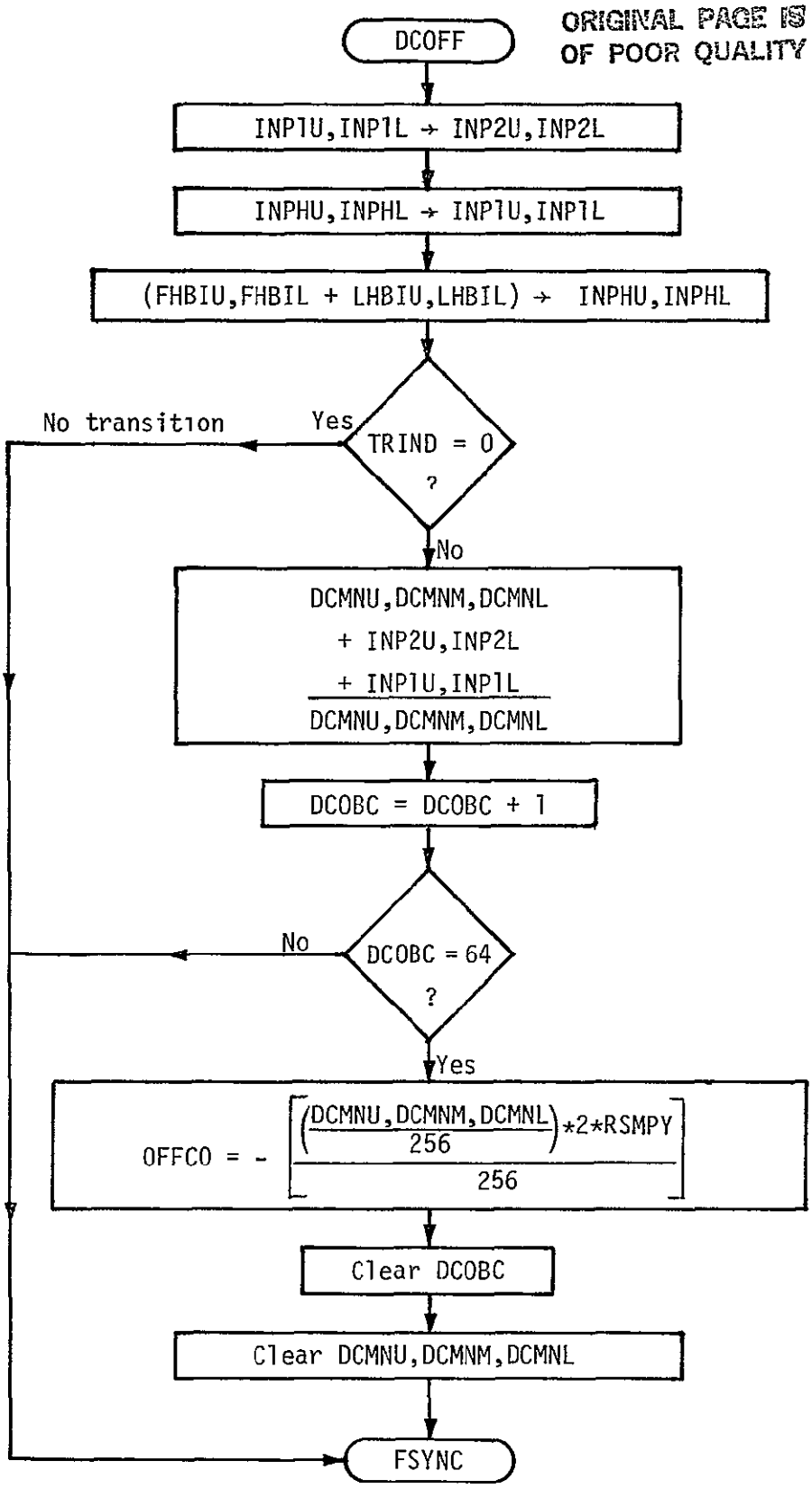

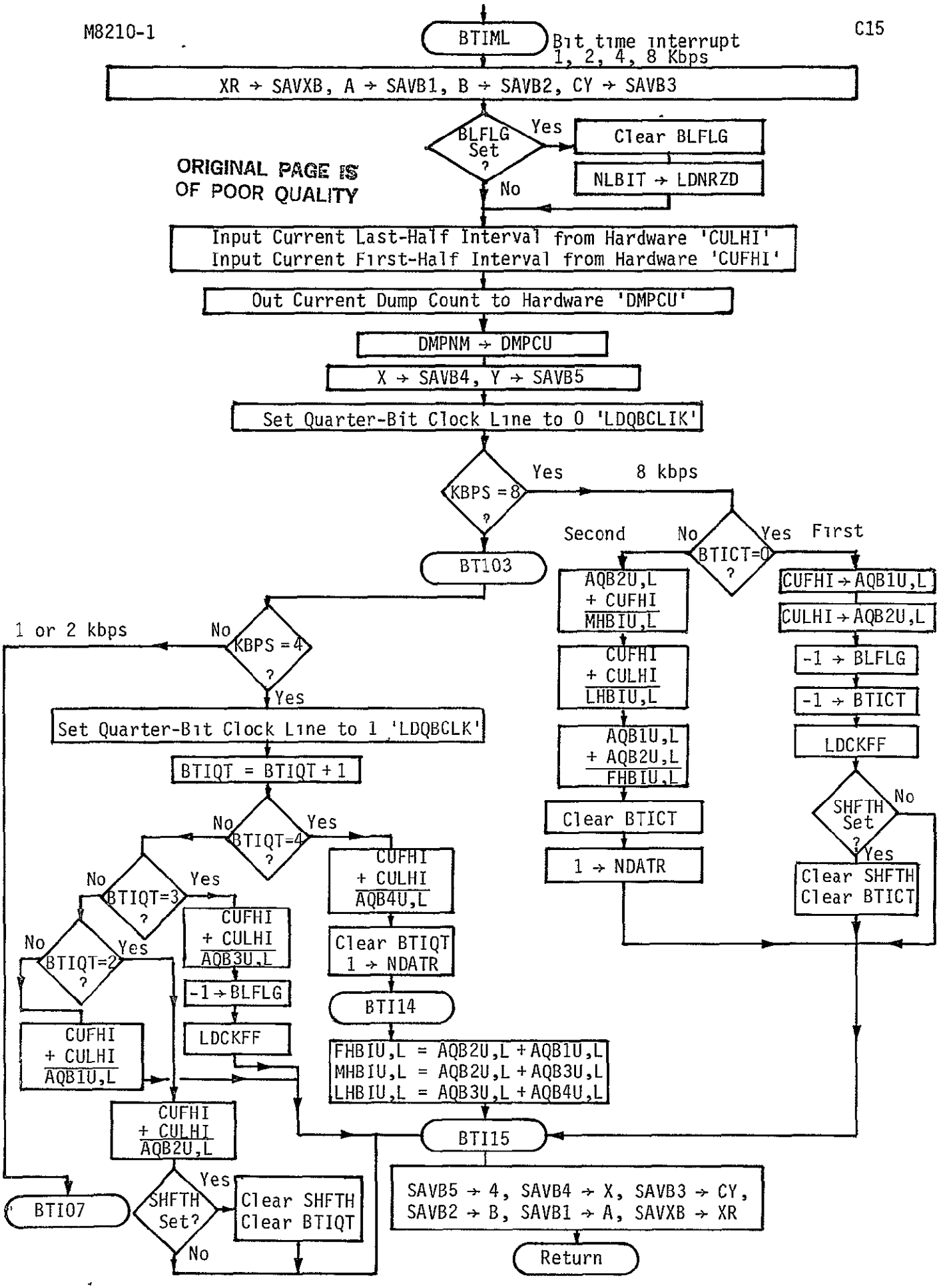

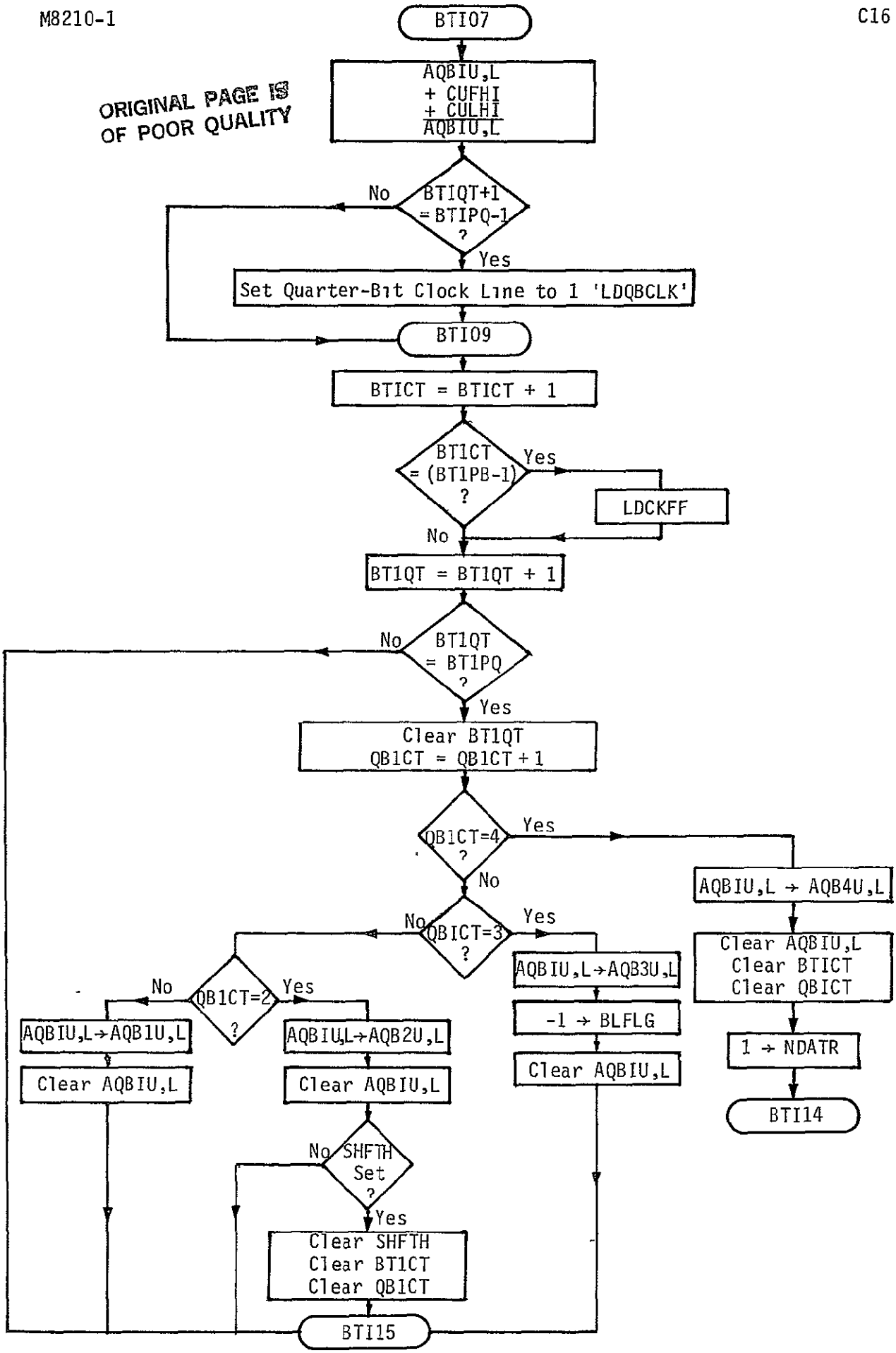

Bit time interval for 16 kbps only

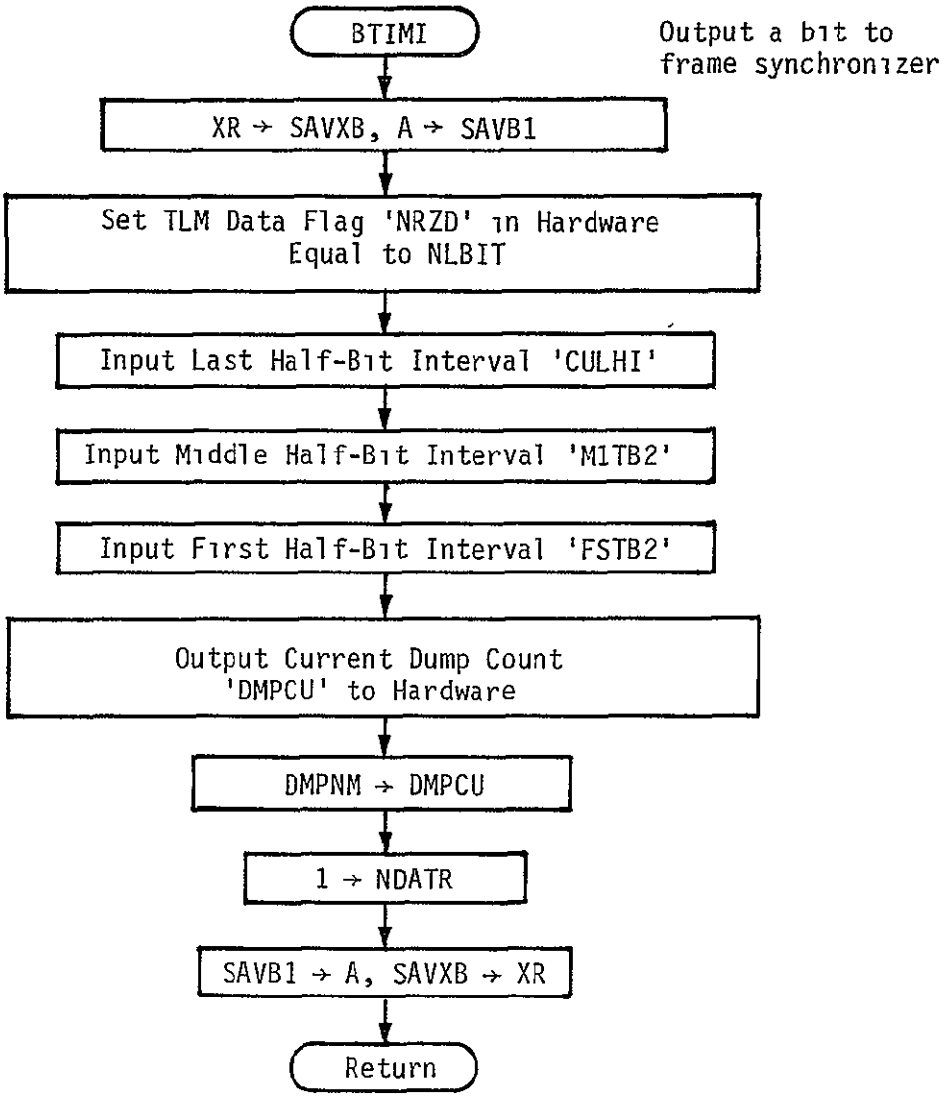

Echo Configuration to Hardware

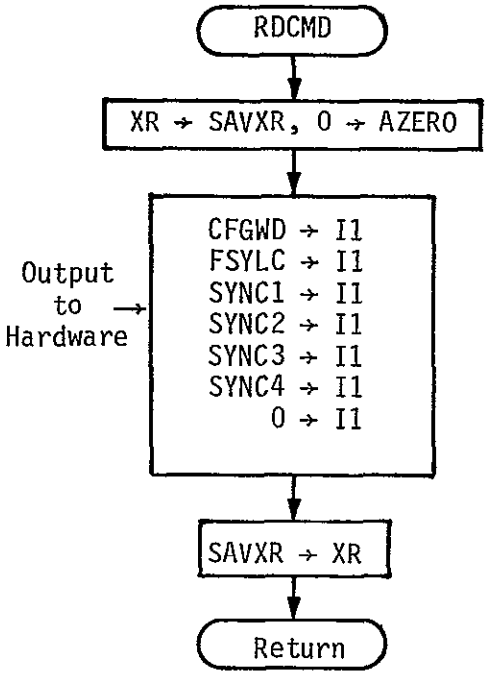

Hardware issues PROGM Interrupt six times to set configuration

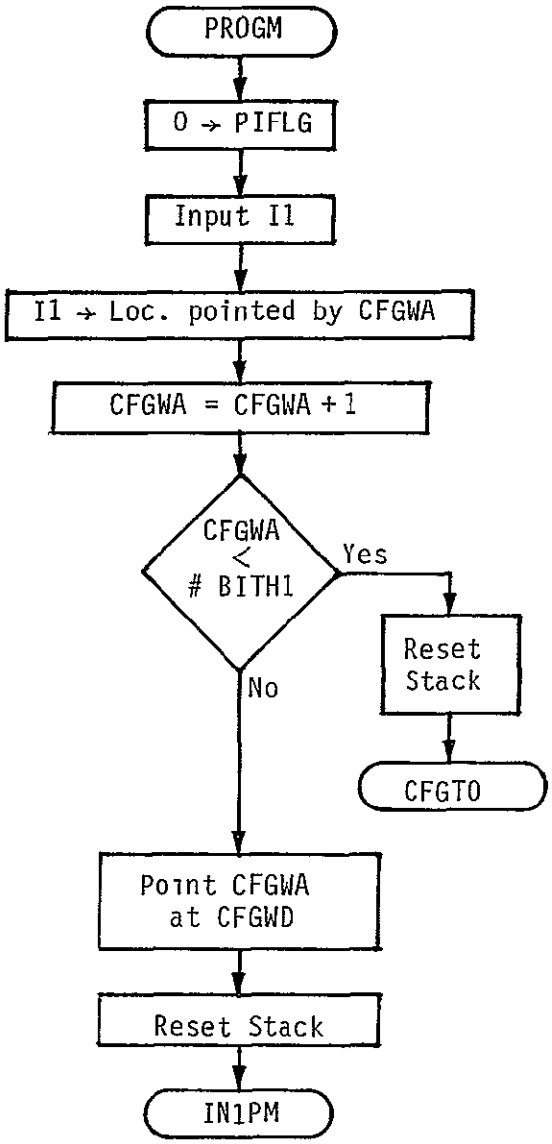

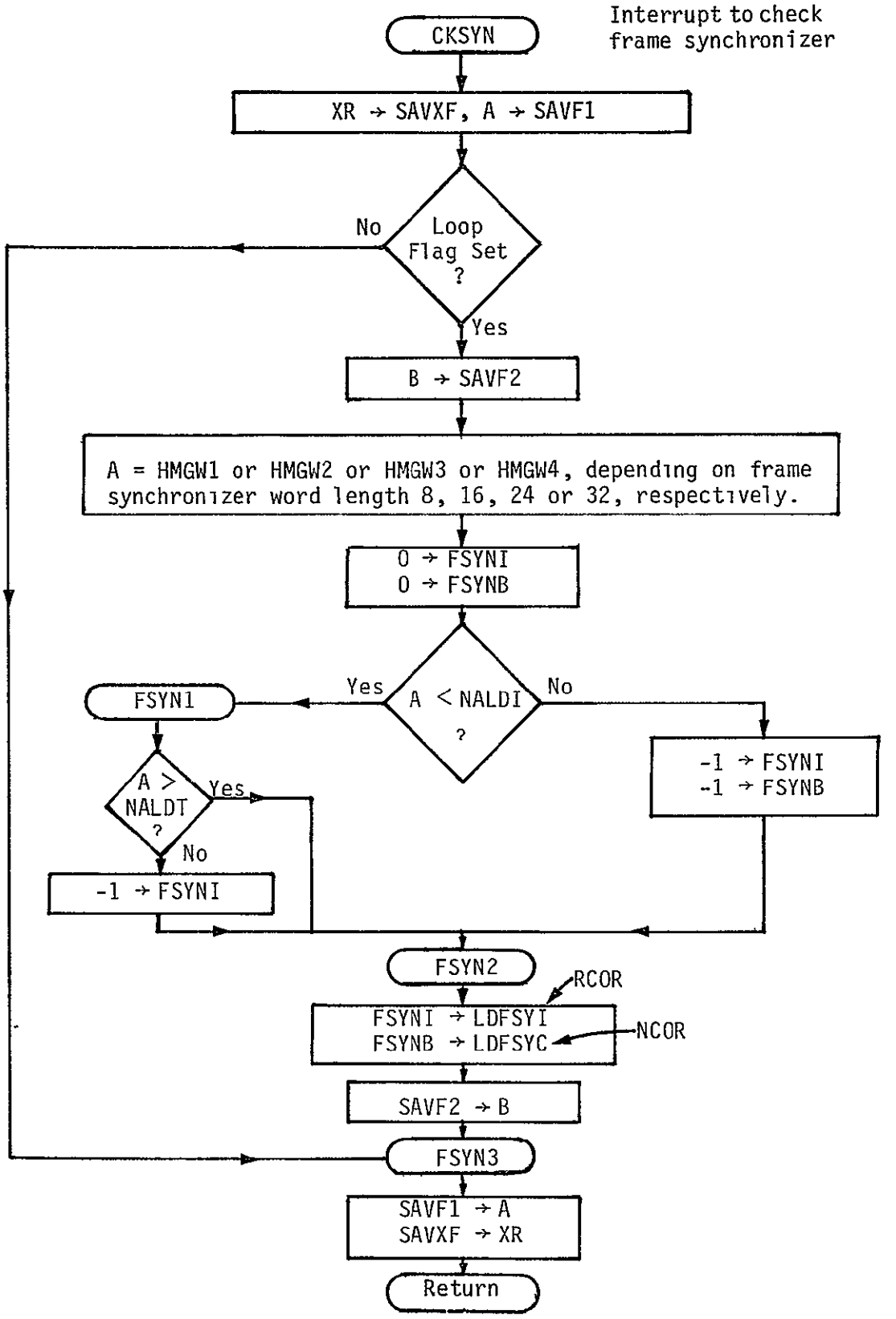
Interrupt to check frame synchronizer
CKSYN
XR → SAVXF, A → SAVF1
No
Loop Flag Set ?
Yes
B → SAVF2
A = HMGW1 or HMGW2 or HMGW3 or HMGW4, depending on frame synchronizer word length 8, 16, 24 or 32, respectively.
0 → FSYNI
0 → FSYNB
Yes
A < NALDI ?
No
FSYN1
A > NALDT ?
Yes
No
-1 → FSYNI
-1 → FSYNI
-1 → FSYNB
FSYN2
RCOR
FSYNI → LDFSYI
FSYNB → LDFSYC
NCOR
SAVF2 → B
FSYN3
SAVF1 → A
SAVXF → XR
Return

APPENDIX D

AMENDMENTS TO BIT SYNCHRONIZER ACQUISITION TIMES

The bit synchronizer shall acquire in four seconds with a probability of at least 0.9, with the E_b/N_0 value specified in Table D.1 below for the given data format.

Table D.1. Data Format Versus Data Rate E_b/N_0 Values

Format	E_b/N_0 (dB) Required				
	1 kbps	2 kbps	4 kbps	8 kbps	16 kbps
NRZ L, M, S	9.5	6 5	4.5	2.5	5 5
Biphase L, M, S	9 5	7 5	5 5	3 5	5 5

10.0 SHUTTLE/TDRSS AND GSTDN COMPATIBILITY ANALYSIS

While Task 5, Space Shuttle/TDRSS and GSTDN Compatibility Analysis, was directed at the overall system compatibility, many of the analyses were performed as part of the individual communication subsystems, such as the S-band network equipment and the Ku-band communication system. Under this task, Axiomatix attended all TDRSS design reviews, evaluated review material and, together with NASA JSC personnel, generated Review Item Dispositions (RID's). The final TDRSS design review which Axiomatix attended was the TDRSS Ground Segment Final Design Review at TRW, September 22-24, 1981. At this design review, Axiomatix was still concerned that the ground segment decoder could not achieve branch synchronization with the all-zero sequence. An action item was submitted at the design review to resolve this problem. The final resolution was to inform the users in the payload ICD (NASA JSC ICD No. 2-19001) that branch synchronization is not achieved until the number of transitions is greater than 64 and the maximum number of consecutive bits without a transition is less than 64 within any sequence of 512 bits.

During the design review, TRW stated that the Ku-band open-loop pointing budget would be revised. While relaxation of the open-loop pointing budget could be troublesome for Shuttle Ku-band acquisition, it was learned that TRW intends to tighten this budget. Axiomatix reviewed the current pointing budget and found that no changes had been made during the past two years. An action item was written in order to prompt TRW to update the pointing budget in light of current knowledge regarding the system parameters.

This section discusses two of the analyses performed to establish compatibility between the Shuttle Ku-band communication system and the TDRSS. These analyses involve (1) the TDRSS Antenna Scan for Shuttle Acquisition and (2) the Power Spectral Density of Staggered Quadriphase PN With Identical Sequences. For additional analyses concerning Shuttle/TDRSS and GSTDN compatibility, refer to sections of this report dealing with the individual communication subsystems.

10.1 TDRSS Antenna Scan for Shuttle Acquisition

Axiomatix was asked to review and comment on an investigation funded by Goddard Space Flight Center regarding the feasibility of effecting a TDRS scan during Shuttle acquisition. This study was conducted in response to a

concern voiced by NASA/JSC and Axiomatix as to the ability of the TDRS Ku-band to open-loop point to within 0.22° of the Shuttle.

The study explores the possibility of using externally generated (NASA) or internally generated (TDRSS) scan patterns. In the former case, a NASA-supplied processor inputs updated state vectors to the TDRSS from the NASA Network Control Center (NCC). The disadvantage of this approach is that, in order to account for TDRSS/NASA propagation delays of the state vectors and signal status, the scan must be slowed down. The latter approach uses a TDRSS computer to generate a scan, which conceivably could result in a faster scan since the NASA/TDRSS interface is eliminated. Since it corrects on-track errors only, the use of a Δt adjustment is not considered an acceptable solution.

Axiomatix finds no fault with the conclusions reached in the Goddard study; however, the fundamental systems question--how to implement an acquisition procedure--was not addressed, i.e., "what signal is the TDRSS supposed to find?" It is unlikely that the Shuttle will be able to open-loop point to the TDRS accurately enough to provide a strong signal, and we cannot expect both the TDRS and the Shuttle to scan simultaneously.

10.2 Power Spectral Density of Staggered Quadriphase PN with Identical Sequences

Axiomatix Report No. R8010-7, "The Power Spectral Density of Staggered Quadriphase PN With Identical Sequences," dated October 27, 1980, analyzes some of the TDRSS waveforms to determine the power spectral density and the effect on processing gain against interference.

THE POWER SPECTRAL DENSITY OF STAGGERED QUADRIPHASE PN WITH IDENTICAL SEQUENCES

Contract No. NAS 9-16067

Interim Report

Prepared by

M. K. Simon

Axiomatix

9841 Airport Blvd., Suite 912
Los Angeles, California 90045

Axiomatix Report No. R8010-7
October 27, 1980

THE POWER SPECTRAL DENSITY OF STAGGERED QUADRIPHASE PN WITH IDENTICAL SEQUENCES

By

Marvin K. Simon

1.0 INTRODUCTION

Staggered quadriphase PN is a direct-sequence spread spectrum technique which employs a complex spreading waveform. Such a communication system offers twice the processing gain of the corresponding system employing a real spreading waveform since, in the former, the interference energy will be distributed equally in the two quadrature channels while, in the latter, all the interference energy appears in the data channel.

More often than not, the two PN sequences will be independent of one another and, thus, the power spectral density (PSD) of the spread spectrum waveform is determined by the waveform of either sequence In this report, we examine the effect on the PSD using the same PN sequence on both channels (except for the 1/2-chip delay between the two).

2.0 CALCULATION OF THE POWER SPECTRAL DENSITY

A staggered quadriphase PN spread spectrum signal may be written in the form

$$x(t) = \sqrt{2S}\, Re\left\{m(t)s(t)\, \exp(j\omega_0 t)\right\} \tag{1}$$

where S is the average signal power, m(t) is a unit power digital data modulation, ω_0 is the carrier frequency in rad/sec, and s(t) is the complex spreading waveform, namely,

$$s(t) = \left[PN_1(t) + j\, PN_2(t)\right]/\sqrt{2} \tag{2}$$

Here we consider the case where $PN_1(t) = PN(t)$ and $PN_2(t) = PN_1(t - \Delta/2)$, where Δ is the PN chip interval. Assuming for simplicity that m(t) is a real modulation, e.g , BPSK, combining (1) and (2) then gives

$$x(t) = \sqrt{S}\, m(t)\left[PN(t)\cos\omega_0 t - PN(t-\Delta/2)\sin\omega_0 t\right] \tag{3}$$

Furthermore, since the data rate of m(t) is typically much lower than the PN chip rate (large processing gain), we may ignore m(t) in our power spectrum calculation. Thus, we are interested in the PSD of the normalized signal

$$y(t) = PN(t)\cos\omega_0 t - PN(t-\Delta/2)\sin\omega_0 t \tag{4}$$

The autocorrelation function of y(t) is easily seen to be

$$\begin{aligned} R_y(\tau) &\triangleq \overline{\langle y(t)\, y(t+\tau)\rangle} \\ &= R_{PN}(\tau)\cos\omega_0\tau + \frac{1}{2}\left[R_{PN}(\tau+\Delta/2) - R_{PN}(\tau-\Delta/2)\right]\sin\omega_0\tau \end{aligned} \tag{5}$$

where $\langle\ \rangle$ denotes time average, the overbar denotes statistical average, and $R_{PN}(\tau)$ is the autocorrelation function of the PN sequence. Taking the Fourier transform of (5), we get

$$\begin{aligned} S_y(\omega) &= \frac{1}{2}\left[S_{PN}(\omega-\omega_0) + S_{PN}(\omega+\omega_0)\right] \\ &\quad + \frac{1}{2}\int_{-\infty}^{\infty} R_{PN}(\tau+\Delta/2)\sin\omega_0\tau\, e^{-j\omega\tau}\, d\tau \\ &\quad - \frac{1}{2}\int_{-\infty}^{\infty} R_{PN}(\tau-\Delta/2)\sin\omega_0\tau\, e^{-j\omega\tau}\, d\tau \end{aligned} \tag{6}$$

Letting $x = \tau+\Delta/2$ or $\tau-\Delta/2$ in the second and third terms of (6), the sum of these two terms becomes

$$\frac{1}{2j}\int_{-\infty}^{\infty} \frac{1}{2} R_{PN}(x)\left[e^{-j(\omega-\omega_0)(x-\Delta/2)} - e^{-j(\omega+\omega_0)(x-\Delta/2)}\right] dx$$

$$- \frac{1}{2j}\int_{-\infty}^{\infty} \frac{1}{2} R_{PN}(x)\left[e^{-j(\omega-\omega_0)(x+\Delta/2)} - e^{-j(\omega+\omega_0)(x+\Delta/2)}\right] dx$$

$$= \frac{1}{2} S_{PN}(\omega-\omega_0) \sin\left[(\omega-\omega_0)\Delta/2\right] - \frac{1}{2} S_{PN}(\omega+\omega_0) \sin\left[(\omega+\omega_0)\Delta/2\right] \tag{7}$$

Finally, using (7) in (6) gives the desired result, namely,

$$\boxed{\begin{aligned} S_y(\omega) = {} & \frac{1}{2} S_{PN}(\omega-\omega_0)\left\{1 + \sin\left[(\omega-\omega_0)\Delta/2\right]\right\} \\ & + \frac{1}{2} S_{PN}(\omega+\omega_0)\left\{1 + \sin\left[(\omega+\omega_0)\Delta/2\right]\right\} \end{aligned}} \tag{8}$$

The corresponding result for independent PN sequences $PN_1(t)$ and $PN_2(t)$ would be simply

$$\boxed{S_y(\omega) = \frac{1}{2} S_{PN}(\omega-\omega_0) + \frac{1}{2} S_{PN}(\omega+\omega_0)} \tag{9}$$

Note that (8) and (9) are valid independent of the shape of the PN pulse.

As an example, consider the common case of a rectangular PN pulse. For long codes, we may then describe the PSD of the sequence by its envelope, namely,

$$S_{PN}(\omega) = \Delta\left[\frac{\sin\left(\frac{\omega\Delta}{2}\right)}{\frac{\omega\Delta}{2}}\right]^2 \tag{10}$$

Substituting (10) into (8) yields

$$S_y(\omega) = \frac{\Delta}{2}\left\{\frac{\sin\left[(\omega-\omega_0)\Delta/2\right]}{(\omega-\omega_0)\,\Delta/2}\right\}^2\left[1+\sin\left[(\omega-\omega_0)\Delta/2\right]\right]$$

$$+\frac{\Delta}{2}\left\{\frac{\sin\left[(\omega+\omega_0)\Delta/2\right]}{(\omega+\omega_0)\,\Delta/2}\right\}^2\left[1-\sin\left[(\omega+\omega_0)\Delta/2\right]\right] \qquad (11)$$

Figure 1 is an illustration of $S_y(\omega)$ as described by (11). For simplicity, we show the result for positive ω only with the understanding that $S_y(\omega)$ is an even function of ω Also shown in dotted lines is the corresponding result for independent PN sequences obtained by substituting (10) into (9).

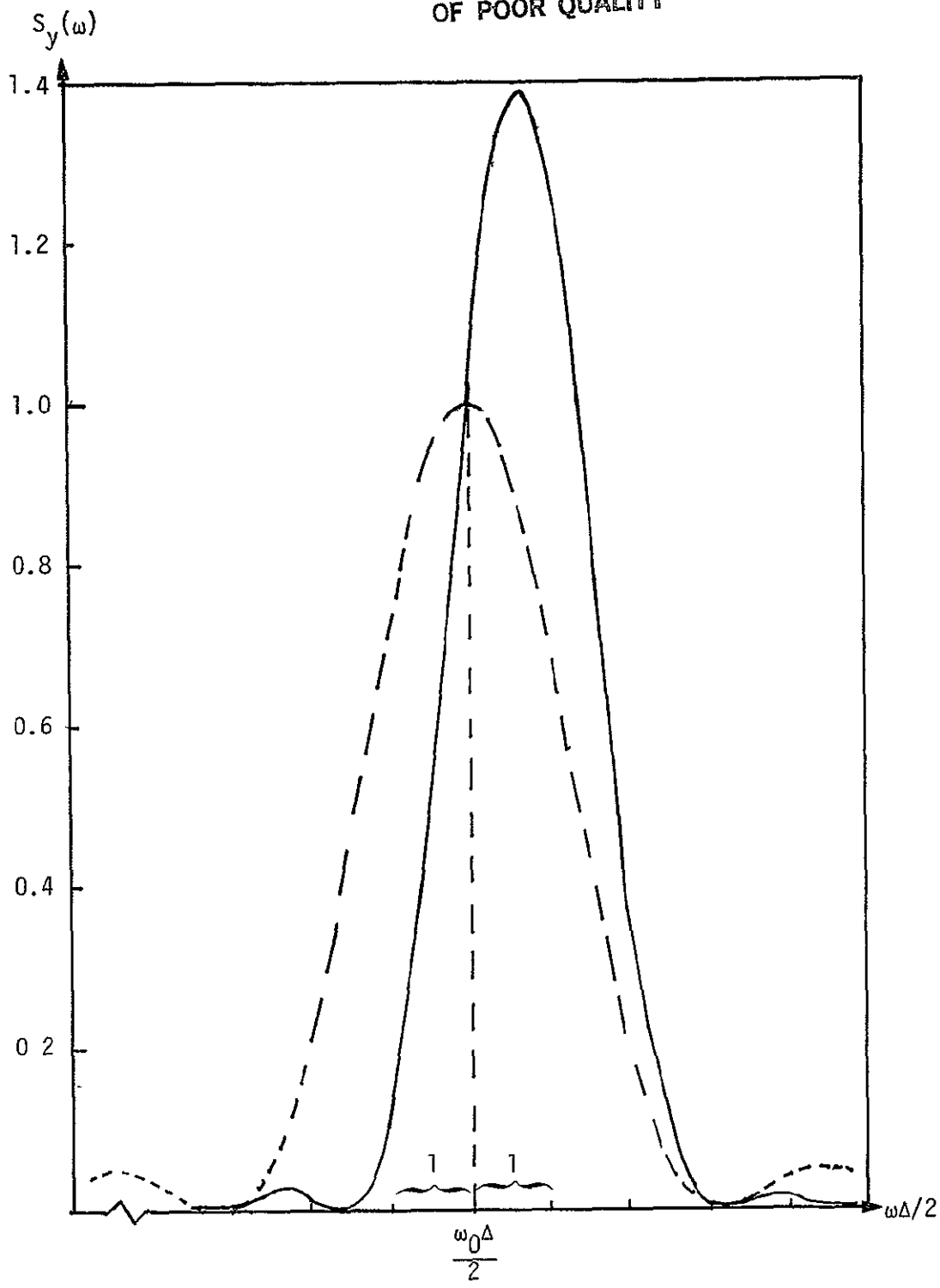

Figure 1. Power Spectral Density for Staggered Quadriphase PN